THM Modelling of the Bentonite Buffer During Water Uptake for NWMO's Emplacement Room

NWMO-TR-2023-05 **February 2024**

Daniel Malmberg

Ola Kristensson

Alex Spetz

Clay Technology Lund AB

nwmo
NUCLEAR WASTE MANAGEMENT ORGANIZATION
SOCIÉTÉ DE GESTION DES DÉCHETS NUCLÉAIRES

Nuclear Waste Management Organization
22 St. Clair Avenue East, 4th Floor
Toronto, Ontario
M4T 2S3
Canada

Tel: 416-934-9814
Web: www.nwmo.ca

THM Modelling of the Bentonite Buffer During Water Uptake for NWMO's Emplacement Room

NWMO-TR-2023-05

February 2024

Daniel Malmberg, Ola Kristensson, Alex Spetz
Clay Technology Lund AB

Document History

Title:	THM Modelling of the Bentonite Buffer During Water Uptake for NWMO's Emplacement Room		
Report Number:	TR-2023-05		
Revision:	R000	Date:	February 2024
Clay Technology Lund AB			
Authored by:	Daniel Malmberg, Ola Kristensson, Alex Spetz		
Verified by:	Billy Fälth		
Approved by:	Billy Fälth		
Nuclear Waste Management Organization			
Reviewed by:	Chang Seok Kim, Ken Birch, Ruiping Guo, Peter Keech		
Accepted by:	Paul Gierszewski		

Revision Summary		
Revision Number	**Date**	**Description of Changes/Improvements**
R000	2024-02	Initial issue

ABSTRACT

Title: **THM Modelling of the Bentonite Buffer During Water Uptake for NWMO's Emplacement Room**
Report No.: **NWMO-TR-2023-05**
Author(s): Daniel Malmberg, Ola Kristensson, Alex Spetz
Company: Clay Technology Lund AB
Date: February 2024

Canada's concept for isolation of the used fuel is based on final storage in a deep geological repository. The used fuel will be placed inside copper-coated containers, which are surrounded by highly compacted bentonite blocks to support the container and to prevent the potential release of radionuclides. Gaps between the bentonite blocks and rock wall will be filled with granular bentonite.

While the clay is unsaturated at installation, water uptake from the surrounding rock will lead to an increase in moisture content, and eventually the bentonite is expected to become fully saturated. As bentonite is a montmorillonite rich clay, this water uptake will cause it to swell and fill any remaining voids in the emplacement room. The swelling will also begin to homogenize the dry densities between the different clay components, while at the same time a swelling pressure will develop.

In this report thermo-hydro-mechanical modelling of the evolution in the bentonite buffer during water uptake in NWMO's emplacement room concept is presented. The modelling was carried out in a stepwise manner, where the initial focus was to start out from simplistic models and thereafter constructing more realistic representations of the geometry and materials. The scope was then expanded to carry out a sensitivity analysis of the geometry as well as to investigate how the THM evolution of the bentonite buffer was affected by the properties of the host rock.

One major simplification of the modelling is that the host rock was not included in the modelled geometry. Its influence on the evolution in the bentonite was instead included in the models using boundary conditions which were constructed to represent generic crystalline or sedimentary host rocks. The rate of inflow from the rock was varied between different models to analyze how the THM evolution in the bentonite buffer changed if the selected host rock had high or low water inflow rates.

The modelling explored different inflow scenarios (e.g., homogeneous and heterogeneous inflows) and effects of various dry densities of the buffer components on the final state of the buffer.

TABLE OF CONTENTS

Page

LIST OF TABLES

Page

LIST OF FIGURES

Page

1. INTRODUCTION

NWMO's planned repository for used nuclear fuel consists of a geological repository situated at a depth of between 500 and 800 meters. The site of the repository was not determined when this modelling was carried out, both crystalline and sedimentary geospheres were considered as host rocks for the repository.

Tunnels, so-called emplacement rooms, will be blast excavated in the host rock. Due to the excavation method, there will be a variation in the cross-sectional area of the tunnels. A smooth driving surface within the emplacement room will be achieved by the construction of a concrete floor.

The used fuel will be encapsulated into copper-coated steel containers, so called Used Fuel Containers (UFCs). These will be placed in a buffer box, consisting of two Highly Compacted Bentonite (HCB) blocks with a cavity inside to accommodate the UFC. The buffer boxes will be placed in a stacked configuration in NWMO's emplacement room, see Figure 1-1. At installation, the buffer boxes are separated by HCB spacer blocks to reduce the maximum temperature in the buffer. The remaining gap between the walls/ceiling and the buffer boxes will be filled up with granular bentonite, denoted Gap Fill Material (GFM). A schematic illustration of the geometry is shown in Figure 1-1.

The chosen bentonite has a high montmorillonite content, which implies a high swelling capacity. When the buffer takes up groundwater from the host rock it will swell, and remaining voids will be filled. Initial density heterogeneities will, to some extent, decrease and the buffer will homogenize. Since the emplacement room provides a confined space, the swelling will generate compressive stress, a swelling pressure.

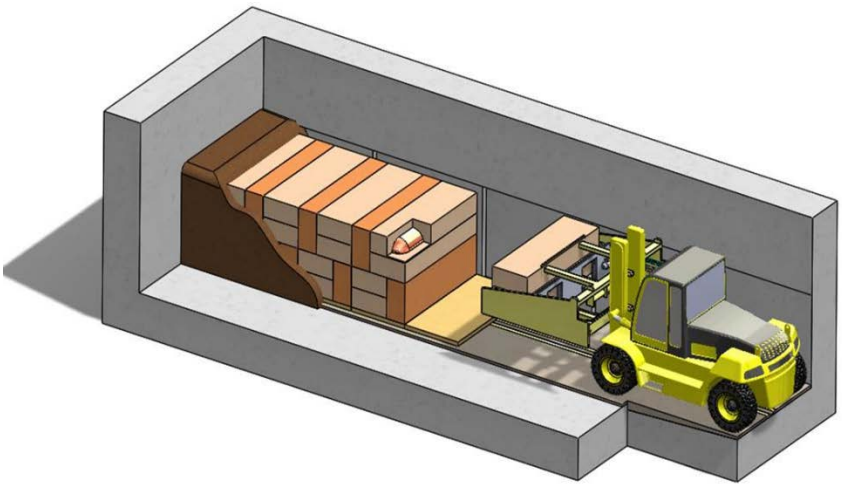

Figure 1-1: Schematic illustration of the stacking of buffer boxes in the emplacement room

The water uptake, swelling, and density homogenization change the properties of the clay due to its strong dependence on water content and dry density. Bentonite has a strong hydro-mechanical coupling (Karnland et al. 2006 and Dixon 2019) where changes in the mechanical state change its hydraulic properties and vice versa. There is a dependence between thermal and hydraulic processes as well.

To investigate how the bentonite buffer will behave in the repository, and how well it will fulfill defined safety functions, numerical models can be used to study, for example: temperature evolution in the repository, water uptake evolution in the buffer, development of swelling pressure, and the density homogenization process of the buffer. To obtain representative simulations of the bentonite buffer, it is often necessary to solve fully coupled thermo-hydro-mechanical (THM) models.

The work presented here was carried out 2016 - 2023 and was previously reported in separate NWMO Technical Memos for Step 1, Step 2, and Tasks 1 - 4 respectively. The described numerical modelling of the evolution in the buffer during the water-uptake phase was performed using the FEM solver CODE_BRIGHT, previously used in, for example, modelling included in the license application by SKB in Sweden (Åkesson et al. 2010a & 2010b).

To give an overview of the work, brief descriptions of all the modelling activities are given in Section 2. Then, to avoid unnecessary repetition, the common part of the model setup is described in Section 3. Descriptions of the different modelling exercises, their results, and conclusions are provided in Sections 4-9. Finally, a general discussion and conclusions from the work are given in Section 10.

The first set of models in Step 1 and Step 2 can be categorised as scoping models where the primary goal was to test the ability to model the system using CODE_BRIGHT. These were carried out in a stepwise manner with increasing complexity and are described in Section 4 and Section 5.

After completion of these first steps, a more extensive modelling program was initiated. The focus of the program was to assess local THM evolution of the bentonite buffer during the water uptake phase. Typical local representations consisted of one vertical stack of buffer boxes with belonging spacer blocks and GFM. Four different tasks were analyzed, these are reported in Sections 6-9. These tasks typically investigated how the THM evolution in the bentonite buffer was influenced by different conditions such as:

- The rate of water inflow
- The heterogeneity of the water inflow
- Variations in installed densities and cross-sectional area of NWMO’s emplacement room
- Different host-rock sites

2. SUMMARY OF THE MODELLING CARRIED OUT BY CLAY TECHNOLOGY

In this section a brief description of each step/task in the modelling is provided.

Step 1: Proof of Concept
The first step focused on analyzing whether models with a simplified geometry; for example, using only the upper buffer box row; were feasible. The modelling was performed using a stepwise strategy, with increasingly more complex models. The results provided insights into the expected THM evolution in the bentonite buffer and showed that CODE_BRIGHT could be used to analyze the THM evolution during the water-uptake phase.

Step 2: Improving Representations
The second step of the modelling was primarily aimed at developing more realistic models, focusing on improving the geometry. In the Step 2 models both rows of buffer boxes (i.e., a vertical stack of buffer boxes) were included. This allowed for analyzing the influence of an offset between the two rows. This analysis was used as a foundation for the models developed in Tasks 1 to 4, with respect to both the modelled geometry and the material model setup. After establishing the modelling capability in Step 1 and Step 2, the numerical investigations were undertaken in four sequential tasks.

Task 1: Heterogeneous Wetting
In Task 1, the modelling carried out in Steps 1 and 2 was used as a starting point when analysing the THM evolution during heterogeneous inflow conditions. Tasks 1, 2 and 3 assumed a generic crystalline host rock. The previous models assumed that water would enter the emplacement room homogenously. This would be representative of a host rock with no “macroscopic” fractures, where only the porous “matrix” provided water to the buffer. For many cases, however, water will be provided to the buffer through fractures. Such localized inflow will potentially change the way the buffer swells and affect the final state of the bentonite buffer system. The models investigated both localized inflow at a single position of the emplacement room and heterogenous wetting of individual buffer boxes.

Task 2: Fracturing Due to Drying
In Task 2, methods for evaluating fracturing of the bentonite buffer in dry conditions were developed. These methods were intended for scenarios where there was no water inflow into the tunnel and where the buffer would dry/shrink, and fractures might occur. The main method decoupled the mechanical process from the hydraulic and thermal processes, which enabled sequential use of TH-models followed by postprocessing where the potential for fracturing was estimated. This was used in Task 4 where drying in a buffer box prior to installation was investigated.

Task 3: Sensitivity Study
A sensitivity study was carried out using the models of heterogeneous wetting simulated in Task 1 as a starting point. The goal was to understand how different emplacement room cross-sections and variations in the installed dry densities of the HCB and GFM could influence the THM evolution of the bentonite buffer. The effect of open airgaps between different buffer components was also studied.

Task 4: Sedimentary Host Rock & Drying before Installation
Task 4 consisted of two separate subtasks. The first subtask was similar to Task 1 but incorporated a representation for a sedimentary host-rock. The change in rock type implied

changes to the modelled geometry, boundary conditions, and the buffer material parameters. The last change came from groundwater of higher salinity in the sedimentary rock which affect the hydro-mechanical behavior of the buffer significantly. In the second subtask, the TH evolution and potential fracturing of a single HCB buffer box during transport from the surface packaging plant down into NWMO's emplacement room was analyzed using the method developed in Task 2.

3. GENERAL INFORMATION ABOUT THE MODELLING

To avoid unnecessary repetition when describing the individual modelling steps/tasks, this section gives an overview of the theory and setup common to all models. All FE-models shared the same general formulation and had similar setups regarding geometry, constitutive laws, initial and boundary conditions. In this section, this common part of the models and calibration of the material parameters for different cases are described.

3.1 Numerical Tools

The modelling was carried out using the finite element solver, CODE_BRIGHT (Olivella et al., 1996 and Olivella et al., 2023), which is capable of simulating fully coupled THM processes in unsaturated porous media. CODE_BRIGHT was used together with the pre- and post-processor GiD (Coll et al. 2018), where geometries were created, simulations defined, and results analyzed. The FE-solver has been used extensively for modelling engineered barrier systems in nuclear waste repositories. As an example, numerical simulations using CODE_BRIGHT provided inputs to the license application in Sweden (Åkesson et al. 2010b). In addition, the open-source data analysis and visualization application ParaView was used in Task 4.

3.2 Theoretical Background

CODE_BRIGHT is based on a traditional geo-mechanical porous formulation. A detailed theoretical description can be found in (Olivella et al. 1996), here a summary is given. The mathematical description can be divided into different categories as follows:

- Balance equations
- Equilibrium restrictions
- Constitutive equations
- Initial conditions
- Boundary conditions

The balance equations and equilibrium restrictions cannot be changed in CODE_BRIGHT. In the formulation, displacements $\boldsymbol{u}$, liquid pore pressure p_l, gas pore pressure p_g, and temperature, T are selected as independent variables. The remaining variables are called dependent, and are governed by material-specific constitutive relations, described in Section 3.3. In addition, initial conditions (described in Section 3.5), and boundary conditions (described in Section 3.6) must be defined.

The gas pressure was prescribed to 0.1 MPa in all simulations since the relatively low temperatures (<100 °C) will not generate vapour to such extent as to increase the gas pressure significantly above atmospheric pressure.

In the formulation used in CODE_BRIGHT each point has three components: minerals (m), water (w), and air (a), and an assumption of three immiscible phases: solid (s), liquid (l), and gas (g) is made. Here, the solid phase only consists of the mineral component (i.e., $m = s$), so the component superscript index m will not be used in the following.

From the structural assumptions of the mixture, the following primitives can be defined:

- mixture/total volume element (v),
- solid phase volume (v_s),
- liquid phase volume (v_l),
- gas phase volume ($v_g = v - v_s - v_l$), and
- pore volume ($v_p = v - v_s$).

Further primitives, regarding mass and energy are introduced for the constituents:

- solid mass (m_s),
- water mass in liquid (m_l^w),
- water mass in gas (i.e., water vapour mass) (m_g^w),
- dry air mass in gas (m_g^a),
- specific internal energy for minerals in solid (e_s),
- specific internal energy for water in liquid (e_l^w),
- specific internal energy for water in gas (e_g^w), and
- specific internal energy for air in gas (e_g^a).

Using these primitives, the following quantities can be defined:

- porosity: $\phi = v_p/v$
- solid (specific) density: $\rho_s = m_s/v_s$
- liquid (specific) density: $\rho_l = m_l/v_l$
- liquid water mass per liquid phase volume: $\theta_l^w = m_l^w/v_l$
- water vapour mass per gas phase volume: $\theta_g^w = m_g^w/v_g$
- dry air mass per gas phase volume: $\theta_g^a = m_g^a/v_g$
- degree of liquid saturation: $S_l = v_l/v_p$
- degree of gas saturation: $S_g = v_g/v_p$
- water content: $w = m_l/m_s$

3.2.1 Mass Balance of Solid

The solid mass per mixture volume element can be expressed as,

$$\frac{m_s}{v} = \frac{m_s}{v_s}\frac{v - v_p}{v} = \rho_s(1 - \phi)\,. \tag{3-1}$$

By using this, the mass balance equation for the solid can be written as,

$$\frac{\partial}{\partial t}\big(\rho_s(1 - \phi)\big) + \nabla \cdot (\boldsymbol{j}_s) = 0\,. \tag{3-2}$$

$\boldsymbol{j}_s$ is the mass flux of the solid:

$$\boldsymbol{j}_s = \rho_s(1 - \phi)\frac{d\boldsymbol{u}}{dt}\,, \tag{3-3}$$

where $d\boldsymbol{u}/dt$ is the velocity of the solid skeleton.

3.2.2 Mass Balance of Water

The water mass per mixture volume element can be expressed as:

$$\frac{m^w}{v} = \frac{m_l^w + m_g^w}{v} = \theta_l^w S_l \phi + \theta_g^w S_g \phi \,, \tag{3-4}$$

By introducing a source term f^w and fluxes of water in liquid and gas phase ($\boldsymbol{j}_l^w$ and $\boldsymbol{j}_g^w$) the mass balance of water can be expressed as:

$$\frac{\partial}{\partial t}\left(\theta_l^w S_l \phi + \theta_g^w S_g \phi\right) + \nabla \cdot \left(\boldsymbol{j}_l^w + \boldsymbol{j}_g^w\right) = f^w \,. \tag{3-5}$$

3.2.3 Balance of Forces

The quasi-static formulation of the balance of momentum (balance of forces) for the porous media reads,

$$\nabla \cdot \boldsymbol{\sigma} + \boldsymbol{b} = \boldsymbol{0} \,, \tag{3-6}$$

where the total stress, $\boldsymbol{\sigma}$, and body force, $\boldsymbol{b}$, are included. In the present formulation ordinary continuum mechanics sign conventions are used, i.e., stress components are positive for tensile conditions.

3.2.4 Energy Balance for the Medium

A continuity equation for energy can be formulated by adding the specific internal energies, e_p^e, for all phases p and elements e per volume element:

$$\frac{\sum e_p^e m_p^e}{v} = e_s \rho_s (1-\phi) + e_l^w \theta_l^w S_l \phi + e_g^w \theta_g^w S_g \phi + e_g^a \theta_g^a S_g \phi \,, \tag{3-7}$$

a source term f^e, and fluxes $\left(\boldsymbol{i}_c, e_l^w \boldsymbol{j}_l^w, e_g^w \boldsymbol{j}_g^w, e_g^a \boldsymbol{j}_g^a\right)$. The first element, $\boldsymbol{i}_c$, in the given set of fluxes, is the conductive heat flux of the mixture as a whole and the other energy fluxes are due to mass transport of the constituents with respect to the solid. The energy balance equation can thus be written as:

$$\begin{aligned} &\frac{\partial}{\partial t}\left(e_s \rho_s (1-\phi) + e_l^w \theta_l^w S_l \phi + e_g^w \theta_g^w S_g \phi + e_g^a \theta_g^a S_g \phi\right) + \\ &\qquad \nabla \cdot \left(\boldsymbol{i}_c + e_l^w \boldsymbol{j}_l^w + e_g^w \boldsymbol{j}_g^w + e_g^a \boldsymbol{j}_g^a\right) = f^e \,. \end{aligned} \tag{3-8}$$

3.2.5 Equilibrium Restrictions

In addition to the balance equations, there are three equilibrium restrictions, a thermal, a mechanical and a phase-change equilibrium restriction. The thermal equilibrium restriction states that all constituents are assumed to have a common temperature. In the mechanical equilibrium restriction, the effect from inertia is assumed to be insignificant (i.e., quasi-static conditions).

The timescale of the water phase changes is considered much shorter than the timescale of other processes in the porous medium, thus the two phases (vapour and liquid water) are assumed to always be in equilibrium. By adopting this, the psychrometric law is obtained for water:

$$\tilde{\theta}_g^w(p_l,T) = \frac{\tilde{p}_g^w(T)M_w}{R(273.15+T)}\exp\left(\frac{-(p_g-p_l)M_w}{R(273.15+T)\tilde{\rho}_l(p_l,T)}\right). \tag{3-9}$$

In the expression above, M_w, is the molar mass of water, R the gas constant, and p_g^w the partial vapour pressure.

3.2.6 Strain, Stress and Suction

Here, definitions of the small strain tensor and entities related to stress are given. CODE_BRIGHT uses a small strain formulation,

$$\boldsymbol{\varepsilon} = \frac{1}{2}\left(\frac{\partial \boldsymbol{u}}{\partial \boldsymbol{X}} + \frac{\partial \boldsymbol{u}}{\partial \boldsymbol{X}}^T\right), \tag{3-10}$$

where it is possible to add strain contributions. Material models are expressed in terms of the stress, $\boldsymbol{\sigma}$, which can be decomposed in a spherical and deviatoric part,

$$\boldsymbol{\sigma} = \frac{1}{3}\mathrm{tr}(\boldsymbol{\sigma})\mathbf{1} + \boldsymbol{s}\,, \tag{3-11}$$

where $\mathrm{tr}(\,)$ denotes the trace operator and $\mathbf{1}$ the second order unit tensor. The spherical part is used to define pressure,

$$p = -\frac{1}{3}\mathrm{tr}(\boldsymbol{\sigma}) \tag{3-12}$$

and the deviatoric stress is used to define the von Mises stress,

$$q^2 = \frac{3}{2}\boldsymbol{s}\cdot\boldsymbol{s}\,. \tag{3-13}$$

The net stress is defined as,

$$\boldsymbol{\sigma}' = \boldsymbol{\sigma} + \max(p_l,p_g)\mathbf{1}\,, \tag{3-14}$$

and its spherical part is used to define net pressure, or net mean stress,

$$p' = -\frac{1}{3}\mathrm{tr}(\boldsymbol{\sigma}')\,. \tag{3-15}$$

When expressing the water retention properties of materials, a variable called suction, s, is related to the degree of water saturation. In CODE_BRIGHT suction is expressed in terms of liquid pore pressure and gas pore pressure according to,

$$s = p_g - p_l\,. \tag{3-16}$$

3.3 Constitutive Relations and Parameter Value Calibration

As mentioned earlier, to close the formulation, variables are selected as independent or dependent and material specific constitutive relations are specified where dependent variables are given by expressions of independent variables. In CODE_BRIGHT, the independent variables are temperature, liquid pore pressure, gas pore pressure, and displacements. A summary of the constitutive relations is given in Table 3-1.

Table 3-1: Constitutive relations used in the CODE_BRIGHT models

RELATION	VARIABLE NAME	VARIABLE
Fourier's law	Conductive heat flux	$\boldsymbol{i}_c$
Darcy's law	Liquid and gas advective flux	$\boldsymbol{q}_l$
Retention curve	Liquid phase degree of saturation	S_l
Fick's law	Vapour and air non-advective fluxes	$\boldsymbol{i}_g^w$
Mechanical model	Stress tensor	$\boldsymbol{\sigma}$
Liquid phase density	Liquid density	ρ_l
Gas phase law	Gas density	ρ_g

The material parameters were, to a large degree, the same in the different setups/modelling tasks. However, as the properties of bentonite exhibit a strong density dependence, which cannot always be incorporated using the constitutive laws available in CODE_BRIGHT, variations were necessary between different models. This section describes the general parameter value adoption process and lists the fundamental parameter values used in all the modelling (e.g., specific density, specific heat, etc.). However, the parameter values used to parametrize the different constitutive laws described here are given in the respective modelling sections.

3.3.1 Fundamental Material Properties

Several parameters for the bentonite buffer and the UFC are the same in all the models. They are listed in Table 3-2. The solid density of the Bentonite was taken from Dixon (2019) while the specific heat was taken from Åkesson et al (2010a). The parameters of the UFC were calculated to agree with the weighted properties of the UFC.

Table 3-2: Fundamental parameter values used in the modelling

Parameter		Bentonite	UFC	Concrete
Solid density	[kg m^{-3}]	2750	7951	2000
Specific heat	[J kg^{-1} K^{-1}]	800	715	1000

3.3.2 Heat Flux

The heat flux in the models is the conductive heat flux, calculated using Fourier's law:

$$\boldsymbol{i}_c = -\lambda \nabla T \tag{3-17}$$

Here, λ is the thermal conductivity which can be parameterized as a function of the degree of saturation. In the case of the UFC and concrete materials this is not needed, but in bentonite materials there is a clear dependence (see Åkesson et al. 2010a). For the HCB blocks the following expression was used in the modelling:

$$\lambda(S_l) = \lambda_{\mathrm{dry}} \cos^2\left(\frac{\pi S_l}{2}\right) + \lambda_{\mathrm{sat}}\, sin^2\left(\frac{\pi S_l}{2}\right) \tag{3-18}$$

The thermal conductivity of granular material behaves slightly different with respect to the degree of saturation, and another relation was used for the GFM:

$$\lambda(S_l) = \lambda_{sat}^{S_l} \lambda_{dry}^{(1-S_l)} \tag{3-19}$$

3.3.3 Liquid Flux

The liquid flux $\boldsymbol{j}_l^w$ introduced in the mass balance of water is represented by Darcy's law:

$$\boldsymbol{j}_l^w = \boldsymbol{q}_l \theta_l^w = -\theta_l^w \frac{k k_{rl}}{\mu_l} \mathbf{1}(\nabla p_l - \rho_l \boldsymbol{g})\,, \tag{3-20}$$

where $\boldsymbol{q}_l$ is the Darcy flux, k is the intrinsic permeability, k_{rl}, the relative liquid permeability, μ_l the liquid viscosity, ρ_l the liquid density, p_l the liquid pressure, and $\boldsymbol{g} = g\boldsymbol{e}_z$ the gravitational acceleration vector.

A relation for the hydraulic conductivity (K) as function of dry density was derived in Dixon (2019):

$$K(\rho_d) = K_0 \left(\frac{\rho_d}{\rho_{d0}}\right)^{\beta} \tag{3-21}$$

K_0 and ρ_{d0} are reference values of hydraulic conductivity and dry density, respectively and β a parameter determining the shape of the relation. In CODE_BRIGHT, the required parameter is the intrinsic permeability, which is related the hydraulic conductivity through the equation:

$$K = k \frac{\rho_l g}{\mu_l} \tag{3-22}$$

By using the approximate values of $\rho_l = 1000$ kg/m^3, $g = 10$ m/s^2 and $\mu_l = 10^{-3}$ Pa·s, Equation (3-22) can be reduced to:

$$K = k\ 10^7 \tag{3-23}$$

The density dependence of the intrinsic permeability shown in Equation (3-21) cannot be directly implemented in CODE_BRIGHT. The hydraulic permeability as function of porosity can instead be written on the form:

$$k(n) = k_0 \cdot \exp\left[b \cdot \left(\phi - \phi_{ref}\right)\right] \tag{3-24}$$

Here ϕ_{ref} is a reference porosity and k_0 and b are parameters. The value of b was estimated by minimizing the difference between Equations (3-22) and (3-24) in a given dry density/porosity interval, while selecting k_0 and ϕ_{ref} at a suitable point.

For the relative permeability, the following (cubic) relation was recommended by Åkesson et al. (2010a), and was used for the modelling of the buffer materials in the modelling here:

$$k_{\mathrm{r}}(S_l) = S_l^3 \tag{3-25}$$

For the other materials (UFC and concrete) the relative permeability was assumed to be one (1).

3.3.4 Water Retention Curve for the Buffer Materials

Two types of water retention curves, expressing the relation between suction $s = p_g - p_l$ and degree of water saturation S_l, were used for the materials in the models. Both are van Genuchten type curves. The first is a regular van Genuchten curve (van Genuchten 1980):

$$S_l(s) = \left(1 + \left(\frac{s}{P_0}\right)^{\frac{1}{1-\lambda_0}}\right)^{-\lambda_0} \tag{3-26}$$

The second curve is an extended van Genuchten curve:

$$S_l(s) = \left(1 + \left(\frac{s}{P_0}\right)^{\frac{1}{1-\lambda_0}}\right)^{-\lambda_0} \left(1 - \frac{s}{P_d}\right)^{\lambda_d} \tag{3-27}$$

P_0, λ_0, P_d and λ_d are fitting parameters.

The values of the fitting parameters were determined as follows:

1. Experimental retention data (RH vs. water content (w)) for free swelling conditions was selected for each material.
    - HCB ($w_{init} = 20$ %): Two data sets for $w_{init} = 17.5$ and 27% presented by Dueck (2004), respectively, were used for the HCB with $w_{init} = 20$ %.
    - GFM ($w_{init} = 3$ %): One data set for $w_{init} = 0$%, presented by Dueck and Nilsson (2010).
2. Relationships between suction at free swelling condition (s_{free}) and the water content (w) were adopted on the form $s_{free}(w) = \exp[\alpha + \beta \cdot w]$.
    - For the HCB, this was based on the data set for $w_{init} = 17.5$% and resulted in the parameter values: α= 7.2 and β=0.203 (s_{free} in MPa).
    - For the GFM, this was based on the data set for $w_{init} = 0$% and resulted in α= 5.35 and β=0.133.
3. A “confined swelling curve” was constructed by assuming a linear build-up of swelling pressure from the initial saturation value and full saturation:

$$s_{conf} = s_{free} - p_{conf} \tag{3-28}$$

where

$$p_{conf} = s_{free}(e_i)\frac{w - w_i}{w_f - w_i} \tag{3-29}$$

The retention curves were fitted using the experimental data.

a) The constraints on the parameters in Equation (3-26) were:

- P_0 was set as a function of the other parameters and the initial point (S_{l0}, s_0):

$$P_0 = \frac{s_0}{\left(S_{l0}^{\frac{1}{\lambda_0}} - 1\right)^{1-\lambda_0}} \tag{3-30}$$

- The parameter λ_0 was tuned to ensure that the retention curve follows the retention data for confined swelling above the initial point.

b) The constraints on the parameters in Equation (3-27) were:

- P_0 was set as a function of the other parameters and the initial point (S_{l0}, s_0):

$$P_0 = \frac{s_0}{\left(\left(\frac{S_{l0}}{\left(1 - \frac{s_0}{P_d}\right)^{\lambda_d}}\right)^{\frac{1}{\lambda_0}} - 1\right)^{1-\lambda_0}} \tag{3-31}$$

- The suction level for $S_l = 0$ was set to 400 MPa, by setting $P_d = 400$ MPa.
- The parameter λ_d was tuned by hand to fit the data below the initial value.
- The parameter λ_0 was tuned by hand to make sure that the retention curve follows the retention data for confined swelling above the initial point.

4. The moisture diffusivity defined in Equation (3-32) was based on the derivative of the retention curve. It was evaluated and checked to be consistent with experimental data on moisture diffusivity evaluated from water uptake tests. For instance, Sellin et al. (2017) found values in the interval 3.6-5.3 x·10^{-10} m^2/s for a MX-80 specimen with a void ratio of 0.7.

$$D(S_l) = \frac{k \cdot k_{rl}(S_l)}{n \cdot \mu} \cdot \frac{ds}{dS_l} \quad (\mathrm{m}^2/\mathrm{s}) \tag{3-32}$$

3.3.5 Liquid Density

The liquid density in CODE_BRIGHT is given by the equation:

$$\rho_l = \rho_{l0}\exp\left(\beta[p_l - p_{l0}] + \alpha T\right) \quad (3\text{-}33)$$

Throughout the modelling the default parameter values in CODE_BRIGHT were used: $\rho_{l0} = 1002.6$ kg m^{-3}, $\beta = 4.5 \times 10^{-4}$ MPa^{-1} and $\alpha = -3.4 \times 10^{-4}$ °C^{-1}.

3.3.6 Vapour Diffusion in the Buffer Materials

The inclusion of thermal processes implies that moisture transport due to vapour diffusion also should be included. The gas mass flux $\boldsymbol{j}_g^w$ in the mass balance of water is equal to the vapour mass flux, $\boldsymbol{i}_g^w$. In CODE_BRIGHT this is driven by gradients in vapour mass fraction in the gas phase ($\omega_g^w = \theta_g^w/\rho_g$):

$$\boldsymbol{i}_g^w = -\left(n\rho_g(1 - S_l)D_m^w\right)\nabla\omega_g^w \,. \quad (3\text{-}34)$$

Here, ρ_g is the gas density and D_m^w is the diffusion coefficient of vapour in the gas phase. The latter is calculated as $D_m^w = \tau \cdot 5.9 \cdot 10^{-6} \cdot (273.15 + T)^{2.3}/p_g$ (m^2/s), where τ is the vapour tortuosity and T is the temperature.

The gas density is defined using the so-called ideal gas law, i.e. the equation of state for a hypothetical ideal gas where the particles in the gas are not subject to any interparticle interaction:

$$\rho_g = \rho_g^a + \rho_g^w = \frac{M_a}{RT}\left(p_g - \mathrm{RH}(s,T)p_{v,sat}\right) + \frac{M_w}{RT}\mathrm{RH}(s,T)p_{v,sat} \quad (3\text{-}35)$$

The relative humidity is given by Kelvin's law:

$$\mathrm{RH(s,T)} = \exp\left(\frac{-sM_w}{RT\rho_w}\right) \quad (3\text{-}36)$$

and the saturated vapour pressure by:

$$p_{v,sat} = 136075 \cdot 10^6 \exp\left(\frac{-5239.7}{T}\right). \quad (3\text{-}37)$$

The molecular weight of water is $M_w = 0.018$ kg/mol and that of air is $M_a = 0.02895$ kg/mol. $R = 8.314$ J/K/mol is the gas constant.

3.3.7 Thermal and Hydraulic Parameter Values

In Step 1 and 2, Task 1 and 2 the material parameters for the buffer components were not changed, and the values are given below in Table 3-3 (thermal) and Table 3-4 (hydraulic). In Tasks 3 and 4, the hydraulic parameters were updated due to changes in both initial dry density and initial water content. These updated values are given in the sections where the models results are described.

Table 3-3: Thermal parameters for the buffer

			HCB	GFM
Thermal conductivity	λ_{dry}	(W/mK)	0.5	0.35
	λ_{sat}	(W/mK)	1.3	1.3

Table 3-4: Hydraulic parameters for the buffer in Steps 1 & 2 and Tasks 1 & 2

			HCB	GFM
Intrinsic permeability	k_0	(m^2)	$2.1 \cdot 10^{-21}$	$2.1 \cdot 10^{-20}$
	n_{ref}	(-)	0.382	0.487
	b	(-)	21.1	21.1
Relative permeability	k_r	(-)	S_r^3	S_r^3
Vapour diffusion tortuosity	τ (-)	(-)	1	1
Water retention curve	P_0	(MPa)	64	3.2
	λ_0	(-)	0.18	0.23
	P_d	(MPa)	400	400
	λ_d	(-)	1.2	3.25

3.3.8 Mechanical Material Models

The UFC and concrete were simulated using a linear elastic model, and only Young's modulus and Poisson's ratio had to be defined.

The mechanical behaviour of the bentonite materials was represented using a modified version of the Barcelona Basic Model (BBM) where a large set of parameters is needed. In BBM, the total strain increment ($d\boldsymbol{\varepsilon}$) is decomposed in three additive strain contributions, elastic ($d\boldsymbol{\varepsilon}^e$), plastic ($d\boldsymbol{\varepsilon}^p$), and hydraulic ($d\boldsymbol{\varepsilon}^h$),

$$d\boldsymbol{\varepsilon} = d\boldsymbol{\varepsilon}^e + d\boldsymbol{\varepsilon}^p + d\boldsymbol{\varepsilon}^h. \quad (3\text{-}38)$$

The parameter values determining the elastic and hydraulic strain increments in BBM were the same for all modelling except for Task 4 (see Section 9). The parameter values are listed in Section 3.3.8.1 where motivation for the selection is given as well. The parameters defining plastic strains are described in Section 3.3.8.2. When calibrating the plastic parameters, the "final state" (or rather the fully homogenized state) of the buffer was utilized as a target state. Since this varied greatly between the models presented in this report, the plastic parameter set had to be updated for each modelling task, in some cases even for individual models within a task. In Section 3.3.8.2, the strategy used to determine the plastic parameters is described. The parameter values are presented in each of the modelling sections.

3.3.8.1 BBM Mechanical Parameters: Elastic and Hydraulic Strain

The adoption of elastic parameters essentially followed the strategy outlined by Åkesson et al. (2010a). The elastic strain increment is decomposed in a spherical and a deviatoric part:

$$d\boldsymbol{\varepsilon}^e = -\frac{1}{3}d\varepsilon_v^e\mathbf{1} + d\boldsymbol{e}^e\,, \tag{3-39}$$

where the volumetric strain is given by,

$$d\varepsilon_v^e = \frac{dp'}{K},\ K = \max\left[\frac{(1+e)p'}{\kappa_i(s)}, K_{min}\right], \tag{3-40}$$

$$\kappa_i(s) = \kappa_{i0}(1+\alpha_i s)\,, \tag{3-41}$$

and the deviatoric part is given by,

$$d\boldsymbol{e}^e = \frac{d\boldsymbol{s}}{2G}, G = \frac{3(1-2\nu)}{2(1+\nu)}K\,. \tag{3-42}$$

The hydraulic strain increment is spherical,

$$d\boldsymbol{\varepsilon}^h = -\frac{1}{3}d\varepsilon_v^h\mathbf{1}\,, \tag{3-43}$$

where the volumetric strain increment is given by,

$$d\varepsilon_v^h = \frac{\kappa_s(p',e,s)}{(1+e)(s+p_{atm})}ds\,. \tag{3-44}$$

The expression above contains the function,

$$\kappa_s(p',e,s) = \kappa_{s0}h(p',e)\exp(\alpha_{ss}s)\,, \tag{3-45}$$

describing the swelling from water uptake. $\kappa_s(p',e,s)$ in turn contains $h(p',e)$ defined as,

$$h(p',e) = \begin{cases} 1 & \text{if } p' < p_{ref} \\ 10^{-20} & \text{if } p' > p_{swell}(e) \\ 1 - \dfrac{\ln(p') - \ln(p_{ref})}{p_{\mathrm{swell}}(e) - \ln(p_{ref})} & \text{otherwise.} \end{cases} \tag{3-46}$$

The swelling pressure function, $p_{\mathrm{swell}}(e)$, is defined according to Equation (3-51). Due to the large difference between the initial water content in the HCB blocks and pellets, respectively, and to limit the potential shrinkage of the blocks, a suction dependence of κ_s was adopted for the blocks as given by the exponential function in Equation (3-45). For block material, a value of α_{ss} = -0.03 was adopted so that the void ratio would not fall below ~0.5 for high suction values. This threshold value was motivated from evaluating experimental shrinkage curves (Börgesson 2001).
The elastic parameters: K_{min} and p_{ref} were specified as described in Åkesson et al. (2010a):

- "The K_{min} value was set low (≤20 MPa), in order to adhere to the BBM model as far as possible."
- "The reference pressure p_{ref} was set to a level below the final swelling pressure for the void ratio in question."

In all the modelling except for Task 4, the pair (K_{min}, p_{ref}) was set to (20,1) and (6, 0.3) MPa for blocks and GFM, respectively.

Table 3-5: Elastic parameters for the buffer components

		HCB	GFM
Porous elasticity	κ_{i0} (-)	0.12	0.12
	α_i	-0.043	-0.0062
	K_{min} (MPa)	20	6
Swelling modulus	κ_{s0} (-)	0.3	0.3
	α_{ss} (-)	-0.03	0
	α_{sp}	777[1)]	
	p_{ref} (MPa)	1	0.3
Poisson's ratio	v (-)	0.2	0.2

[1)]This value activates Equation (3-46) in CODE_BRIGHT

Parameter values for the elastic component of the BBM model used in all the modelling except Task 4 are given in Table 3-5, while the values used in Task 4 are given in Section 9.1.2.4.3.

3.3.8.2 BBM Mechanical Parameters: Plastic Strain

The elastic region is bounded by the flow/yield surface,

$$f = q^2 - M^2(p' + p_s)(p_0 - p'), \tag{3-47}$$

where the parameters/variable, M, p_s and p_0 are present. When BBM behaves inelastically, the plastic strain increment is given by,

$$d\boldsymbol{\varepsilon}^p = d\Lambda \frac{\partial g}{\partial \boldsymbol{\sigma}}, \tag{3-48}$$

where the magnitude is given by $d\Lambda$, the plastic multiplier, which is obtained from the consistency condition, $df = 0$. The direction of the strain increment is given by the partial derivative of the plastic potential,

$$g = \alpha q^2 - M^2(p' + p_s)(p_0 - p'), \tag{3-49}$$

with respect to stress. The plastic potential contains the parameter α which determines the amount of non-associativity in the model. In this work a value of $\alpha = 0.5$ was used. The internal hardening variable p_0 is governed by the hardening law,

$$dp_0^* = \frac{1 + e}{\lambda_0 - \kappa_{i0}} p_0^* d\varepsilon_v^p, \tag{3-50}$$

where the plastic modulus λ_0 is introduced.

A similar strategy for the determination of yield surface parameters, M, p_s and p_0^* to that which was outlined by Åkesson et al. (2010a) was used here. The calibration strategy was based on use of the two functions developed from evaluating experimental data:

1) a relation between the swelling pressure and the dry density:

$$P_{swell} = 10^{(c_2 \cdot \rho_d{}^2 + c_1 \cdot \rho_d + c_0)}, \quad (3\text{-}51)$$

2) a relation between the von Mises stress at failure (q_f) and the net mean stress (p'),

$$q_f = a \cdot p'^b. \quad (3\text{-}52)$$

These functions were calibrated to agree with MX-80 bentonite. For the swelling pressure defined in Equation (3-51), with p_{swell} in kPa and ρ_d in kg/m^3, the parameter values used were: c_0 = -1.74, $c_1 = 4.12 \cdot 10^{-3}$; $c_2 = -3.94 \cdot 10^{-7}$ (Åkesson et al. 2010a). The parameter values for the von Mises stress at failure defined in Equation (3-52) (with p' and q in kPa) were $a = 2.45$; $b = 0.77$ (Börgesson et al. 1995).

It should be noted that the defined swelling pressure curve implemented in the code was used to influence the pressure dependence of the swelling modulus through α_{sp} as given in Equation (3-46).

Three conditions are used to derive the three parameters (see Figure 3-1 right):

1. The net mean stress at the critical state point is equal to the swelling pressure (p_{swell}) for the void ratio in question. This gives the following relation between p_s and p_0^*:

$$p_0^* = p_s + 2 \cdot p_{\mathrm{swell}} \quad (3\text{-}53)$$

2. The von Mises stress at the critical state point (q_f) is given by Equation (3-52) and the swelling pressure for the void ratio in question. This gives a relation between p_s and M:

$$M = \frac{q_f}{p_{swell} + p_s} \quad (3\text{-}54)$$

3. The tensile stress at failure (σ_{tf}) is half the value of the von Mises stress at failure (q_f). This specifies a second point along the yield surface at:

$$[p', q] = \left[-\frac{\sigma_{tf}}{3}, \sigma_{tf}\right] = \left[-\frac{q_f}{6}, \frac{q_f}{2}\right] \quad (3\text{-}55)$$

A combination of the condition $F = 0$ at yield (see Equation (3-47) and the three conditions (Equation (3-53) to Equation (3-55)) gives the following quadratic equation:

$$\left(\frac{q_f}{2}\right)^2 = \left(\frac{q_f}{p_{swell} + p_s}\right)^2 \left(\mathrm{p_s} - \frac{q_f}{6}\right)\left(2 \cdot p_{swell} + p_s + \frac{q_f}{6}\right) \quad (3\text{-}56)$$

After some re-arrangements, the following solution can be obtained:

$$p_s = \left(\frac{2}{\sqrt{3}} - 1\right) p_{swell} + \frac{1}{3\sqrt{3}} q_f \quad (3\text{-}57)$$

Once this is solved, the p_0^* value and M can be readily calculated from Equations (3-53) and (3-54). The void ratio dependence of these parameters is illustrated for MX-80 data in Figure 3-2.

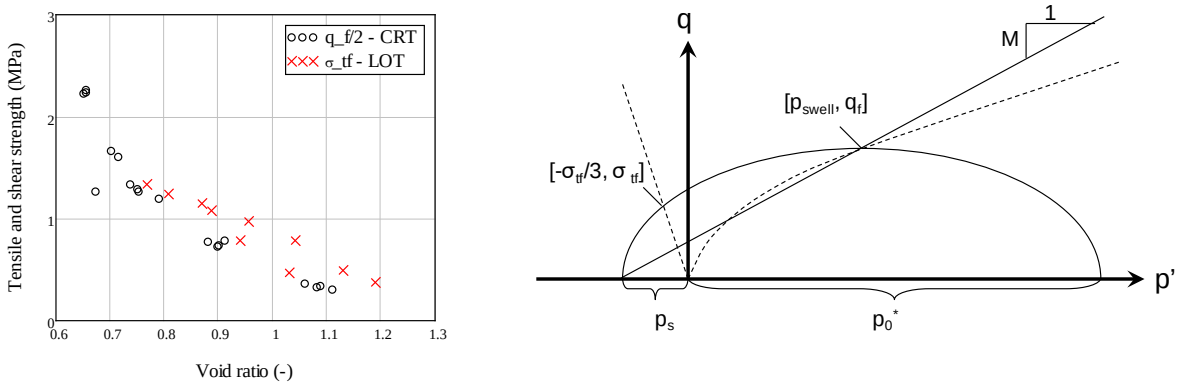

Figure 3-1: Tensile and shear strength data (left, Dueck et al. 2011 and Karnland et al. 2000) and yield surface (right)

The yield surface parameters for the GFM can be set using the initial void ratio, while the corresponding parameters for the HCB are derived using a target void ratio, equal to the homogenized void ratio. The reason for this is that there is no mechanism for "contracting" the yield surface during isotropic swelling, which typically will occur in the HCB material. Thus, if the initial void ratio of the HCB material is used for calibrating the plastic parameters, the yield surface would not correspond well with the approximate final state of the HCB. The λ_0 modulus for the GFM was calculated as the modulus of p_{swell} between the initial void ratio (e_i) and the homogenized (target) void ratio (e_f):

$$\lambda_0 = -\frac{e_i - e_f}{\ln[p_{swell}(e_i)] - \ln[p_{swell}(e_f)]} \tag{3-58}$$

The λ_0 modulus for blocks was calculated as the tangent modulus of p_{swell} at the homogenized (target) void ratio (e_f):

$$\lambda_0 = -\frac{p_{swell}(e_f)}{\frac{d}{de_f} p_{swell}(e_f)} \tag{3-59}$$

Plastic BBM parameters common to all modelling except Tasks 3 and 4 are given in Table 3-6 below. The parameters for Tasks 3 and 4 are given in Section 8 and 9, respectively.

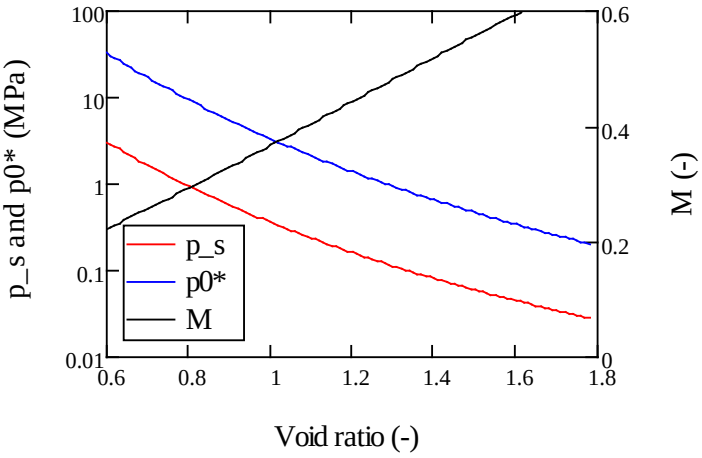

Figure 3-2: Yield surface parameters as functions of the void ratio

Table 3-6: Mechanical parameters used for the buffer materials

			HCB	GFM
Target void ratio			0.719	0.719
Porous elasticity	κ_{i0}	(-)	0.12	0.12
	α_i		-0.043	-0.0062
	K_{min}	(MPa)	20	6
Swelling modulus	κ_{s0}	(-)	0.3	0.3
	α_{ss} 2)	(-)	-0.03	0
	α_{sp}		(*)	(*)
	p_{ref}	(MPa)	1	0.3
Poisson's ratio	v	(-)	0.2	0.2
Plastic stress strain modulus	λ_0	(-)	0.163	0.181
Critical state line parameter	M	(-)	0.264	0.348
Tensile strength	p_{s0}	(MPa)	1.49	0.454
Non-associativity parameter	α	(-)	0.5	0.5
Pre-consolidation stress	p_0^*	(MPa)	15.25	4.27
	p_c	(MPa)	1	1

3.4 Model Geometry, Components, and Symmetries

When carrying out fully coupled THM simulations, it is useful to keep the model geometries as simple as possible. One common way to simplify/reduce the size of the problem is to use all available symmetries.

The planned layout of the emplacement room has one symmetry plane, see Figure 3-3. As part of the modelling in Step 2, it was investigated if the geometry could be simplified further. A first step was to align the UFCs in the upper and lower row of buffer boxes as shown in the lower part of Figure 3-3. Then the effect of including the offset between the buffer boxes in the geometry was evaluated by simulating two different geometries with and without offset (see Figure 3-4). The rightmost geometry in Figure 3-4 was used in subsequent modelling (Tasks 1 – 4), with some modifications depending on the purpose of the modeling task. The analysis (described in Section 5.2) showed that while the temperature field was altered, the influence on the hydromechanical evolution was insignificant. Hence, for a major part of the modelling, the geometry was constructed with no offset between the upper and lower row of buffer boxes, which created several symmetry planes. This allowed for significantly reduced model geometries.

The model geometry used in most of the FEM modelling is shown in the in Figure 3-4, right. It consisted of all the materials inside the emplacement room (HCB, GFM, UFC and concrete slab). However, the surrounding host rock was not included. The interaction between the host rock and the bentonite buffer was considered by using adapted boundary conditions, which are described in Section 3.6.

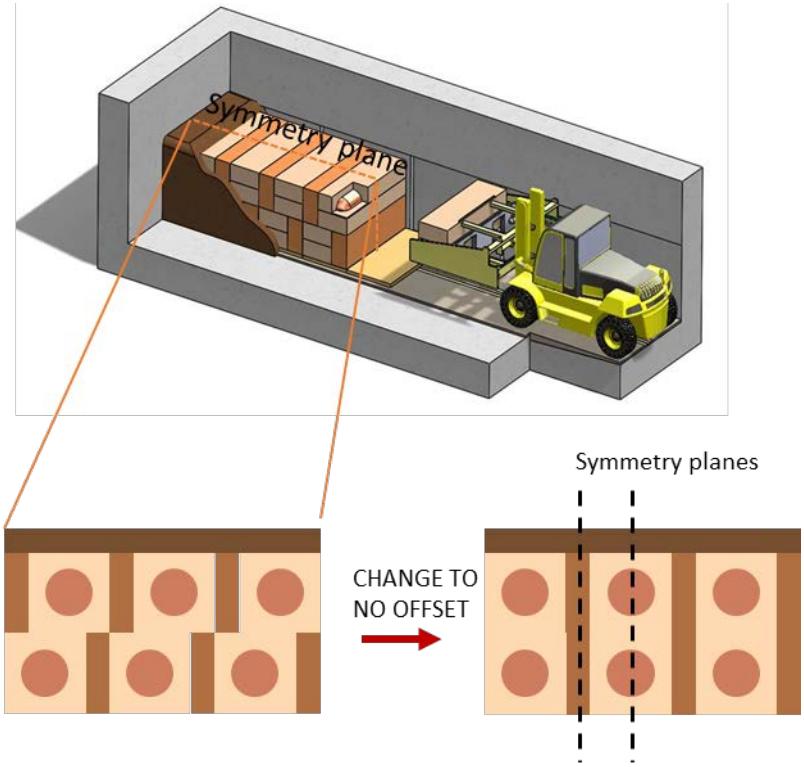

Figure 3-3: Schematic of the emplacement room (top) and model conceptualization with and without offset between the upper and lower rows of buffer boxes (bottom)

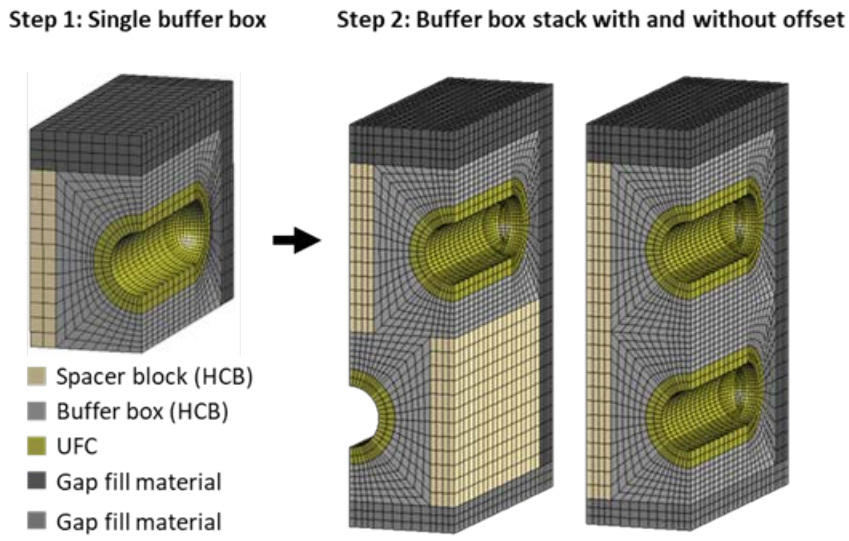

Figure 3-4: Evolution of the model geometry during the early scoping calculations

3.5 Initial Conditions

The initial conditions were defined using the available data on the buffer components and the UFC. Note that the evolution during the pre-installation phase was not considered, this was studied separately within Task 4.

In CODE_BRIGHT, the initial conditions are defined by temperature, porosity, suction (gas pore pressure – liquid pore pressure) and stress. The initial temperature in all constituents/materials was set equal to the ambient temperature in the host rock site at the depth of 500 m – 800 m:

- Crystalline rock of the Canadian Shield (Ignace): 11°C (Guo 2017)
- Sedimentary rock of Southern Ontario (South Bruce): 17°C (Guo 2018)

For all base case scenarios, present in Step 1 & 2, and Tasks 1, 2 and 4, the initial dry density of the buffer components was set according to Dixon (2019):

- HCB 1700 kg/m^3
- GFM: 1410 kg/m^3

In Task 3 (Section 8) a sensitivity analysis was carried out in which the initial dry density was varied. Given a solid density of 2750 kg/m^3 (Dixon 2019) and the dry densities of the buffer materials, the initial porosity was calculated.

According to NWMOs reference values, the initial water content, w_{ini}, of the bentonite was set to 20 % for the HCB and 2 % for the GFM in Steps 1 & 2, and Tasks 1 and 2. However, in Tasks 3 and 4 an updated water content of 3 % was used for the GFM.

From the initial water content and dry density, the initial suction was estimated by using retention curves for MX-80 bentonite under free swelling conditions (Dueck 2004; Dueck and Nilsson 2010). The initial suction values associated with the two water contents above were:

- HCB: 20 MPa
- GFM: 169 MPa (w_{ini} = 2 %), 143 MPa (w_{ini} = 3 %).

The initial stress in all the models should in principle be set to zero. To avoid numerical issues with BBM, however, a small initial effective stress is prescribed (-0.01 MPa). The stresses in CODE_BRIGHT are defined such that negative values are compressive stresses.

3.6 Boundary Conditions

All three processes simulated in the models, thermal, hydraulic and mechanical, had separate boundary conditions as described below. As was discussed in Section 3.4 the host rock was not explicitly included in the geometry. However, implicitly it was included by adopting suitable boundary conditions, as described in this section.

3.6.1 Thermal Boundary Conditions

In all models simulating the THM evolution in a buffer box stack, the same UFC heat load was used. Figure 3-5 shows the heating power evolution applied at the inner hollow surface of the UFCs (Guo 2017).

Here, the temperatures on the outer boundaries were prescribed using results from large-scale thermal models. These were presented in Guo (2017) for a crystalline host rock and Guo (2018) for a sedimentary host rock.

The prescribed temperature on the surfaces of the emplacement room (ceiling/walls/floor) is shown in Figure 3-6. It increases from the initial temperature of 11 °C (crystalline rock, d = 500 m) and 17 °C (sedimentary rock, d = 800 m) to a peak temperature of 73 °C and 84 °C, respectively.

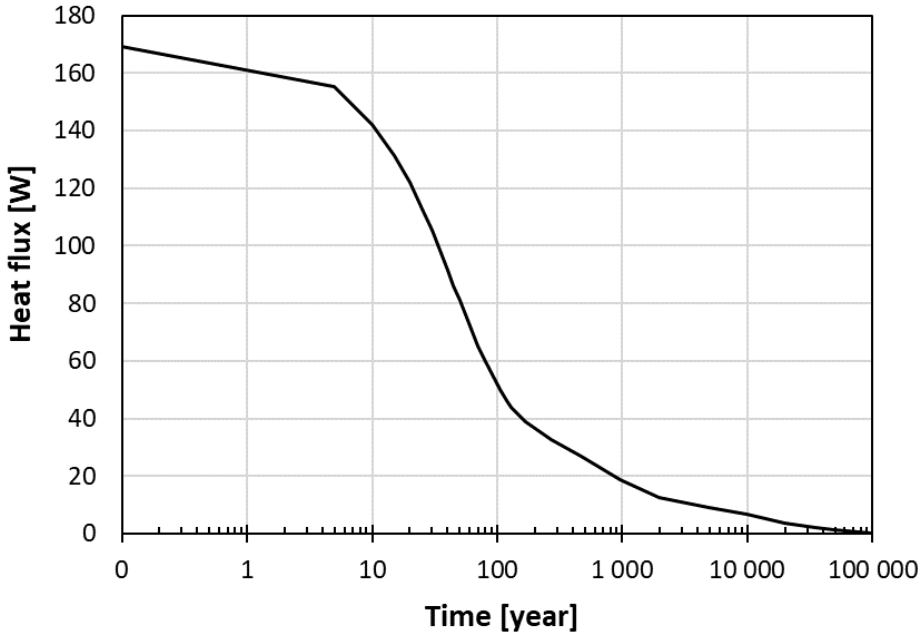

Figure 3-5: Heat flux generated by a single UFC containing 48 used fuel bundles (year 0 is the year of installation) from the tabulated values in (Guo 2017)

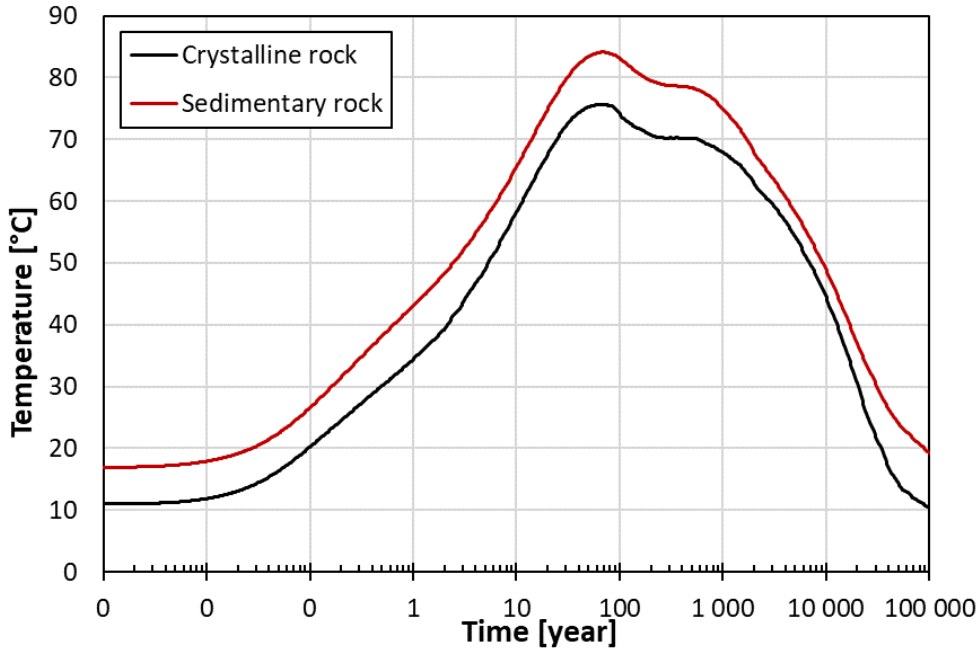

Figure 3-6: Prescribed temperature on the wall/ceiling/floor of the emplacement room in the models with crystalline rock (black solid line) and sedimentary rock (red solid line)

3.6.2 Hydraulic Boundary Conditions

The inflow into the bentonite buffer was prescribed using different hydraulic boundary conditions to evaluate how the THM evolution in the bentonite buffer was affected by the rate of water inflow (fast or slow). Two hydraulic boundary conditions were used:

- free access to water, achieved by keeping the rock wall boundary saturated by prescribing atmospheric liquid pressure, and
- flux-limited access to water, achieved by prescribing a limited water inflow as long as the bentonite is unsaturated.

The boundary conditions used to prescribe the hydraulic behaviour on the boundary was on the form:

$$j_{\mathrm{l}} = \gamma(p_{\mathrm{l}}^{0} - p_{\mathrm{l}}) \tag{3-60}$$

Here j_l is the mass flow rate over the boundary, p_{l}^{0} the prescribed liquid pressure, p_l the actual liquid pressure at the boundary and γ a constant which effectively sets the strength of the boundary condition.

To specify free access of water (i.e., to always keep the liquid pressure on the rock wall boundary equal to atmospheric pressure, 0.1 MPa), p_{l}^{0} was set equal to 0.1 MPa and the value of γ was set equal to 10^5 kg s^{-1} MPa^{-1}. The high value of γ allows for a large water inflow over the boundary, if the value of the liquid pressure, p_{l}, deviates significantly from the value of p_{l}^{0} on the boundary.
In principle, a higher value of p_{l}^{0}, corresponding to the hydrostatic pressure at the depth of the repository (5 MPa at 500 m and 8 MPa at 800 m), should be used. However, to avoid high liquid pressures developing in the buffer, which can cause severe numerical problems with the mechanical material model, the prescribed liquid pressure was set to 0.1 MPa. If a value corresponding to the hydrostatic pressure was prescribed, that would speed up the rate of water inflow, and increase the total pressure (i.e., the effective stress plus the pore pressure) in the models.

In the flux-limited case, a relation between the hydraulic properties of the rock and γ according was derived assuming that 1) the mass flow through the rock is governed by Darcy's law, and 2) the rock does not dry:

$$\boldsymbol{q}_{\mathrm{l}} = -\frac{k_l}{\mu_l}\nabla p_l \tag{3-61}$$

Assuming a linear variation in pressure this can be written as:

$$\boldsymbol{q}_{\mathrm{l}} = -\frac{k_l}{\mu_l}\frac{\Delta p_l}{\Delta l}, \tag{3-62}$$

where Δp_l is the pressure drop from hydrostatic conditions and Δl is the distance from the emplacement room wall to the position in the rock mass where hydrostatic conditions prevail. Setting p_{l}^{0} equal to the hydrostatic liquid pressure at the depth of the repository gives,

$$j_{\mathrm{l}} = -\gamma\Delta p_l\,. \tag{3-63}$$

Combining Equations (3-62) and (3-63) in the direction of j_l leads to,

$$\gamma = \frac{\rho_l k_l}{\mu_l} \frac{1}{\Delta l}. \tag{3-64}$$

Using the values $k_l = 10^{-20}$ m², ρ_l = 1000 kg/m³, μ_l = 10^{-9} MPa·s and Δl = 50 m, gives,

$$\gamma \approx 2 \cdot 10^{-10} \frac{\text{kg}}{\text{MPa} \cdot \text{s} \cdot \text{m}^2}. \tag{3-65}$$

3.6.3 Mechanical Boundary Conditions

The mechanical influence of the host rock on the buffer material was to act as an immobile wall confining the swelling of the buffer. This could be directly implemented using boundary conditions.

Two types of mechanical boundary conditions were used in all the CODE_BRIGHT models.

1. On all outer boundaries roller conditions were prescribed (i.e., no displacement allowed in the surface's normal direction and zero traction in the tangential direction)
2. On the inner surface of the hollow UFC, traction-free boundary conditions were prescribed. Using this together with a suitable material parameterisation of the waste container shell (to make it sufficiently stiff) allows the UFC to be displaced by the movement of the clay (due to shrinkage or swelling) without allowing any deformation of the UFC itself.

3.7 Verification and Validation of Models

When carrying out numerical simulations it is important to make sure that model solution is "well behaved", and that the resolution of the models is high enough to capture the simulated processes. Furthermore, one must ensure that the material models and the parameterisation of these give a correct behaviour of the simulated materials.

Verification and validation were carried out separately for most of the tasks and information are found in Appendix A - Appendix D. Below a description of how the numerical accuracy and material model validation was carried out is given.

3.7.1 Numerical Accuracy

The two most important aspects to check in terms of the numerical accuracy are that the solution is:

1. mesh independent, and
2. time-step independent.

Mesh independence here means that the solution does not depend on the grid resolution used when discretizing the geometry. To ensure this for each new model setup, a variation on the

base case model was simulated in which the number of nodes along lines was increased by a factor of two (2). The time to saturation in the model and the maximum and minimum effective stress during the simulation were then evaluated. A requirement was that these values should differ by less than 1% between the original model and the fine mesh model for the solution in the former to be considered mesh independent.

Time-step independence is another important factor when evaluating the quality of the solution in FEM models. Taking too long time-steps means that important processes can be missed, and that the solution diverges from the "true" solution. CODE_BRIGHT uses an adaptive time-step algorithm, which means that the time-step is set to optimize the number of Newton-Raphson iterations taken for each time-step. The Newton-Raphson iterations in each time-step is terminated when the user defined tolerance for each variable is reached. To ensure that the solution was time-step independent, models with fine enough tolerances were simulated so that the number of time-steps taken during the simulation was a least a factor of two larger than in the base case model. The requirement on the solution was that the time until saturation and min/max net mean stress during the simulation differed by less than 1% between the base case model and the fine time step model.

3.7.2 Validation of the Bentonite Mechanical Material Model

The validation of the material models was limited to verifying the mechanical behaviour of the buffer. The mechanical material model used for simulating the bentonite materials (HCB and GFM) was the Basic Barcelona Model, see Section 3.3.8.
To validate that the parameter set gave a good representation of the behavior of MX-80 bentonite, two validation procedures were in general carried out. These are listed in Table 3-7 together with the acceptance criteria.

Table 3-7: Material model verification exercises and acceptance criteria

Verification procedure	Acceptance criteria
Comparison of the net-mean stress as function of void ratio at full water saturation to the measured relation for p_{swell}	The stress state in the selected reference points in the buffer lies between $0.9 \times p_{swell}(e)$ to $2 \times p_{swell}(e)$, where $p_{swell}(e)$ is defined from Equation 10.10 in Åkesson (2010a)
Comparison of the deviatoric stress in the bentonite with the measured stress at failure at a given net-mean stress (see, Åkesson 2010a).	The deviatoric stress in the reference points in the buffer is not significantly larger than the measured stress at failure

An example of the net mean stress plotted against void ratio in the final saturated state is shown in Figure 3-7. This example was taken from the Task 1, subtask 1.2 modelling described in Section 6.2 and the validation exercise of this model is described in some detail in Appendix C.2.

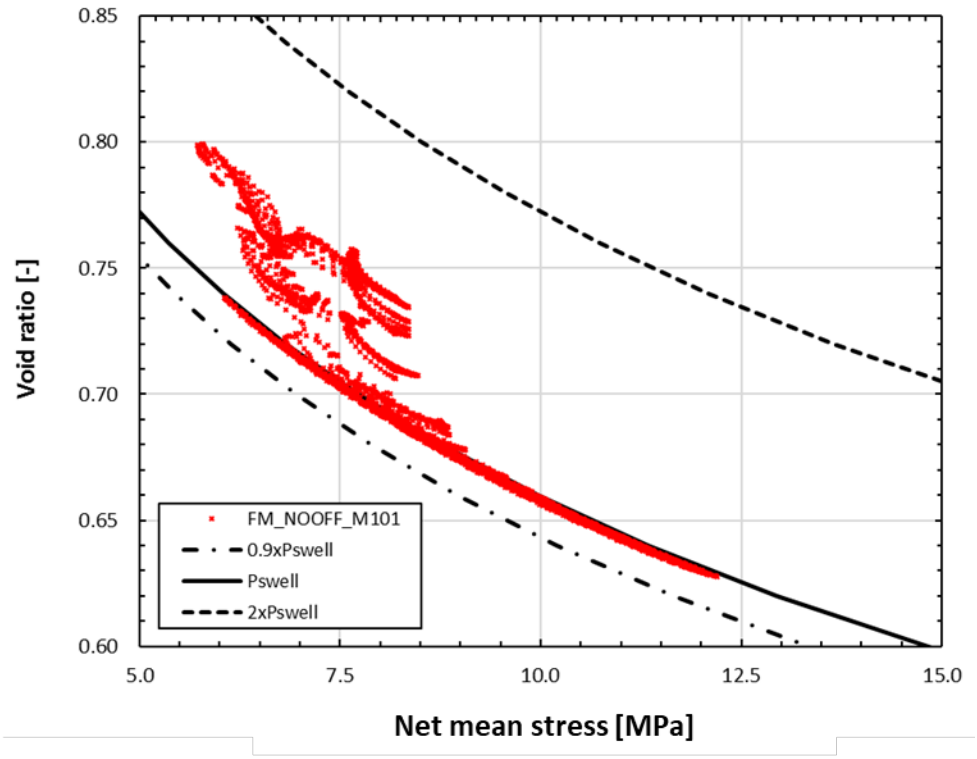

Figure 3-7: Net mean stress versus void ratio at saturation from the base case model in Task 1 – subtask 1.2

The plot in Figure 3-7 shows the final state in all the nodes in the buffer (red crosses) and the swelling pressure curve (black solid line). Also included is a lower bound of 0.9 times the swelling pressure (black dash-dotted line) and a curve identifying two times the swelling pressure (black dashed line). If the buffer behaves as intended, all points that only undergoes swelling should end up on, or very close to the swelling pressure curve.

Points in the buffer which undergoes both swelling and compression can, due to the hysteretic behavior of bentonite, be expected to end up at a higher net mean stress than the swelling pressure for the corresponding void ratio. A suitable upper limit is 2 times the swelling pressure, which corresponds well with the measured swelling pressure during compression (see Dueck et al. 2019 and references therein).

A further check was in general carried out by analyzing the relation between deviatoric and net mean stress in the buffer blocks after full water saturation. This can be compared to the measured stress at failure at a given net-mean stress for saturated MX-80 bentonite (see, for example, Åkesson et al. 2010a) - no points should lie significantly above this relation. An illustration is shown in Figure 3-8 where data from the final state in the base case model from Task 1 – Subtask 1.2 is shown (red crosses) together with measured net mean stress at failure (black solid line).

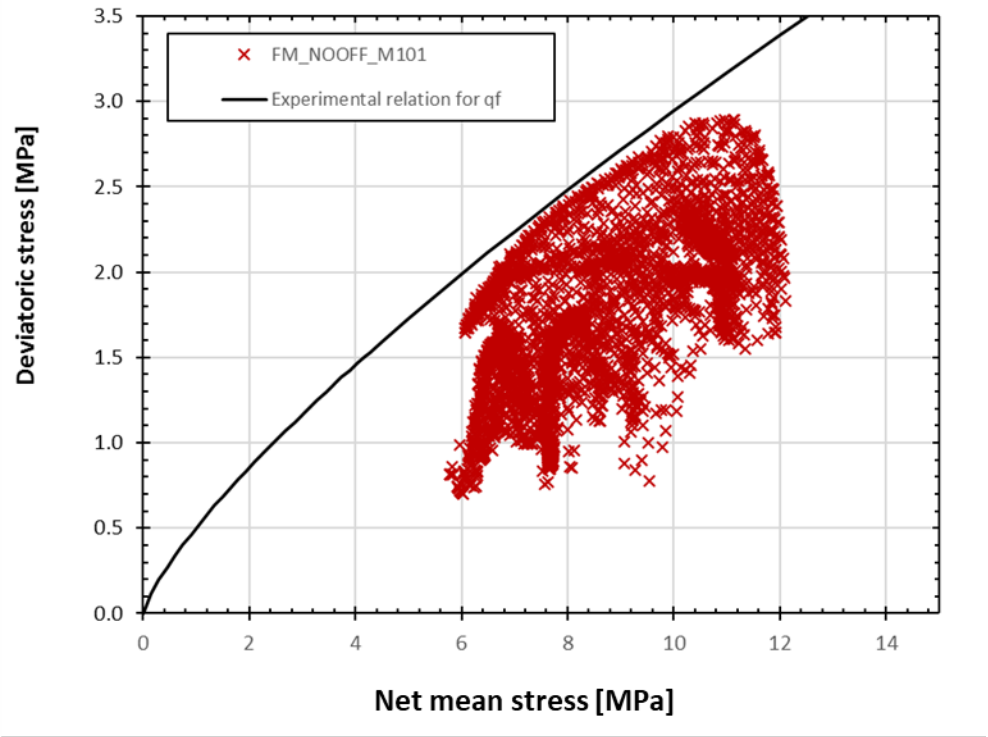

Figure 3-8: Net mean stress versus deviatoric stress once all points in the buffer were fully water saturated (data from the base case model Task 1 – subtask 1.2)

4. STEP 1: PROOF OF CONCEPT

The first part of the modelling, Step 1, aimed at testing the capability of the models to confirm that they were up for the subsequent tasks. A partial goal was to analyse the evolution in the buffer around a single UFC during the transient saturation phase. Initially, the models simulated only Hydro-Mechanical (HM) processes, but when these showed promising results, the thermal process was added.

4.1 Model Setup

The setup of the models in this step is broadly the same as that described in Section 3. However, as this was the first step in the modelling, a simplified model geometry was used. A single buffer box with the surrounding buffer GFM and the adjacent spacer block were included. The simulated buffer box belonged to the upper row of buffer boxes.

An overview of the geometry is shown in Figure 4-1 (left and middle panel). In the rightmost panel of Figure 4-1 the discretized geometry generated using the pre-processor GiD 10.0.8 is shown.

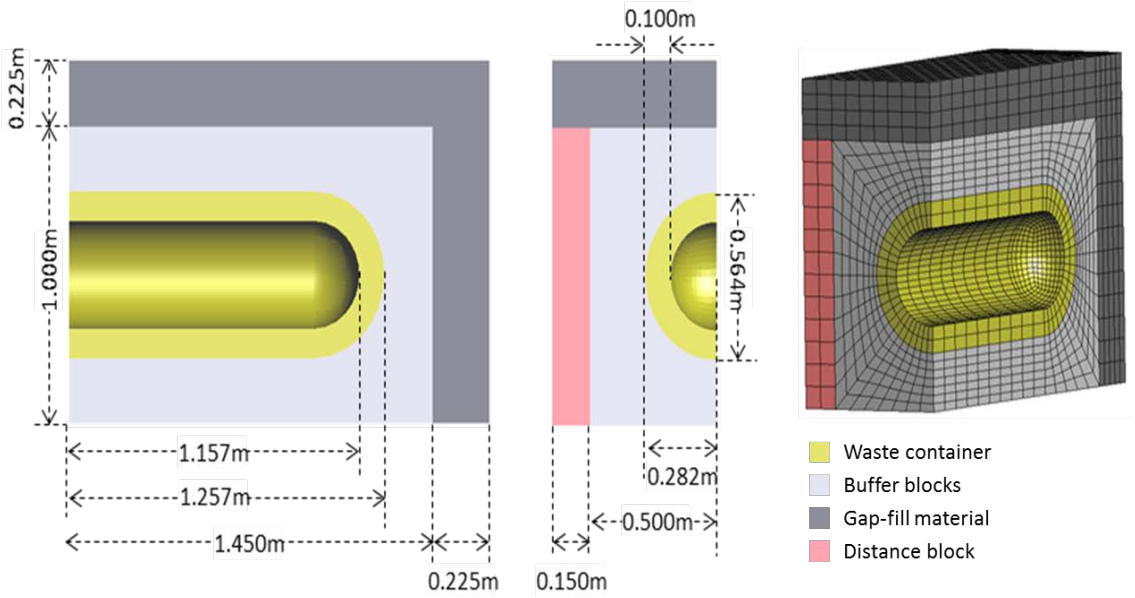

Figure 4-1: Overview of the geometry and mesh used in the base case

4.2 Initial and Boundary Conditions

The initial conditions of the buffer are described in Section 3.5. The initial suction and porosity used for the UFC are given in Table 4-1.

The boundary conditions of the models are described in Section 3.6. The hydraulic boundary conditions were:

- Free access to water (HM models, to simulate high-permeability rock)
- Flux-limited access to water (HM models, to simulate low-permeability rock)
- No access to water (only THM models, to analyse the evolution in an extremely dry scenario)
-

These conditions were prescribed on all the “outer” surfaces of the GFM.

4.3 Material Parameters

The material parameters used to model the buffer are given in Table 3-3 (thermal parameters), Table 3-4 (hydraulic parameters), Table 3-5 (mechanical parameters, elastic part) and Table 3-6 (mechanical parameters, plastic part).

The THM parameters used to simulate the UFC is given in Table 4-1.

Table 4-1: THM parameters for the UFC

			UFC
Initial suction	s_0	MPa	23
Initial porosity	Φ_0	-	0.001
Intrinsic permeability	k_0	m^2	10^{-30}
Relative permeability	k_r	(-)	1
Water retention curve	P_0	MPa	10
	λ_0	(-)	0.3
Thermal conductivity	λ	W/mK	300
Specific heat for solid	c	(J/kgK)	715
Young modulus	E	GPa	60
Poisson ratio	v	(-)	0.3

4.4 Results

A total of nine (9) models were constructed, and these are listed in Table 4-2 together with the model names. The first set of models simulated only hydro-mechanical processes. The second set of models also included the thermal process, leading to more complex, but also more realistic evolutions.

Table 4-2: Overview of simulated models

Model ID	Process	Model name	Description
HM_BC	HM	NWMOPC_HM_BC1.gid	Base case model for HM case
HM_FLUX_LIM	HM	NWMOPC_HM_BC1_SLOW_WET.gid	Same as HM_BC except flux limited water inflow
HM_MESH	HM	NWMOPC_HM_BC1_MESH.gid	Mesh verification of HM_BC
HM_DT	HM	NWMOPC_HM_DT.gid	Time-step verification of HM_BC
THM_BC	THM	NWMOPC_THM_BC_4a.gid	Base case model for THM case
THM_DRY	THM	NWMOPC_THM_DRY_4.gid	Same as THM_BC, except no water inflow
THM_FLUX_LIM	THM	NWMOPC_THM_BC_4_FLUXLIM.gid	Same as THM_BC, except flux limited water inflow
THM_BC_MESH	THM	NWMOPC_THM_BC_4a_MESH.gid	Mesh verification of THM_BC
THM_BC_DT	THM	NWMOPC_THM_BC_4a_DTIME.gid	Time-step verification of THM_BC

The models THM_BC_MESH and THM_BC_DT were used to verify the numerical accuracy of the solution for the base case THM model (THM_BC). Furthermore, the results in the base case were analyzed to validate the material model used for the clay components. These exercises are described in Appendix A.

4.5 Saturation Time of the Buffer

One interesting property of the results is the time it takes for the buffer to saturate. In these probing models, the evaluated saturation time cannot be used to quantify the time it will take to saturate the buffer, as the inflow conditions and the geometry are too simplistic. The simplified geometry used (see Figure 4-1) probably leads to an underestimation of the saturation time. The three different rates of inflows simulated in these models can instead be used to better understand how the (T)HM evolution depends on the rate of water inflow.

In Figure 4-2 the degree of saturation as function of time in three points in the buffer blocks are shown from the base case HM model (brown-solid line), the flux-limited HM model (blue-solid line), the base case THM model (black-solid line) and the flux-limited THM model (red-solid line). Naturally, the THM model with no water inflow did not saturate, and hence was not included in these plots. As can be seen the slopes of the curves become rather shallow as the buffer gets close to full saturation. The very slow wetting close to full saturation is due to the very low suction gradient in the bentonite at this stage. If hydrostatic pressure was prescribed on the tunnel wall (rather than atmospheric pressure) this long tail in the saturation curve would be significantly decreased.

Hence, rather than to focus on the time until full saturation it is more useful to check, for example, the time until the degree of saturation reaches 98 % or 99 %. The times until 98 % saturation is reached in the THM models are shown in Table 4-3.

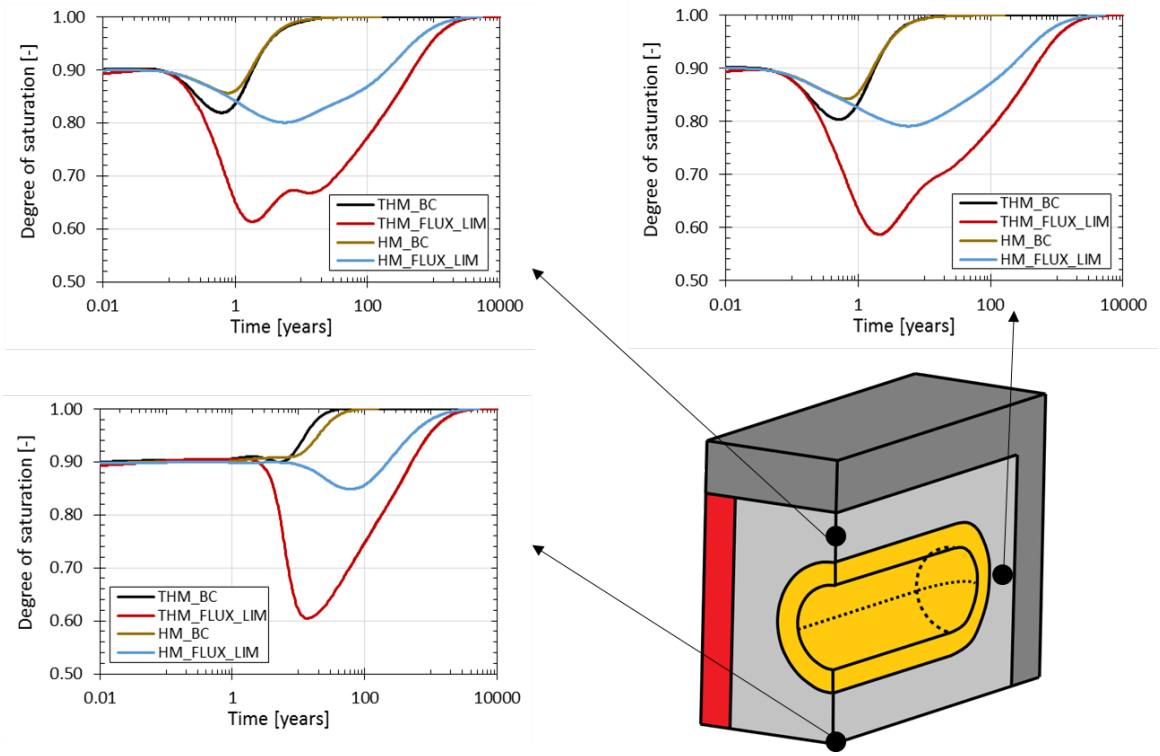

Figure 4-2: Degree of saturation in the buffer (evaluated in the three points depicted in the lower-left part of the figure)

Table 4-3: Time until degree of saturation of 98 % in the THM models

Model	Time until S_l = 98 %
THM Base case	19.5 years
THM Flux-limited case	3,940 years

4.6 Final State of the Buffer

The mechanical evolution in these probing models was analysed by looking at the final state in the buffer, in terms of dry density. The results of the HM and THM models are discussed separately below.

4.6.1 HM Models

The final dry densities are shown in Figure 4-3. The left graph shows the results from the model with free access to water and the right graph shows the result from the flux-limited model. The final dry-densities differed somewhat due to the different time evolution of the swelling, which was caused by a different hydraulic evolution. In the case of free-access to water a "sequential mode" of swelling/compression took place, whereas the flux limited case gave rise to a "simultaneous mode" of swelling/compression.

- **Sequential swelling/compression:** In models with a high water inflow into the buffer the low permeability of the bentonite slows down water transport inside the GFM/HCB. This means that the outer parts relatively quickly can reach close to full saturation while the inner parts remain dry for a significant time. This gives rise to a sequence of swelling/compression where the buffer in the outer parts swells first and compress adjacent materials. Once water reach the inner parts of the buffer these regions starts to swell, leading to compression of the outer parts of the buffer.
- **Simulataneous swelling/compression:** In models with a very low water inflow the suction driven water redistribution within the buffer can be faster than the rate of water inflow. In such cases all parts of the buffer will be in moisture equilibirum at all times and hence the whole buffer volume (HCB and GFM) will swell almost simultaneously.

One point of caution here is the dry density distribution at the UFC hemi head. As can be seen in Figure 4-3 the dry density in the buffer block about the UFC hemi head was low at the interface towards the UFC and increased towards the GFM. The density in the GFM was, however, lower than the density in the block. This behaviour is discussed further in Section 4.7.1.

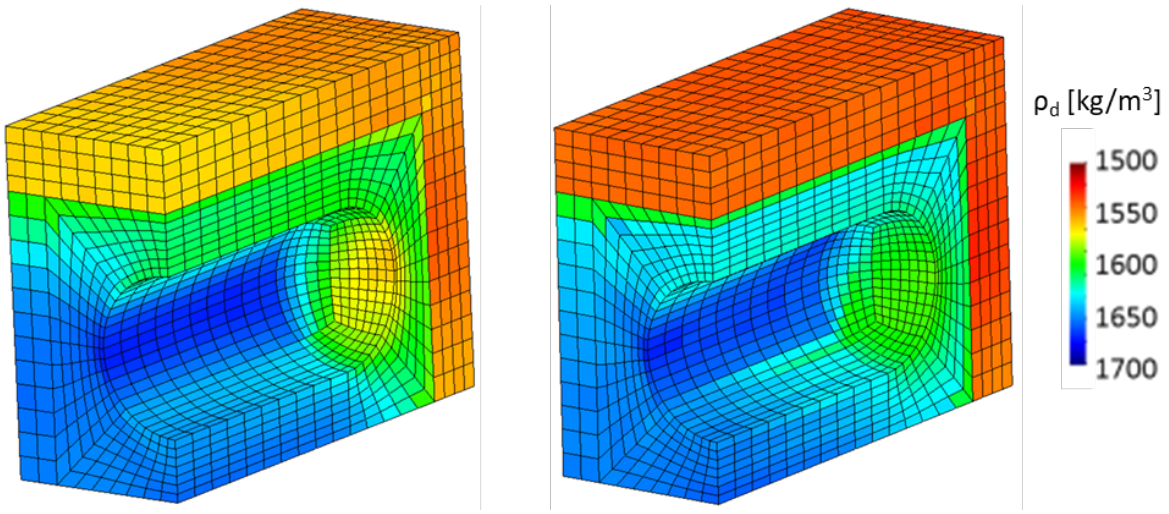

Figure 4-3: Final dry density after full water saturation in the HM models (free access to water (left) and limited access to water (right)

4.6.2 THM Models

The final dry-density state in the THM models is shown in Figure 4-4 and Figure 4-5. As can be seen the final dry density in the base case and flux-limited cases are very similar to the corresponding HM models (Figure 4-3). This is expected as the thermal processes has no direct coupling to the mechanical evolution – the only influence is indirect, via its impact on the hydraulic evolution.

The extremely dry case (Figure 4-5), in which no water inflow was allowed, showed a very different behaviour from the other models. Instead of wetting due to water inflow, only temperature and suction driven moisture redistribution took place. Initially, a rather quick redistribution of moisture due to water vapour diffusion occurred, causing drying near the UFC. Simultaneously, a suction driven transport of liquid water into the GFM, due to the initially much higher water content in the blocks as compared to in the GFM, caused drying in the outer parts of the blocks and wetting in the GFM. This led to shrinking of the block material (i.e., an increase in dry density, see Figure 4-5) and swelling in the GFM.

At the end of the simulation, a very low density near the UFC could be observed (Figure 4-5). However, this was probably just an artefact of the numerical implementation: the grid elements representing the buffer and the UFC were attached to each other. Hence, as the buffer shrunk, the innermost element of the buffer blocks experienced significant tensile stresses, which led to stretching of the material. In a more realistic model, the small gap between the UFC and the buffer would have prevented this.

It can be seen in Figure 4-5 that in the dry model, the dry density in the GFM decreased a little bit with time, while the density in the buffer blocks increased:

1. In the GFM the moisture content increased due to uptake of water from the blocks
2. In the buffer blocks the moisture content decreased, which led to shrinking of the blocks and to an associated slight increase in dry density

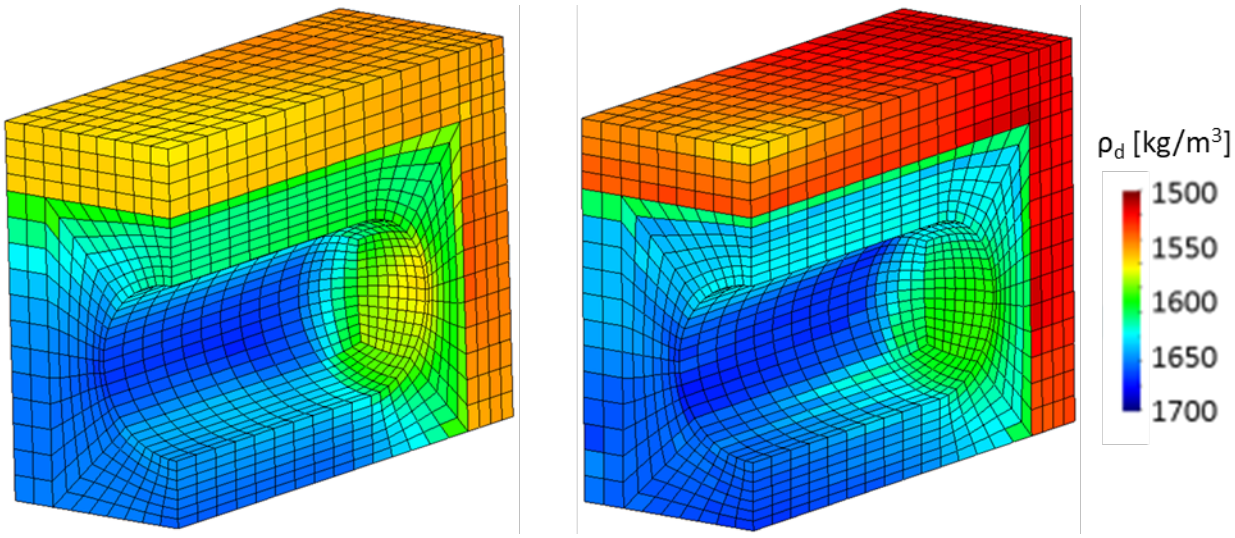

Figure 4-4: Final dry density after full water saturation in the THM models (left: free access to water and right: flux-limited access to water)

It is worth mentioning that the final densities in the dry model should be treated with some caution – the material model was only coarsely calibrated to available shrinkage curves of MX-80 bentonite, and further analysis would be necessary for a more detailed understanding of the degree of shrinkage of the buffer blocks that will take place. Drying and the associated shrinkage can lead to formation of fractures, which in turn are unfavourable regarding the function of the buffer. In Section 7 methods enabling evaluation of if and where fractures may occur are developed and in Section 9.2 these are employed when drying of the buffer box before installation is studied.

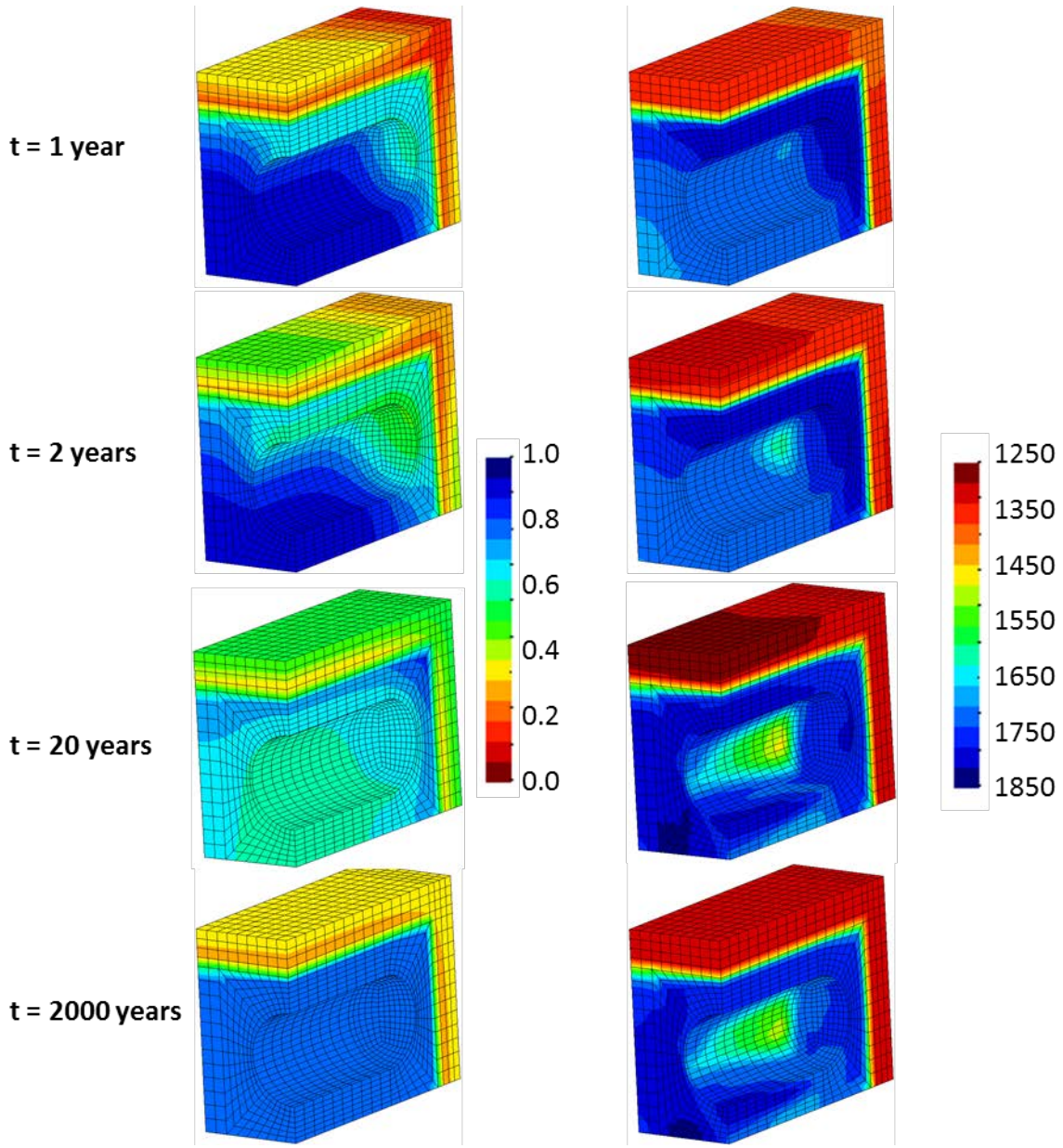

Figure 4-5: Liquid saturation (left) and Dry density (right) at four different times from the THM model with no access to water (the THM dry model)

In the left graph of Figure 4-6, the water content against void ratio is evaluated in two points which undergo significant drying. A decrease in water content of about 9 percentage points leads to a decrease in void ratio of about 0.08. This corresponds rather well to the experimentally evaluated shrinking seen in Börgesson (2001). This decrease was followed by an increase of the water content by about 4 percentage points, which led to an increase of the void ratio by about 0.03. In the final state the void ratio had decreased by about 0.05.

In the right graph of Figure 4-6 the time-evolution of liquid saturation in three points of the buffer is shown. The graph shows that the hydraulic evolution has not quite reached steady state at the end of simulation due to the remaining heat output from the UFC.

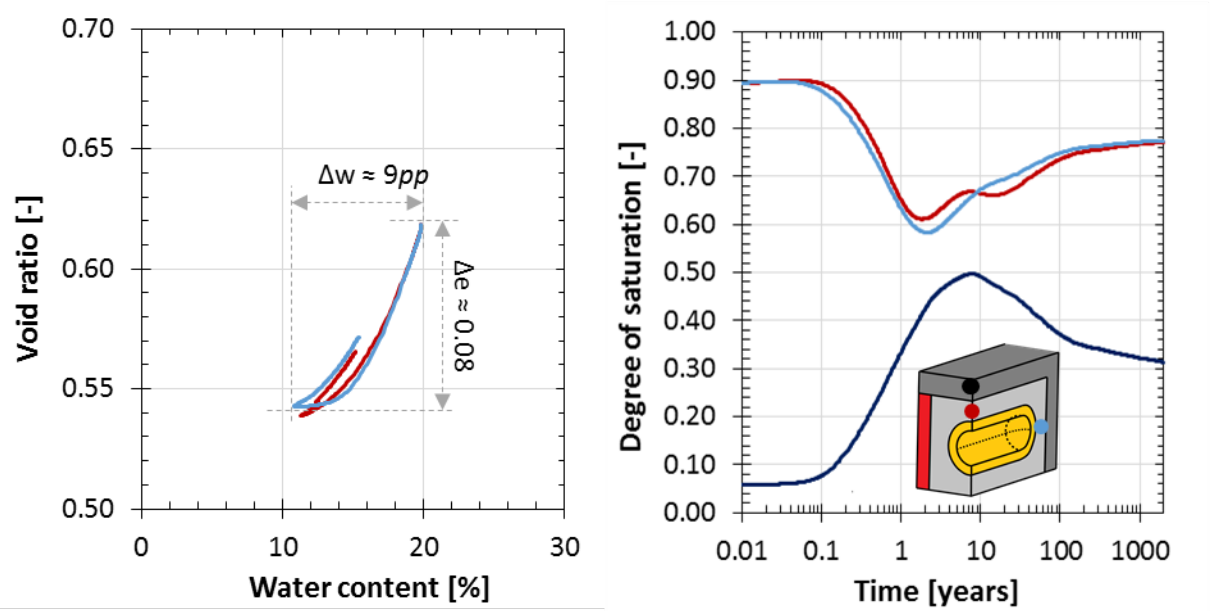

Figure 4-6: Water content against void ratio (left) and time-evolution of liquid saturation (right) from the dry THM model

4.7 Discussion

4.7.1 Dry Density at the UFC Hemi Head

The HM and THM modelling of NWMO's emplacement room configuration carried out in Step 1 of the modelling showed that the evolution in the buffer could be simulated using CODE_BRIGHT. The modelling did, however, raise several questions regarding the behaviour of the buffer in front of the UFC. In Figure 4-7 the dry density distribution in front of the UFCs hemi head from the two HM models is shown.

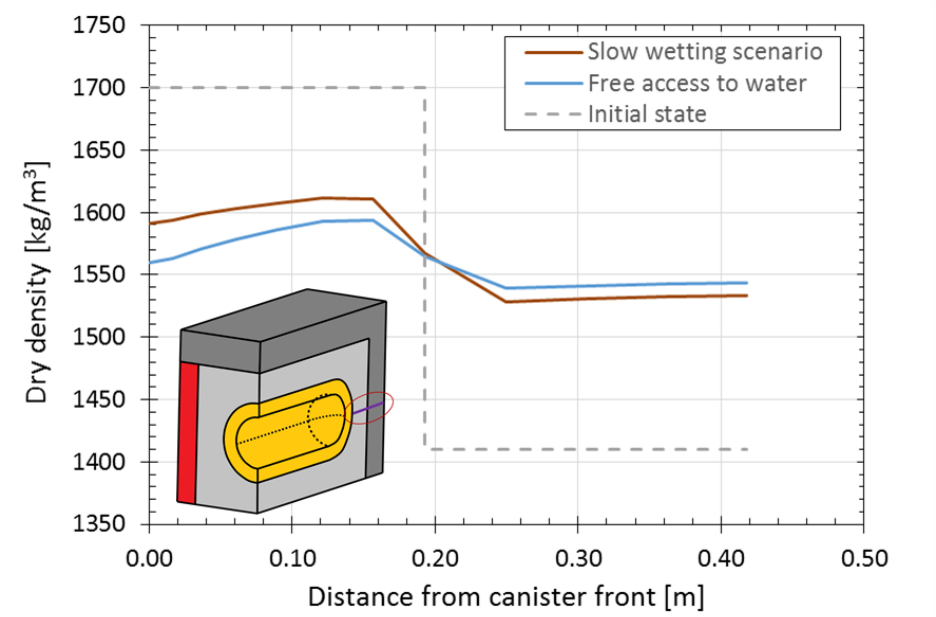

Figure 4-7: The dry-density distribution along the purple line in the illustration of the modelled geometry

The dry density in the buffer blocks increased in the direction from the front of the UFC towards the GFM. This was somewhat counterintuitive compared to what was expected. Usually, an outwards decrease in density gradient would be expected, even if the gradient was very small.

The mechanics behind this outwardly increasing gradient could be associated with whether it was an effect which could be expected to occur in the real buffer or if it was due to the formulation of the material model (BBM) could not be determined in Step 1 of the modelling. It was further analyzed in the next part of the modelling, Step 2, and is discussed in Section 5.3.1.

4.7.2 Drying of Blocks

The THM models showed significant drying of the bentonite blocks particularly in the model with limited water inflow. This drying led to shrinkage that could be estimated by experimental shrinkage curves (see Börgesson 2001). The decrease in volume of the clay due to uneven drying could in turn lead to fracturing of the blocks. This was seen in large-scale tests done by SKB (see Johannesson et al. 2014).

Given the magnitude of drying seen in the flux limited and dry THM models, the degree of saturation in the blocks decreased from 0.9 to about 0.5, and there was a significant risk of potential cracks of the buffer blocks. The extent of the potential cracks on the stability of the UFC was not as part of the Task 1 modelling study. It was, however, analyzed in Task 2 of the modelling, described in Section 7 in this report.

4.8 Summary and Conclusions

The modelling of stage 1 showed that CODE_BRIGHT could be used to model coupled THM processes in NWMO's emplacement room concept using a simplified geometry. The results were in general as expected, even though some peculiarities remained regarding the final dry density gradient in front of the UFC.

The modelling identified some issues of importance for the future modelling program:

- The large initial suction difference between the buffer blocks and GFM could lead to significant drying of the blocks, which in turn might cause shrinking and/or fracturing of the blocks shortly after installation.
- The temperature driven moisture re-distribution in the blocks would lead to drying of the clay buffer near the UFC, in particular if the water inflow from the host rock was low. This could in turn lead to cracking of the blocks.
- Due to the hysteretic nature of bentonite, with different behavior during compaction as compared to during swelling due to decreasing suction, there would be a significant persistent density difference between the buffer blocks and GFM in the final state. Hence the final dry density remained below 1600 kg/m^3 in the GFM zone.

5. STEP 2: IMPROVING REPRESENTATIONS

The modelling carried out in Step 2 is a continuation of the modelling in Step 1, described in Section 4. In Step 2 more realistic geometries were considered including both the upper and lower rows of buffer boxes. One of the main goals of this modelling exercise was to analyze how the offset between the upper and lower rows of buffer boxes could affect the behavior of the THM evolution in the buffer.
Furthermore, the density gradient in the buffer situated around the UFC hemi head and more parts of the mechanical evolution could be analyzed due to the more accurate representation in the models. The dry density field at the UFC hemi head was also studied in more detail by using simplified 2D models. These studies are described in Appendix D.

5.1 Model Description

5.1.1 Geometry and Mesh

The geometry was created to represent the actual setup as close as possible while keeping the modelling domain relatively small. The reduced geometry could not represent the actual offset between the upper and lower rows correctly as no symmetry planes were present perpendicular to the emplacement room axis in the original configuration. A proper realization of this geometry would thus require the inclusion of many UFCs to achieve realistic conditions. Instead, two geometries were constructed:

- No offset: The lower and upper rows of buffer boxes were assumed to be aligned, (i.e., the UFCs in the upper row placed exactly on top of those in the lower row)

- Maximum offset: The lower and upper rows of buffer boxes were assumed to be fully misaligned (i.e., the UFCs in the upper row situated exactly in between those in the lower row).

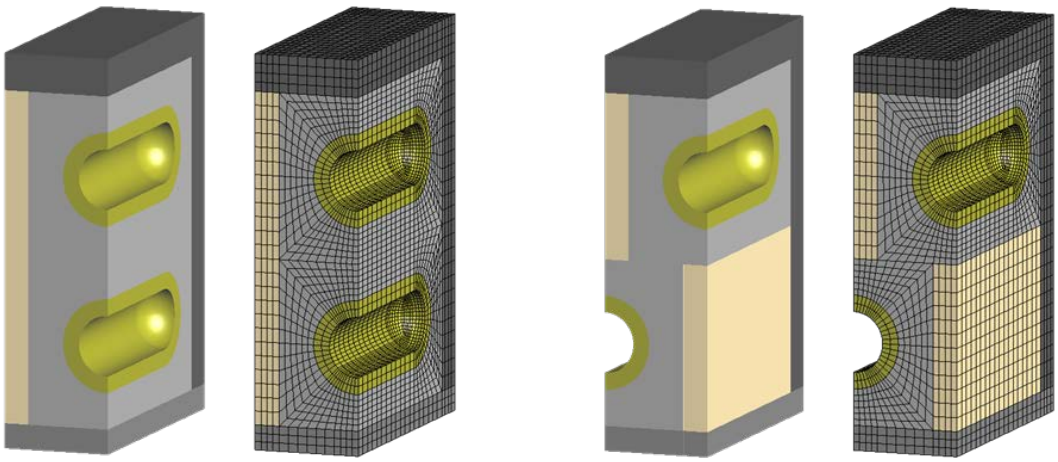

Figure 5-1: Overview of the geometry and finite element discretization used for the no offset case (left) and maximum offset case (right)

Any effects due to the offset between the UFCs in the upper and lower rows were quantified by evaluating the difference in results between these two geometries. An overview of the two geometries is shown in Figure 5-1. The figure also includes a depiction of the mesh as generated by the pre-processor GiD 10.0.8.

5.1.2 Model Setup

The initial and boundary conditions were prescribed according to the description in Sections 3.5 and 3.6. The hydraulic boundary conditions were:

- Free access to water (to simulate high-permeable rock)
- Flux-limited access to water (to simulate low-permeable rock)

The models simulated in Step 2 showed convergence problems when a hydraulic boundary condition was prescribed directly on the lower horizontal HCB boundary (at the interface towards the tunnel floor). In later models (Task 1 and onwards) a concrete slab was included at this position which reduced the numerical difficulty. In Step 2, however, only the THM base case model could be solved with water access through the tunnel floor. The remaining models assumed no water inflow through the floor.

The THM material model parameters used for the HCB, GFM and UFC were identical to those used in the Step 1 modelling (see Section 4.3).

5.2 Results

The results are presented in two parts in this section:

- the thermal (THM models only) and hydraulic results
- the mechanical evolution and final state

To ensure that the model solutions were well behaved, the base case THM model was analyzed to verify the numerical accuracy and to validate the material model. This strategy is described in Section 3.7 and the analysis is given in Appendix B.

A total of eight (8) models were constructed, and these are described in Table 5-1 and Table 5-2 together with the names of the model files. As discussed above, only the THM base case model was simulated with water supplied directly to the buffer blocks through the floor. In the remaining models, a zero-flux condition was prescribed on this surface for numerical purposes.

Table 5-1: Overview of simulated HM models

Model ID	Process	Model name	Description (1)
HM_NO_BC	HM	NWMOPC_HM_BC_REPORT.gid	Base case HM model with no offset geometry
HM_NO_FL	HM	NWMOPC_HM_STEP2_BC_REPORT2_FLUXLIM6.gid	Same as HM_NO_BC with flux limited water inflow
HM_MO_BC	HM	NWMOPC_HM_S2_G3B_par4.gid	Same as HM_NO_BC with full UFC offset

(1)None of these models had water inflow through the floor.

Table 5-2: Overview of simulated THM models

Model ID	Process	Model name	Description (1)
THM_NO_BC	THM	NWMOPC_THM_STEP2B_BC.gid	Base case model for THM case with no offset geometry
THM_NO_NFW	THM	NWMOPC_THM_STEP2B_BC3.gid	Same as THM_NO_BC with no water inflow through the floor
THM_NO_FL	THM	NWMOPC_THM_STEP2B_FL3.gid	Same as THM_NO_NFW with flux limited water inflow
THM_MO_NFW	THM	NWMOPC_THM_S2_G3B_par4_DM2_OKr_2_DM.gid	Same as THM_NO_NFW with full UFC offset
THM_NO_MESH	THM	NWMOPC_THM_STEP2B_BC3_MESH.gid	Mesh and time-step verification of THM_NO_NFW

(1)Only ‘THM_NO_BC’ had water inflow through the floor.

5.2.1 Thermal Evolution in The Buffer

The thermal evolution in the models THM_NO_NFW and THM_NO_FL are illustrated in Figure 5-2 by evaluating the temperature evolution in twelve points in the buffer box and GFM. These models were chosen to illustrate the small differences in temperature evolution that arose from significantly different hydration rates. As also can be seen, the spread in temperature at any given time is rather small in all analysed points except the region between the two UFCs (points P21 and P22), where the temperature is significantly higher. The different colours correspond to the different points analysed as seen in the lower-right corner.

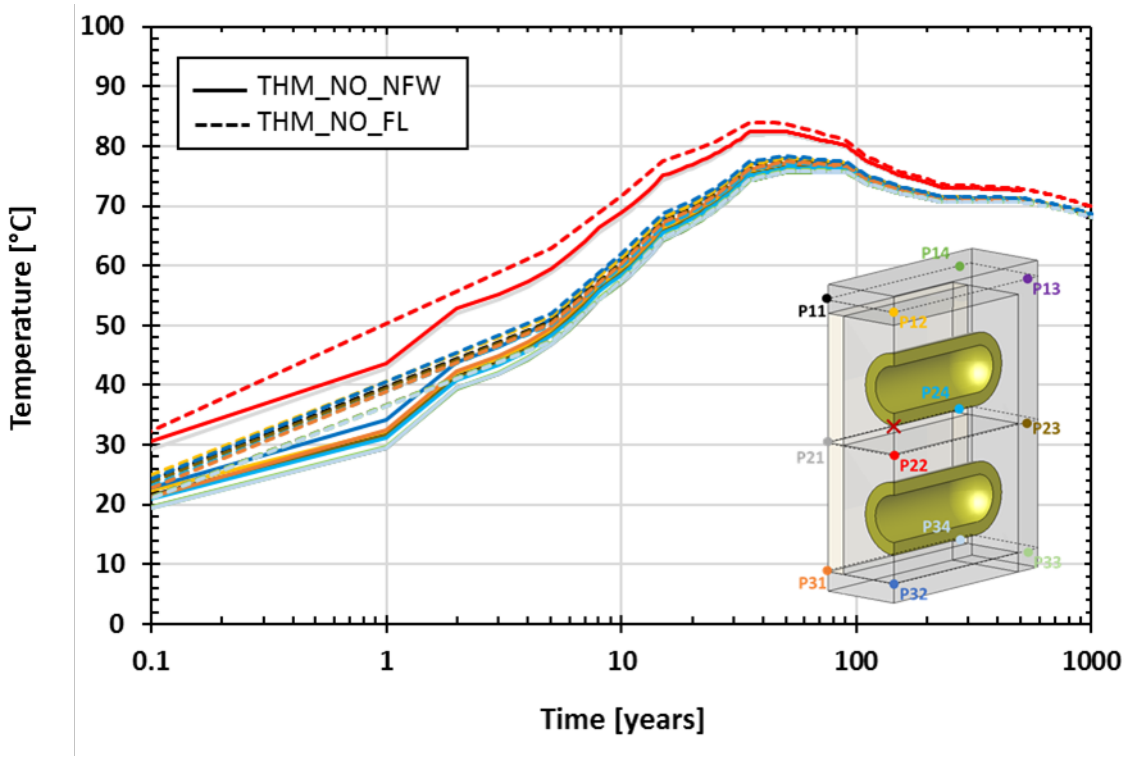

Figure 5-2: Thermal evolution in the buffer component in the THM base case model with no water through the floor (THM_NO_NFW, solid lines) and the flux-limited model with no floor water (THM_NO_FL, dashed lines)

The maximum temperature attained in the buffer was 82.6°C in the area just below the centre of the upper UFC (marked with a red cross in the depiction of the geometry in Figure 5-2). The different hydration rates seen in the two models (see also Section 5.2.2) had a very small impact on the thermal evolution. The difference that is seen around 1 year after installation is due to larger spacing between data points in the flux limited case, and hence is not a sign of any actual difference in temperature.

5.2.2 Hydraulic Evolution in the Buffer

The hydraulic evolution in the HM and THM base case models with no offset was analysed by evaluating the evolution of liquid saturation in four points in the buffer box and in eight points in the GFM. Thereafter the evolution was compared to the hydraulic evolution in the models with other boundary conditions and/or geometries.

It is noted that the hydraulic boundary conditions used in these models were not based on any hydrogeological evaluations of potential sites and hence were constructed for a generic host rock. The time until saturation in the models can be used to understand the relevant timescales for how long it will take until the buffer is saturated, but to make detailed predictions of the saturation time in different places of the emplacement room, site specific conditions would need to be used to construct detailed representations of the host rock.

5.2.2.1 Base Case Models with the No-Offset Geometry

In Figure 5-3 the hydraulic evolution in the base case HM model with no offset is shown for several points in the HCB buffer blocks and the GFM. The evolution was analysed both on the vertical plane intersecting the UFCs and on that intersecting the distance block. The evolution in the base case THM model with the no offset geometry is shown in Figure 5-4.

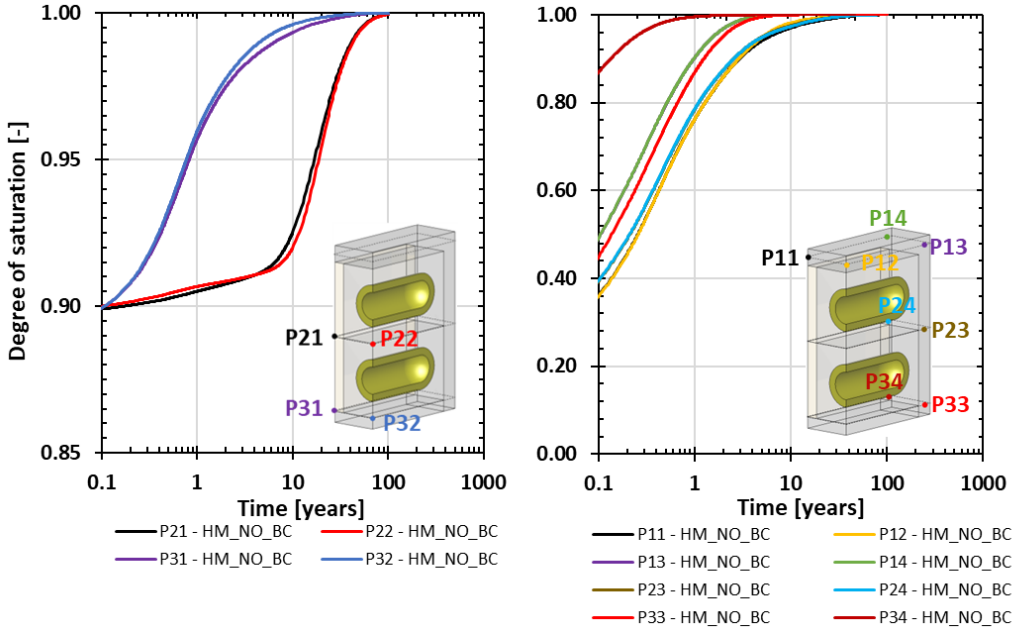

Figure 5-3: Hydraulic evolution in the buffer blocks and GFM in the model HM_NO_BC

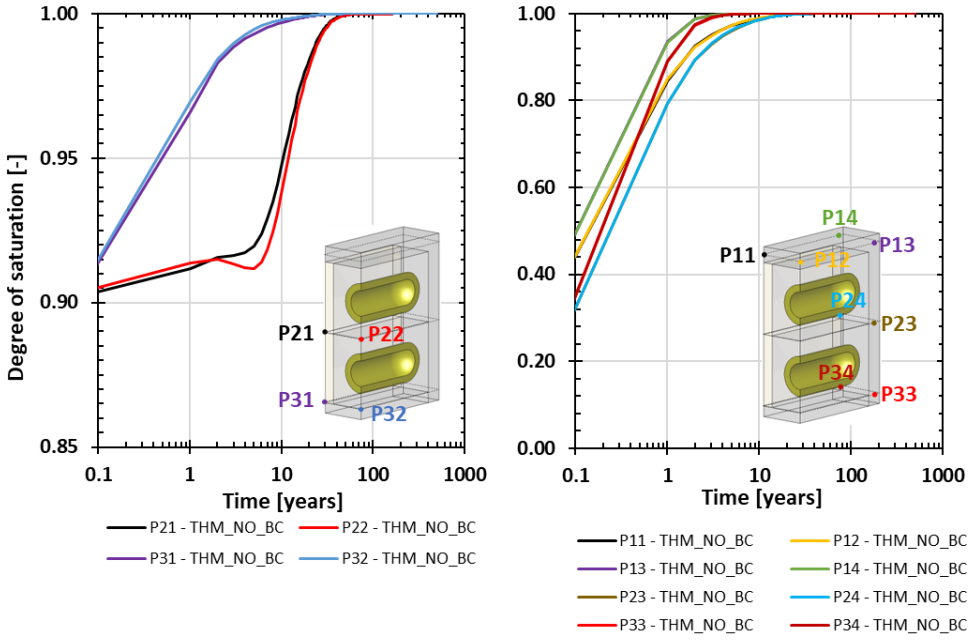

Figure 5-4: Hydraulic evolution in the buffer blocks and GFM in the model THM_NO_BC

Relatively small deviations can be seen between the points in each pair formed by opposite points on each vertical plane. A significant difference can only be seen for the pair P21 and P22 in the THM model, which is caused by drying.

5.2.2.2 Hydraulic Evolution with no Water Through the Floor

In Figure 5-5 the degree of saturation with time is shown in two points of the buffer blocks (left panel) and GFM (right panel). Results are shown from the THM base case model (solid lines) and the THM base case model without water supply through the floor (dashed lines). The results show that the water inflow through the floor is only of significant relevance (in terms of the hydraulic evolution) in the buffer blocks just below the lower UFC.

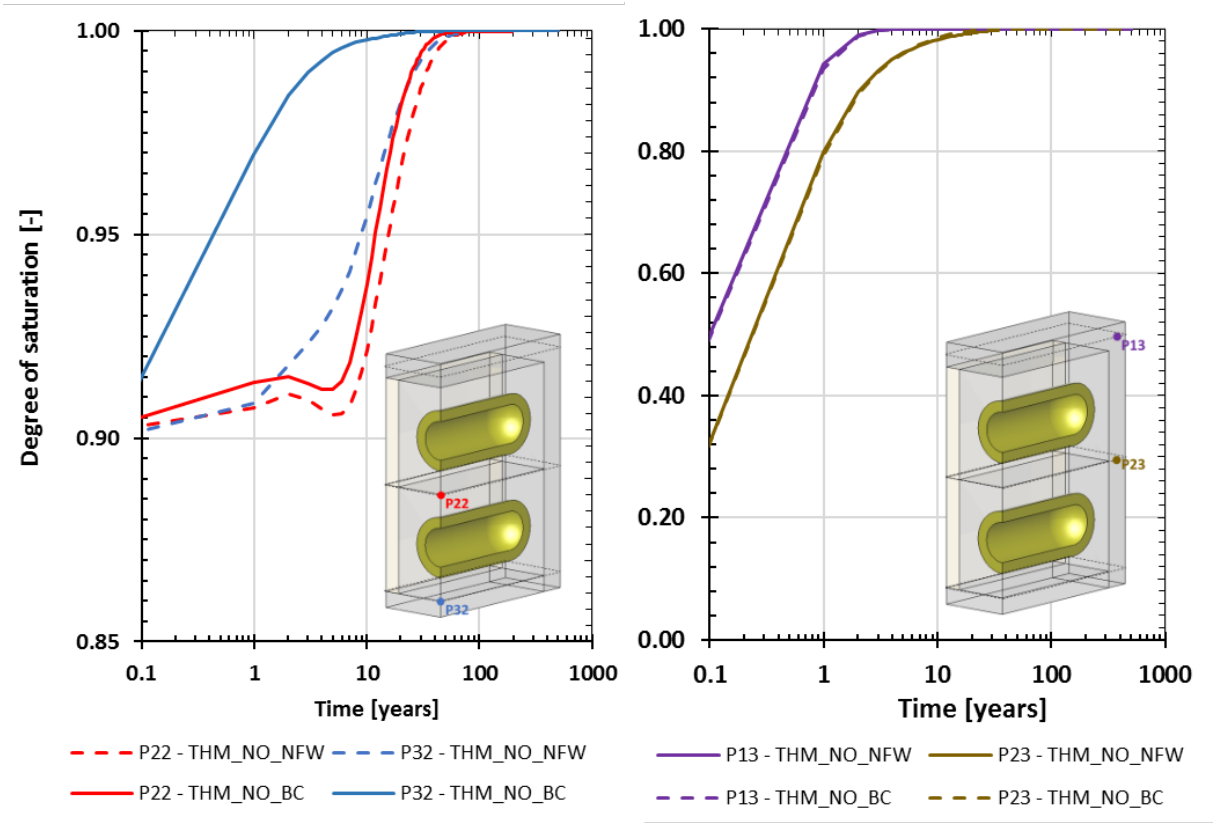

Figure 5-5: Hydraulic evolution in the base case THM model (solid lines) and the base case model without water supply trough the floor (dashed lines)

5.2.2.3 Hydraulic Evolution in (T)HM Models – Maximum Offset Geometry and Flux-Limited Case

Figure 5-6 shows the degree of saturation with time in two points of the buffer blocks obtained from the HM models. Both the base case with the no offset geometry and the models with maximum offset geometry and with a flux-limited boundary condition are shown. As can be seen

the differences between the geometries have a very small effect on the hydraulic evolution, while the flux-limited boundary condition leads to considerably longer saturation times.

In Figure 5-7 the evolution of degree of saturation is given for two points in the GFM for the same models as discussed in Figure 5-6. In free-access to water cases the GFM was saturated before the buffer blocks, while in the flux-limited case the GFM was saturated last.

Note that the somewhat peculiar shape in the early evolution seen in some of the graphs in Figure 5-6 and Figure 5-7 is due to lack of output data points during the first few years of modelled time.

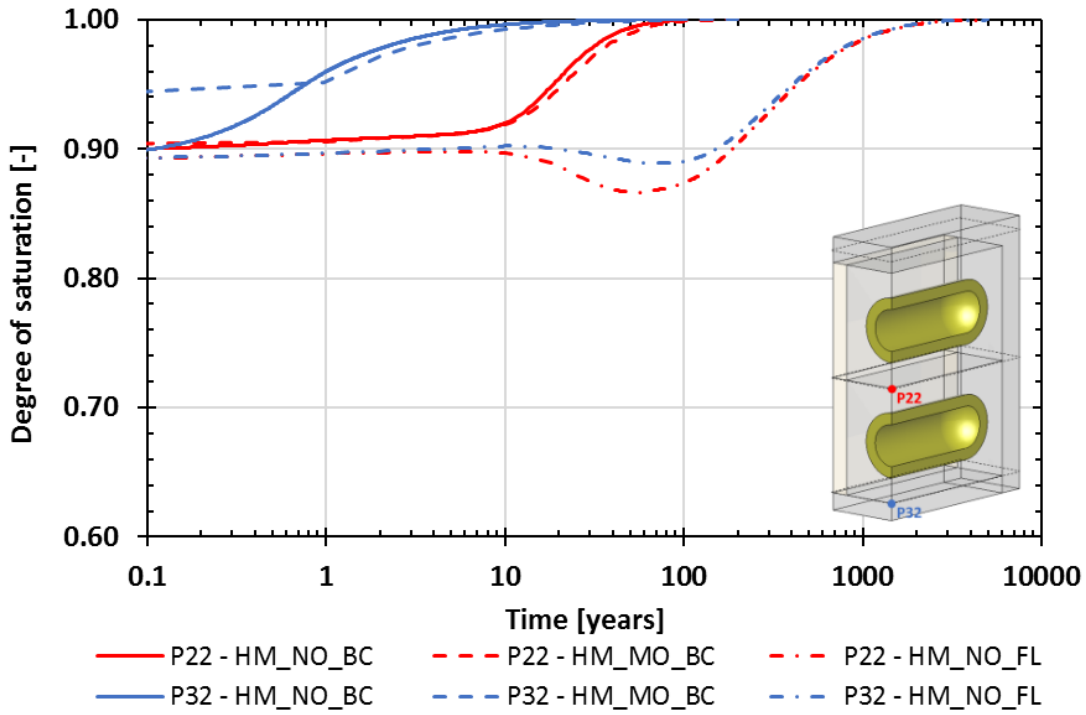

Figure 5-6: Comparison of the hydraulic evolution in the buffer blocks between the different HM models

In Figure 5-8 the degree of saturation in two points in the buffer blocks is shown from the THM models with no water entering into the blocks through the floor. The model THM_NO_NFW was used as base case here and compared with the model with maximum UFC offset (THM_MO_NFW) and the flux limited case. The figure also shows that the different geometries have a very small effect on hydraulic evolution, while the flux-limited boundary conditions again lead to considerably longer saturation times.

In Figure 5-9 the evolution in two points in the GFM blocks is shown for the same models as in Figure 5-8.

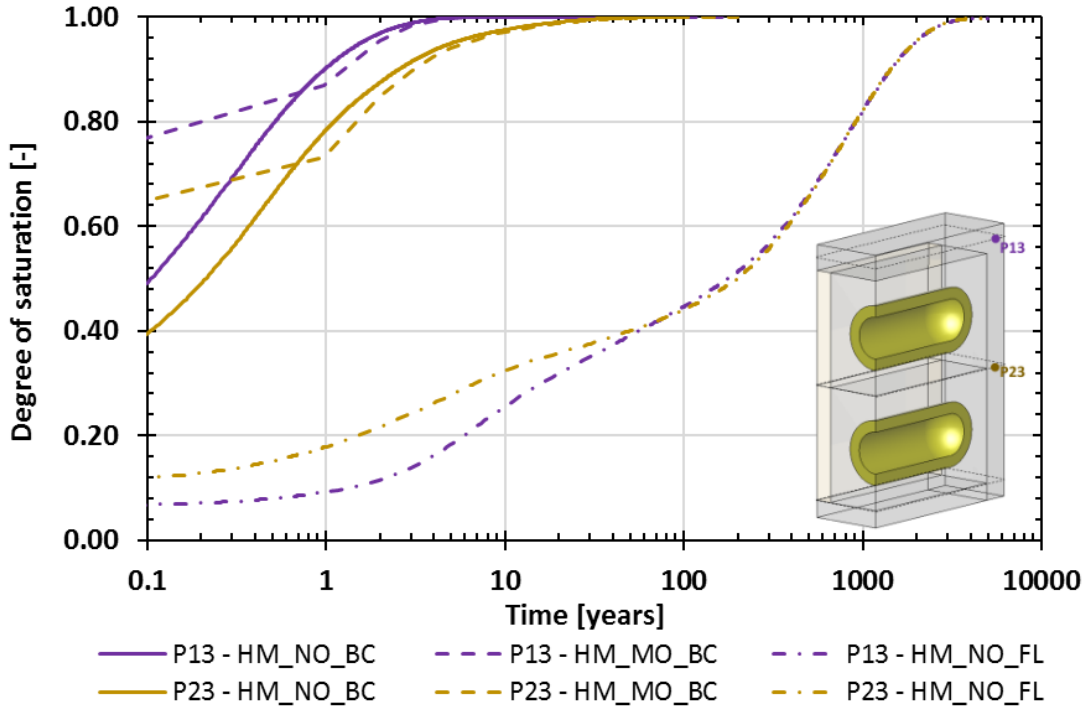

Figure 5-7: Comparison of the hydraulic evolution in the GFM between the different HM models

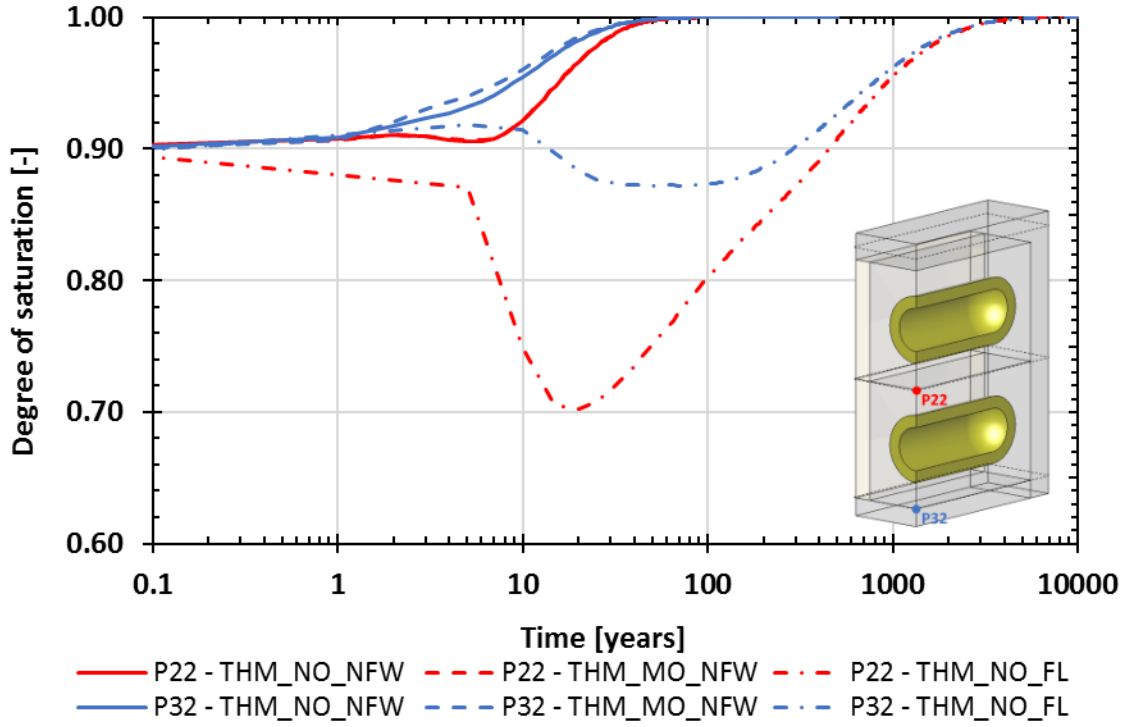

Figure 5-8: Comparison of the hydraulic evolution in the buffer blocks in THM models

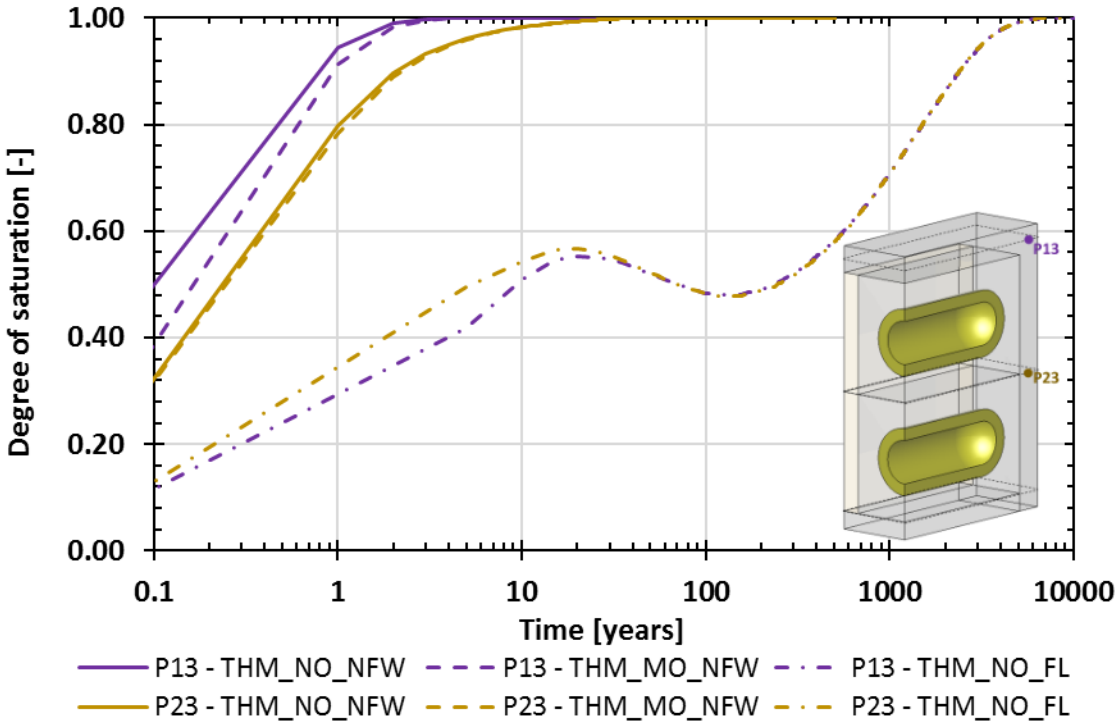

Figure 5-9: Comparison of the hydraulic evolution in the GFM between the different THM models

5.2.3 Mechanical Evolution and Final State

The mechanical evolution is described in three sections: first the stress evolution during the saturation phase is analysed in the base case THM model (Section 5.2.3.1), then the UFC displacements is analysed from all models (Section 5.2.3.2) and finally the final state in terms of dry density and swelling pressure is described (Section 5.2.3.3).

5.2.3.1 Stresses - Evolution and Final State

Since the stress evolution is similar in all models, only the THM base case model is analyzed here. In Figure 5-10 the evolution in net mean stress – void ratio plane is shown. All the points in the HCB blocks show a similar behaviour. Due to water uptake the buffer swells, resulting in an increase in both void ratio and net mean stress which continues until the swelling pressure curve is reached (at full water saturation).

The analysed points in the GFM show a different behaviour as these primarily undergo compression (due to swelling of the buffer blocks) except the very early stage in the model. They end up on a point above the swelling pressure curve, which is consistent with the behaviour of bentonite clay in, for example, oedometer tests (different paths in the p_{eff} – e plane during swelling and compression, see for example Dueck & Nilsson 2010).

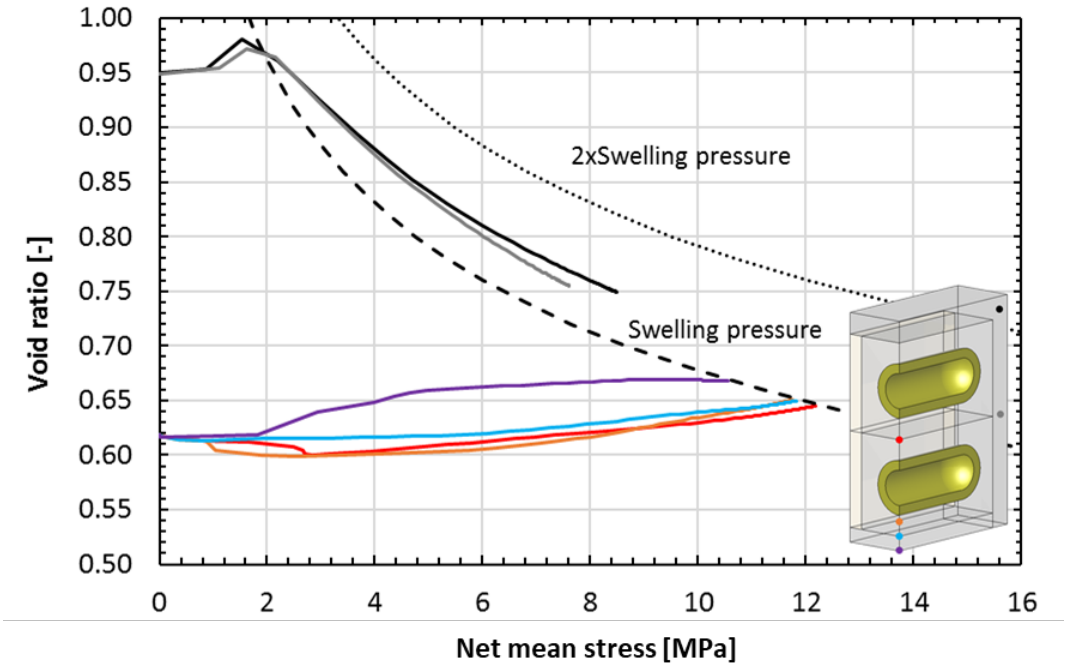

Figure 5-10: Evolution in the net mean stress – void ratio plane for selected points in the THM base case model

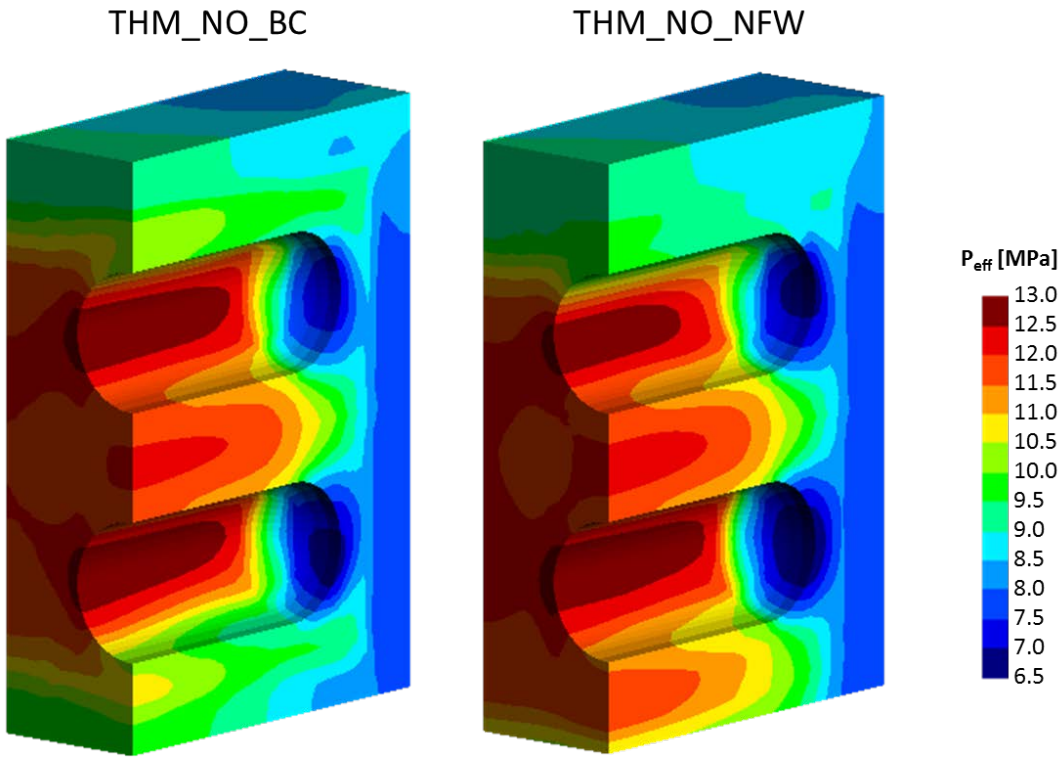

Figure 5-11: Final net mean stress in the THM base case model (left) and base case model with no water through the floor (right)

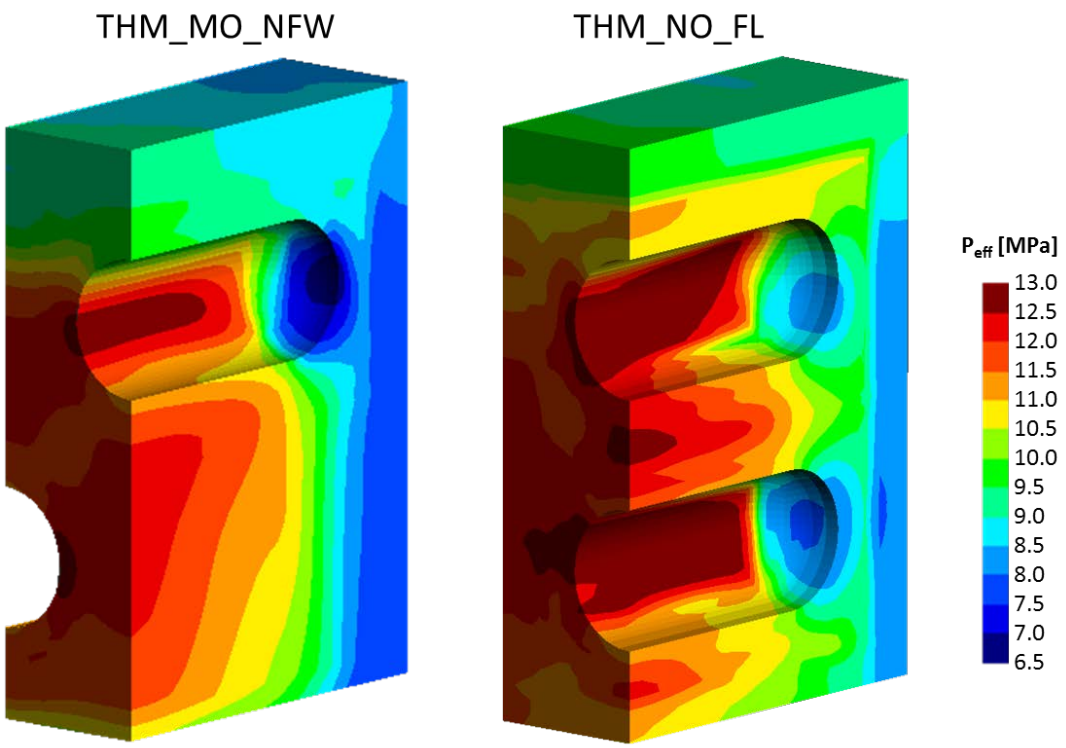

Figure 5-12: Final net mean stress in the THM model with the maximum offset geometry (left) and the THM model with limited water flux (right)

In Figure 5-11 and Figure 5-12 the final net mean stress is shown in the THM models. Removing the water inflow through the floor impacts the net mean stress below the lower UFC (see Figure 5-11). The reason is that in the model in which water inflow through the flow was prescribed, the HCB below the lower UFC experienced more swelling, leading to a lower dry density and thus a lower net mean stress in the final state. Comparing models THM_NO_NFW (Figure 5-11, right) with THM_MO_NFW (Figure 5-12, left) it is clear that the relative position of the upper and lower UFCs has a small effect on the final net mean stress. The model (Figure 5-12, right) shows a significant effect of the limited water inflow on the final net men stress, indicating a much more heterogeneous pressure distribution.

5.2.3.2 UFC Displacement

The displacement of the UFCs in the HM models are shown in Figure 5-13 and in the THM models in Figure 5-14. In the HM models the final displacement of the upper UFC is about 20 mm upwards in all models while the lower UFC moves about 11 mm upwards in the fast-wetting models and about 5 mm in the slow wetting models.

In the THM models a larger variability is seen, which is mainly due to the varying boundary conditions used. In the base case model, the upper UFC moves about 20 mm upwards, while in the models with no water through the floor, it is only lifted by about 15 mm, except in the flux-limited case where an uplift of about 17 mm is seen. The uplift is the same in both the maximum

and no offset geometry and hence the offset between the upper and lower rows of UFCs does not seem to have any significant impact on the vertical movement of the upper UFCs.

The lower UFC shows a similar pattern – in the base case model an uplift of about 11 mm can be observed, while in the models with no water through the floor the upwards movement is only about 5 mm.

In all THM models without water inflow through the floor, as well as in the flux-limited HM model, some initial downwards movement of the UFCs is seen in the figures. This movement is considerably larger in the flux-limited models, compared to those with free access to water. In the models with free access to water and water flow through the floor no such downward movement is recorded. The downwards movement is caused by 1) wetting and swelling in the upper parts of the GFM and buffer box (due to inflow through the ceiling of the emplacement room, and 2) drying of the buffer blocks below the UFCs – leading to some shrinking. Both these effects can lead to a downwards directed force on the UFCs. As water enters the buffer blocks in between the UFCs and below the lower UFCs the buffer swells, causing a net upwards movement of both UFCs in all models once full water saturation has been reached.

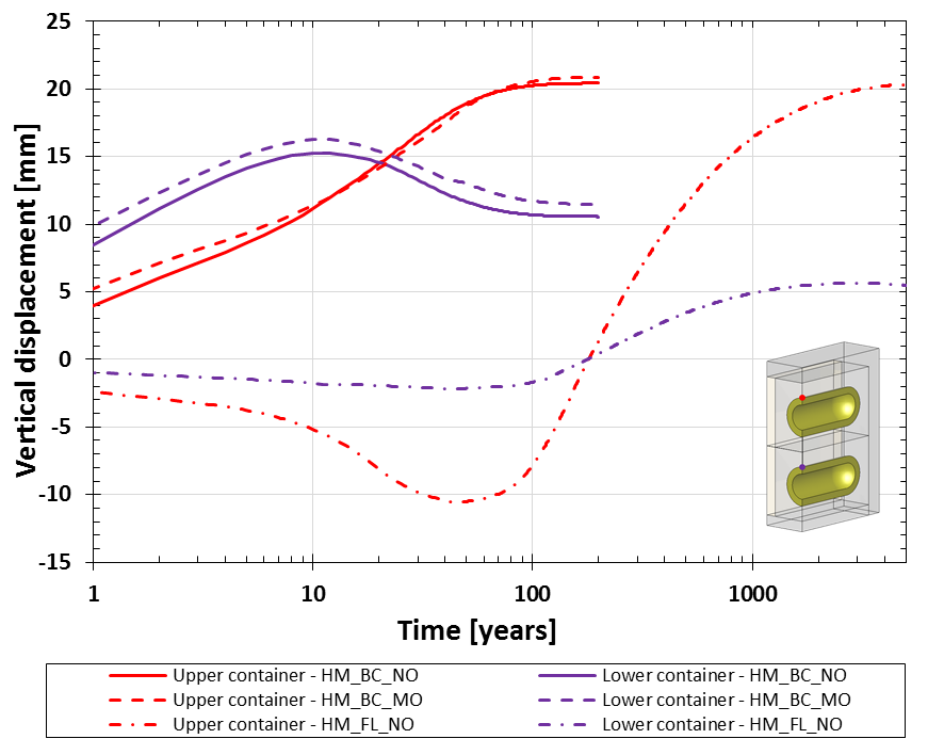

Figure 5-13: UFC displacement in the three HM models

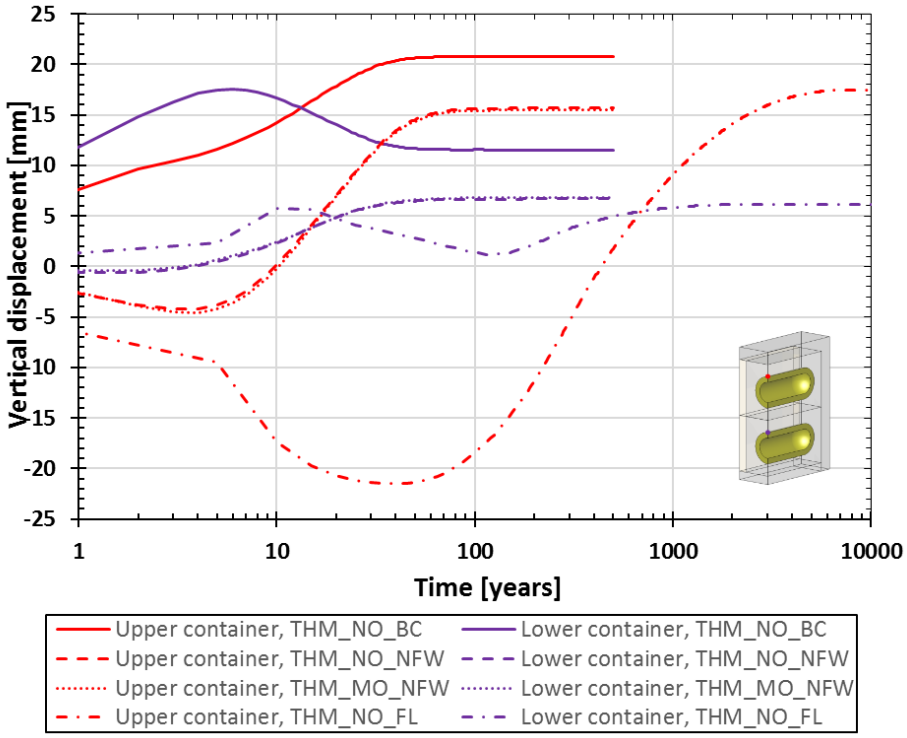

Figure 5-14: Vertical displacement of the UFCs in the three THM models with free access to water

5.2.3.3 Final Dry Densities

The final dry densities from all HM models are shown in Figure 5-15. As can be seen the final dry-densities differ between the three models, in particular between the base case and the flux-limited case. This is, as described in Section 4.6.1, caused by a different time evolution of the swelling – which in turn is caused by a different hydraulic evolution.

In the free-access to water case the outer GFM is quickly saturated whereafter the outer parts of the blocks begin to swell and starts compressing the GFM, in Section 4.6.1 this was identified as a sequential swelling/compression process.. In the flux-limited case the buffer undergoes a much slower wetting, which leads to an almost simultaneous swelling of the entire buffer volume, leading to a more homogeous (in terms of dry density) final state.

In Figure 5-16 and Figure 5-17 the final dry densities in the models THM_NO_BC and THM_NO_NFW are compared to evaluate the effect on the final dry density of the no water through the floor simplification. The most prominent difference is the density below the lower UFC which is considerably higher in the THM_NO_NFW model due to less swelling in this region. In between the UFCs and above the upper UFC almost no difference in the dry density can be discerned.

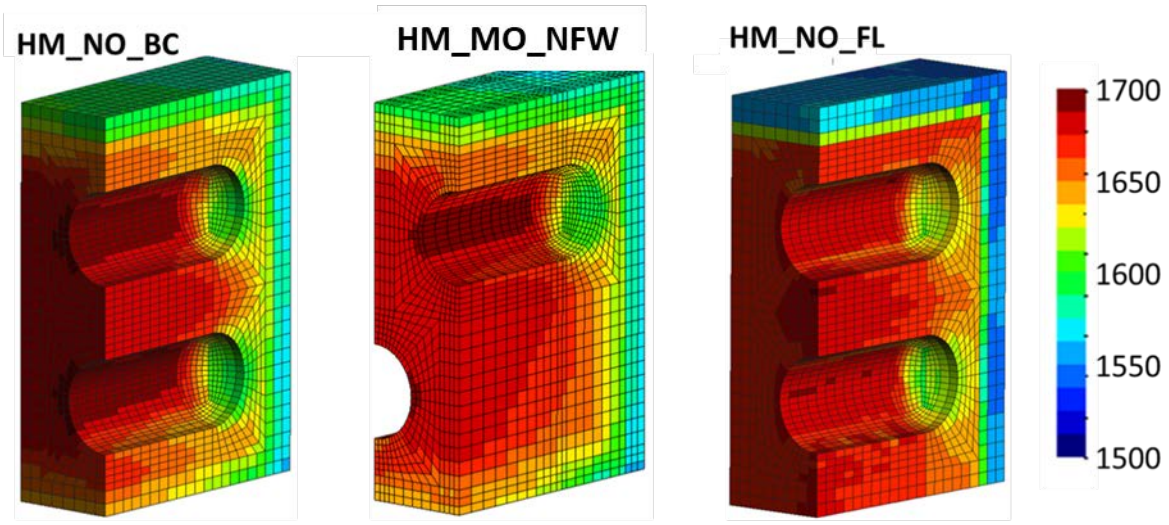

Figure 5-15: Final dry densities in the HM models

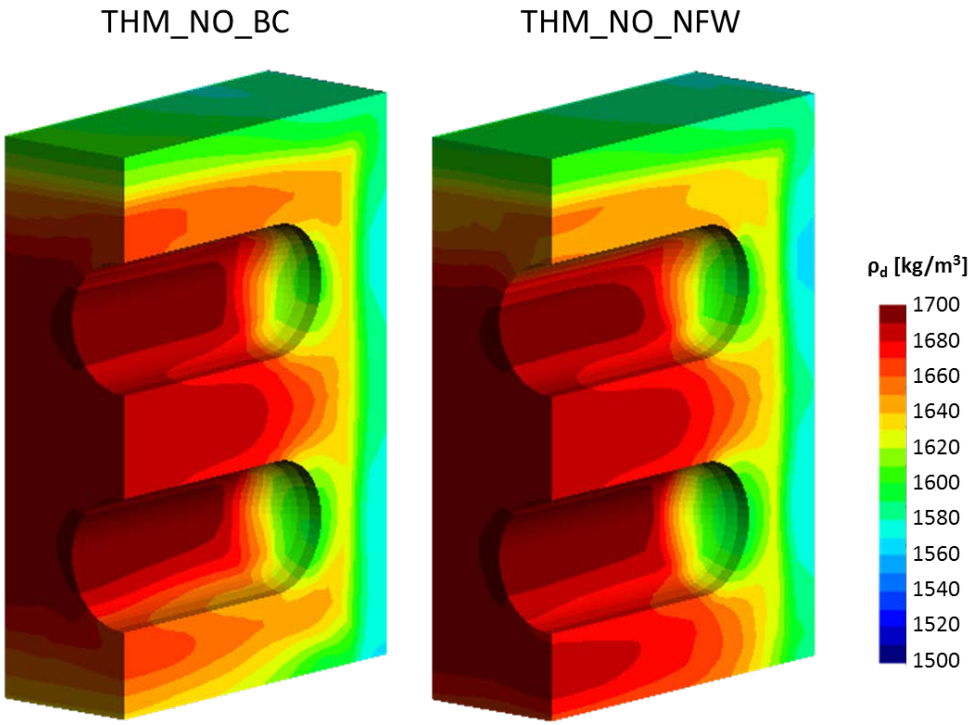

Figure 5-16: Final dry densities in the THM base case model (left) and THM base case model with no water flow through the floor (right)

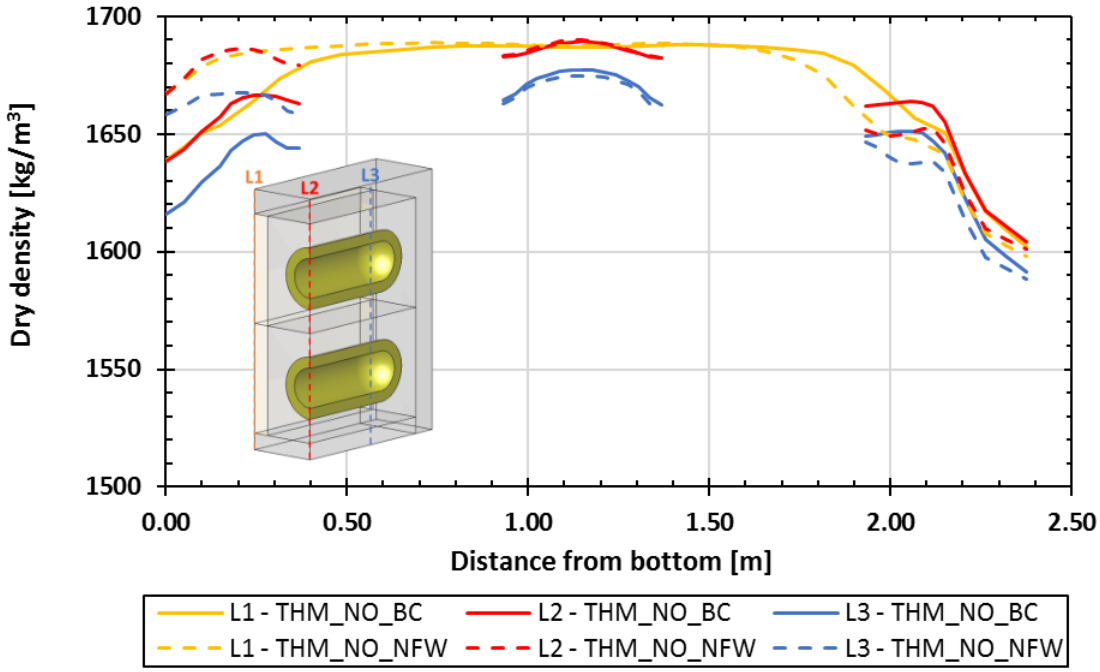

Figure 5-17: Vertical dry density profiles from the THM models showing the importance of water inflow through the floor

In Figure 5-18 the final density in the maximum offset model and the flux limited model is shown and in Figure 5-19 the dry density profiles from these models are shown together with the results from THM_NO_NFW to facilitate comparison.

As can be seen the change in UFC offset has an almost negligible effect on the final dry densities, while the slow hydration rate case shows some deviations above the upper UFC, where a much more heterogeneous dry density distribution can be seen, as compared to the other models. Hence the flux-limited case is considerably less homogeneous in the final state than the fast-hydration models.

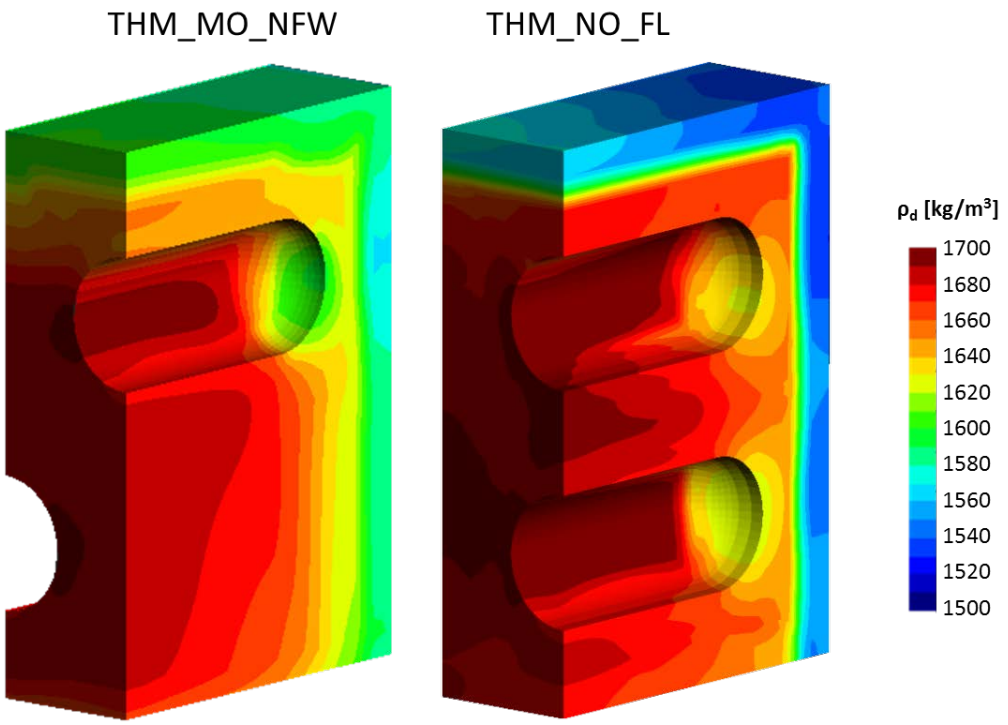

Figure 5-18: Final dry densities in the THM model with maximum offset (left) and THM model with a flux-limited water inflow (right)

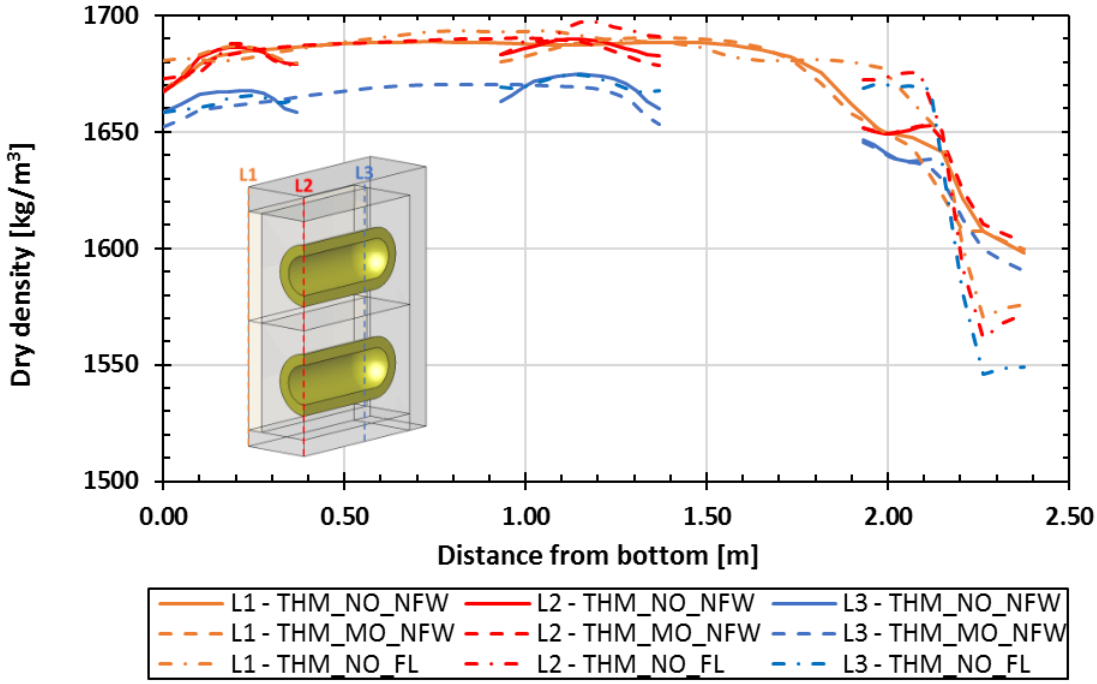

Figure 5-19: Final dry density profiles in the THM models with no water inflow through the floor into the buffer blocks

5.3 Discussion

5.3.1 Bentonite Dry Density at the UFC Hemi Head

A detailed study of the dry density field between the UFC gable and tunnel wall was motivated by findings of what was thought to be a “counterintuitive” appearance when performing the simulations for Step 1. The study is described in Appendix E. The appearance/feature consisted of a drop in dry density in profiles evaluated towards the UFC gable.

To study this in a convenient way, hydro-mechanical plane 2D models with and without a steel UFC were developed. For a full description of the study and the results see Appendix E, in short, however, the following were concluded:

- A decrease in dry density close to the UFC also occurred for a UFC without hemi-head.
- The UFC acted as a constraint on the deformation.
- The UFC protected the buffer close to the gable from mechanical influence from other parts of the buffer.
- In the steel UFC model, the normal stresses at the UFC/buffer interface were always compressive, indicating that no gaps would open even if there had been a possibility for this in the model.

When slip between the UFC and clay buffer was accounted for in a model, the overall trend was that the decrease in dry density was somewhat less pronounced, but the feature was nevertheless present.

5.3.2 Water Inflow Through the Floor

Water inflow applied directly onto the bottom surface of the HCB blocks could not be used in all models due to convergence issues. The effect on the results when not including this could be evaluated by comparing the base case THM model (in which water inflow could be applied directly to the blocks) to the base case where no inflow was applied at the blocks.

The most notable effects were:

- the density below the lower UFC was higher in the model without water inflow, and
- the uplift of both UFCs was smaller in the model without water inflow.

To understand the effects of the water inflow simplification on the maximum offset model and the flux limited model, the results presented in Sections 5.2.3.2 and 5.2.3.3 can be analyzed:

- **Maximum offset model:** The density distribution and UFC uplift were very similar in the model with no offset (THM_NO_NFW) and the model with maximum offset (THM_MO_NFW) and hence the density distribution and UFC uplift seen in the base case model with no offset (THM_NO_BC) was most likely a good approximation of the evolution in a model with maximum offset and water inflow through the floor.
- **Flux limited model:** There was some difference between the model with no offset and no water through the floor (THM_NO_NFW) and the flux-limited model with no offset (THM_NO_FL). The effect of water inflow through the floor was not evaluated for the

flux-limited case, but since the water re-distribution in the buffer was quicker than the water inflow in this model (i.e. the suction gradients in the buffer were always small) it was judged that it could be ignored.

5.4 Summary and Conclusions

The results from the models simulated as part of Step 1 (describe in Section 4), showed that near the hemi head of the UFC, there was a decrease in dry density. This feature was further analysed in this section which led to the conclusion that this decrease in density near the UFC remained also with a differently shaped container (a rectangular parallelepiped shape). The cause of this feature is the difference in homogenized densities in horizontal sections above/below the UFC and at container mid-height. This difference causes an inhomogeneous stress field, which affects the dry density near the hemi head.

The modelling carried out in Step 2 showed that the THM evolution during the transient saturation phase in the buffer could be modelled using CODE_BRIGHT with a realistic geometry. Some general conclusions can be drawn from the modelling:

- Simulating the thermal processes using a prescribed temperature on the placement-room walls (determined from large-scale thermal models) showed good results.
- There would be a persistent dry density difference between the buffer blocks and GFM in the final state. One of the causes for this could be the path dependence of bentonite, with different mechanical response during compaction (under saturated conditions) compared to during expansion (swelling). Hence the final dry density remained below 1600 kg/m^3 in the GFM zone.
- The difference between the no offset geometry and the maximum offset geometry were very small. Hence, in future modelling it should be enough to only consider one of these geometries.
- Water inflow from the tunnel floor had significant effect on the mechanical evolution in the lower parts of the bottom buffer box, and on the displacement of both the lower and upper UFCs.

Regarding the modelling strategy a few important lessons can be drawn:

- Prescribing a water flux directly on the surface of the high-density buffer blocks caused significant numerical problems.
- The time required for the calculations were significant (e.g., about a month for the flux limited THM models). This meant that simulating many UFCs in a single model at the present level of detail was not tractable.

6. TASK 1: HETEROGENEOUS WETTING

The work within Task 1 was based on the work carried out in Step 1 and Step 2. Whereas previous modelling only considered homogeneous water inflow with two different inflow rates, the modelling in Task 1 focused on other hydration scenarios. In the emplacement room, water inflow can occur:

- through a few high-flowing fractures,
- through many low-flowing fractures,
- through a combination of fractures and the rock matrix.

To analyze the effect of the different water inflow conditions on the THM evolution in the buffer, two different subtasks were carried out:

- **Subtask 1.1**: Swelling of the buffer and movement of UFCs assuming a local water inflow into the emplacement room.
- **Subtask 1.2**: Heterogeneous wetting of a single buffer-box stack

The analysis of Subtask 1.1 is described in Section 6.1 and the analysis of Subtask 1.2 in Section 6.2.

6.1 Subtask 1.1 - Swelling of the Buffer and Movement of UFCs Assuming a Local Water Inflow into the Emplacement Room

The purpose of this subtask was to analyze how the dry density in a single buffer box stack is affected by local water inflow and the subsequent swelling. The scenario investigated is that water inflow occurs in only a narrow region of a given emplacement room (e.g., through a single water-bearing fracture). The bentonite close to this region will swell and exert a pressure on the neighbouring dry buffer-box stacks. If the exerted force is large enough, the dry buffer box stacks may displace, causing more room for the wet bentonite to swell into. This can lead to very low dry densities in the bentonite buffer near the water bearing region.

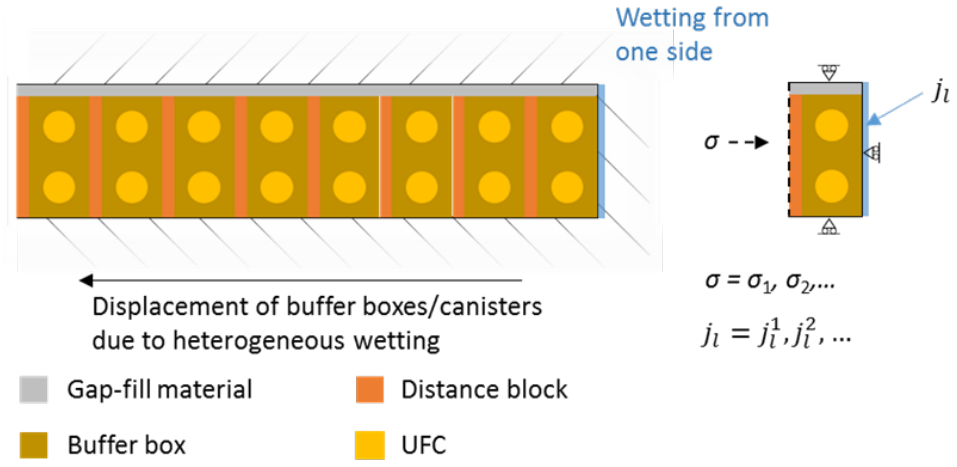

Figure 6-1: Schematic illustration of the process considered in subtask 1.1

A version of this scenario is illustrated in Figure 6-1, which shows a plane cut through the geometry. Water uptake at one end of the emplacement room may cause displacement of UFCs along the emplacement room. In Figure 6-1, right, a local model of the buffer-box stack taking up water is illustrated. The local model may be used to design appropriate mechanical boundary conditions for a global analytical model.

To analyze the effect of such a wetting pattern, a two-step strategy was applied:

1) **Local FE model**: The model consisted of a FE model that simulated the hydro-mechanical evolution in a buffer box stack with surrounding GFM during the water-uptake stage. The analysis was similar to the models carried out in Step 2 discussed in Section 5, except that the buffer box stack was allowed to swell in the direction of the emplacement room. Using this FE model a relation between the dry density and the force exerted on the adjacent buffer box stack could be determined.
2) **Global analytical model:** The displacement of the dry buffer-box stacks in the emplacement room, due to the pressure exerted by the swelling buffer-box stack, was quantified using an analytical model. This considered the friction against the emplacement room's walls and floor and the closing of the gaps between the buffer box stack, using input from the local FE model.

Using the results from the local and global models the effects of "local swelling" in one end of the emplacement room could be evaluated.

6.1.1 Global Analytical Model

Each buffer-box stack was assumed to be separated to the next stack with a distance w_{gap}, which was assumed to be equal between each stack (the layout is illustrated in Figure 6-2). No other gaps between individual buffer blocks were considered. Water uptake and swelling of the buffer-box stack at one end of the emplacement room would cause the buffer to expand and close the open gap between it and the neighboring buffer-box stack. Once the gap is closed the swelling buffer-box stack will exert a force on its neighbor which corresponds to the swelling pressure multiplied by the contact area. If this force is greater than the friction force generated when sliding a dry buffer box along the long axis of the emplacement room, the dry stack will be pushed towards its neighboring stack of dry buffer boxes.

The friction force, generated by sliding N_{stack} number of buffer boxes, scales linearly with N_{stack} while the force generated by the swelling buffer box stack will decrease when it expands. Hence, an equilibrium state exists where the friction force from displacing N_{stack} dry buffer-box stacks corresponds to the swelling force generated after the wet buffer-box stack expands a distance N_{stack} x w_{gap}.

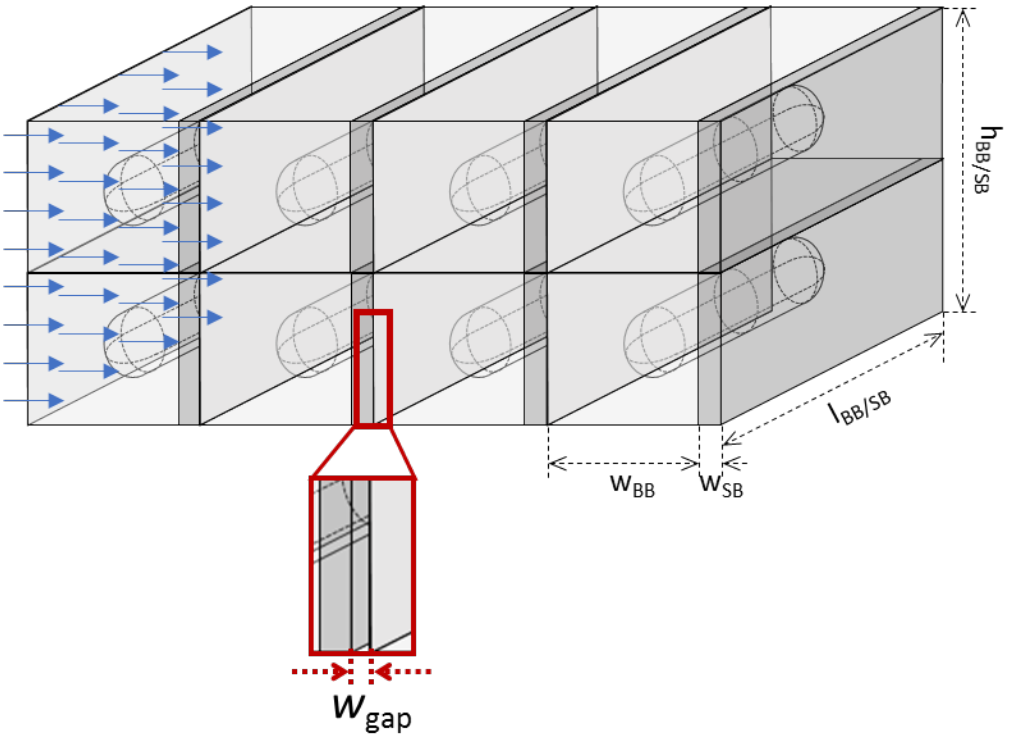

Figure 6-2: Basic geometry assumed in developing the analytical model

The analytical model is described in full in Appendix F, the the friction force, $F_{friction}$ and the swelling forces, F_{swell} is given below.

$$F_{\text{friction}} = \frac{u}{w_{\text{gap}}} \times \left[\frac{\rho g w_{\text{GFM}}(w_{\text{BB}}+w_{\text{SB}})}{2}\int_{z_{\text{top}}}^{z_{\text{floor}}}\left(1-e^{-2K\tan(\theta)z/w_{\text{GFM}}}\right)dz + M_{\text{stack}}g\tan\theta\right], \quad (6\text{-}1)$$

$$F_{\text{swell}} = P_{\text{swell}}(\rho_{\text{d}}) \times h_{\text{BB/SB}} \times l_{\text{BB/SB}} \quad (6\text{-}2)$$

The swelling force, F_{swell}, is as a function of swelling pressure function, P_{swell}, which is defined in Appendix F. The dry density, ρ_{d}, of the swelling buffer-box stack can be written as a function of N_{stacks}:

$$\rho_{\text{d}}(N_{\text{stacks}}) = \rho_{d0}\frac{h_{\text{BB/SB}} \times l_{\text{BB/SB}} \times (w_{\text{BB}}+w_{\text{SB}}) - 2 \times V_{UFC}}{h_{\text{BB/SB}} \times l_{\text{BB/SB}} \times (w_{\text{BB}}+w_{\text{SB}}) - 2 \times V_{UFC} + h_{\text{BB/SB}} \times l_{\text{BB/SB}} \times N_{\text{stacks}} w_{\text{gap}}} \quad (6\text{-}3)$$

By combining Equations 6-1, 6-2 and 6-3 the number of displaced buffer box stacks and the average dry density in the "swelling" buffer box stack were calculated for various friction angles and initial gap values.

The results are shown in Figure 6-3 where the number of displaced buffer boxes (left) and average dry density in the buffer box stack (right) is plotted as function of friction angle for three different values of the initial gap, w_{gap}. As can be seen, the dependence on the friction angle is rather weak for the values shown.

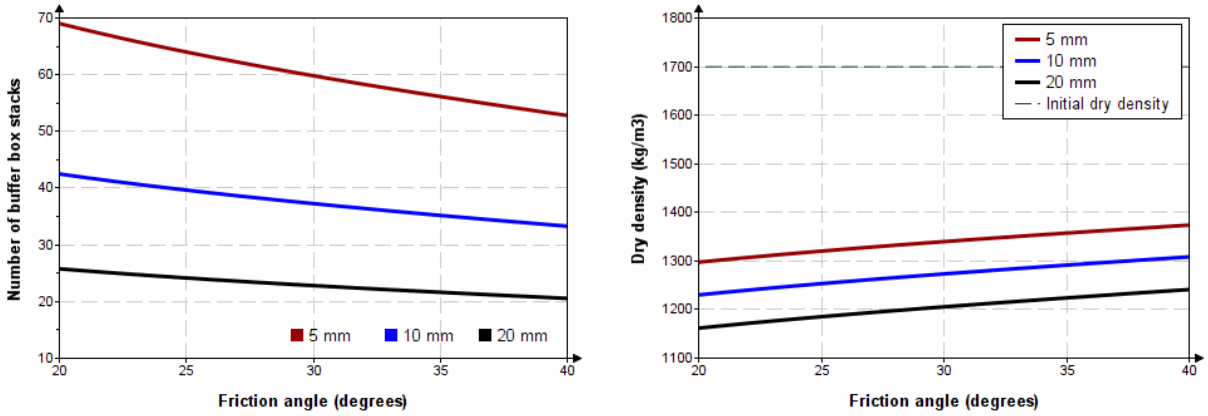

Figure 6-3: Number of displaced buffer boxes (left) and final dry density in the swelling buffer box

Figure 6-3 shows that the dependence on the initial gap width is significant. Three different values of the initial gap width are shown: 5 mm (red line), 10 mm (blue line) and 20 mm (black line). As can be seen in Figure 6-3 (right) the target average dry density of 1600 kg/m^3 was not met for any one of the initial gap values evaluated.

6.1.2 Local FE-Model Setup

The purpose of the local FE model was to analyze the relationship between the force exerted on the dry HCB buffer boxes and the expansion of the swelling buffer box. To carry out this analysis a new geometry was constructed, including gap material that allowed for a pre-determined amount of expansion of the buffer box stack and GFM to take place in the direction of the dry buffer boxes (which were not included in the FE-model). The geometry and mesh constructed are described in Section 6.1.2.1 and the initial and boundary conditions and material model parameters are described in Sections 6.1.2.2 and 6.1.2.3, respectively.

6.1.2.1 Geometry and Mesh

The geometry constructed included the buffer box, the surrounding GFM, and a so-called gap material. The model geometry and mesh are shown in Figure 6-4. The gap material was included to allow for a limited expansion of the buffer box stack (due to swelling) in the direction parallel to the emplacement room.

The gap material used a bi-linear elasticity model with the elasticity modulus dependent on the volumetric strain in the gap material. An illustration of the stress-strain relationship in this material model is shown in Figure 6-5. For values lower than the volumetric strain limit, $\varepsilon_{v,limit}$, the value of the Young modulus was set to E_O, while for a volumetric strain equal to or larger than $\varepsilon_{v,limit}$, the value was set to E_C. Setting the proper values of E_O, E_C and $\varepsilon_{v,limit}$ allows the buffer to swell freely up to a given strain value whereafter further expansion is prevented. By varying the value of $\varepsilon_{v,limit}$ between different models and measuring the force exerted on the gap

material after full saturation (when $\varepsilon \geq \varepsilon_{v,limit}$) gives a relationship between displacement and swelling force which can be compared to the simple analytical estimate in Equation 6-2.

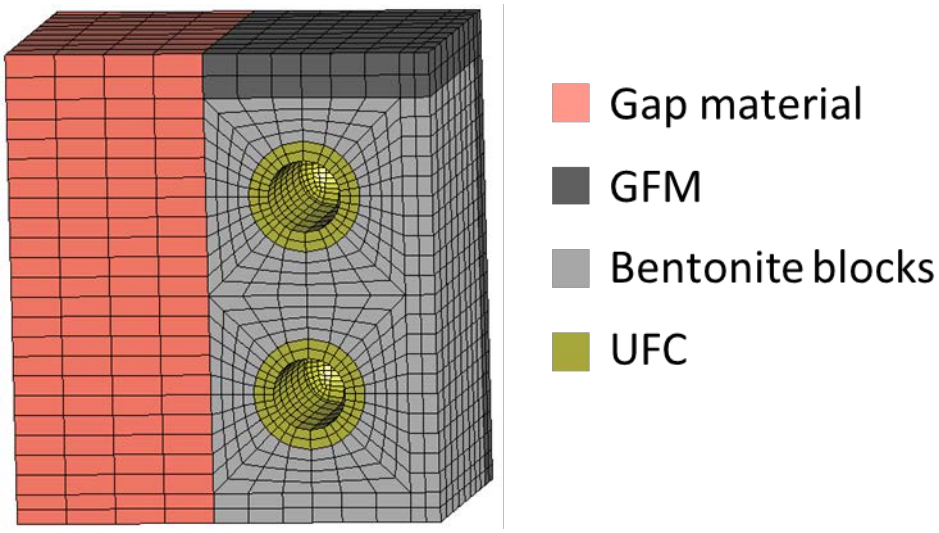

Figure 6-4: Geometry and mesh used in the FE-model in subtask 1.1

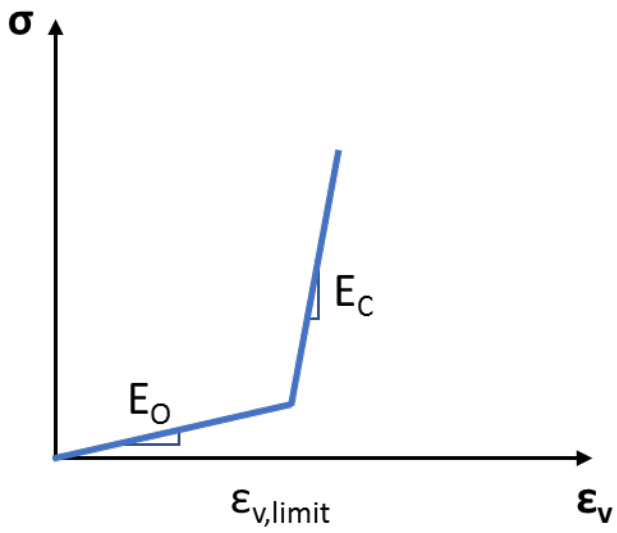

Figure 6-5: Illustration of the stress-strain relationship in the bi-linear elasticity model used for the airgap

6.1.2.2 Initial and Boundary Conditions

The liquid pressures in the HCB, UFC and gap material were prescribed on all nodes. Initially the suction in the HCB, UFC and gap material was set to 23 MPa and in the GFM to 161 MPa. The suction in the buffer blocks and gap material was then linearly ramped from 23 MPa to 0 MPa during the first 10 years and the suction in the GFM was linearly ramped from 161 MPa to 0 MPa during the same time period. After 10 years the suction was kept at 0 MPa in all nodes and the model continued until termination after 20 years. This approach was used to simplify the numerical solution and essentially simulated a fully homogeneous water uptake scenario.
The mechanical boundary conditions were prescribed as roller boundaries on all outer surfaces.

6.1.2.3 Material Model Parameters

The THM material model parameter values for the bentonite and UFC materials were the same as those used in Steps 1 and 2 and are described in Sections 3.3.7 and 3.3.8. The parameters used for the gap material are given in Table 6-1.

Table 6-1: THM parameters for the gap material

			Gap material
Initial porosity	n	-	0.999
Intrinsic permeability	k_0	m^2	10^{-30}
Relative permeability	k_r	(-)	1
Water retention curve	P_0	MPa	10
	λ_0	(-)	0.3
Solid density	ρ_s	kg/m^3	1200
Poisson ratio	v	(-)	10^{-5}
Open gap Young modulus	E_O	MPa	1
Close gap Young modulus	E_C	MPa	1000
Volumetric strain limit	$\varepsilon_{v,\,limit}$	-	0.1-0.4[1)]

[1)]Value varied between different models

6.1.3 Results from Local FE-Model

The results obtained from the models are given below, except for the results from the validation exercises carried out, which are given in Appendix C. The constructed models are listed in Table 6-2.

Table 6-2: FE models constructed and simulated in subtask 1.1

Model ID	Description	$\varepsilon_{vol,lim}$
S3_S11_M001	Base case model	0.1
S3_S11_M001FM0	Base case model + Finer mesh	0.1
S3_S11_M001T	Base case model + Finer time stepping	0.1
S3_S11_M002	Base case model, except value of $\varepsilon_{vol,lim}$	0.2
S3_S11_M003	Base case model, except value of $\varepsilon_{vol,lim}$	0.3
S3_S11_M004	Base case model, except value of $\varepsilon_{vol,lim}$	0.4

The swelling force was evaluated by integrating the effective stress in the FEM models. The integration was performed on the surface defining the interface between the gap material and buffer box (the surface of the GFM was not included) in the undeformed configuration. The results are plotted in Figure 6-6 as solid squares. In the figure the swelling force calculated using Equation (6-2) is shown (solid red line). The results of the FE models show that Equation (6-2) overestimates the exerted swelling force. The reason is that Equation (6-2) does not account for the compression of the GFM when the HCB swells, which leads to a lower dry density in the FE models. Comparing the results from the FE models and Equation (6-2) does, however, show that the difference between the two is constant, and the FE model results can be well fitted by Equation (6-2) if this is multiplied by a factor of 0.6. The latter is shown in Figure 6-6 as the solid orange line.

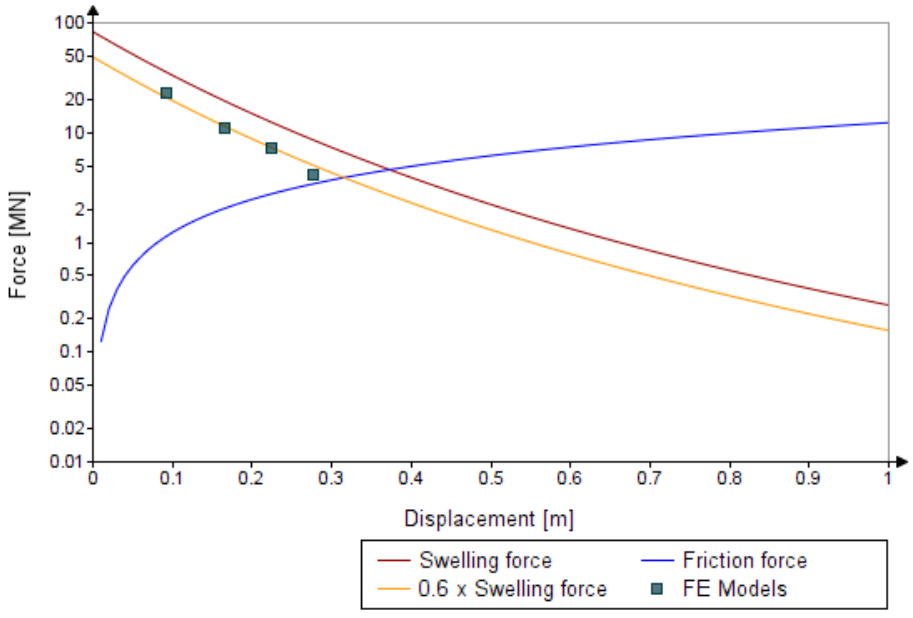

Figure 6-6: Calculated force as function of displacement

Models with larger displacements than 0.3 m led to numerical instabilities and hence could not be analyzed. This means that it is difficult to speculate on the validity of the orange solid line in Figure 6-6 for larger displacements than 0.3 m.

The average dry density in the swelling buffer box was calculated analytically in Appendix F and is given by Equation F-18. Inserting a displacement of 0.4 m in Equation F-18 gives an average dry density well below 1300 kg/m^3, which was much below the target average dry density of 1600 kg/m^3.

6.1.4 Combined Results of Local FE Model and Global Analytical Model

Using the reduced swelling force from the local FE-models the results presented in Section 6.1.1 were re-calibrated, as shown in Figure 6-7. The reduction in swelling pressure led to slightly higher average dry densities. In Figure 6-3 the dry density for an initial gap of 5 mm was in the range 1300 – 1380 kg/m^3, whereas in Figure 6-7 the dry density range for the same initial gap width is approximaely 1350 – 1410 kg/m^3.

However, the dry densities were still well below the designated target dry density of 1600 kg/m^3 for all evaluated values of the friction angle and initial gap width. As can be expected, smaller initial gaps (e.g. red solid line) gave higher final dry densities, i.e., it is important to minimize any gaps between buffer boxes during installation.

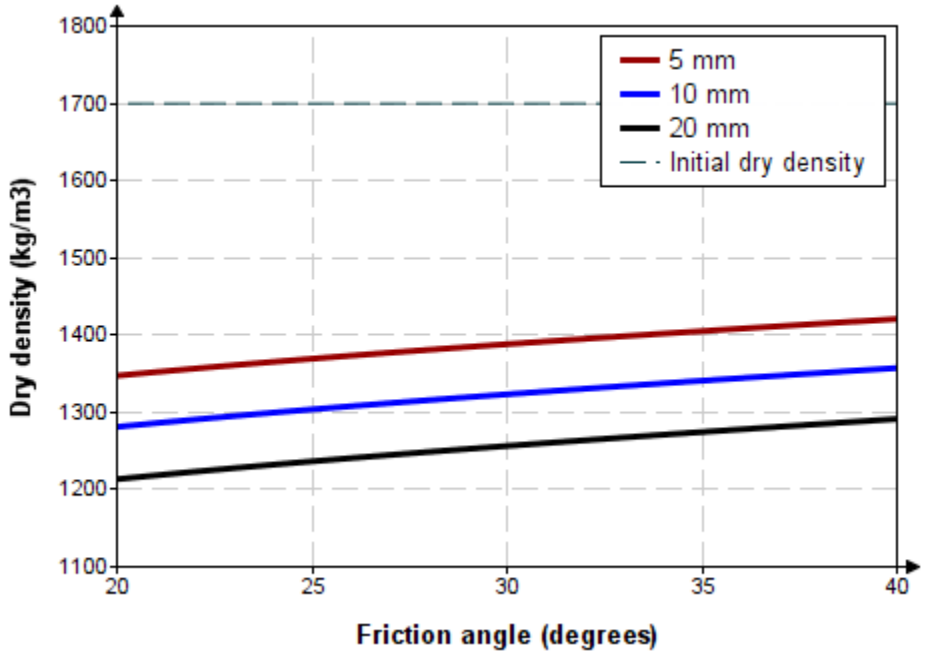

Figure 6-7: Final dry density (e.g. steady state) as function of friction angle

6.1.5 Discussion

The evaluation of the displacement of dry buffer-boxes due to water inflow in one end of the emplacement room showed that the scenario would likely lead to a significant reduction in the dry density of the buffer-box stack situated at the water inflow. The study indicates that the final dry densities will be well below the stated minimum dry density of 1600 kg/m^3.

The analysis was carried out using several assumptions and as a result, the swelling (and hence reduction in dry density) might be overestimated. Some of these are:

- **Perfect Alignment of Buffer Boxes**
  In the analysis all buffer boxes were assumed to glide exactly parallel to the long axis of the emplacement room. This assumed that all the buffer boxes were initially placed and perfectly aligned with the emplacement room long-axis. The assumption was not realistic as slight misalignments could result in less displacement.
- **Homogeneous water uptake and swelling**
  The assumption that the buffer-box stacks glided along the emplacement room tunnel also meant that the buffer box stack which took up water would swell homogeneously in the same direction.
- **Water inflow through one single point at the end of the emplacement room**
  If several water-bearing fractures intersected a single emplacement room at different places, buffer-box stacks near the intersecting fractures would swell. This would prevent further movement along the emplacement room and hence decrease the available gap that any single buffer box could expand into.

Even accounting for these assumptions, it is likely that if the emplacement room is intercepted by a single fracture the subsequent swelling of the buffer material near the fracture would lead to significant displacement of dry buffer box stacks and a reduction in dry density of the swelling buffer parts well below 1600 kg/m^3. To avoid this scenario, some points are worth considering:

- In the case of high flowing fractures intersecting the emplacement room, a solid buffer-box (e.g., a buffer box with no UFC inside) could be placed at the position of the fracture.
- To reduce the room for swelling along the emplacement room long-axis the gaps between buffer blocks present after installation should be minimized.

6.1.6 Conclusions

The analysis of the displacement of buffer-boxes along the emplacement room due to water inflow in one end, showed that significant swelling of the buffer box situated next to the water inflow point would occur.

The main cause is the presence of gaps between buffer blocks after installation which effectively leaves a large open volume for the bentonite to swell into. This is to some degree compensated by the friction force generated when the swelling buffer box “pushes” the dry buffer boxes further away due to the generated swelling pressure. The high dry density of the buffer blocks ($\rho_{d,initial}$ = 1700 kg/m^3) means that the swelling pressure can reach high values, while the friction force from the sliding dry buffer boxes is rather small.

The swelling of the buffer box situated next to the water inflow point was large enough for the average dry density to reach values below ρ_d = 1500 kg/m^3, significantly below the target average dry density of 1600 kg/m^3. This means that the safety function of the buffer in regions near high flowing fractures may be compromised.

6.2 Subtask 1.2 – Heterogeneous Wetting of One Buffer-Box Stack

The aim of the models constructed in Subtask 1.2 was to study how heterogeneous water inflow would affect the evolution in the bentonite, with respect to the time to saturation and swelling/homogenisation. To this end several different inflow scenarios were constructed and modelled. In Section 6.2.1 the modelled scenarios and model setup are described. The results are then presented in Section 6.2.2, a discussion of the results is given in Section 6.2.3 and finally conclusions from the modelling are given in Section 6.2.4.

6.2.1 Model Setup

When studying heterogeneous wetting of a single buffer-box stack, several cases were analyzed, water could flow through:

- one or both side walls,
- the ceiling, and
- the floor of the emplacement room.

To model wetting through the ceiling and floor, the same geometry as that of Step 2 was used except for one model. To analyze water inflow through one sidewall, a larger geometry had to be used. The asymmetric flow demanded a full representation of the buffer-box stack, the vertical plane through the emplacement room center was no longer a symmetry-plane. The geometry is shown in Figure 6-8 together with the original geometry from Step 2. The geometry was based on that used in Step 2 (see Section 5) and was created to represent the emplacement room setup as close as possible while keeping the modelling domain relatively small. An addition to the previous modelling was that a concrete slab was included below the bentonite buffer.

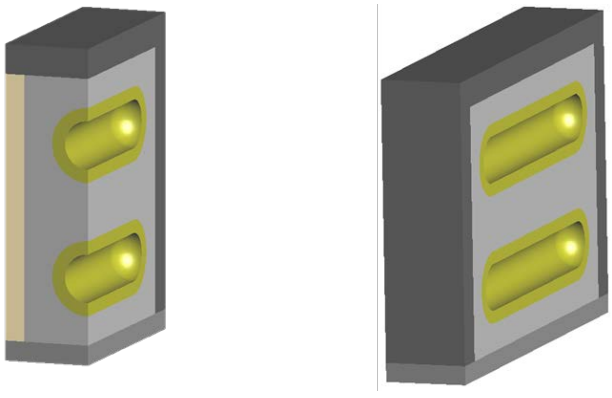

Figure 6-8: Illustration of geometries used when simulating wetting through one or both sidewalls

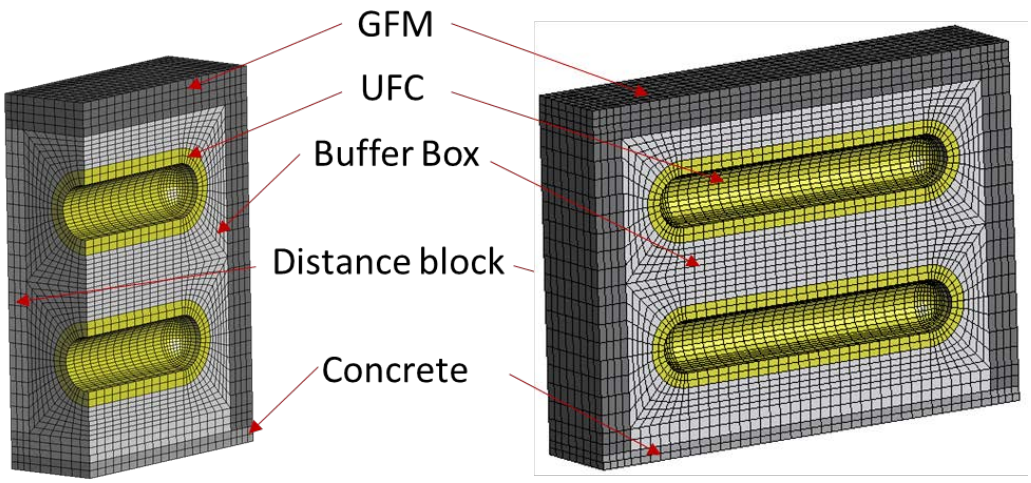

Figure 6-9: Overview of the geometries and finite element discretization used for the models in Subtask 1.2

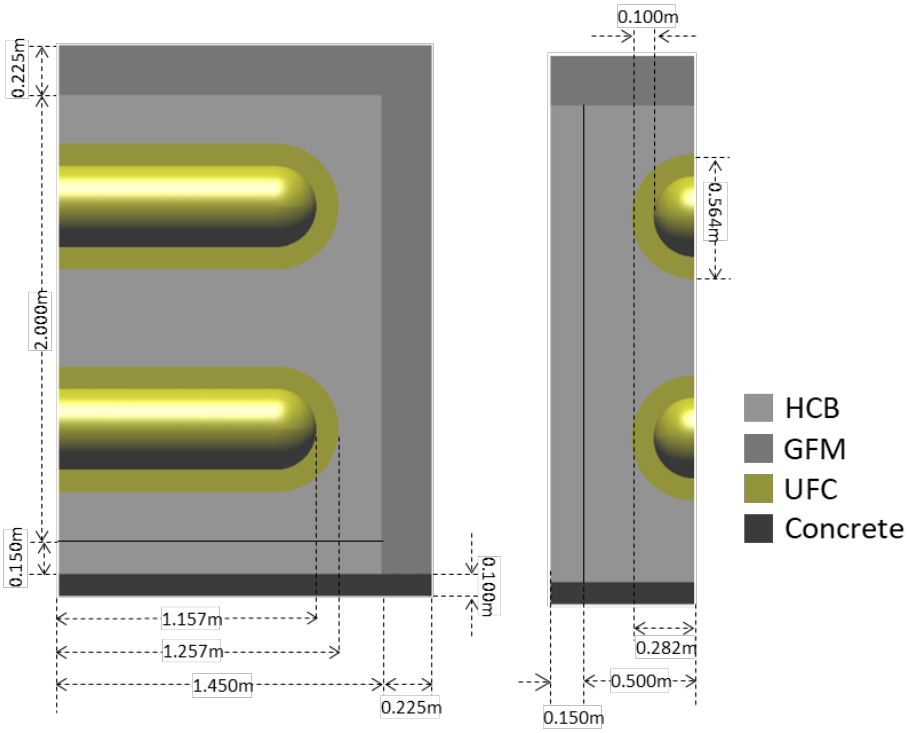

Figure 6-10: Overview of the geometry with dimensions

An overview of the geometries and mesh is shown in Figure 6-9. Two geometries were simulated, one simulating a quarter of a buffer box stack and the other one simulating half a buffer box stack. The larger model was used in the case with water inflow through one sidewall. The dimensions of the geometry including one quarter of a UFC is shown in Figure 6-10, the dimensions of the geometry with half a buffer box can easily be derived from this illustration.

The initial conditions used in the models were described in Section 3.5 and the boundary conditions in Section 3.6. However, the hydraulic boundary condition was slightly modified here: water inflow was only prescribed on a single interface between the buffer and the emplacement room (ceiling, wall(s) and floor respectively), differing from the description in Section 3.6, where water inflow was prescribed on all outer surfaces.

6.2.1.1 Material Model Parameters

The THM material model parameter values for the bentonite materials and the UFC are listed in Table 3-3 - Table 3-6 and Table 4-1, respectively. In this task a concrete slab was included in the models, the material parameters of the concrete are given in Table 6-3.

Table 6-3: Initial conditions and THM parameters for the concrete

			Concrete
Initial suction	s	MPa	23
Initial porosity	n	-	0.01
Initial stress	σ	MPa	-0.11
Initial temperature	T	°C	11
Intrinsic permeability[1)]	k_0	m^2	$10^{-20}/10^{-21}$
Relative permeability	k_r	(-)	1
Water retention curve	P_0	MPa	9
	λ_0	(-)	0.3
Thermal conductivity	λ	W/mK	1.2
Vapour diffusion tortuosity	τ (-)	(-)	0.01
Specific heat for solid	c	(J/kgK)	1000
Solid density	ρ_s	kg/m^3	2000
Young modulus	E	GPa	200
Poisson ratio	v	(-)	0.3

[1)]The lower value was used in model FM_NOOFF_M105b

6.2.2 Results

The results from the verification of the numerical accuracy, as well as the material model validation can be found in Appendix C. The models constructed and simulated are listed in Table 6-4. The third column gives a description of the hydraulic boundary condition that was used for each model.

Table 6-4: Models constructed and simulated in subtask 1.2

Model ID	Description	Hydraulic BC
FM_NOOFF_M101	Base case model	Free access to water on all outer boundaries
FM_NOOFF_M101FM[1]	Base case model + Finer mesh	Free access to water on all outer boundaries
FM_NOOFF_M101FT[1]	Base case model + Finer time stepping	Free access to water on all outer boundaries
FM_NOOFF_M102	Identical to FM_NOOFF_M101 except hydraulic BC	Free access to water through ceiling
FM_NOOFF_M102FL	Identical to FM_NOOFF_M101 except hydraulic BC	Flux-limited access to water though ceiling
FM_NOOFF_M103	Identical to FM_NOOFF_M101 except hydraulic BC	Free access to water through both side walls
FM_NOOFF_M104b	Identical to FM_NOOFF_M101 except hydraulic BC	Free access to water through the floor
FM_NOOFF_M104FL	Identical to FM_NOOFF_M101 except hydraulic BC	Flux-limited access to water though the floor
FM_NOOFF_M105b	Base case, but full geometry and different hydraulic BC	Free access to water through on one side wall

[1]Models used for the numerical verification described in Appendix C.

6.2.2.1 Thermal Evolution

The thermal evolution in the bentonite buffer shows little variation between the different models. The maximum temperatures recorded in the bentonite and on the surface of the UFC are listed in Table 6-5.

Table 6-5: Maximum temperature recorded in the Subtask 1.2 models

Model ID	Max temperature in bentonite [°C]
FM_NOOFF_M101	83.09
FM_NOOFF_M102	83.20
FM_NOOFF_M102FL	85.14
FM_NOOFF_M103	83.08
FM_NOOFF_M104b	83.43
FM_NOOFF_M104FL	85.31
FM_NOOFF_M105	83.43

As is seen the variations are very small. The flux-limited models record slightly higher temperatures. This is unsurprising as dry bentonite has a lower thermal conductivity and hence a larger temperature gradient will be present with a slightly higher temperature near the UFCs.

6.2.2.2 Hydraulic Evolution

In Figure 6-11 the saturation evolution in the buffer box in all models except FM_NOOFF_M105b is shown, and Figure 6-12 shows the evolution in the GFM. As can be seen, the mode of hydration has a clear effect on the hydraulic evolution in both the GFM and HCB. Points close to the water-bearing surface saturates faster than points further away. Considerably longer saturation times are observed in the models where water enters through the floor/ceiling than in the other models with free access to water on the water-bearing surfaces (solid lines). The impact of the flux-limited boundary condition can also be clearly discerned (dash-dotted lines), these show a considerably longer saturation time. The flux-limited model with water uptake through the floor saturates a bit faster than the flux-limited model with water uptake only through the ceiling.

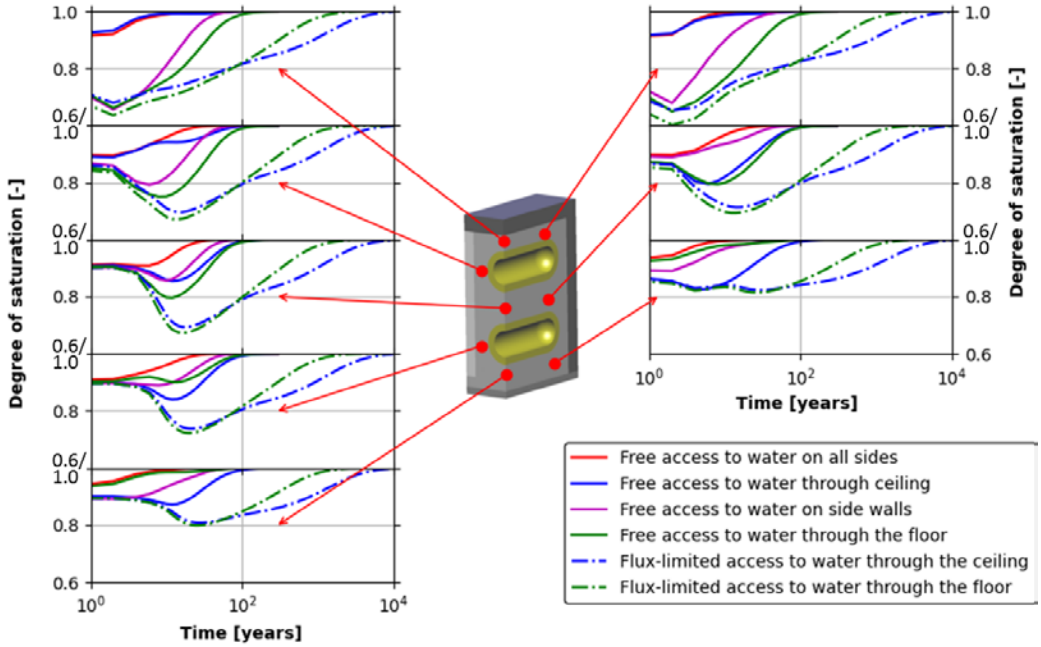

Figure 6-11: Saturation evolution in the buffer box in all models from subtask 1.2 except FM_NOOFF_M105b

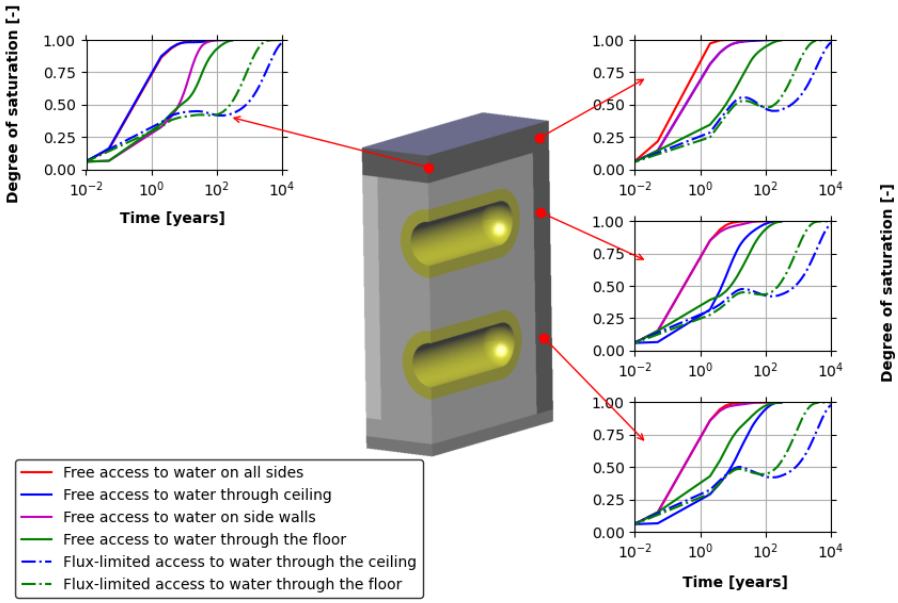

Figure 6-12: Saturation evolution in the gap-fill material in all models from Subtask 1.2 except FM_NOOFF_M105b

Figure 6-12 indicates that the flux-limited models show faster saturation than the models with free access to water in the early period. This was associated with different time steps used for these models. The flux-limited models were simulated for a much longer time period (10,000 years) with less frequent data intervals, and as a result, the early saturation of these models is not comparable during the time period.

The hydraulic evolution in the model with water inflow through a single sidewall (FM_NOOFF_M105b) is illustrated in Figure 6-13, where the evolution is compared to the model with water inflow through both sidewalls (FM_NOOFF_M103). The water enters on the right side of the geometry in the illustration. The evolution in the points near the mid-point of the UFC shows a rather similar evolution in both models, while the evolution closer to the dry wall differs significantly.

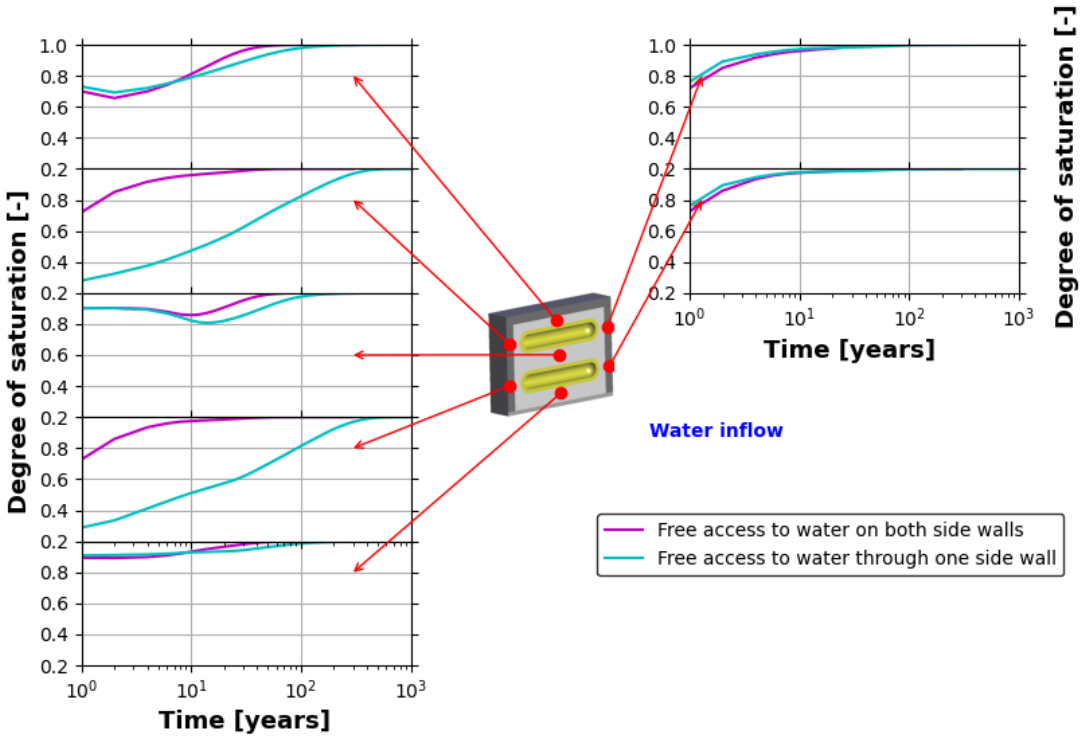

Figure 6-13: Saturation evolution in the model with water inflow through both side walls (FM_NOOFF_M103) and the model with water inflow through one side wall (FM_NOOFF_M105b)

6.2.2.3 Mechanical Evolution

The mechanical evolution in the models was analyzed by evaluating several different quantities. Here, the displacement and load on the UFC are discussed first, and the distribution of swelling pressure and dry density in the buffer thereafter.

Displacement of, and Normal Stress on, the UFCs

The displacement of the UFCs is shown in Figure 6-14 and Figure 6-15. The evolution depends on how water enters the buffer box, both in terms of rate and direction of the inflow. The flux-limited models and the model with free access to water through the ceiling (Figure 6-14) show a large vertical downward displacement of the upper UFC during the transient saturation phase (about 30 mm), while the model with free access to water through the floor shows an upward directed movement of approximately 30 mm for the lower UFC. In all the models the final displacement is similar with both UFCs having been displaced upwards by about 10 mm to 20 mm once the buffer is fully saturated.

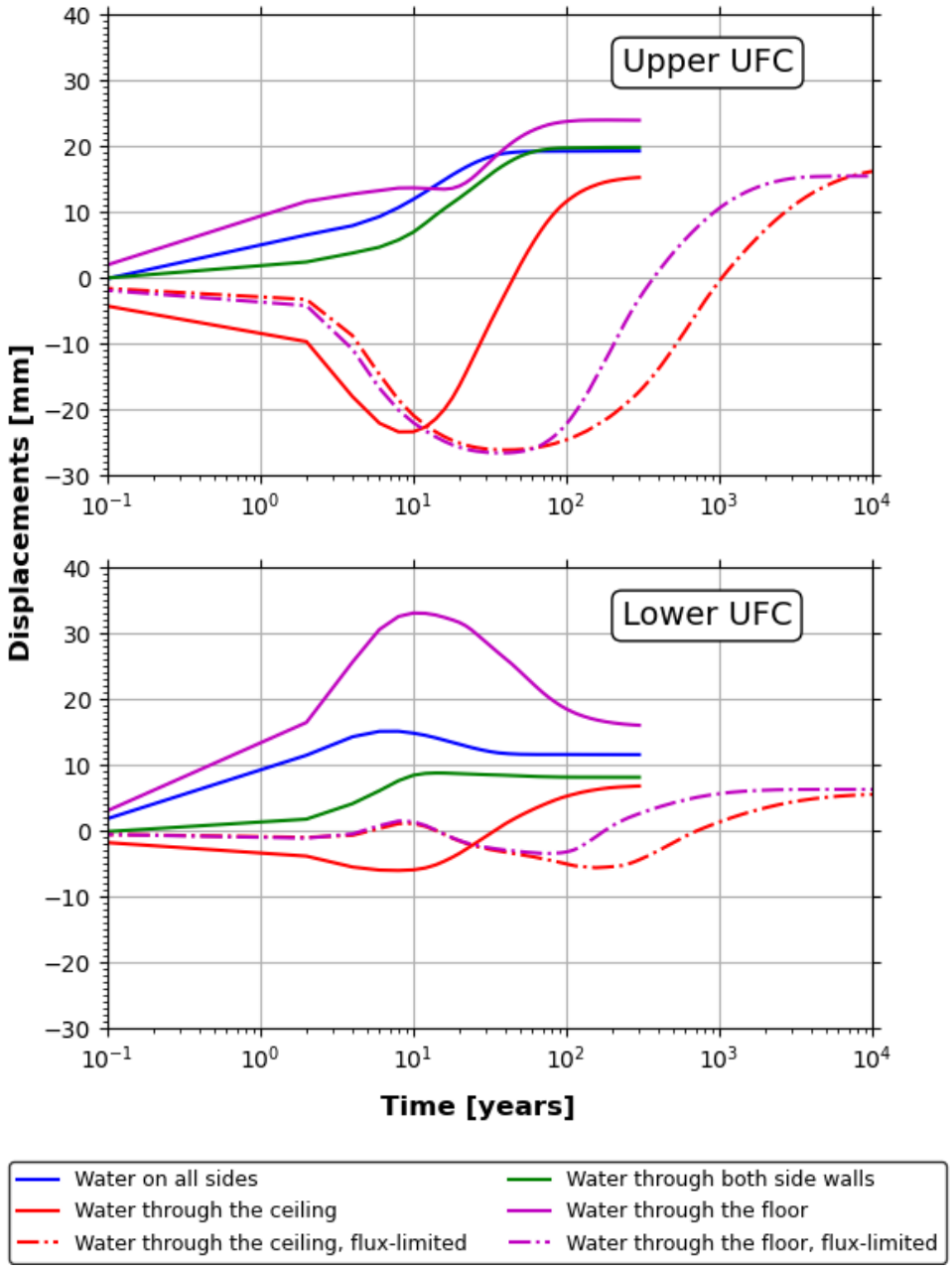

Figure 6-14: Vertical displacement of the UFC in all models, except FM_NOOFF_M105b.

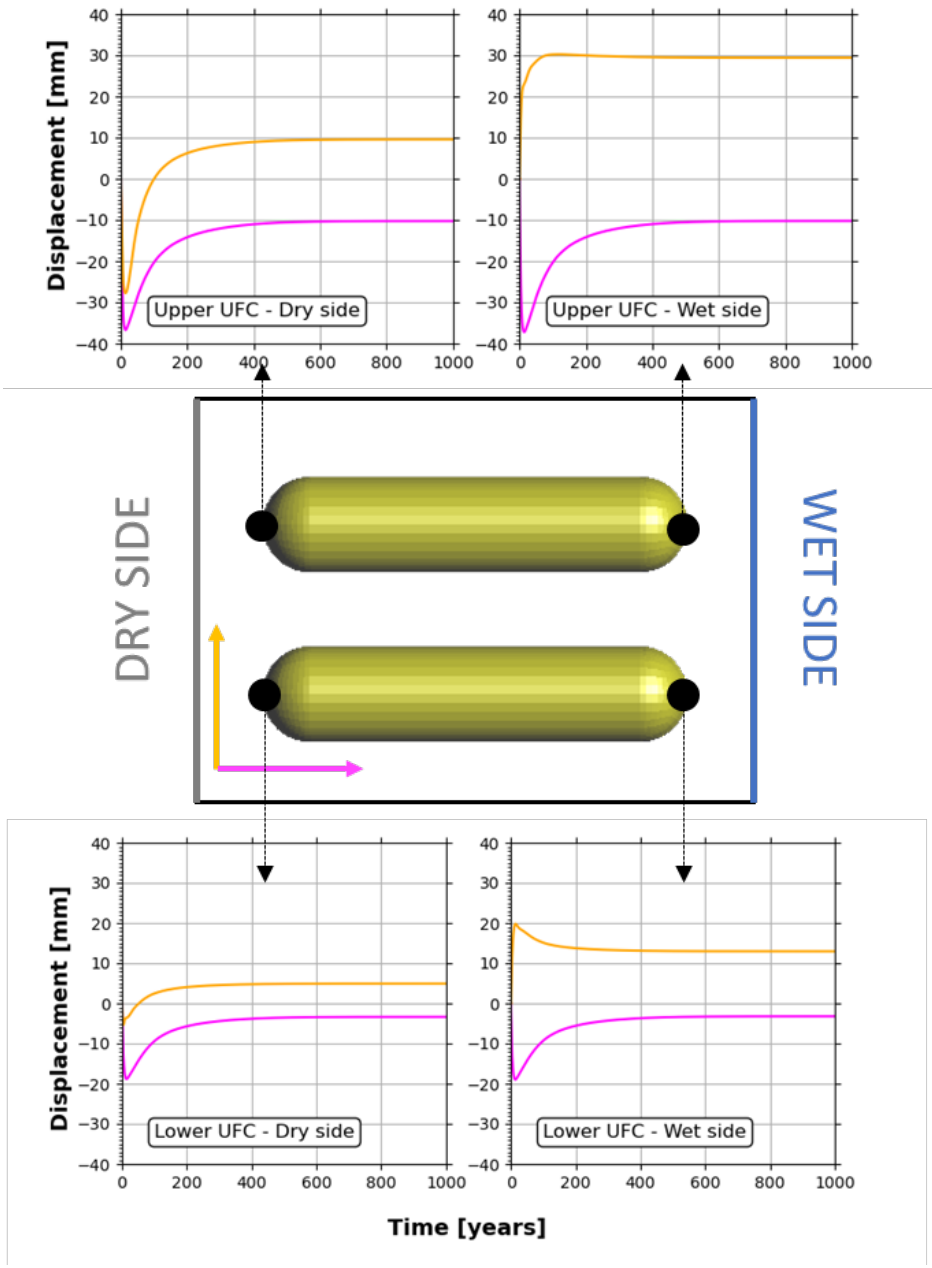

Figure 6-15: Displacement of the UFC in the model simulating water entering through one side wall (FM_NOOFF_M105b)

In Figure 6-15 the displacement of the UFC in the model with water entering through only one side wall is shown. The purple line identifies horizontal displacement and the orange line vertical displacement. The displacement was analyzed on the two endpoints of both the upper and lower UFC.

Horizonal displacement: almost identical evolution when comparing the wet and dry side of each UFC. When comparing the upper and lower UFC the upper UFC was displaced about 10 mm after full saturation, while the lower UFC was displaced about 5 mm.

Vertical displacement: different evolution on the wet side as compared to the dry side for both UFCs. In other words, the UFCs may tilt during the swelling of the buffer. Furthermore, there is quite a large difference when comparing the upper and lower UFCs: the upper UFC was displaced 10 mm to 30 mm while the lower UFC was displaced 5 mm to 12 mm.

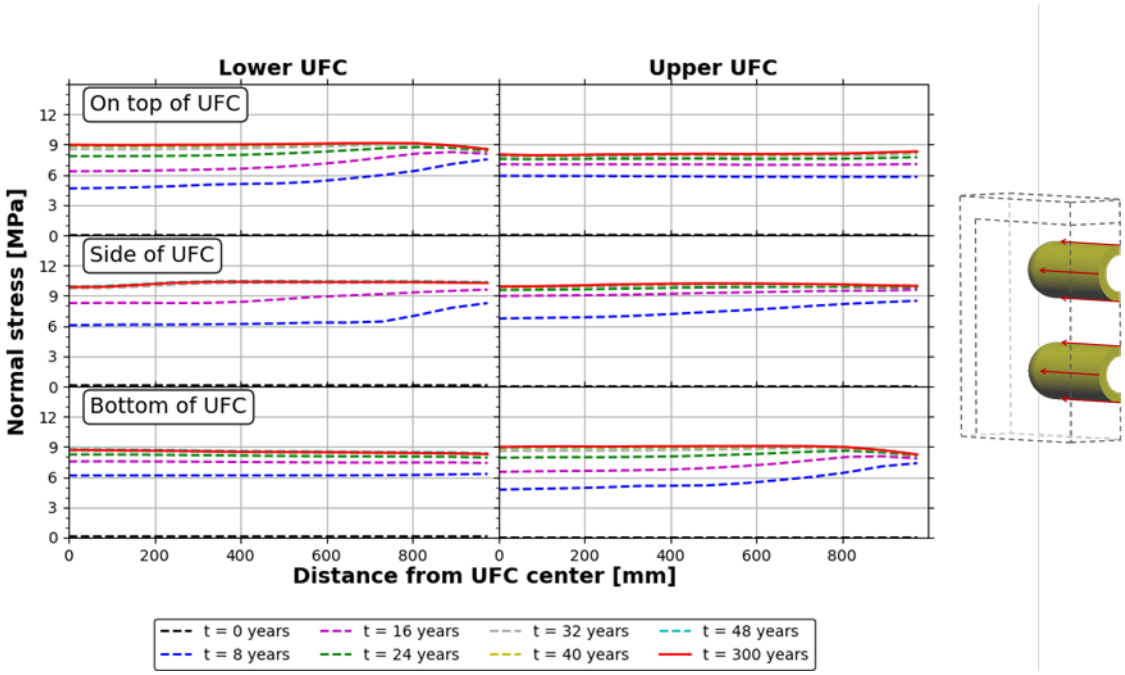

Figure 6-16: Normal stress acting on the UFC in the base case model

The normal stress (positive values correspond to compressive stress) acting on the UFCs was also analyzed. In Figure 6-16 the normal stress is plotted as a function of distance from the center of the UFC at different times from the base case model (with free access to water on all sides). The normal stresses on the UFCs increase with time as the swelling pressure in the surrounding buffer materials increases due to water uptake. Although some variations in the normal stress along the surface of UFCs are seen in the early stages, due to the heterogeneous development of swelling pressure, the normal stresses in the final state are essentially constant over the entire surfaces of the UFCs. In the models the pore pressure caused by the hydrostatic pressure at the depth of the repository was not included. Hence, to get the actual final load on the UFC the values in Figure 6-16 should be added to the expected hydrostatic water pressure in the emplacement room.

In Figure 6-17 the normal stress acting on the UFC is compared between the different models. Small variations are seen, and the simulated normal stresses in the final state are in the range of 9 MPa to 10 MPa. The values for Model M105b in Figure 6-17 are only shown on the “wet side” (i.e., the side near the wall with water inflow). In Figure 6-18 the normal stress along the entire UFC in this model is shown. As can be seen, the normal stress is generally higher on the dry side of the model (i.e., the side of the UFC closest to the dry wall). The water inflow is on the right side of the geometry (on the right side in the figure). The reason for this is the slightly higher dry density on the dry side, due to the early compression of the GFM in that region.

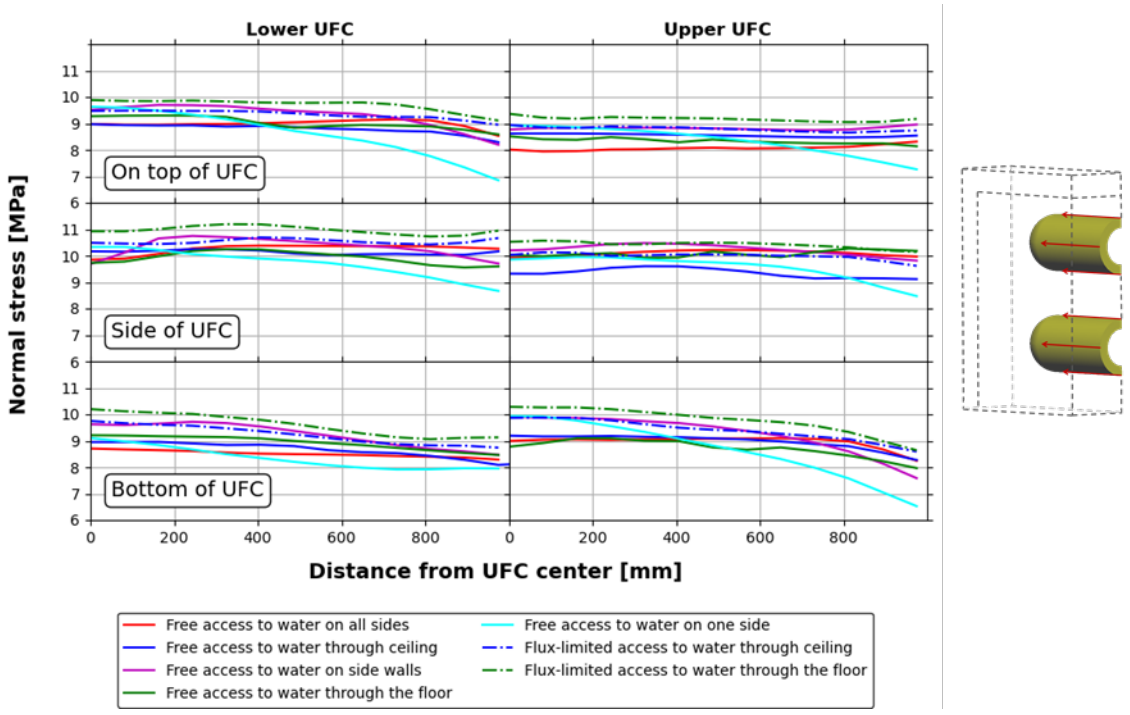

Figure 6-17: Normal stress on the UFC caused by the swelling of the buffer in the final (water saturated state)

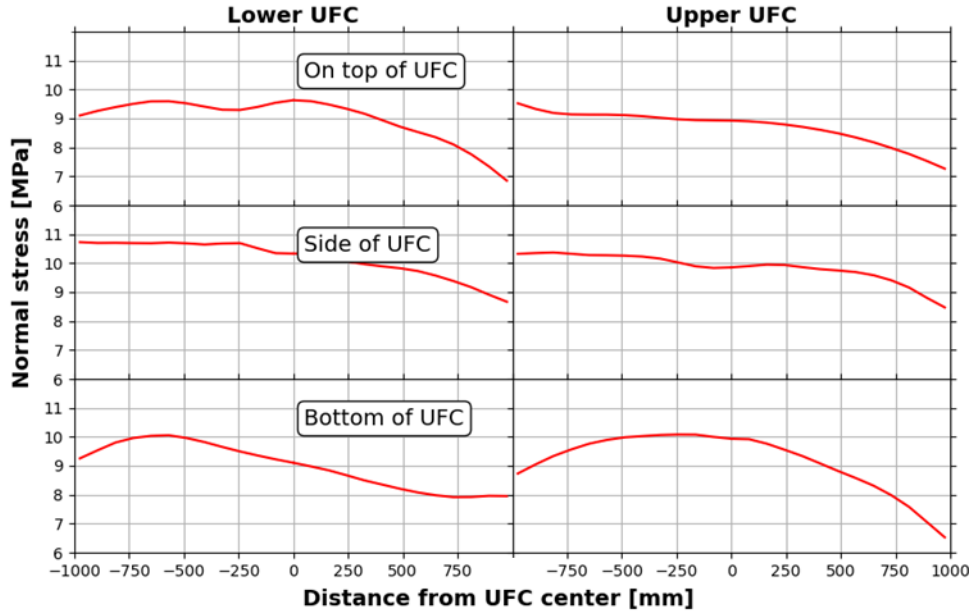

Figure 6-18: Normal stress on the UFC in model FM_NOOFF_M105b

Dry Density and Swelling Pressure

The final dry density and swelling pressure were closely coupled. The net mean stress at full saturation is equal to the swelling pressure in the models. In Figure 6-19, Figure 6-20 and Figure 6-21 the net mean stress, evaluated in the final water saturated state, is shown in the top panel and the dry density in the bottom panel.

In Figure 6-19 the results from the models with free access to water through one or more surfaces are shown. The different modes of water inflow give rise to slightly different final states although the general picture is the same in all models. The highest swelling pressures and dry densities (about 12 MPa and 1680 kg/m^3 respectively) are found in the HCB block along the cylindrical shells of the UFCs. In front of the hemi head of both the upper and lower UFC, the dry density is quite low with swelling pressures between 5 MPa and 6 MPa and dry densities around 1580 kg/m^3.

This confirms the results seen in the Step 2 modelling (Section 5) which showed that the lowest dry density in the HCB block was seen near the hemi heads, where the dry density was also around 1580 kg/m^3.

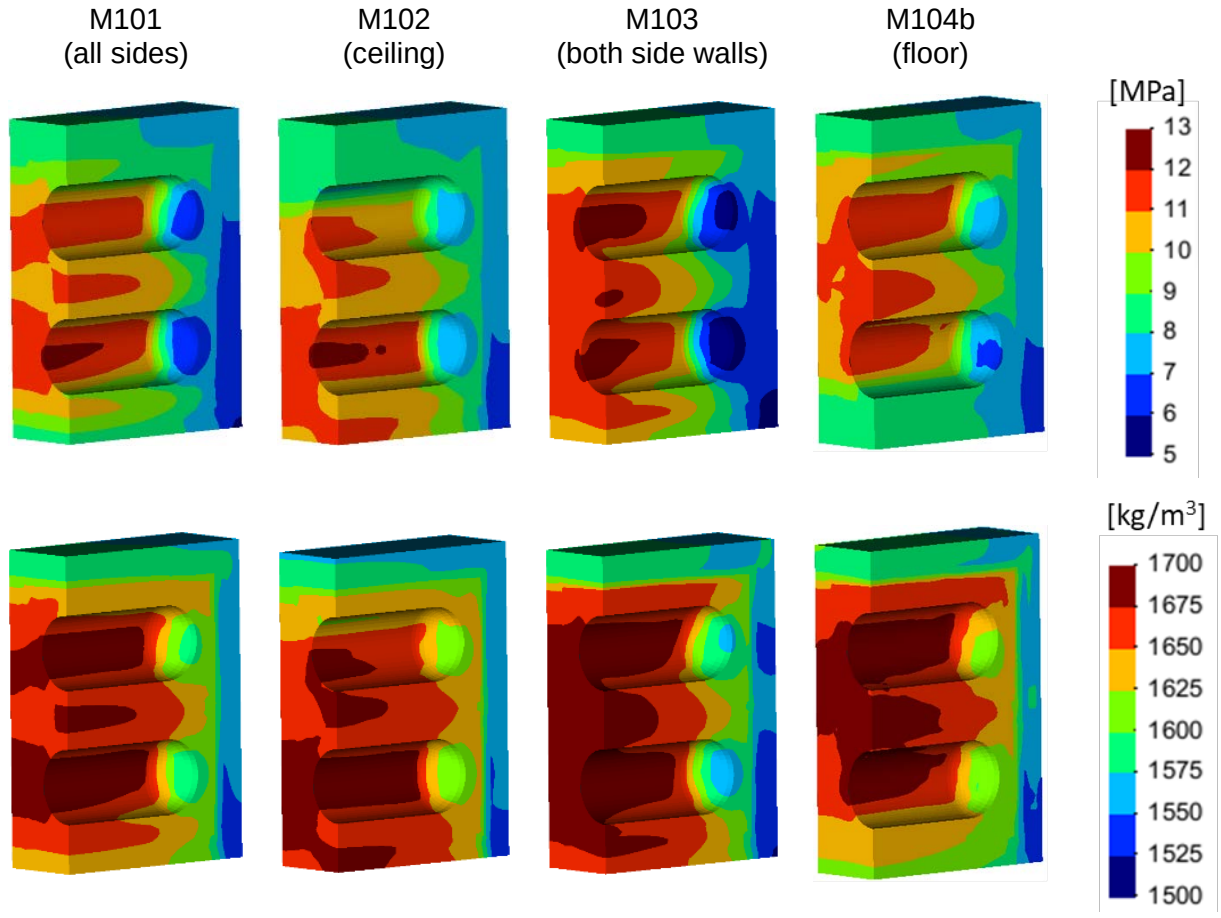

Figure 6-19: Final net mean stress (top row) and dry density (bottom row) in all models with free access to water on one or more surfaces

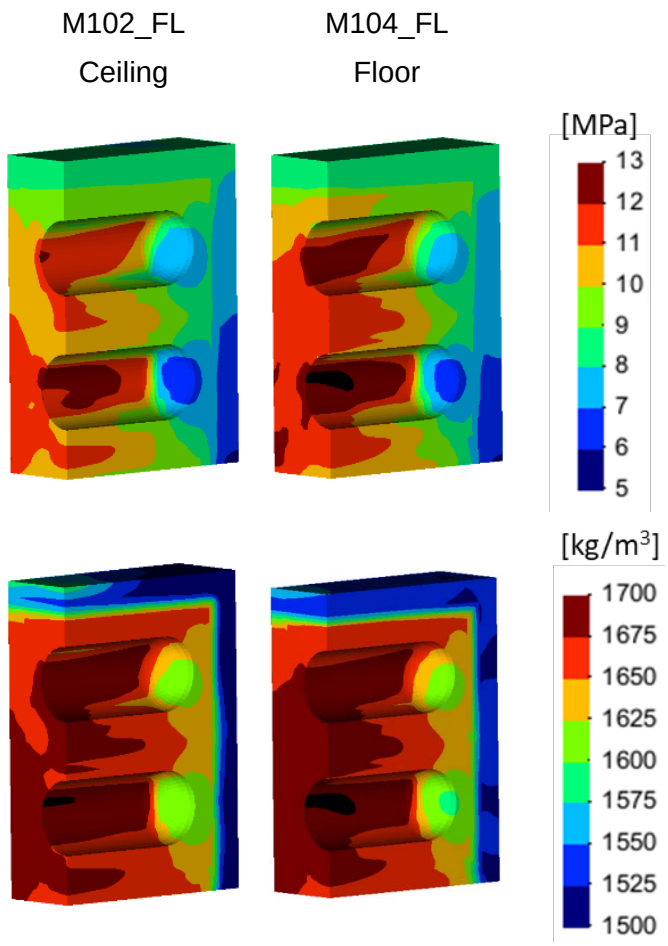

Figure 6-20: Final net mean stress (top row) and dry density (bottom row) in all models with flux-limited access to water on one or more surfaces

The dry density and net mean stress at full saturation in the models with a flux limited inflow is shown in Figure 6-20. The dry density in the HCB is generally somewhat higher as compared that shown in Figure 6-19 while the dry densities in the GFM is lower. Hence, the dry density field in the models with flux-limited access to water is slightly more heterogeneous when compared to the models with a faster inflow rate. However, these differences are small.
The final state in the model with free access to water through one side wall (Figure 6-21) shows a clear effect of the mode of water inflow. The dry density and swelling pressure on the wet side (right side of the geometry) is lower than on the dry side of the geometry (left side in the figure).

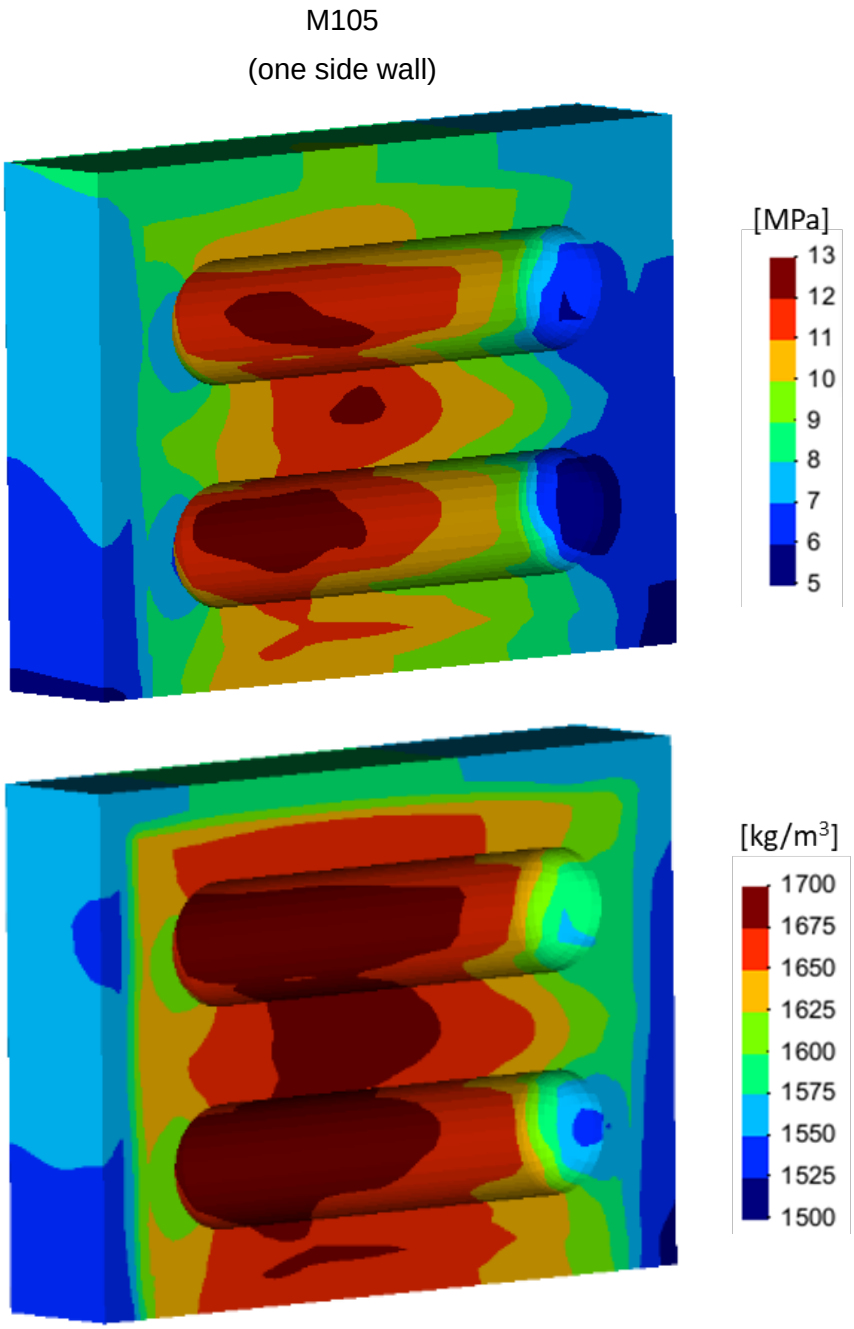

Figure 6-21: Final net mean stress (top) and dry density (bottom) in the model with free access to water on one side wall

6.2.3 Discussion

Several different modes of water inflow were considered:

- through one or both side walls,
- through the ceiling, and
- through the floor of the emplacement room.

The rate of water inflow was also varied for both the cases of water through the ceiling and through the floor. While some variation in the transient evolution was seen in terms of the time to saturation, the displacement of UFCs and stress development, the final state of these properties (UFC displacement and stress), as well as the final dry density fields did not significantly vary between the models with different water inflow scenarios. This indicates that the latter does not affect the final dry densities and swelling pressure distributions.

Differences in the transient evolution when varying how water flows into the buffer were, as expected, seen in the models. In models with a high inflow rate (free access to water), the rock provides more water than the bentonite can take up per unit time. In such cases, the hydraulic evolution in the model is governed by the hydraulic properties of the bentonite. The low permeability of the HCB leads to large gradients in saturation and thus the bentonite will first swell in the region near the water inflow location.

In models with a low rate of water inflow (flux-limited access to water), where the rock provides much less water than what the bentonite can take up per unit time, this effect becomes less pronounced. In such models, the water inflow is so slow that no suction gradients persist in the buffer and hence the entire HCB swells almost simultaneously.

As the buffer reaches full saturation, the dry density field move towards a homogeneous state. However, due to path dependence seen in bentonite (the void ratio – swelling pressure relation differ depending on whether the buffer undergoes swelling or consolidation) some heterogeneities will persist. This effect is not directly implemented in CODE_BRIGHT, but to some degree its effects are taken into consideration by the selected material parameters: the value of plastic stress-strain modulus was chosen so that parts of the bentonite which undergo consolidation lie above the dry density – swelling pressure relation in the variable space of void ratio vs net mean stress.

6.2.3.1 Limitations of the modelling

The models presented here only investigated a limited set of cases with heterogeneous water inflow. It is likely that other heterogeneous wetting scenarios will be seen in the repository, such as inflow through a fracture (e.g., line-inflow) and perhaps point inflows. To study this type of heterogeneous wetting, the surrounding rock mass should be included in the model and fractures should be directly modelled.

The presented models simulated a single buffer box stack. Any interaction with neighbouring buffer box stacks were not considered. Further modelling with larger geometries would be needed to investigate what effects this may have.
It is important to stress that the time to full saturation for the present models (from about 100 years to 10 000 years) is only a consequence of the chosen boundary conditions. These, in

turn, were not designed/calibrated as to be representative for a specific site, as it has not yet been decided. Hence, any conclusions on the time until saturation from the models presented here are extremely uncertain.

6.2.4 Conclusions

The analysis of heterogeneous water inflows into the emplacement room considered several different water-uptake scenarios in which water inflow was localized to either the floor, wall(s) or ceiling of the emplacement room. The results showed only small variations in the temperature evolution, while the transient hydraulic evolution and to some degree the transient mechanical evolution showed large differences, depending on the modes of hydration. The final states of the bentonite buffer did not differ much from each other in the modelled scenarios. However, in some of the models, the final dry density around the hemi-head of the UFC was lower than that of the base case, which could impact the safety function of the buffer.

The effect of using different hydration modes on hydraulic evolution is relatively straight forward, points close to the water-bearing surface saturate faster than points further away. Furthermore, the models with a flux-limited inflow, originally designed to simulate inflow from a low-permeability rock matrix, showed a significantly longer time to full saturation.

The change in the mechanical evolution is a direct function of the mode of hydration. In the transient phase, parts of the buffer taking up water and generating a swelling pressure can induce compression of relatively dry parts, especially so for the GFM which has a relatively low stiffness. As an example of this, the largest simulated displacement of the UFC's is seen in the model with free access to water through the floor during the transient saturation phase. However, as the buffer fully saturates, and hence all parts of the buffer undergo swelling, the differences in dry density decrease significantly, leading to rather similar final states, irrespective of the mode of hydration.

In conclusion, given the cases analyzed here, no major long-term impacts on the safety function of the buffer can be expected due to heterogeneous water uptake, except perhaps regarding the density near the hemi-head of the UFC.

7. TASK 2: FRACTURING DUE TO DRYING

The main goal of this task was to estimate the open volumes caused by drying-shrinkage-fracturing. A secondary goal was to evaluate if and where fracture formation would occur. The main part of this section contains a description of the methods developed for performing the estimation and evaluation mentioned above. Due to limitations in the postprocessor and time available to finish this task, the main goals were not reached. However, the method described in this section was utilized in Task 4, where the drying and potential for fracturing of the HCB during transportation was studied, see Section 9.2.

Shrinkage and fracture formation are here discussed in the case of dry conditions. Without any inflow, water will be redistributed in the buffer due to vapour flow driven by temperature gradients and liquid water flow driven by suction gradients. The buffer will become dryer at positions close to the UFC and shrink. The shrinkage may in turn generate stress states which induce failure of the material and cause fractures in the bentonite buffer.

The motivation behind studying this process was the existence of potential issues which relate to fracture formation:

- Scenarios where fractures could act as open paths through the buffer.
- Shifting of the UFCs and changed overall thermal properties of the buffer which could affect the maximum temperature of the bentonite.
- Buffer breakout with subsequent intrusion of GFM could lead to difficulties to meet the density requirements.

The water content, void ratio, and degree of saturation, are defined:

$$w = \frac{dm_w}{dm_s}\,, e = \frac{dV_p}{dV_s}\,, S_l = \frac{dV_w}{dV_p}. \tag{7-1}$$

These are expressed in terms of mass elements, dm, and volume elements, dV, since they are local/pointwise entities. The mass/volume elements have subscripts, w, s and p indicating that they belong to water, solid, or pore entities, respectively.

The following sections provide brief discussions on shrinkage due to drying and fracture formation and a method for estimating open volumes created from fracturing by using experimental data. Finally, another analysis method aimed at evaluating if and where fractures form is outlined.

7.1 Shrinkage

When subjected to drying (i.e., a decrease in water content), a sample of bentonite with stress-free boundaries shrinks due to a decrease in the mean distance between montmorillonite mineral sheets. If the sample on the other hand is prevented to deform, stresses will be generated.

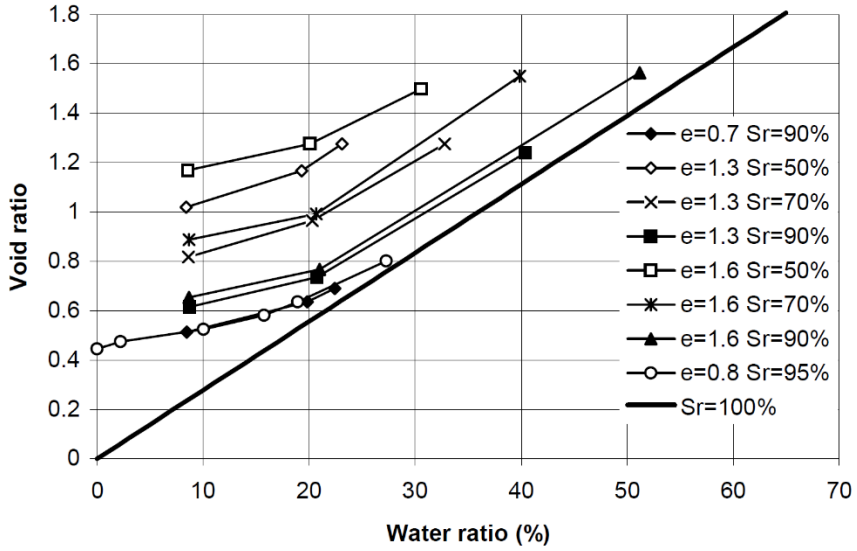

Figure 7-1: Shrinkage curves of MX-80 with different initial void ratio and water content (water ratio)

Typical experimental findings for free drying conditions, in the form of so called “shrinkage curves”, are shown in Figure 7-1, obtained from Börgesson (2001). One common feature for all curves in Figure 7-1 is a “knee” at *w* = 20 %. Above this value the void ratio change agrees with that of constant degree of saturation, i.e., the lines are parallel to that indicated by $S_l = 100$ %. For water contents below 20 % the void ratio change does not agree with that of constant degree of saturation. The value of water content, where this shift in behavior occurs, is denoted shrinkage limit.

The difference of a volume element of clay at the initial state, dV^0, and at dry conditions, dV^{dry}, can be used for studying the potential open volume created by fracture formation as shown in Figure 7-2. A clay volume with different shrinkage in different parts would introduce gradients in shrinkage. At locations with shrinkage gradients, stress concentrations are likely to develop, which in turn can promote fracture formation.

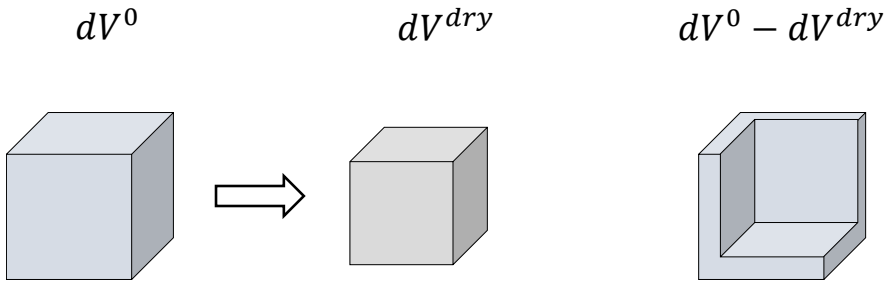

Figure 7-2: Geometrical representation of the free drying process

7.2 Fracture Formation

Fractures form when the mechanical failure resistance of the material is reached. To specify this a material failure criterion is formulated. The failure criterion is usually formulated in terms of the stress state.

As an example, the obtained maximal principal stress, σ_1, could be compared to an experimentally motivated maximal tensile strength, σ_T. Thus, failure occurs when

$$\sigma_1 \geq \sigma_T \, . \tag{7-2}$$

Continuum mechanical sign conventions are adopted where tensile stress is positive.
In Figure 7-3, the tensile strength of MX-80 bentonite, as determined by beam-tests, is given as a function of void ratio for different ranges in water content. The graph shows that the tensile strength is dependent on void ratio which indicates that the failure condition in Equation (7-2) depend on void ratio as well.

If the criterion suggested in Equation (7-2) is too simple for representing the material behaviour accurately, the Mohr-Coulomb criterion,

$$\tau_f = c - \sigma \tan \phi \, , \tag{7-3}$$

often used to describe failure characteristics for geomaterials, could be tested. In the Mohr-Coulomb criterion shear stress at failure, τ_f, is given by the normal stress, σ, and the parameters, c (the cohesion), and ϕ (the friction angle). If the shear stress in the model is greater than Equation (7-3), the material fails. The parameters could, for example, be determined by using the tensile strength and experimental data on the relationship between tensile strength and uniaxial compression.

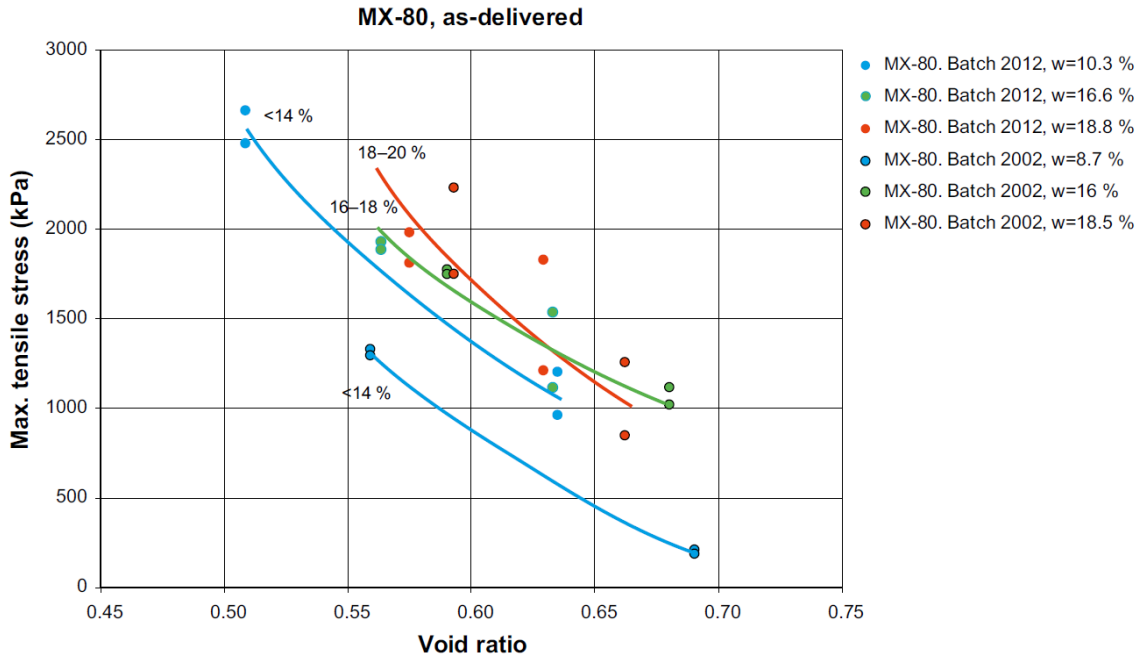

Figure 7-3: The determined tensile strength for the as-delivered MX-80 batches plotted versus void ratio (Sandén et al., 2016)

7.3 How to Estimate Open Volumes Created by Drying using TH-Models

To estimate open volumes which could be generated by drying, a method based on using a TH-model together with an experimental shrinkage curve was tested. A TH-model without water inflow, see Table 7-1, was used for obtaining information about the water content at dry conditions and a shrinkage curve was then utilized to translate the water content to a void ratio at dry conditions.

Table 7-1: Model constructed and simulated in Task 2

Model ID	Description
NWMO_T2_TH_M001	Identical to the flux limited model in Step 2 except for the use of no flow boundary conditions.

The method is described in more detail below, and the outcome obtained from the method by applying it on subsets, points and lines, of the geometry follows.
Degree of saturation, S_l, water density, ρ_l, and the initial void ratio, e^0, were obtained from the TH-model. Using the model data, the water content, w, can be calculated from the expression below,

$$w = \frac{\rho_l}{\rho_s} S_l e^0 \,. \tag{7-4}$$

Here, the solid density, $\rho_s = 2750$ kg/m^3.

w	e
0	0.406
0.021	0.437
0.1	0.487
0.158	0.545
0.19	0.598
0.273	0.801
0.4	1.154

$\tilde{e}(w)$ is obtained by linear interpolation between the data points given above.

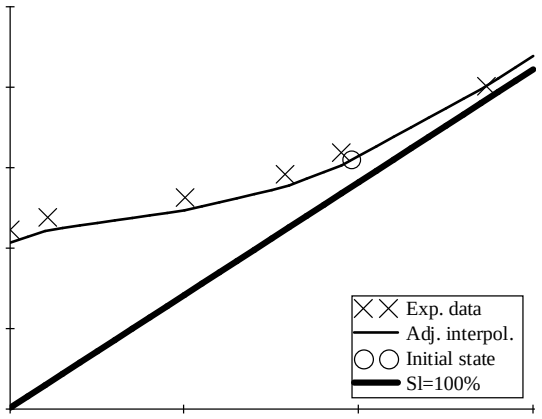

Figure 7-4: Definition of the shrinkage curve (left) and water content vs. void ratio for the shrinkage curve used in the analysis (solid thin line)

To evaluate the shrinkage from the water content, a shrinkage curve function $e = \tilde{e}(w)$ was designed to obtain a void ratio matching the water content, see the left in Figure 7-4 for the definition of the curve. The shrinkage curve function is plotted to the right in Figure 7-4.
The calculations performed to obtain the void ratio at dry conditions were,

$$w^{dry} = \frac{\rho_l}{\rho_s} S_l e^0 \tag{7-5}$$

$$e^{dry} = \tilde{e}\left(w^{dry}\right). \tag{7-6}$$

Thus, the mechanical process is decoupled from the hydraulic process and the mechanical process is assumed to take place under “free shrinkage” conditions. The assumption of “free shrinkage” conditions could be thought of as if the material has no strength and fractures are formed effortlessly. i.e., a conservative assumption in the present analysis.

To evaluate the potential of open volumes, a "volume element ratio", here denoted by ν, was defined. The local volume element difference between the initial and dry condition, $dV^0 - dV^{dry}$, was scaled by the initial volume element dV^0. This ratio can be expressed in terms of initial and dry state void ratios,

$$\nu = \frac{dV^0 - dV^{dry}}{dV^0} = \frac{e^0 - e^{dry}}{1 + e^0}. \tag{7-7}$$

It should be noted that ν is a local/pointwise relative measure of the open volume, generated by drying. To obtain the open volume created by drying for an element in a finite element model, the volume element ratio, ν associated with the element should be multiplied with the initial volume of the element,

$$dV^0 - dV^{dry} = \nu dV^0. \tag{7-8}$$

If the total open volume, V_{open}, is sought for a selected set of elements (e.g., all elements surrounding a UFC), a summation over all elements should be performed.

$$V_{open} = \sum_{\forall\, elements} dV^0 - dV^{dry}. \tag{7-9}$$

The gradient of ν, $\nabla\nu = \partial\nu/\partial\boldsymbol{X}$, is an entity which could give insight about possible fracture formation. $\nabla\nu$ can be used to identify where stress concentrations are likely to occur due to local differences in volume change. At the stress concentrations the material strength might be reached and therefore fractures may form.

7.4 One-Point Evaluation

The method described above was tested using data from the TH model NWMO_T2_TH_M001. To begin with the state at point A (see Figure 7-5), was studied. At the initial state $(w^0, e^0) = (0.198, 0.618)$ and at the state of maximal drying, which occurred at $t \approx 10\ yr$, $(w^{dry}, e^{dry}) = (0.13, 0.52)$. Using $e^0$and e^{dry} give ν = 6.2 %. Thus, 6.2 % of the initially available volume element could become an open volume at dry conditions. It should be remembered, however, that this was evaluated at a point in direct contact with the UFC and therefore subjected to significant drying, which was not representative for all points in the buffer box.

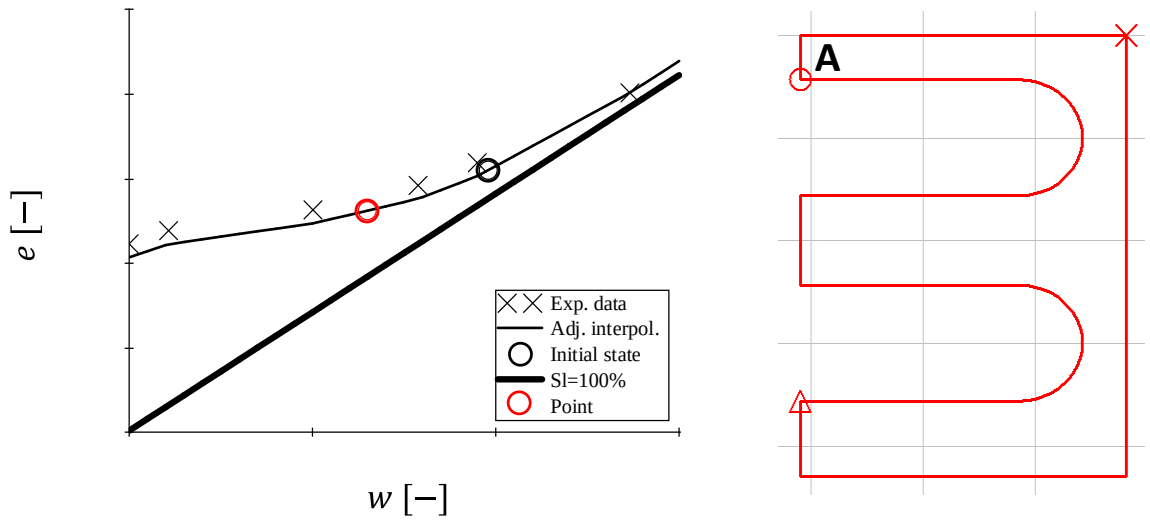

Figure 7-5: (Left) Shrinkage curve information as shown in Figure 7-4 and dry state of point A (red circle)

7.4.1 Line Evaluation

The next step was to expand the evaluation to include the line along the boundary of the mid-plane at $t \approx 10\ yr$. In the left graph of Figure 7-6, the geometry starting point and direction of the l −coordinate and positions of points A and B are shown. The right graph in Figure 7-6 shows the geometry and the positions of sections with high magnitudes of gradient in ν. In Figure 7-7 the resulting profile of ν and its gradient, $\nabla\nu = \partial\nu/\partial l$, are shown together with the position of points A and B, and Section 1, 2 and 3, respectively.

The maximum value, ν = 6.3 % occurs to the right of point A ($l \approx$ 2.5 m) before the rounding of the inner volume of the buffer box. The section between points A and B shows consistent high values. Along the tunnel bottom ($8\ m < l < 9.7\ m$) there is no significant change in volume. The water vapour is driven downwards but cannot escape, which is manifested in negative ν-values, indicating swelling. When moving upwards along the outer boundary the shrinkage increase significantly again.

When studying the lower diagram in Figure 7-7, sections where the magnitude of the ν-gradient (here the derivative with respect to the l-coordinate only) shows that three local maxima/minima are clearly visible. The maxima are indicated by 1 and 3 in Figure 7-6 and Figure 7-7 and the minimum by 2.

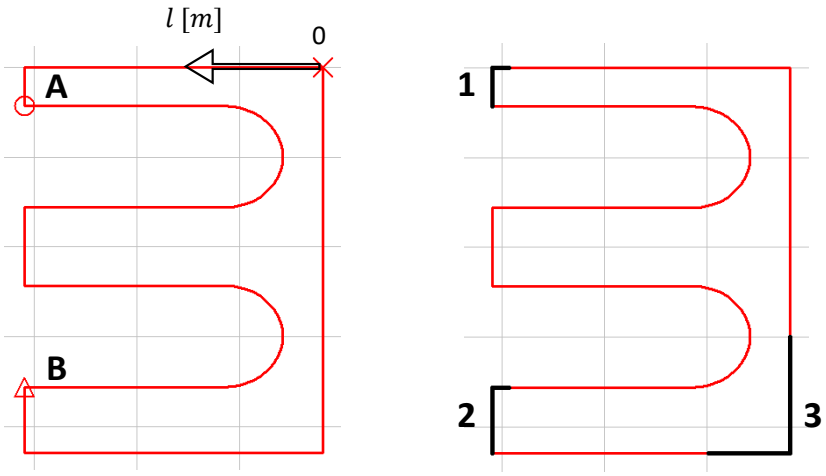

Figure 7-6: Mid plane boundary

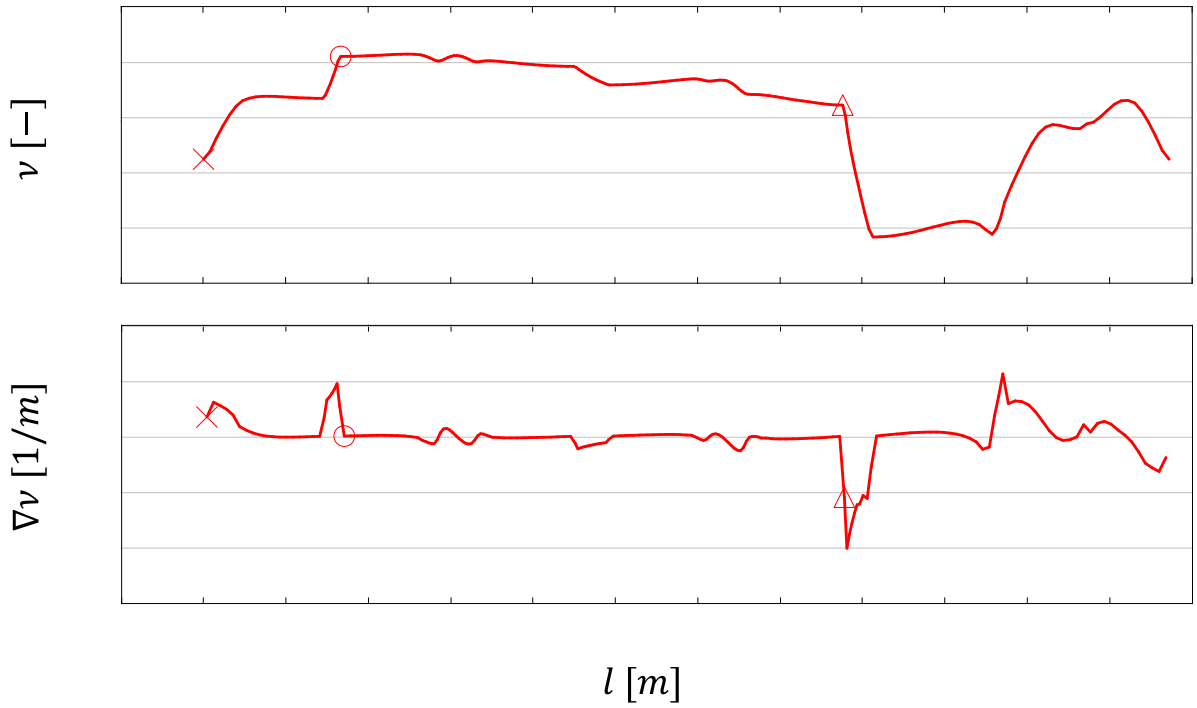

Figure 7-7: The volume ratio measure (top) and its gradient (bottom) obtained along the mid plane boundary

7.5 How to Evaluate the Potential for Fracture Formation Using THM-Models

A continuum THM-model without possibilities for fracture formation could, when used together with a material failure criterion, give an opportunity to evaluate if/where fracturing may be a problem.

However, it should be noted that if fractures could form, i.e., new stress-free boundaries could be generated, the stress field evolution would most probably have sudden and dramatic changes. In light of this, an evaluation using models without possibilities of fracture formation should be considered as being indicative only. If such models are set up properly, however, they would represent the stress field correctly up to the point where the first fracture occurs. The obtained stress field used together with a material failure criterion would give insights on if/where fractures could form.

To meet the requirements for a properly configured THM-model aimed at analyzing the stress field under significant drying/shrinkage, the THM-models used in Task 1 would need to be further developed. The possibility for open gaps to form at the UFC/buffer interface and block joints should be represented in an enhanced model. Also, to ensure the quality of the evaluation, the validity of the mechanical material model should be confirmed further for dry and drying conditions.

As an example of how the capability of the material model parameter setup could be tested, “free shrinkage” was simulated, and the response was compared with the shrinkage curve function. The red curve in Figure 7-8 was obtained by simulating “free shrinkage” with the BBM implemented in Mathcad. The parameter setup was identical to that used in the previous Step 2 modeling (see Section 5). Here the BBM response agrees well with the experimental data and designed shrinkage curve.

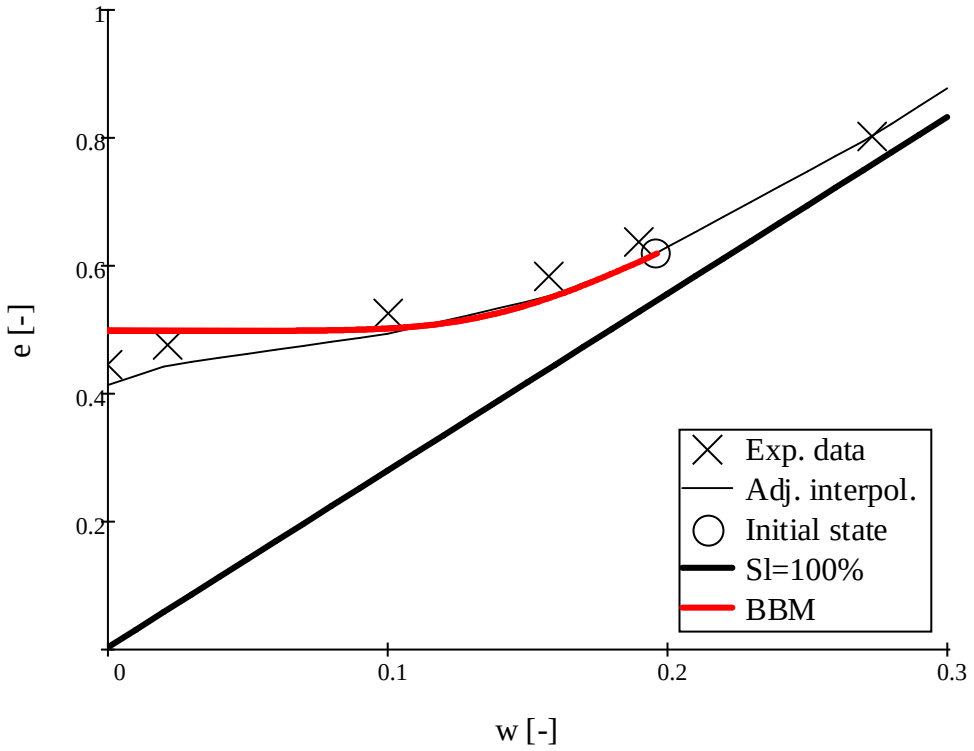

Figure 7-8: Shrinkage curve information as shown in Figure 7-4 together with “free shrinkage response” from using BBM

7.6 Summary and Conclusions

The developed analysis method for estimating open volumes created by drying-shrinkage-fracturing was tested in points and along lines in the geometry. The tests of combined use of a TH-model and shrinkage curve was successful but due to limitations of the post processor, the analysis method could not be applied to the entire geometry.

To accomplish this, development of external software, operating on the result-files obtained from the TH-model, was carried out in Task 4. The theory/method developed here was used to evaluate if fractures could form during transportation of the buffer boxes from the surface to the emplacement room (see Section 9).

Another analysis method, for identifying if and where fracturing could occur, was also discussed. This method would use a THM-model in combination with a material failure criterion expressed in terms of stress. To achieve a representative analysis however, the THM-models used in Task 1 would require further development. The possibility for opening of block joints and UFC/block interfaces would be necessary to obtain a representative stress field. Contact mechanics, which could represent joint opening/sliding, is presently not part of CODE_BRIGHT, whereas COMSOL Multiphysics®, another FE-solver, has such physics available. Mechanics of fractured rock is commonly represented using Finite Difference solvers. This type of numerical solver could therefore be a possibility for representing buffer joints. It is however uncertain how easily the rest of the THM representation included in CODE_BRIGHT could be “imported” to such code. To progress with this analysis method, development of software and/or shift to software using other numerical methods might be required.

8. TASK 3: SENSITIVITY STUDY AND AIRGAPS

Task 3 consisted of two different modelling subtasks described below.

- **Sensitivity analysis:** The effect of varying the initial dry density of the buffer components as well as the thickness of the GFM slot was analyzed.
- **Airgaps:** The effect of including airgaps between different components in the emplacement room was analyzed.

The purpose of the sensitivity analysis was to study the effect from using different initial buffer densities and various cross-sections of the emplacement room. The starting point was the base case developed in Task 1 described in Section 6. The initial conditions and thickness of the gap-fill zone were varied. An updated parameter set for the buffer had to be derived for each analyzed case due to limitations in the employed mechanical material model (BBM). The sensitivity analysis is presented in Section 8.1.

After installation of the different buffer components (buffer box, spacer block and gap fill material), airgaps are expected at several places in the geometry. Models including airgaps were simulated using a simplified geometry. Including airgaps in the full 3D models would lead to substantial numerical challenges. Therefore, a plane 2D geometry was used for analyzing one type of airgap at a time in three different models. The three airgaps were: 1) between buffer box and spacer block, 2) between the gap fill top surface and the ceiling, and 3) between the UFC and buffer box. The models with airgaps are described and the results presented in Section 8.2.

8.1 Task 3 – Sensitivity Analysis

The models are based on the models constructed in Task 1 – Subtask 1.2 described in Section 6.2. The list of models and how they differ in terms of the initial dry density of the buffer components and the geometry are given in Table 8-1.

Table 8-1: Set of models simulated in the sensitivity analysis

Model ID	GFM ρ_d [kg/m^3]		HCB ρ_d [kg/m^3]	GFM thickness (m)	Model Name
	Buffer Box – Wall	Buffer box – Ceiling			
1[1)]	1410	1410	1700	0.225	NWMO_T3_M01_V01
2	1410	1410	1600	0.225	NWMO_T3_M02_V01
3	1550	1500	1750	0.225	NWMO_T3_M03_V01
4	1500	1450	1650	0.225	NWMO_T3_M04_V03
5	1450	1410	1700	0.225	NWMO_T3_M05_V01
6	1410	1410	1700	0.300	NWMO_T3_M06_V01
7	1410	1410	1600	0.300	NWMO_T3_M07_V01
8	1550	1450	1750	0.300	NWMO_T3_M08_V01

[1)]Base case, re-simulated here with respect to Task 1 due to updated hydraulic parameters.

No numerical verification was carried out as the geometry and mesh were similar to those carried out in Task 1 and verified as described in Appendix C. Similarly, the accuracy of the material model was not validated separately for these models as the setup so closely resemble the setup in Task 1.

8.1.1 Model Setup

The geometry was identical to that used in Task 1, described in Section 6.2.1, except for the outer dimension of the GFM in Models 6 – 8 indicated in Table 8-1. The hydro-mechanical parameters of the bentonite buffer materials and the initial conditions had to be updated since:

1) The initial water content of the GFM was changed from 2 % to 3 % in accordance with a change in the repository design specification.
2) The geometry of the emplacement room was changed, leading to a different average density which meant that the plastic parameters had to be updated.

The thermal parameters of the materials were identical to those used in Task 1. The change in hydraulic and mechanical parameters are described separately below.

8.1.1.1 Hydraulic Parameters

Equation (3-24) describes the dependence of the hydraulic permeability on the porosity in the material. To have a single parametrization for HCB and GFM the parameter values in Table 8-2 were used.

Table 8-2: Intrinsic permeability parameter values

Material	k_0	n_{ref} [-]	b [-]
HCB, GFM	1.04×10^{-20}	0.418	20.726

The relative permeability was not changed and is given in Equation (3-26).

To derive parameters for the water retention curve of the bentonite components, the same strategy as described in Section 3.3.3 was used. In the left rows of Figure 8-1 and Figure 8-2 the adopted extended van Genuchten retention curves together with experimental data and adopted functions for free swelling condition are shown. In the right columns the evaluated moisture diffusivity is shown. These should roughly be $5\cdot10^{-10}$ m^2/s to be consistent with water uptake data (Sellin et al. 2017), which is indicated by the dashed black line. The parameter values for the retention curves are given in Table 8-3.

It is worth pointing out that for the HCB with an initial density of 1750 kg/m^3 the initial saturation, S_{l0}, is very close to 1. To define a retention curve which intersects S_{l0} at the given initial suction, the parameters in the retention curve had to be significantly changed with respect to the other HCB densities.

As can be seen in Figure 8-1 and Figure 8-2, the moisture diffusivities evaluated from the HCB and GFM retention curves in general lie above the experimentally measured reference value (dashed black line), in particular when the degree of saturation is larger than the initial value (Table 8-3). The high values of the moisture diffusivities evaluated from the adopted retention curves mean that the rate of water uptake in the blocks may be overestimated in the models. These overestimated moisture diffusivity values could be accommodated by lowering the hydraulic conductivity or altering the retention curves. The hydraulic conductivity is known to carry the largest uncertainty as it is difficult to evaluate experimentally, and the uncertainty is at least on the order of a factor of two (Åkesson et al 2010a). Hence, to reduce the evaluated diffusivity, it would be reasonable to reduce the hydraulic conductivity. However, to keep with NWMO's reference values (NWMO's data clearance form for the crystalline site, APM-REF-01900-300813-R000) this was not done, and hence the rate of water uptake in the blocks may be overestimated in the models.

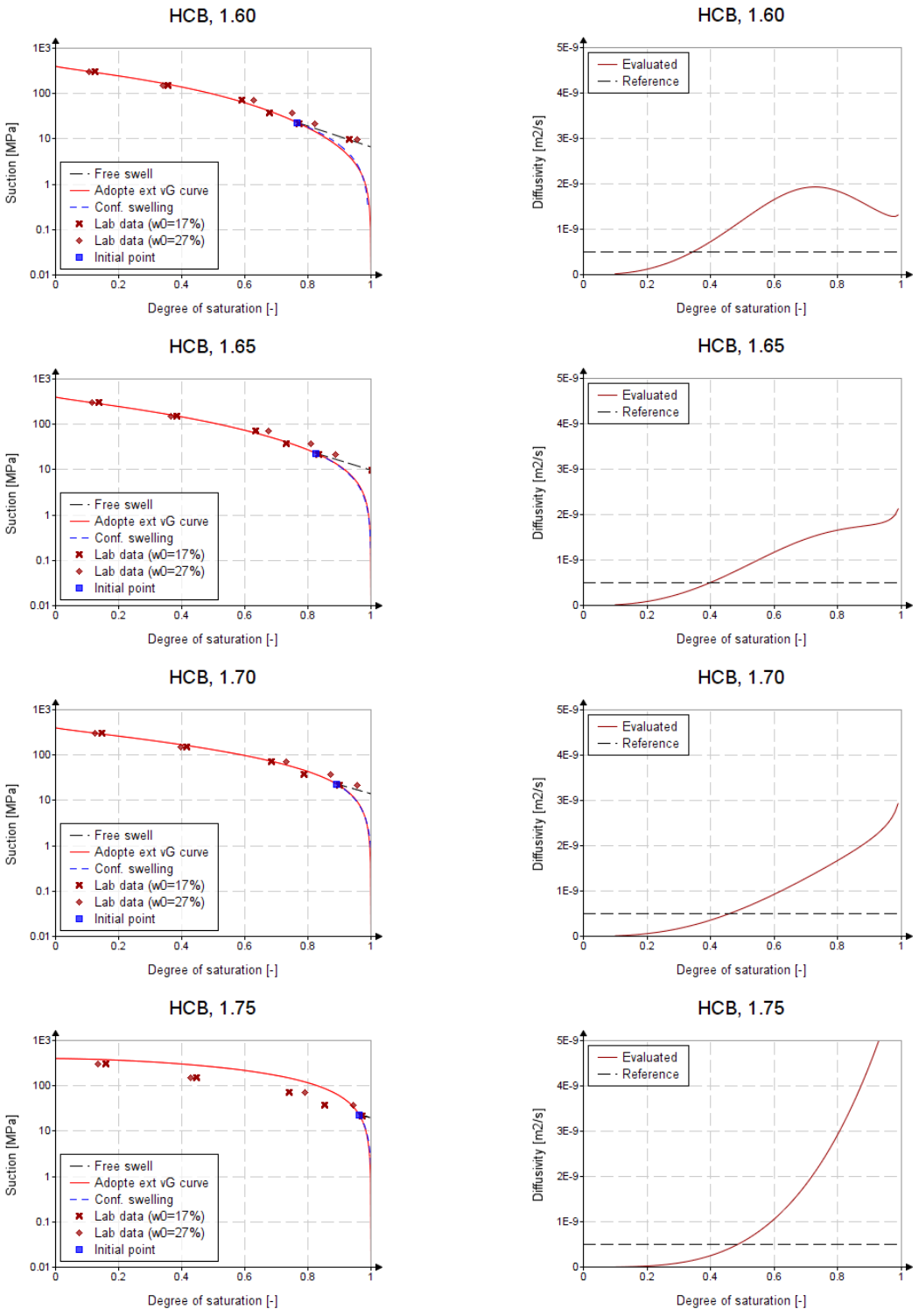

Figure 8-1: Retention data for the HCB representations

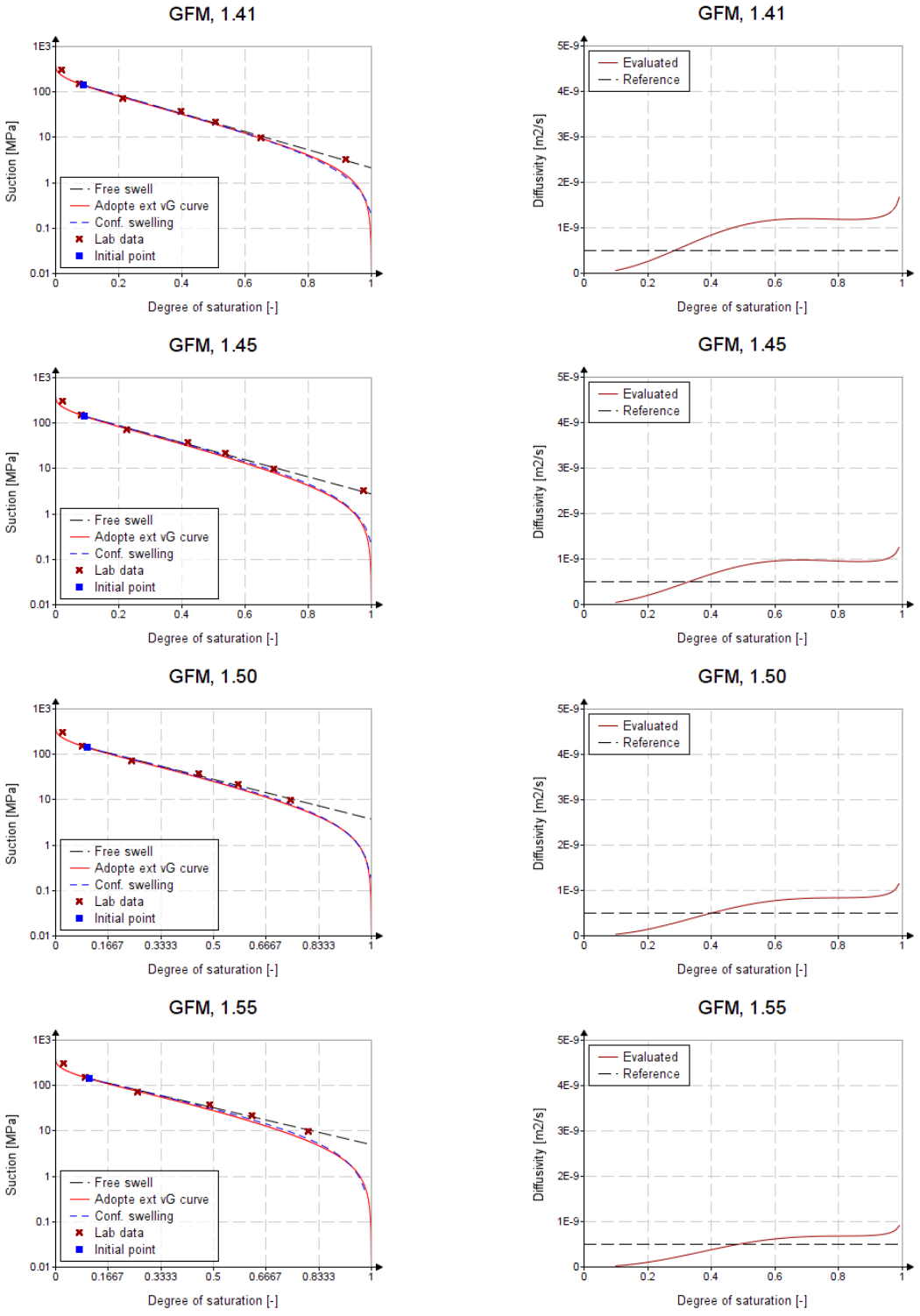

Figure 8-2: Retention data for the GFM representations

Table 8-3: Retention parameters for the HCB and GFM, and initial degree of saturation

Material	P_0 [MPa]	λ_0	P_d [MPa]	λ_d	S_{l0}
HCB, 1.60	5.564	0.11	400	1.20	0.765
HCB, 1.65	19.242	0.15	400	1.20	0.825
HCB, 1.70	65.385	0.18	400	1.20	0.890
HCB, 1.75	2685.0	0.40	400	0.64	0.963
GFM, 1.41	2.979	0.21	400	3.25	0.087
GFM, 1.45	2.946	0.20	400	3.25	0.092
GFM, 1.50	3.958	0.20	400	3.25	0.099
GFM, 1.55	4.286	0.19	400	3.25	0.107

8.1.1.2 Mechanical Parameters of the Buffer Materials

The elastic parameters were not changed and are given in Table 3-5. As described in Section 3.3.8.2, the plastic parameters were derived using initial and homogenized void ratios. As these varied between the different models, a set of plastic parameters was derived for each model. The adopted parameter values are given in Table 8-4 and Table 8-5. The GFM between the wall and buffer box is identified as GFMw, while the GFM between the buffer box and the ceiling is identified as GFMc. This is also illustrated in Figure 8-3 below. In the case where GFMw and GFMc are identical only a single set of parameters (identified as GFM) is given in Table 8-4 and Table 8-5.

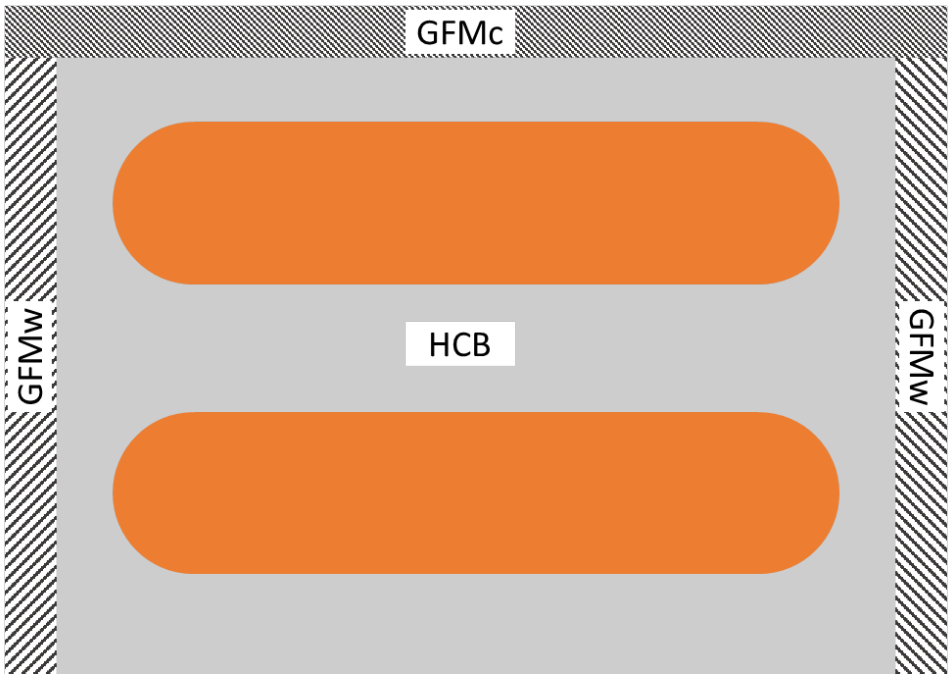

Figure 8-3: Illustration of the different buffer components

Table 8-4: Plastic parameters for buffer materials for models 1-5 (see also Table 8-1)

Model ID			1		2		3			4			5		
			HCB	GFM	HCB	GFM	HCB	GFMw	GFMc	HCB	GFMw	GFMc	HCB	GFMw	GFMc
Initial dry density	ρ_{d0}	kg/m^3	1700	1410	1600	1410	1750	1550	1500	1650	1500	1450	1700	1450	1410
Initial void ratio	e	-	0.618	0.950	0.719	0.950	0.571	0.774	0.833	0.667	0.833	0.897	0.618	0.897	0.950
Target void ratio	e_T	-	0.688	0.688	0.770	0.770	0.622	0.622	0.622	0.710	0.710	0.710	0.682	0.682	0.682
Plastic stress strain modulus	λ_0	-	0.159	0.178	0.171	0.185	0.149	0.160	0.164	0.162	0.171	0.176	0.158	0.173	0.178
Critical state line parameter	M	-	0.252	0.348	0.281	0.348	0.230	0.283	0.304	0.260	0.304	0.328	0.250	0.328	0.348
Tensile strength	p_s	MPa	1.80	0.458	1.13	0.458	2.70	1.105	0.809	1.58	0.809	0.590	1.86	0.590	0.458
Non-assoc. parameter	α	-	0.5	0.5	0.5	0.5	0.5	0.5	0.5	0.5	0.5	0.5	0.5	0.5	0.5
Pre-consol. stress	p_0^*	MPa	18.66	4.31	11.37	4.31	28.64	11.09	7.95	16.26	7.95	5.67	19.34	5.67	4.31
Reference pressure	p_c	MPa	1	1	1	1	1	1	1	1	1	1	1	1	1

NOTE: GFMw is situated between the buffer box and emplacement room walls, while GFMc is situated between the buffer box and the emplacement room ceiling. In models where GFMw and GFMc have the same initial dry density only one set of parametrers is given, called GFM.

Table 8-5: Plastic parameters for buffer materials for models 6-8 (see also Table 8-1)

Model ID			6		7		8		
			HCB	GFM	HCB	GFM	HCB	GFMw	GFMc
Initial dry density	ρ_{d0}	kg/m^3	1700	1410	1600	1410	1750	1550	1450
Initial void ratio	e	-	0.618	0.950	0.719	0.950	0.571	0.774	0.897
Target void ratio	e_T	-	0.706	0.706	0.783	0.783	0.641	0.641	0.641
Plastic stress strain modulus	λ_0	-	0.161	0.179	0.173	0.186	0.152	0.161	0.170
Critical state line parameter	M	-	0.259	0.348	0.286	0.348	0.236	0.283	0.328
Tensile strength	p_s	MPa	1.62	0.458	1.05	0.458	2.38	1.105	0.590
Non-assoc. parameter	α	-	0.5	0.5	0.5	0.5	0.5	0.5	0.5
Pre-consol. stress	p_0^*	MPa	16.64	4.31	10.53	4.31	25.12	11.09	5.67
Reference pressure	p_c	MPa	1	1	1	1	1	1	1

NOTE: GFMw is situated between the buffer box and emplacement room walls, while GFMc is situated between the buffer box and the emplacement room ceiling. In models where GFMw and GFMc have the same initial dry density only one set of parametrers is given, called GFM.

8.1.1.3 Material Parameters for the Non-Bentonite Components

The models used two more components: the UFC and the concrete slab placed beneath the buffer box stack. The properties of these materials were identical with those used in Task 1. The properties of the UFC are described in Section 4.3 and the concrete properties are described in Section 6.2.1.1.

8.1.2 Initial and Boundary Conditions

In Table 8-6 and Table 8-7, the initial conditions of the buffer components are given. The solid density for all clay components is 2750 kg/m^3.

Table 8-6: Initial temperature, liquid pressure and stress for the buffer components

Material	Temperature [°C]	Liquid pressure [MPa]	Stress (isotropic) [MPa]
HCB	11	-22.9	-0.11
GFM	11	-160.9	-0.11

Table 8-7: Initial dry density, void ratio and porosity for the buffer components

Material	Dry density [kg/m^3]	Void ratio [-]	Porosity [-]
HCB, 1.6	1600	0.719	0.418
HCB, 1.65	1650	0.667	0.400
HCB, 1.7	1700	0.618	0.382
HCB, 1.75	1750	0.571	0.363
GFM,1.41	1410	0.950	0.487
GFM,1.45	1450	0.897	0.473
GFM, 1.50	1500	0.833	0.454
GFM, 1.55	1550	0.774	0.436

The initial conditions in the concrete and UFC are given in Table 8-8. The initial liquid pressure in the concrete slab was set according to the initial liquid pressure in the adjacent buffer material (HCB and GFM).

Table 8-8: Initial conditions for the UFC and concrete

Material	Temperature [°C]	Liquid pressure [MPa]	Porosity [-]	Stress (isotropic) [MPa]
UFC	11	-22.9	0.01	-0.11
Concrete	11	-22.9/-160.9	0.01	-0.11

The boundary conditions were set identical to the base case in Task 1 with free access to water on all surfaces in all the models.

8.1.3 Results and Discussion

In this section, different parts of the solutions are analyzed, compared, and discussed. Aside from giving a general overview of the model behavior and the effect of using different initial conditions, the analysis focus on issues related to buffer design requirements. The analysis considers dry density of the bentonite buffer; both globally as well as locally around the hemi head; net mean stress (effective pressure), UFC displacement, and normal stress acting on the UFC surface.

The buffer design requirements are (Birch & Mielcarek 2017):

- The weighted (volume averaged) buffer dry density should be $\geq$ 1600 kg/m^3 (corresponding to a maximum water activity of 0.96)
- The swelling pressure (pressure at full saturation) should be $\geq$ 0.1 MPa.
- The bentonite buffer thickness between the UFC and geosphere should be $\geq$ 0.3 m

As can be seen, the first design requirement is expressed in terms of a volume average of dry density. The dry density requirement is aimed at preventing microbial activity to occur within the buffer. Microbial activity could lead to UFC failure by promoting conditions where sulphide driven corrosion could take place (SKB and POSIVA 2017). The microbial activity is prevented if the pressure (related to water activity) in the buffer is high enough. This pressure may, using a simplified approach, be translated into a dry density if utilizing a swelling pressure function.

8.1.3.1 Overview of the Dry Density Field

Dry density results are given for all eight models in Figure 8-4 - Figure 8-11. The results are shown in the same manner for all models. To the left a contour plot of the dry density field at the end of the simulation is shown. The buffer components in the models were fully water saturated at the end of the simulations. At the bottom right position, the color scale for the given contour plot is shown (identified with an arrow), together with the color scales used for the other models. At the upper right position, a table containing some characteristics of the dry density field is shown. These are the maximum and minimum value as well as the volume averages over the block, GFM and the total buffer.

The general appearance of the dry density field at full saturation is similar between all models. The dry density in the buffer is higher near the UFCs, particularly in a region at the mid of the UFC stretching out horizontally, and lower near and inside the GFM zone.

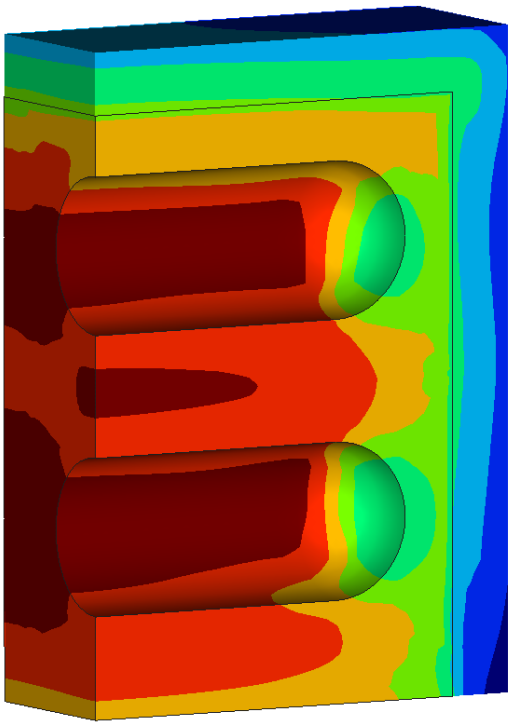

	ρ_d [kg/m^3]
Max	1690
Min	1510
Volume average Block	1650
Volume average GFM	1560
Volume average Total	1630

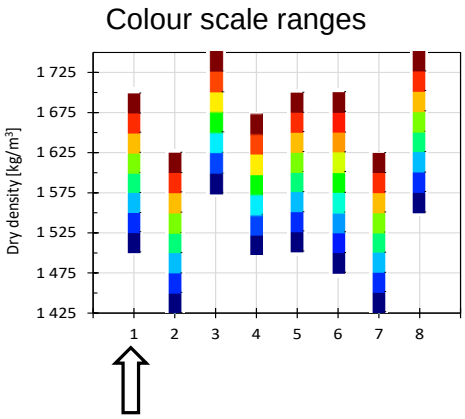

Figure 8-4: Dry density results from Model 1

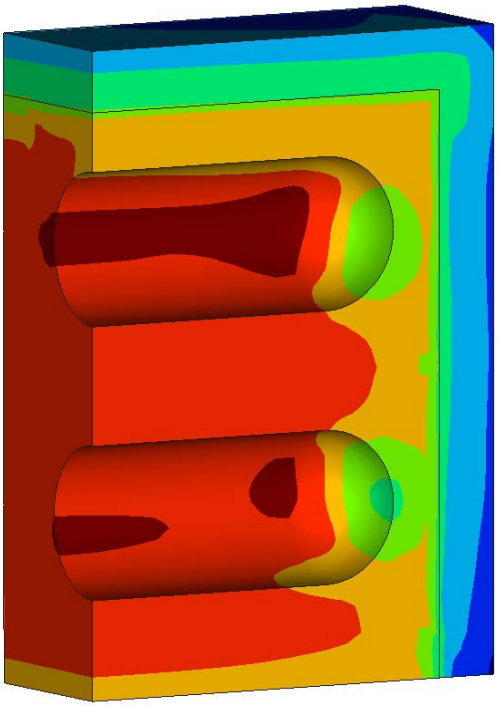

	ρ_d [kg/m^3]
Max	1610
Min	1440
Volume average Block	1570
Volume average GFM	1490
Volume average Total	1550

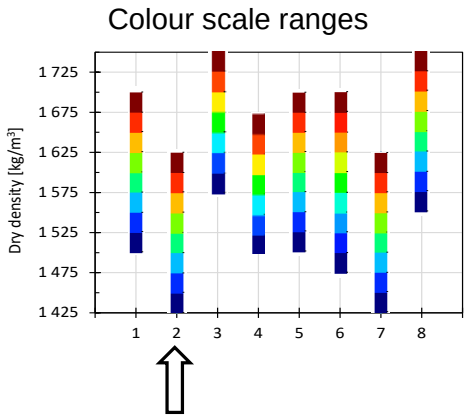

Figure 8-5: Dry density results from Model 2

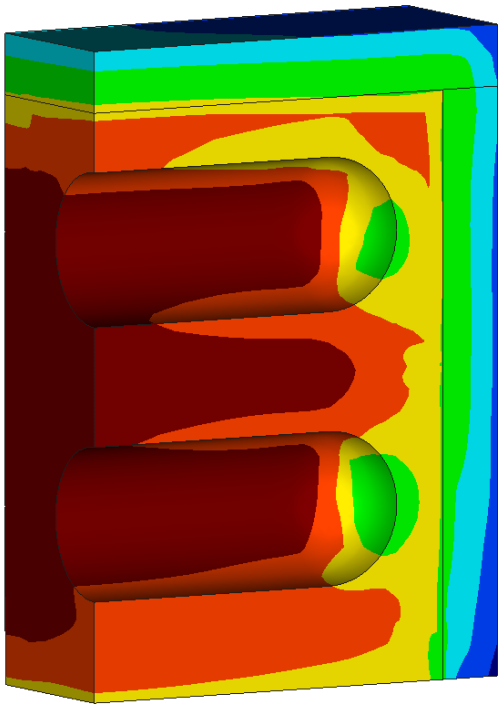

	ρ_d [kg/m^3]
Max	1740
Min	1590
Volume average Block	1710
Volume average GFM	1640
Volume average Total	1700

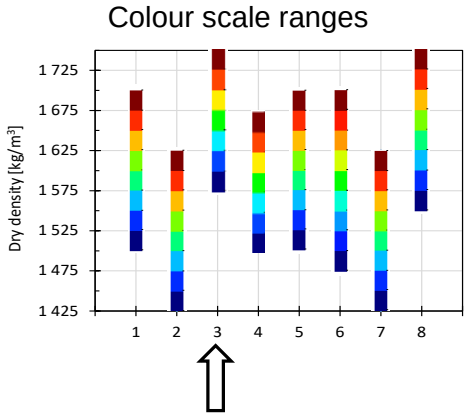

Figure 8-6: Dry density results from Model 3

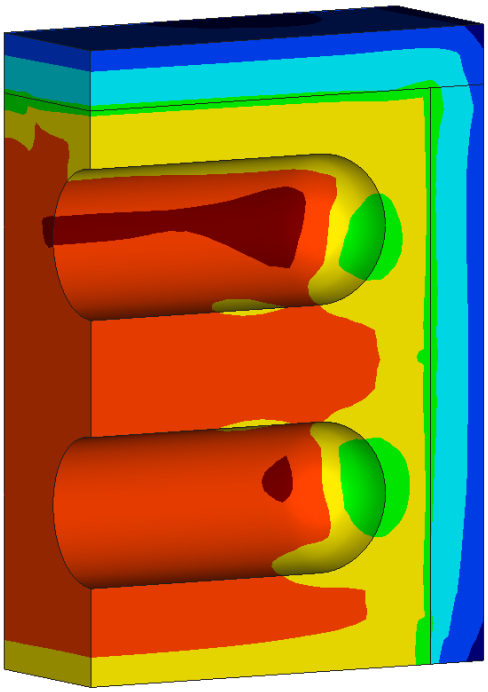

	ρ_d [kg/m^3]
Max	1660
Min	1510
Volume average Block	1630
Volume average GFM	1550
Volume average Total	1610

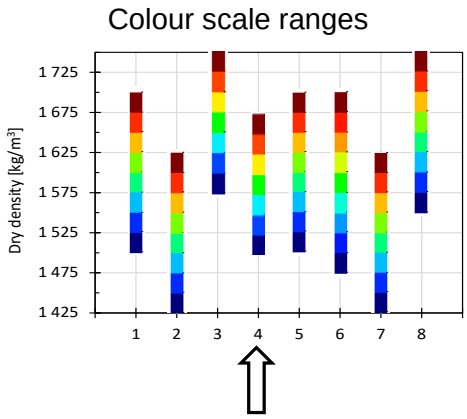

Figure 8-7: Dry density results from Model 4

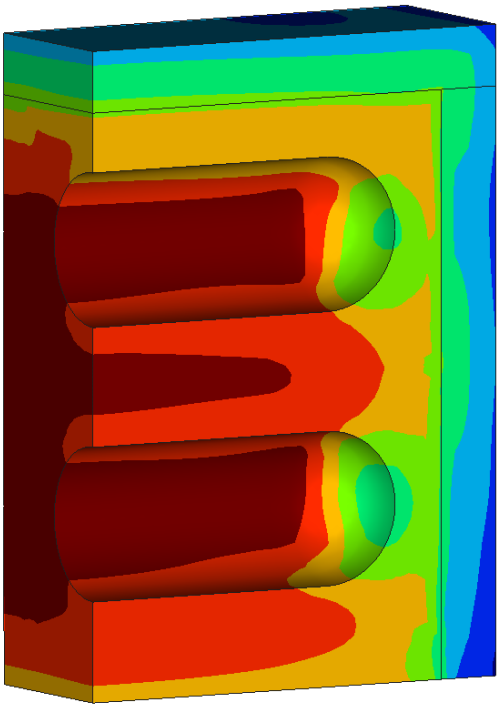

	ρ_d [kg/m^3]
Max	1690
Min	1520
Volume average Block	1650
Volume average GFM	1570
Volume average Total	1630

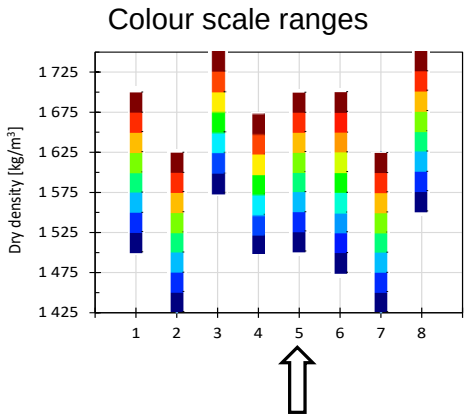

Figure 8-8: Dry density results from Model 5

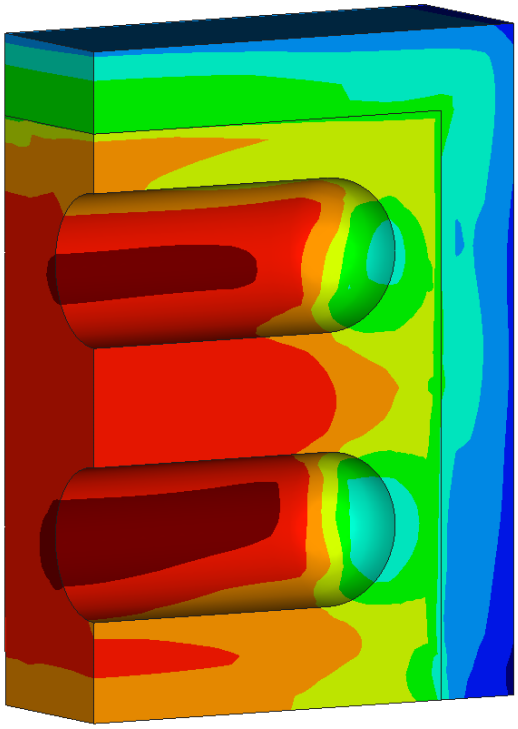

	ρ_d [kg/m^3]
Max	1680
Min	1490
Volume average Block	1640
Volume average GFM	1550
Volume average Total	1610

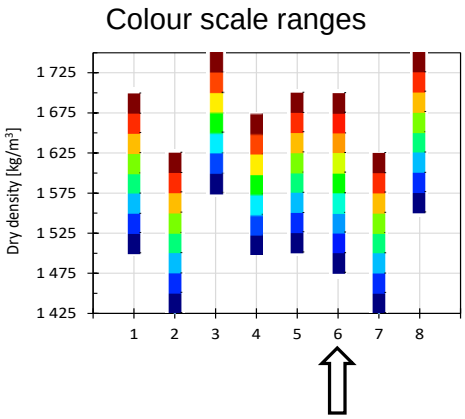

Figure 8-9: Dry density results from Model 6

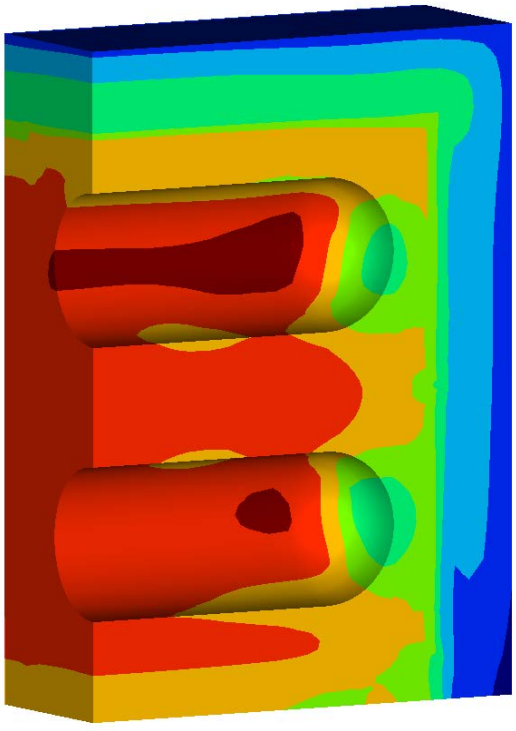

	ρ_d [kg/m^3]
Max	1610
Min	1440
Volume average Block	1570
Volume average GFM	1480
Volume average Total	1540

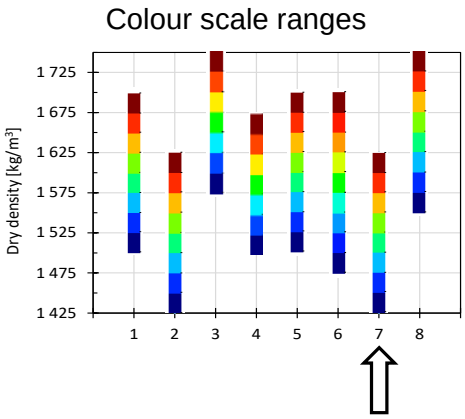

Figure 8-10: Dry density results from Model 7

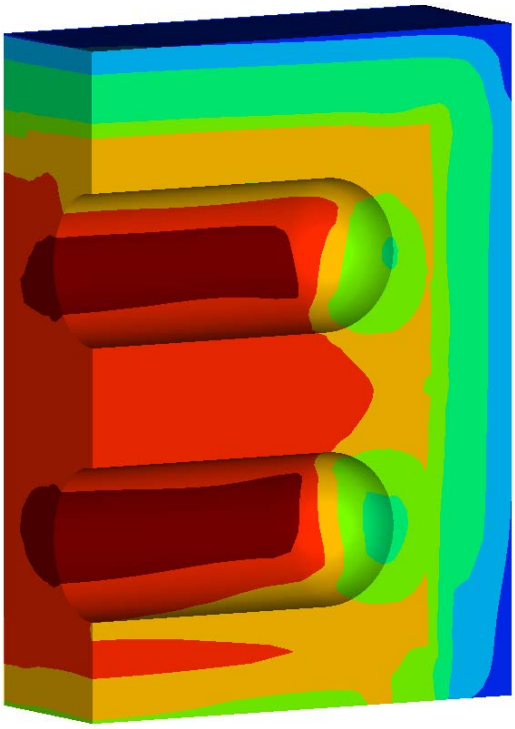

	ρ_d [kg/m^3]
Max	1740
Min	1570
Volume average Block	1700
Volume average GFM	1620
Volume average Total	1680

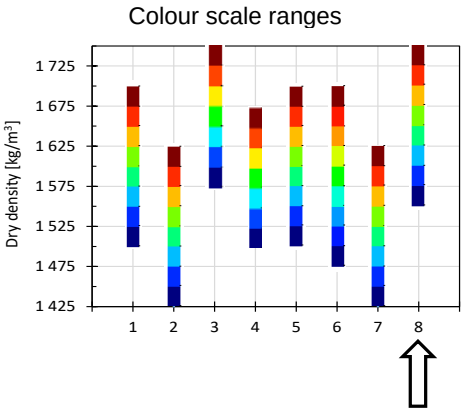

Figure 8-11: Dry density results from Model 8

To give a compact and clear overview of the results a compilation of data describing the characteristics of the dry density field in the different models are given in Figure 8-12, Figure 8-13 and Table 8-9.

The positions where the maximum and minimum values occur are shown in Figure 8-12. The position of the maximum dry-density values is either at the center of the lower UFC (Models 1,5 & 6) or more (about 2/3 of the modelled UFC length) towards the UFC hemi head (Models 2, 3, 4, 7 & 8). Models 1, 5 and 6 have similar initial conditions which could lead to the conclusion that this feature determines the position of the maxima. When studying the other set of Models (2, 3, 4, 7 & 8), however, it becomes clear that this is not the case.

The position of the minimum values is similar in all models except Model 8, near the floor in the GFM situated between the wall and the buffer box. In Model 8 the minimum also occurs close to the wall but unlike the other models, it is positioned near the ceiling.

Them maximum and minimum values are given in both Figure 8-13 and in Table 8-9. They also contain the volume averages of the dry density in the HCB, the GFM and the entire buffer. In Table 8-9 the color code (green, orange, red) indicates agreement with the current buffer design requirement, $\rho_d \geq 1600$ kg/m^3.

Comparing the maximum and minimum values between models leads to no big surprises. Models with higher initial density in the buffer block (Models 3 and 8) attain both higher maximum and minimum dry-density values in the final state and models with lower initial dry density in the buffer block (Models 2 and 7) attain both lower maximal and lower minimal values in the final state.

The current buffer design requirements include that the weighted (volume averaged) buffer dry density should be no less than 1600 kg/m^3. Models 2 and 7 do not meet the requirement as the volume averages over the entire buffer are 1550 kg/m^3 and 1540 kg/m^3 respectively. The rest of the models meet the design requirement. Some models, 1 (1630 kg/m^3), 4 (1610 kg/m^3), 5 (1630 kg/m^3) and 6 (1610 kg/m^3), are close to the design limit, while Models 3 and 8 are well above the limit with 1700 kg/m^3 and 1680 kg/m^3, respectively.

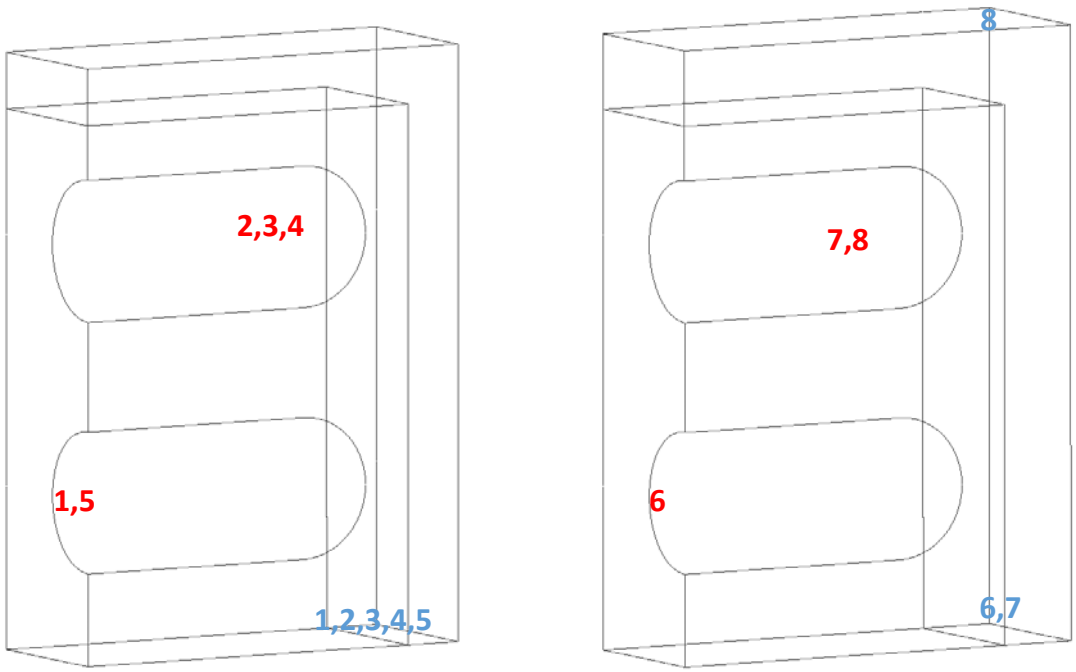

Figure 8-12: Positions of the maximum (red) and minimum value (blue) of the dry density fields (the number indicates model ID)

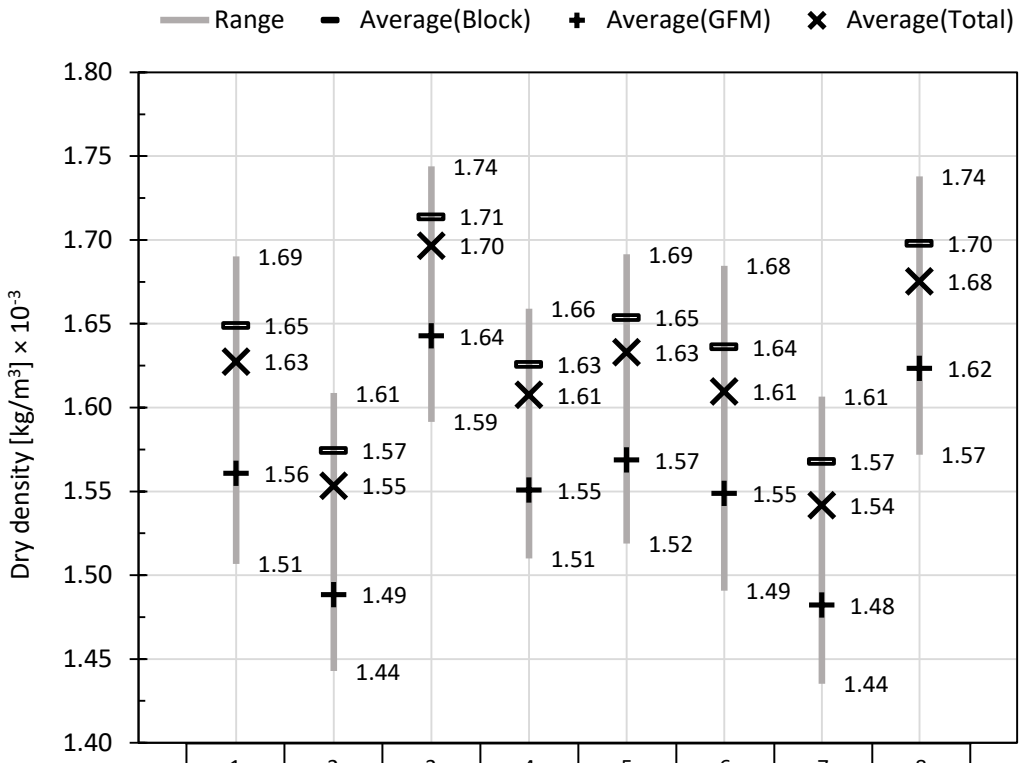

	1	2	3	4	5	6	7	8
ll, GFM ρ_d [kg/m^3]	1410	1410	1550	1500	1450	1410	1.410	1.550
ing, GFM ρ_d [kg/m^3]	1410	1410	1500	1450	1410	1410	1410	1450
	1700	1600	1750	1650	1700	1700	1600	1750
	0.225	0.225	0.225	0.225	0.225	0.3	0.3	0.3

Figure 8-13: Diagram showing characteristics of the dry density field (Min – Max range, volume averages of the block, GFM, and the entire buffer)

Table 8-9: Characteristics for the dry density fields at the end of the simulations

ρ_d [kg/m^3]	1	2	3	4	5	6	7	8
Max	1690	1610	1740	1660	1690	1680	1610	1740
Min	1510	1440	1590	1510	1520	1490	1440	1570
Volume average Block	1650	1570	1710	1630	1650	1640	1570	1700
Volume average GFM	1560	1490	1640	1550	1570	1550	1480	1620
Volume average Total	1630	1550	1700	1610	1630	1610	1540	1680

8.1.3.2 Local Study of Dry Density at the Hemi Head

In the modelling of Step 1 and Step 2 (see Sections 4 and 5), the dry-density field near the hemi head of the UFC showed a locally decreasing trend between the hemi head and the tunnel wall

(see red arrows in Figure 8-14). It was associated with the presence of the stiff UFC in the swelling bentonite. For a detailed study/discussion of this see Appendix E.

This locally decreasing trend of the dry density field could violate the design requirement (that the average buffer dry density must be no less than 1600 kg/m^3). Therefore, density distributions near the hemi head of the UFC were studied below. The profile lines are shown in Figure 8-14 and the dry density profiles are given in Figure 8-16.

The homogenized dry density of the buffer in the horizontal direction between the UFC's hemi head and the tunnel wall was calculated analytically to get a first indication of what could be expected from the FE-simulations. As indicated in Figure 8-14, to handle the difference in length over which to homogenize at the hemi head, the evaluation was performed at two positions to obtain a minimum – maximum range (indicated 'With min' and 'With max'). The homogenized dry density of the buffer was also calculated between the UFCs, denoted 'Without' in Figure 8-14. The calculated values are given in Table 8-10 and Figure 8-15. The analytical values obtained at the hemi head was 92 % to 98 % of that obtained for the section without a UFC.

The values obtained from the analysis above are also included in the plots of the dry density profiles shown in Figure 8-16. There are no big surprises when studying the FE solutions and their correspondence with the values from the analytical analysis. The decrease in dry density towards the hemi head is still significant in these models and the profiles are essentially centered in the analytically calculated minimum – maximum range. Table 8-10 and Figure 8-15 also contain the volume averages of the FE model profiles in front of the upper and lower UFC.

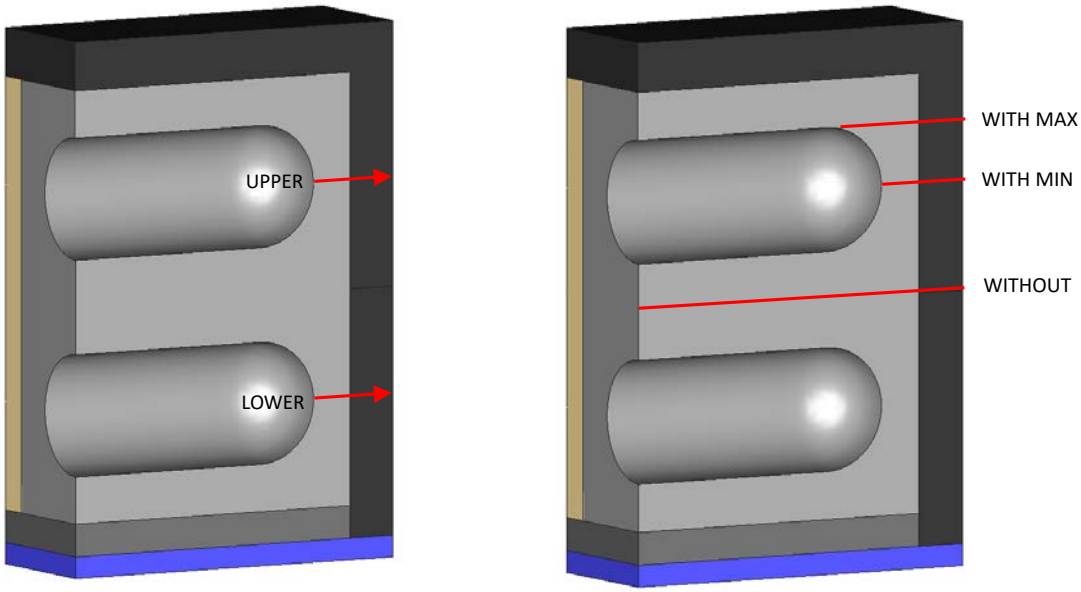

Figure 8-14: Scan lines where dry density is evaluated in the model (left) and analytically (right)

Table 8-10: Horizontally homogenized dry density calculated analytically and numerically

ρ_d [kg/m^3]	1	2	3	4	5	6	7	8
Without	1660	1570	1720	1630	1670	1650	1570	1720
With min	1540	1500	1640	1570	1570	1520	1480	1630
With max	1610	1540	1690	1600	1620	1590	1530	1670
FE hom upper	1580	1510	1660	1580	1590	1560	1500	1640
FE hom lower	1570	1510	1660	1570	1580	1550	1490	1640

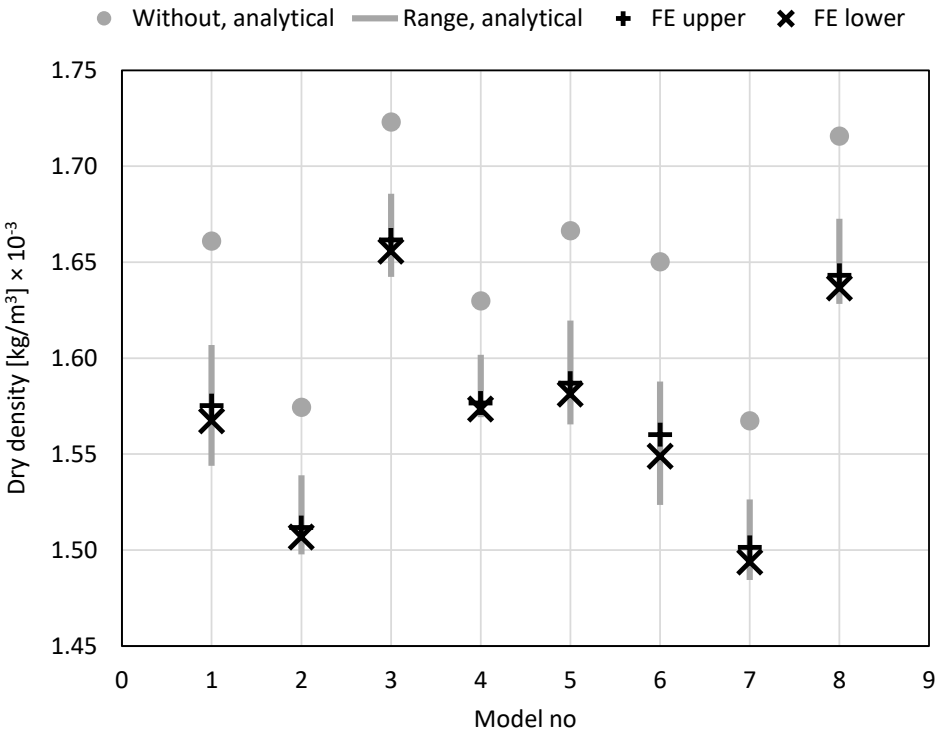

Figure 8-15: Analytically calculated homogenized dry density between the UFCs (indicated 'Without, analytical') and between the hemi head surface and the tunnel wall at two different positions rendering a range (indicated 'Range, analytical')

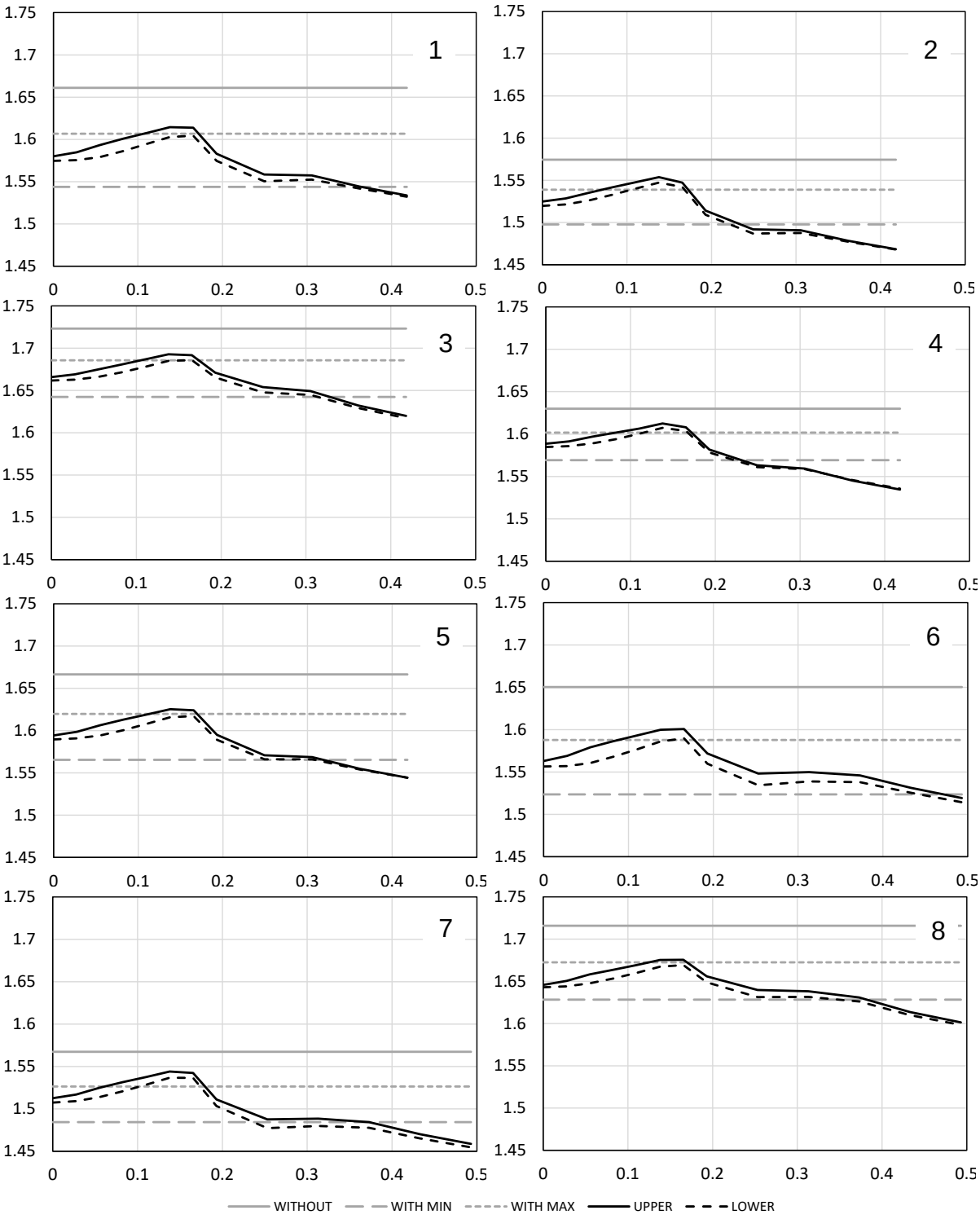

Figure 8-16: Profiles of dry density, [kg/m^3] × 10^{-3}, along a horizontal coordinate, [m], starting at the hemi head and directed towards the rock wall

8.1.3.3 Overview of the Net Mean Stress Field

The material model used to represent the mechanical behaviour of the bentonite buffer, the Barcelona Basic Model, is formulated using net mean stress, p'. This is defined as the difference between the isotropic stress affecting the soil "matrix" in the material ($p = -tr(\boldsymbol{\sigma})/3$) and the max value of the liquid and gas pressure respectively: $p' = p - \max(p_l, p_g)$. The net mean stress is a generalization of the effective stress, $p - p_l$, into the unsaturated regime. In the present modelling $p_l \leq p_g = 0.1$ MPa due to the applied liquid pressure boundary condition (see Section 3.6), which results in that $p' = p - 0.1$ MPa.

The net mean stress results are given for all eight models in Figure 8-17 - Figure 8-24 below. The results are shown in the same manner for all models. The left side of the figures show a contour plot of the net mean stress field of the fully saturated bentonite buffer at the end of the simulation (500 years) when the system is in steady state conditions. The right side of the figures show a range of the net mean stress field for each model. The color scale used for the shown contour plot is indicated with an arrow. At the upper right position, a table containing the maximum and the minimum values is included.

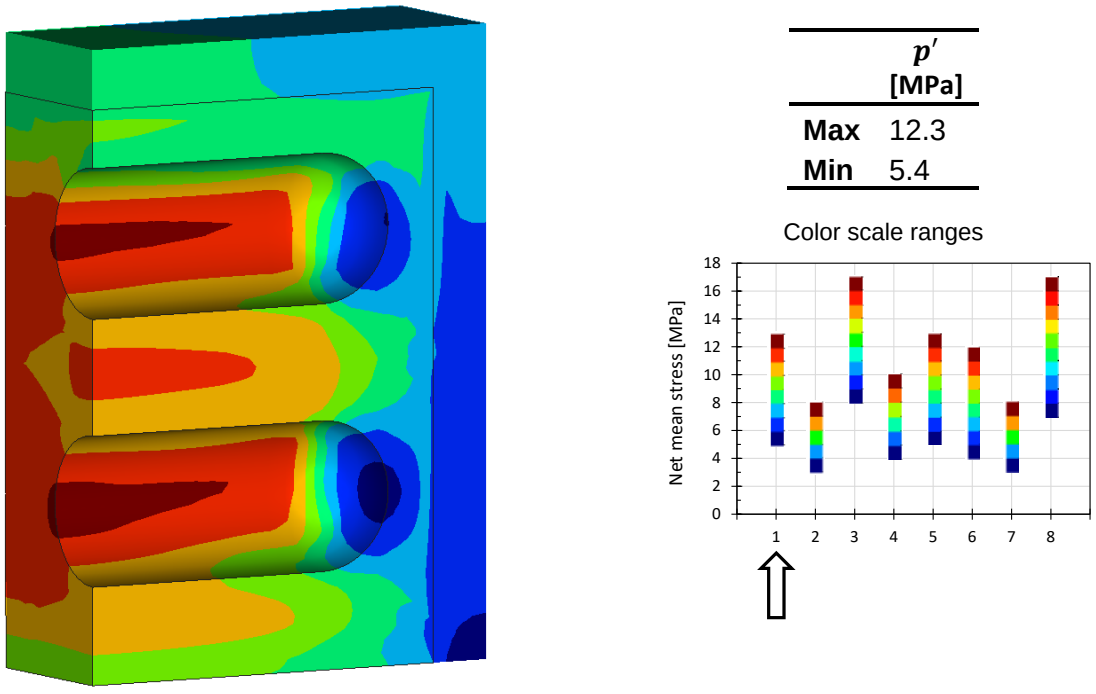

Figure 8-17: Net mean stress results from Model 1

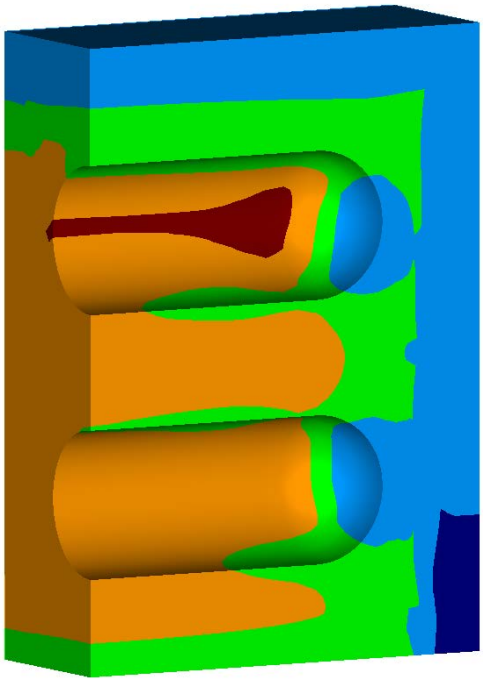

	p' [MPa]
Max	7.2
Min	3.2

Color scale ranges

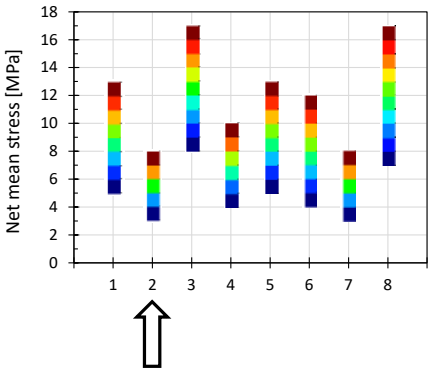

Figure 8-18: Net mean stress results from Model 2

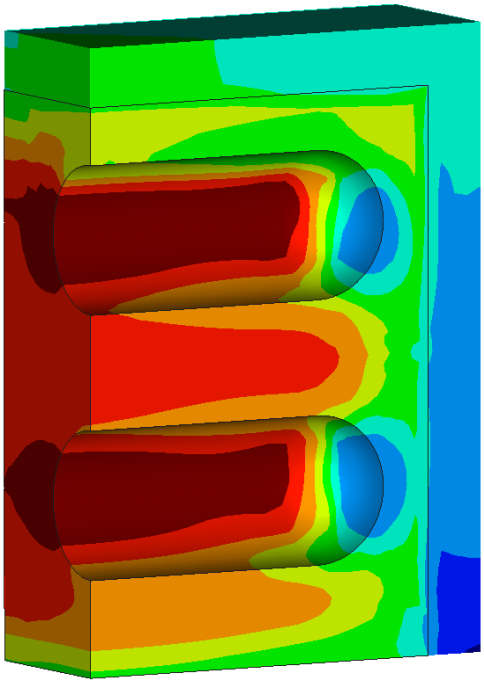

	p' [MPa]
Max	16.9
Min	8.7

Color scale ranges

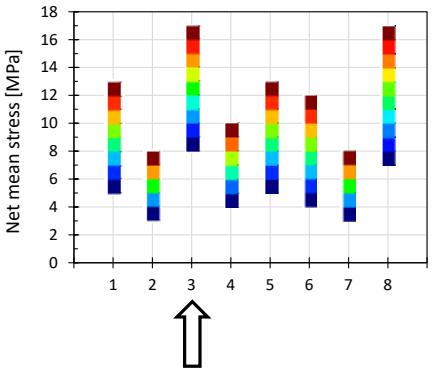

Figure 8-19: Net mean stress results from Model 3

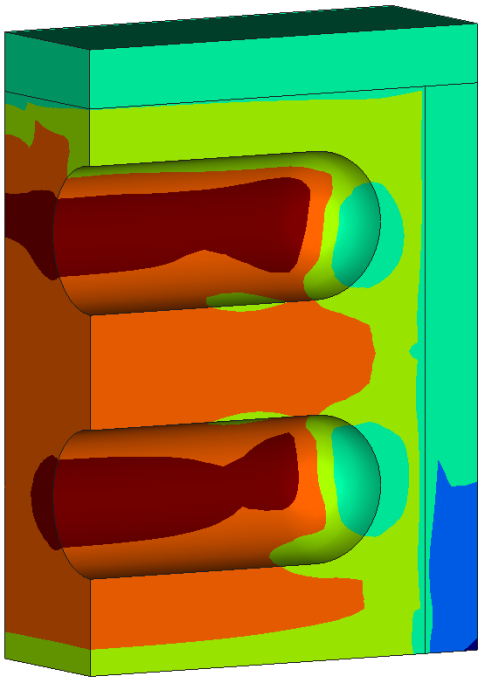

	p' [MPa]
Max	10.0
Min	4.7

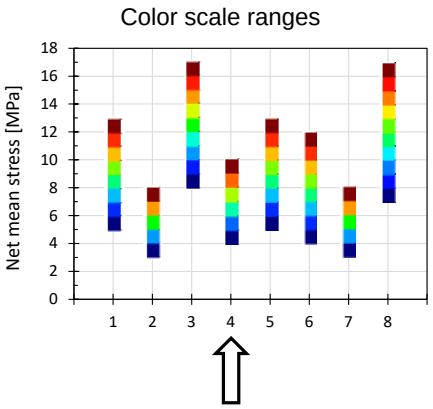

Figure 8-20: Net mean stress results from Model 4

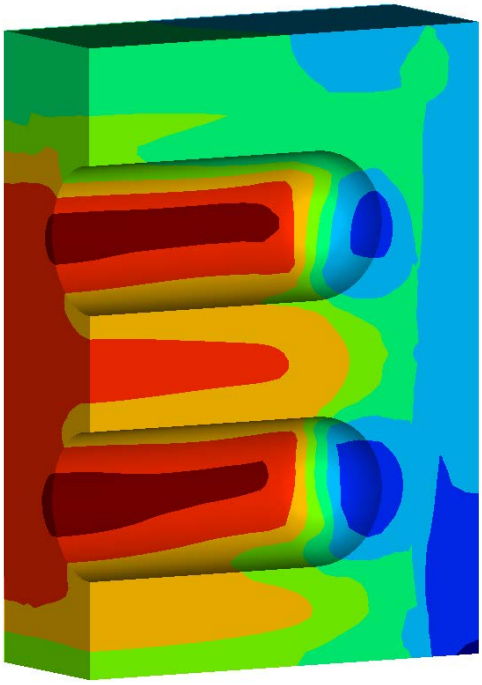

	p' [MPa]
Max	12.4
Min	5.7

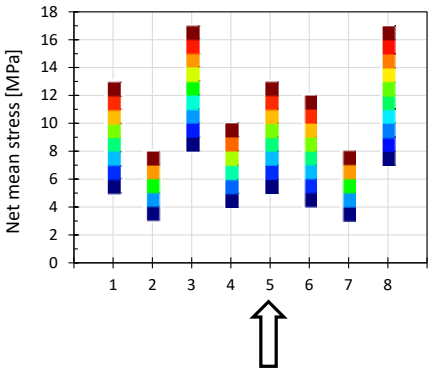

Figure 8-21: Net mean stress results from Model 5

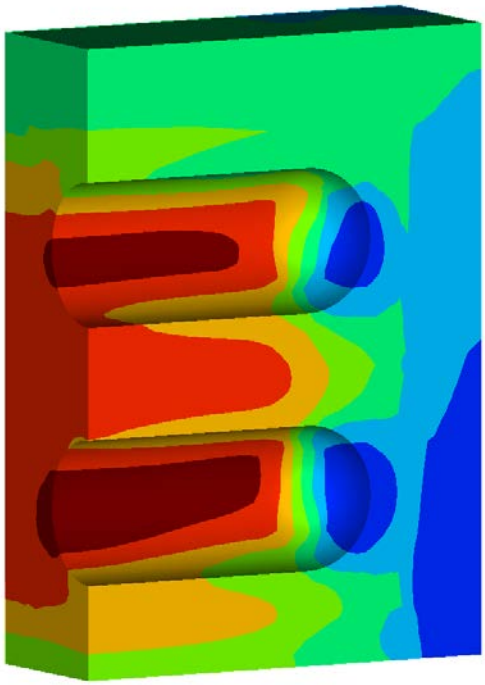

	p' [MPa]
Max	11.8
Min	4.9

Color scale ranges

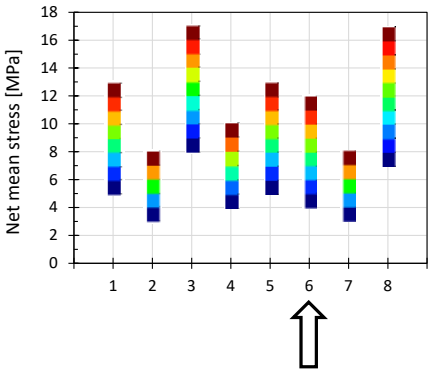

Figure 8-22: Net mean stress results from Model 6

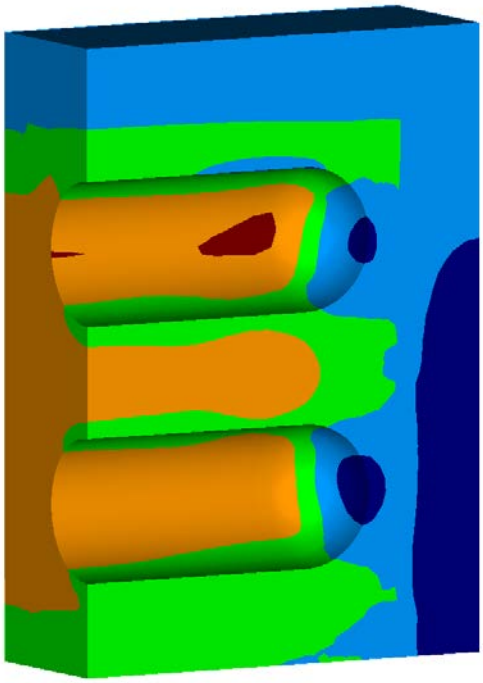

	p' [MPa]
Max	7.1
Min	3.1

Color scale ranges

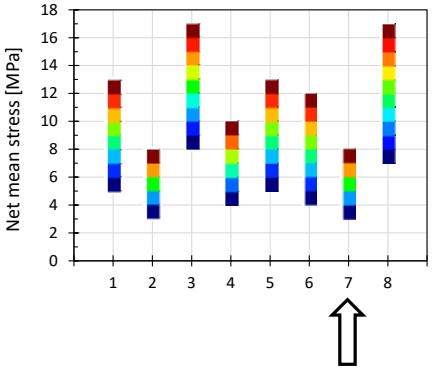

Figure 8-23: Net mean stress results from Model 7

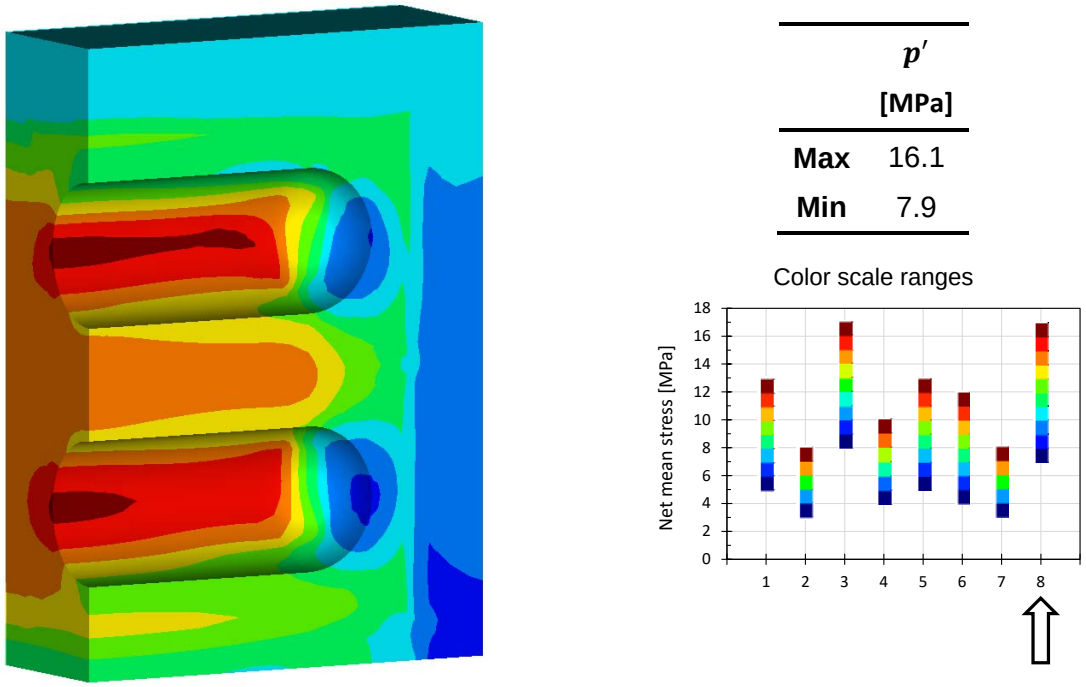

Figure 8-24: Net Mean Stress Results from Model 8

Buffer design requirements state that the swelling pressure upon saturation should be ≥ 0.1 MPa. All eight models met this requirement by a significant margin. When analysing all eight models, the minimum swelling pressure, here identified as the net mean stress, was 3.1 MPa (see Figure 8-26 and Table 8-11), occurring in Model 7 in the GFM close to the tunnel floor (see Figure 8-25). Table 8-11 summarizes the maximum and minimum net mean stress values of individual models.

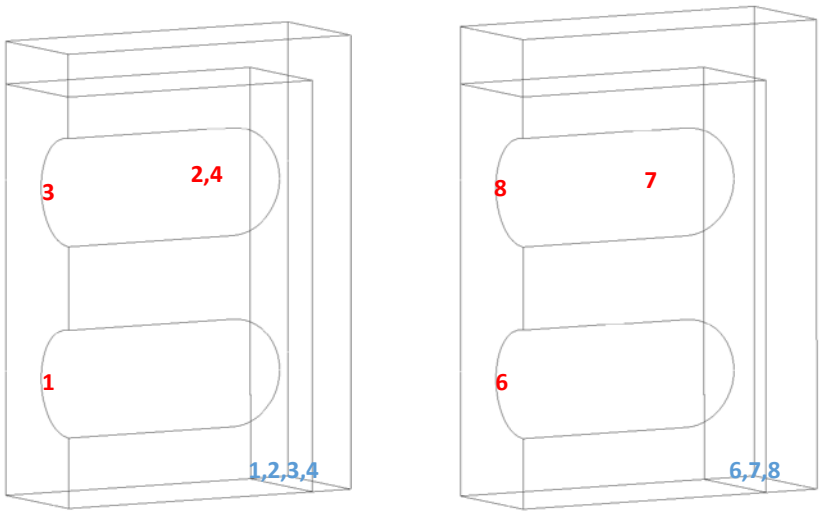

Figure 8-25: Positions of the maximum (red) and minimum value (blue) of the net mean stress fields (model numbers shown)

As can be seen in Figure 8-25 the maximum net mean stress occurs at the UFC interface for all eight models. The maximum stress value ranges from 7.1 MPa – 16.9 MPa (see Figure 8-26 and Table 8-11).

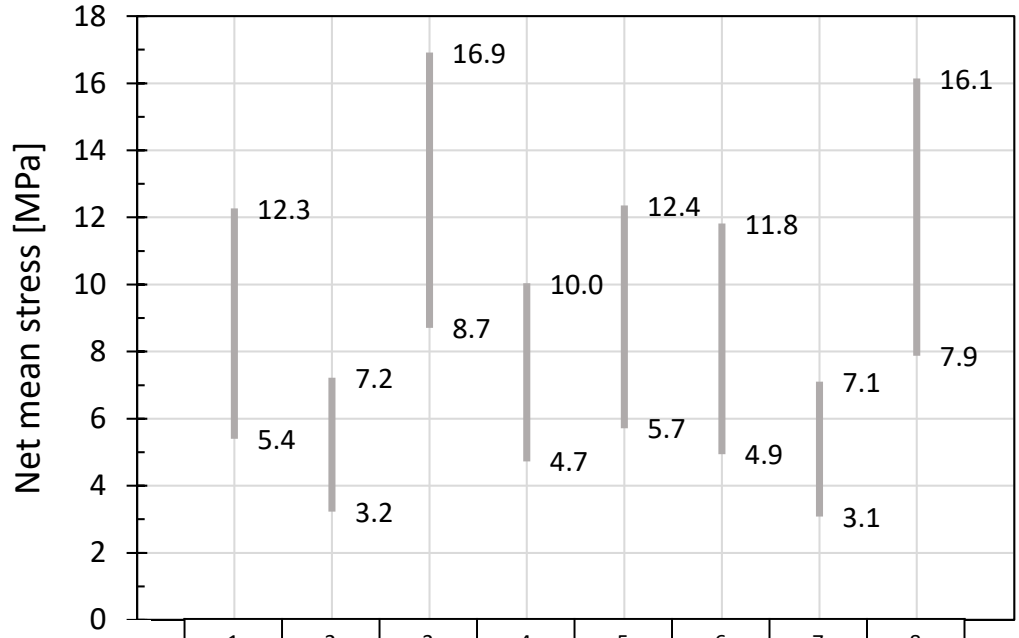

	1	2	3	4	5	6	7	8
GFM ρ_d [kg/m^3]	1410	1410	1550	1500	1450	1410	1.410	1.550
ʒ, GFM ρ_d [kg/m^3]	1410	1410	1500	1450	1410	1410	1410	1450	
	1700	1600	1750	1650	1700	1700	1600	1750
	0.225	0.225	0.225	0.225	0.225	0.3	0.3	0.3

Figure 8-26: Diagram showing the minimum – maximum range of the net mean stress field

Table 8-11: Compilation of the maximum and minimum values for the net mean stress fields obtained at the end of the simulations

p' [MPa]	1	2	3	4	5	6	7	8
Max	12.3	7.2	16.9	10.0	12.4	11.8	7.1	16.1
Min	5.4	3.2	8.7	4.7	5.7	4.9	3.1	7.9

8.1.3.4 UFC Displacements

Due to the assumed symmetries in the model, displacement of the UFCs is only allowed in the vertical direction. In addition, the effective displacement will be uniform due to the high stiffness of the UFC relative to the buffer, see Figure 8-27. Thus, it is enough to analyze the displacement of one point in the UFC. The points selected are indicated by the start of the arrows in Figure 8-27.

In Figure 8-28 the upward displacements of the UFCs are given for all eight models. The upper UFC has been displaced more than the lower UFC due to the adjacent compressible GFM. The larger displacements in Models 6 and 8 depend on the combination of high initial dry density of the block together with the thicker GFM zone.

The buffer design requirements state that there should be no less than 0.3 m of bentonite buffer between the UFC and geosphere. At installation, the minimum vertical distance between the UFC and the GFM is 0.218 m. This gives that, in the analyzed models, the displacements could be up to 0.143 m and 0.218 m for the 0.225 m and 0.3 m thick GFM, respectively. The obtained displacements are one order of magnitude less than what the requirement allows for. Thus, all models fulfill this design requirement with a large margin.

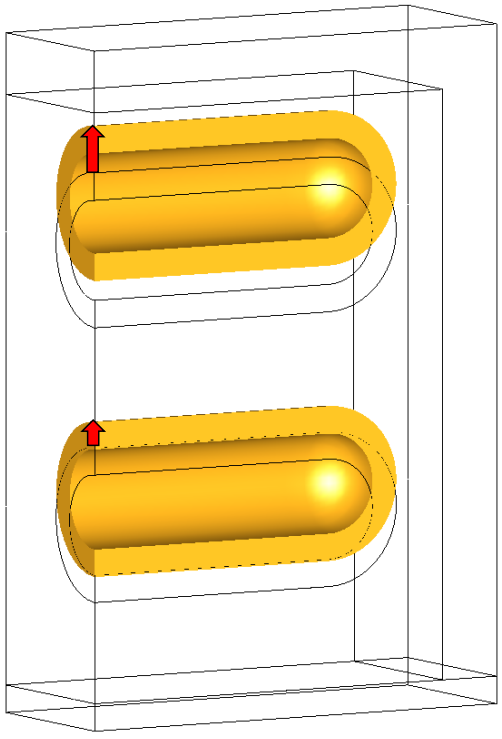

Figure 8-27: Displaced UFCs shown with 10 x the displacement

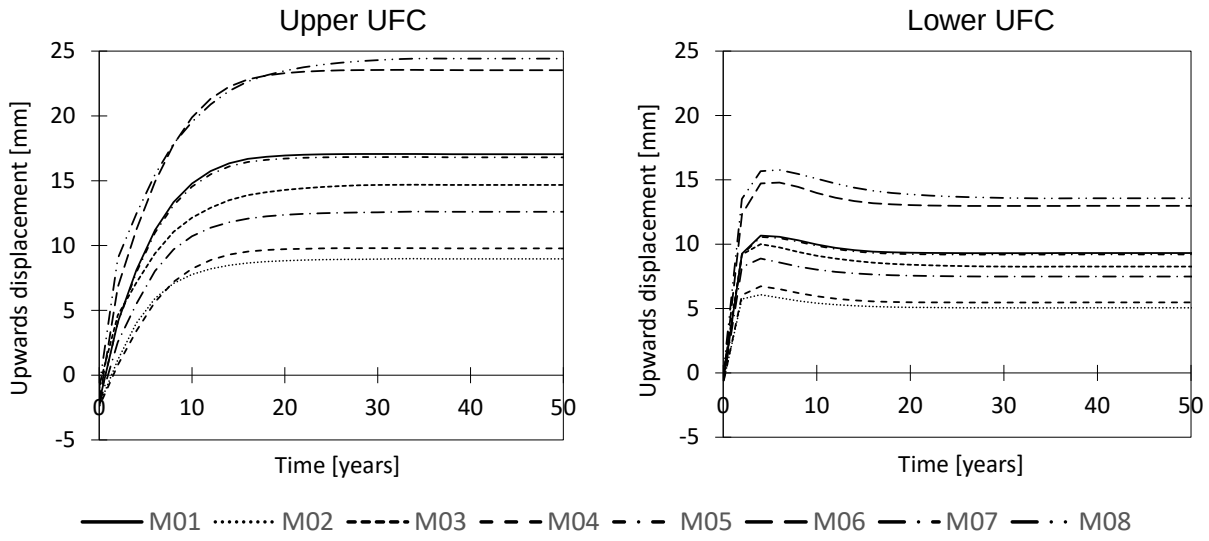

Figure 8-28: Upwards displacement of the UFCs during the first 50 days

8.1.3.5 Normal Stress Acting on the UFCs

The loads generated by the swelling bentonite are of interest when designing the UFC. One could also use the maximum allowed load acting on the UFC as an input to formulate an additional buffer design requirement. Here, however, the normal stress, $\sigma_n = \boldsymbol{n}^T\boldsymbol{\sigma}\boldsymbol{n}$, acting on the UFCs was studied. As given above, the normal stress is obtained by the projection of the total stress tensor, $\boldsymbol{\sigma}$, on the normal direction, $\boldsymbol{n}$, of the studied surface. The normal stress is evaluated along three scan lines for each UFC as shown in Figure 8-29, in Figure 8-30 all models results are compiled.

As expected, the obtained normal stress is heavily influenced by the initial dry density. Models 3 and 8 produce the highest normal stresses (17 MPa), whereas Models 2 and 7 give the lowest values (4 MPa). Common for all models is that the loads on the upper and lower UFCs are very similar and that the 'mid' scan lines show higher values than the other regions. The reason for the high values of the 'mid' scan lines can be found by analyzing the homogenized dry densities in the vertical and horizontal direction, see the right drawing in Figure 8-29, and then using the swelling pressure relation, Equation (3-49), to translate the dry densities to stresses. It should be noted that this only gives an approximate estimate of the normal stress, in general, the swelling pressure will not equal to the normal stress.

Continuing with the study and focusing on the limiting cases, Models 3 and 7 are analyzed. The homogenized dry densities and corresponding swelling pressures, here taken as approximate estimates for the normal stress, are given in Table 8-12. The analytical results in Table 8-12 show a reasonable agreement with the numerical results given in Figure 8-30. For Model 3 the FE-solution gives 16.1 MPa (horizontal) and 12.5 MPa (vertical) which should be compared with 18.3 MPa and 13.8 MPa obtained from the analytical solution. For Model 7 the FE-solution gives 6.5 MPa (horizontal) and 4.7 MPa (vertical) which should be compared with 7.0 MPa and 5.2 MPa obtained from the analytical solution. This indicates that an important factor, contributing to

the different values in normal stress acting on the UFCs in the different orientations, comes from the difference in homogenized dry density in different directions.

Table 8-12: Analytical estimates of normal stress acting on the UFCs in the horizontal and vertical direction

	ρ_d [kg/m^3]		p_s [MPa]	
Model	**Horizontal**	**Vertical**	**Horizontal**	**Vertical**
3	1750	1700	18.3	13.8
7	1600	1560	7.0	5.2

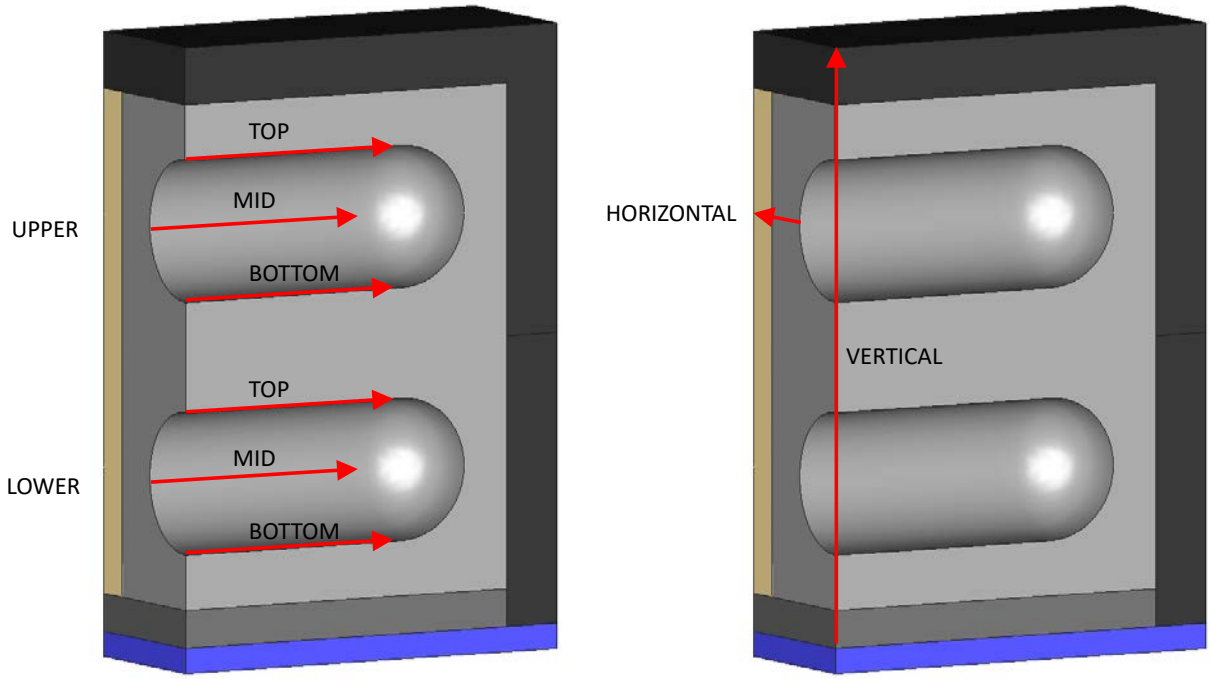

Figure 8-29: (Left) Scan lines where normal stress acting on UFCs is evaluated in the FE-models, (Right) lines where the analytical estimates of normal stress were calculated

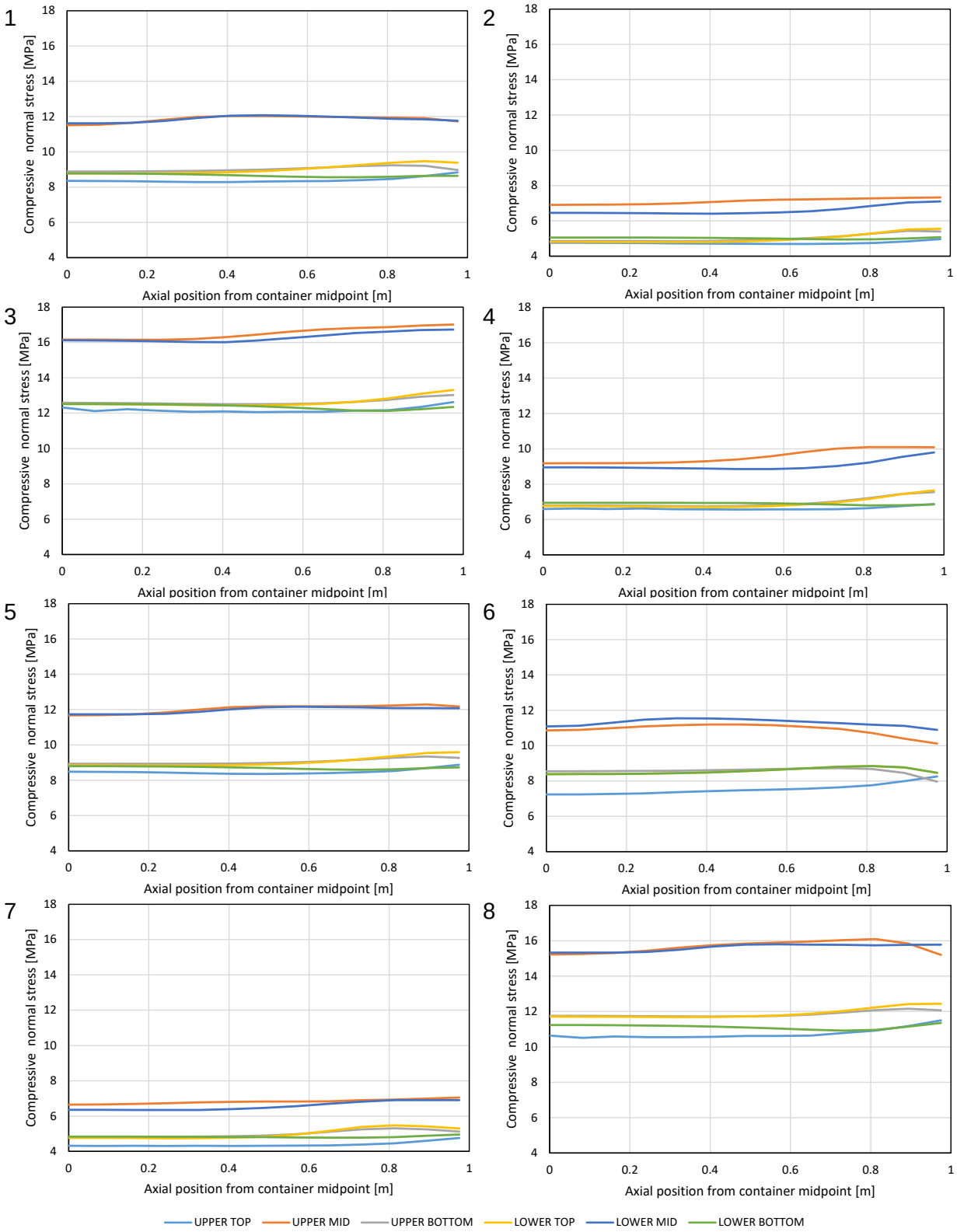

Figure 8-30: Normal stress acting on UFCs along three scan lines at the UFC surface

8.2 Task 3 - Models with Airgaps

After installation of the buffer, airgaps are expected at interfaces between some of the bentonite-based components, as well as between the GFM and the emplacement room ceiling. This study focused on assessing the effect of these airgaps on changes in the dry density of the bentonite buffer at full saturation and on the swelling pressure around the UFCs.

8.2.1 Model Setup

Airgaps after emplacement are expected to be present between the buffer components. Three different airgaps were studied (see Figure 8-31):

- **SIDE:** Between the spacer block and buffer box
- **TOP:** Between the GFM and tunnel ceiling
- **UFC:** Between the UFC and buffer box

The following airgap dimensions were chosen based on the values of the 2021 Engineering Data Clearance Form provided by the NWMO (APM-REF-01900-300813-R000):

- **SIDE:** 1 cm
- **TOP:** 1 cm
- **UFC:** 0.75 cm (average value), 1.5 cm

According to the values of the 2021 Engineering Data Clearance Form (APM-REF-01900-300813-R000), the average size of UFC airgap is 0.75 cm. The UFC will rest on the bottom of the cavity inside the buffer box, meaning that the maximum airgap size (at installation) found above the UFC will be 1.50 cm. Thus, for the UFC airgap, two widths were analyzed, using the average value and the maximum value (2 x average value).

To obtain numerically manageable models only one airgap was included in each modelled geometry. An overview of the models is given in Table 8-13, and the 2D geometries (with mesh) are shown in Figure 8-32. These geometries were constructed by cutting a vertical slice through the full 3D geometries described in Section 6.2 at the mid-length of the UFC. The dimensions of the geometry can thus be seen in the right panel of Figure 6-10. Figure 8-32 shows the UFC (yellow regions), airgaps (red regions), the HCB blocks (grey regions) and GFM (dark grey regions).

Table 8-13: Overview of models with airgaps

MODEL NAME	ID	Airgap	Initial airgap width	Comment
NWMO_T3ag_M01_THM_V04	M01	No airgap	-	
NWMO_T3ag_M01A_THM_V04b	M01A	SIDE	1 cm	
NWMO_T3ag_M01B_THM_V04	M01B	TOP	1 cm	
NWMO_T3ag_M01C_THM_V04	M01C	UFC	0.75 cm	
NWMO_T3ag_M01C2_THM_V04	M01C2	UFC	1.5 cm	
NWMO_T3ag_M01_THM_V04M	M01CM	UFC	0.75 cm	Fine mesh
NWMO_T3ag_M01_THM_V04T	M01CT	UFC	0.75cm	Short timestep

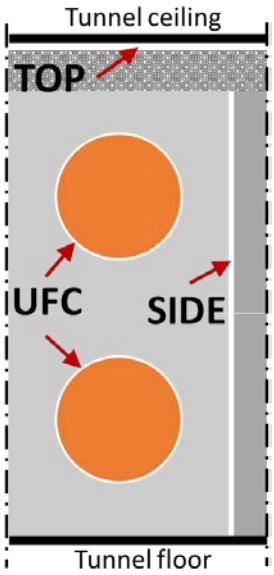

Figure 8-31: Schematic drawing of the model geometry with three different positions of airgaps

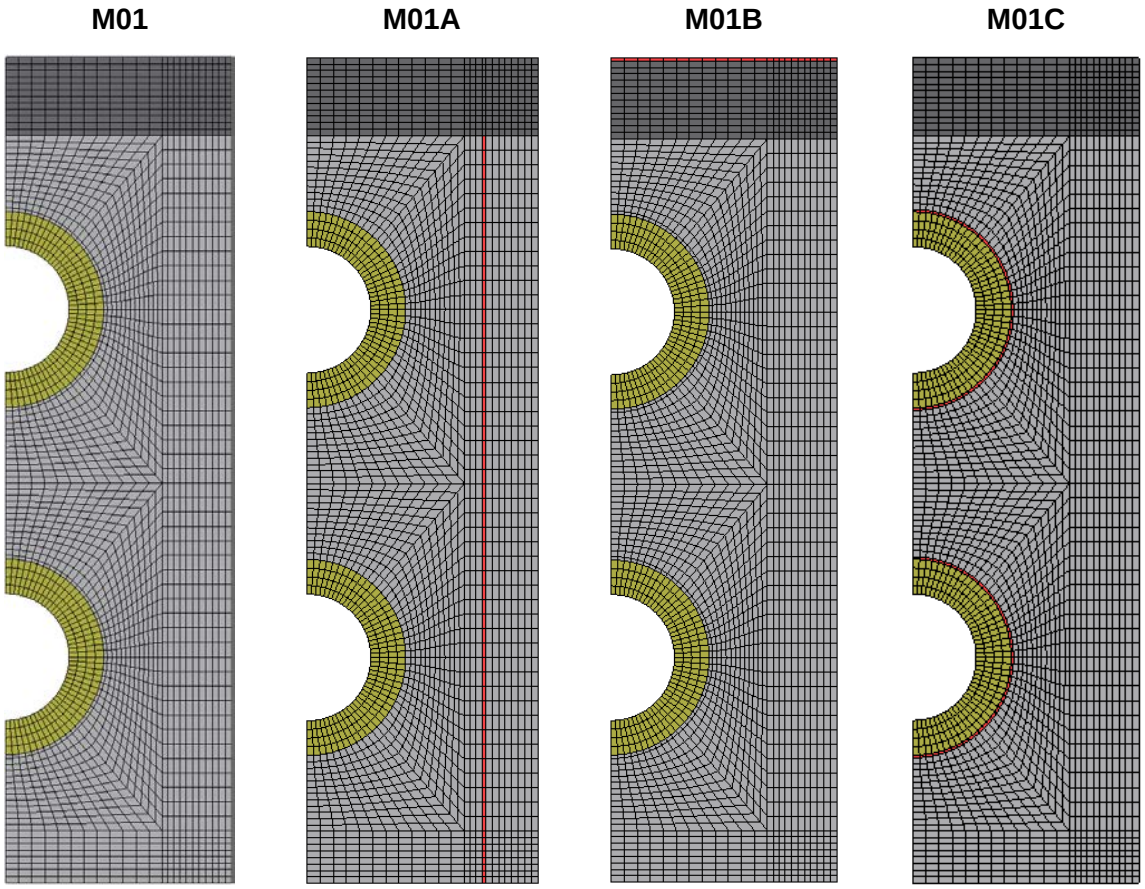

Figure 8-32: Geometries used in the models with airgaps

The material parameters of the bentonite are identical to those in the base case as defined in Section 8.1.1, except for the plastic parameters and the value of p_{ref}. These are given in Table 8-14. The material parameters of the airgap are given in Table 8-15. The airgap was modelled as a bi-linear elastic material with different values of the Young's modulus depending on if the airgap is open or closed. The value of Young's modulus was determined by comparing the volumetric strain in the airgap material with a user defined limiting volumetric strain. When choosing the material parameters of the airgap the Young's modulus for open airgap, E_O, was set as low as possible without causing convergence issues. When simulating airgaps SIDE and TOP, a value of 1 MPa was used, while a value of 5 MPa was used for airgap UFC. The Young's modulus for the closed airgap, E_C, was set to 100 MPa, which was found high enough to avoid further compression of the airgap material once the strain reached the defined limit, ε_v.

Table 8-14: Buffer plastic parameters used for modelling airgaps

			HCB	GFM
Initial dry density	ρ_{d0}	**kg/m^3**	1700	1410
Initial void ratio	**e**	**-**	0.618	0.950
Target void ratio	e_T	**-**	0.688	0.688
Plastic stress strain modulus	λ_0	**-**	0.159	0.200
Critical state line parameter	**M**	**-**	0.252	0.348
Tensile strength	p_s	**MPa**	1.80	0.458
Non-assoc. parameter	**α**	**-**	0.5	0.5
Pre-consol. stress	p_0^*	**MPa**	18.66	4.31
	p_c	**MPa**	1	1
Reference pressure	P_{ref}	**MPa**	1	0.1*/0.3

*The value 0.3 was used in model M01, the value of 0.1 in the other models

Table 8-15: THM parameters for the airgap material

			Airgap
Intrinsic permeability	k_0	**m^2**	10^{-20}
Relative permeability	k_r	**(-)**	1
Water retention curve	P_0	**MPa**	9
	λ_0	**(-)**	0.3
Thermal conductivity	**λ**	**W/mK**	1.2
Vapour diffusion tortuosity	**τ (-)**	**(-)**	0.01
Specific heat for solid	**c**	**(J/kgK)**	1000
Solid density	ρ_s	**kg/m^3**	2000
Young modulus open airgap	E_O	**MPa**	1/5*
Young modulus closed airgap	E_C	**MPa**	100
Limit volumetric strain	ε_v	**-**	99
Poisson ratio	**v**	**(-)**	0.3

*The value of 5 used in models of airgap C, the value of 1 for models of airgap A and B

8.2.1.1 Initial Conditions

The initial conditions are given in Table 8-16. The airgap has the same initial conditions as the adjacent buffer component, except the initial porosity, which was set to 0.99.

Table 8-16: Initial conditions used for the models with airgaps

Material	Temperature [°C]	Liquid pressure [MPa]	Porosity [-]	Stress (isotropic) [MPa]
HCB	11	-22.9	0.382	-0.11
GFM	11	-141.2	0.487	-0.11
AIRGAP	11	-22.9/-141.2*	0.99	-0.11
UFC	11	-22.9	0.001	-0.11

*The value -141.2 was used in the model M01B

8.2.1.2 Boundary Conditions

The boundary conditions are described briefly below:

- **Thermal BC:** Prescribed heat flux/m^2 on the inside of the UFC and prescribed temperature on all outer boundaries. Values were kept from the base case model of Task 3 (see 8.2.1.2).
- **Hydraulic BC:** Free access to water through the ceiling.
  Comment: No-flow conditions were prescribed on the floor. Water access through the floor in these models could not be included as prescribing it directly on the bentonite blocks led to severe convergence problems; the same problem was encountered in in Step 2 and solved in Task 1 by adding a concrete slab beneath the block and GFM. Inclusion of a concrete slab in the airgap models would however require simulating the friction between the concrete and buffer, or alternatively having a poor and numerically difficult representation of the behavior near the floor when simulating the closure of the airgap between the buffer box and the spacer block (SIDE airgap). As shown in Task 1, wetting through the floor has some effect on the final upward displacement of the UFC, but a very small effect on dry densities and swelling pressures in the final state that is the primary concern in these models.
- **Mechanical BC:** Roller conditions on all outer surfaces, except on the inner hollow surface of the UFC, where traction free conditions were prescribed.

8.2.2 Model Results and Discussion

As the models in this subtask differs significantly to the models constructed as part of Task 1 a new set of numerical verification and material model accuracy tests had to be carried out. These are described in Appendix D.

8.2.2.1 Dry Density Distribution

One of the important model results is the dry density distribution after swelling of the buffer (due to water uptake). In Figure 8-33 and Figure 8-34 the dry density at full saturation is shown from the models simulating the closure of airgaps SIDE and TOP (solid lines), compared with a model with no airgap (dashed lines). The model with airgap SIDE (between the buffer box and spacer block) was evaluated on horizontal lines at different heights (below the lower UFC, between the two UFCs and above the upper UFC). The model simulating the closure of airgap TOP (between the top surface of the GFM and the ceiling of the emplacement room) was

evaluated on vertical lines at different distances from the UFC center. The evaluated regions marked as coloured lines are shown in the right side of the figures.

First, it can be noted that the dry density values from the 2D model without airgaps (M01A) are similar to the values from in the 3D base case model. The results from the latter were evaluated on the vertical surface of the geometry intersecting the UFCs (as evaluated at the centre of the UFC, see Figure 8-4), indicating that the 2D geometry gave a good representation of the evolution in this region compared with larger 3D models. The only difference between the 2D and 3D models is that the 3D models show additional swelling in the lower parts due to water inflow through the floor, leading to a higher density in the GFM (green line) and a lower density in the lower part of the block (orange line in Figure 8-33).

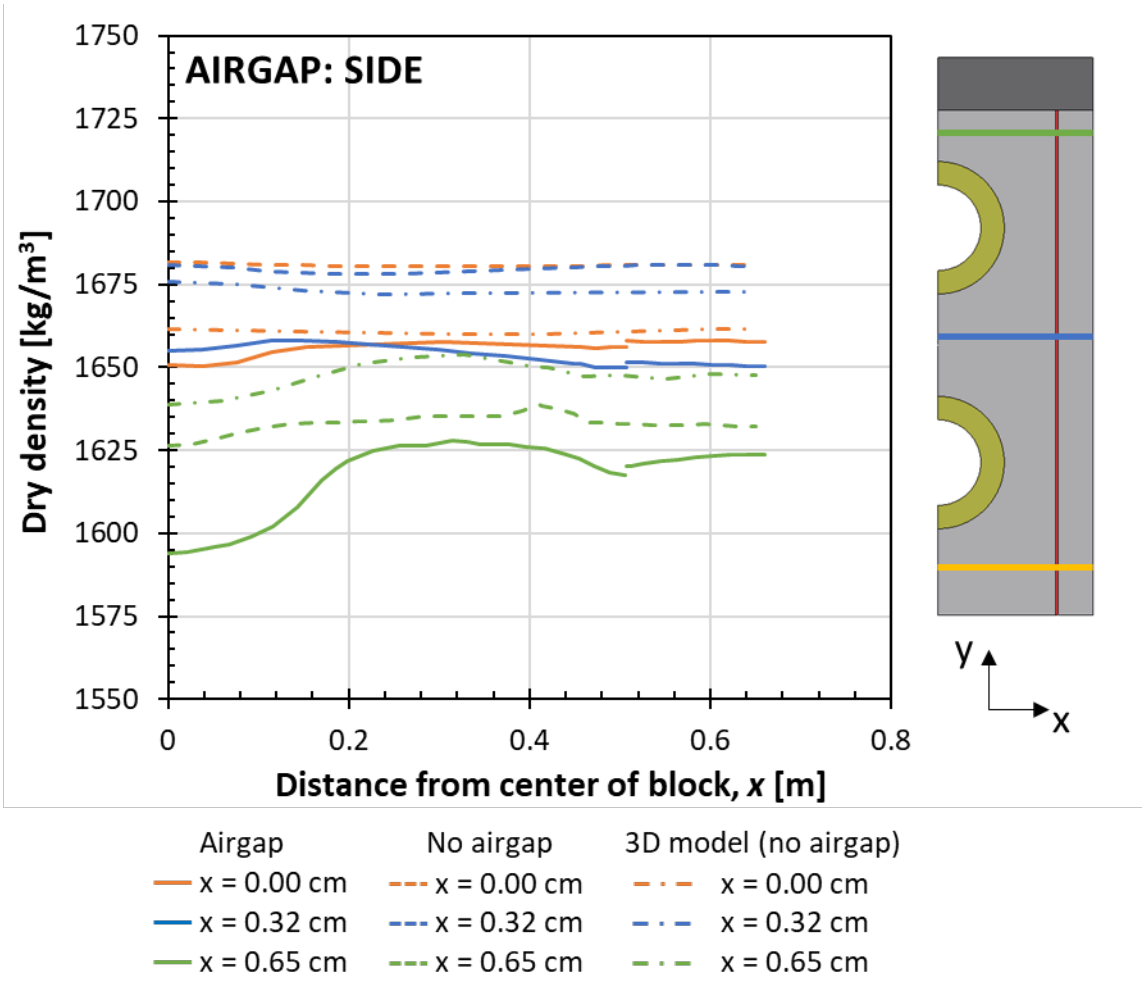

Figure 8-33: Dry density in the final state from the model simulating airgap SIDE

The inclusion of an airgap between the buffer box and the spacer block (Figure 8-33) leads to a decrease in the overall dry density. This is directly linked to the change in volume of the buffer between the initial and final state due to the presence of the airgap. The density profile near the airgap (at a distance from the block center of 0.5 m) shows that the bentonite fills up the empty

airgaps and homogenizes relatively well, although a slight jump in the dry density distribution is observed where the airgap was initially situated. The dry density profile evaluated above the upper UFC shows a significant decrease in dry density just above the UFC, which is not seen in the model without an airgap. It is unclear if this is a numerical artefact.

The inclusion of airgap TOP shows that the average density is slightly lower as compared to the model without an airgap (Figure 8-34). Again, this can be directly attributed to the presence of the airgap, which leads to a change in volume of the buffer between the initial and final state. The dry density profile near the airgap (i.e., at the top of the geometry) is essentially identical in the two models.

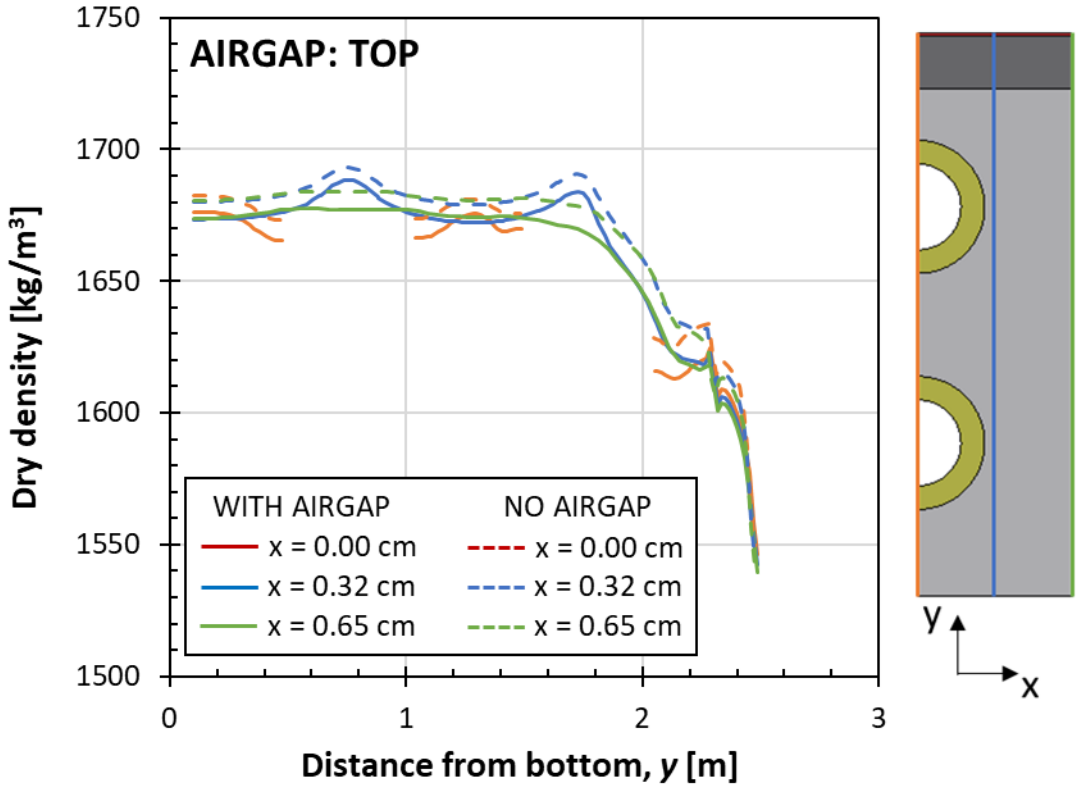

Figure 8-34: Dry density in the final state from the model simulating airgap TOP

Two models analysing the airgap around the UFC were simulated, with the only difference between the two being the initial airgap width. The values 0.75 cm and 1.5 cm were used to analyse the importance of the eccentricity of the UFC, i.e., the fact that the airgap will not be uniform since the UFC rests on the HCB block.

The dry density distributions from the models with airgaps near the lower and upper UFCs are shown as solid lines in Figure 8-35 (initial airgap width 0.75 cm) and Figure 8-36 (initial airgap width 1.5 cm) together with the distributions from the model without airgaps (dashed lines in the same figures). The dry density was evaluated in three radial directions from the surface of the UFC, as shown in the illustration of the geometry included in Figure 8-35 and Figure 8-36.

From the graphs it is clear that the main effect of the airgaps is to decrease the “average” dry density in the entire buffer box rather than a localized decrease in dry density near the UFC. In the horizontal scan lines (blue and yellow solid lines) the decrease in dry density is, however, more significant than in the other analysed regions.

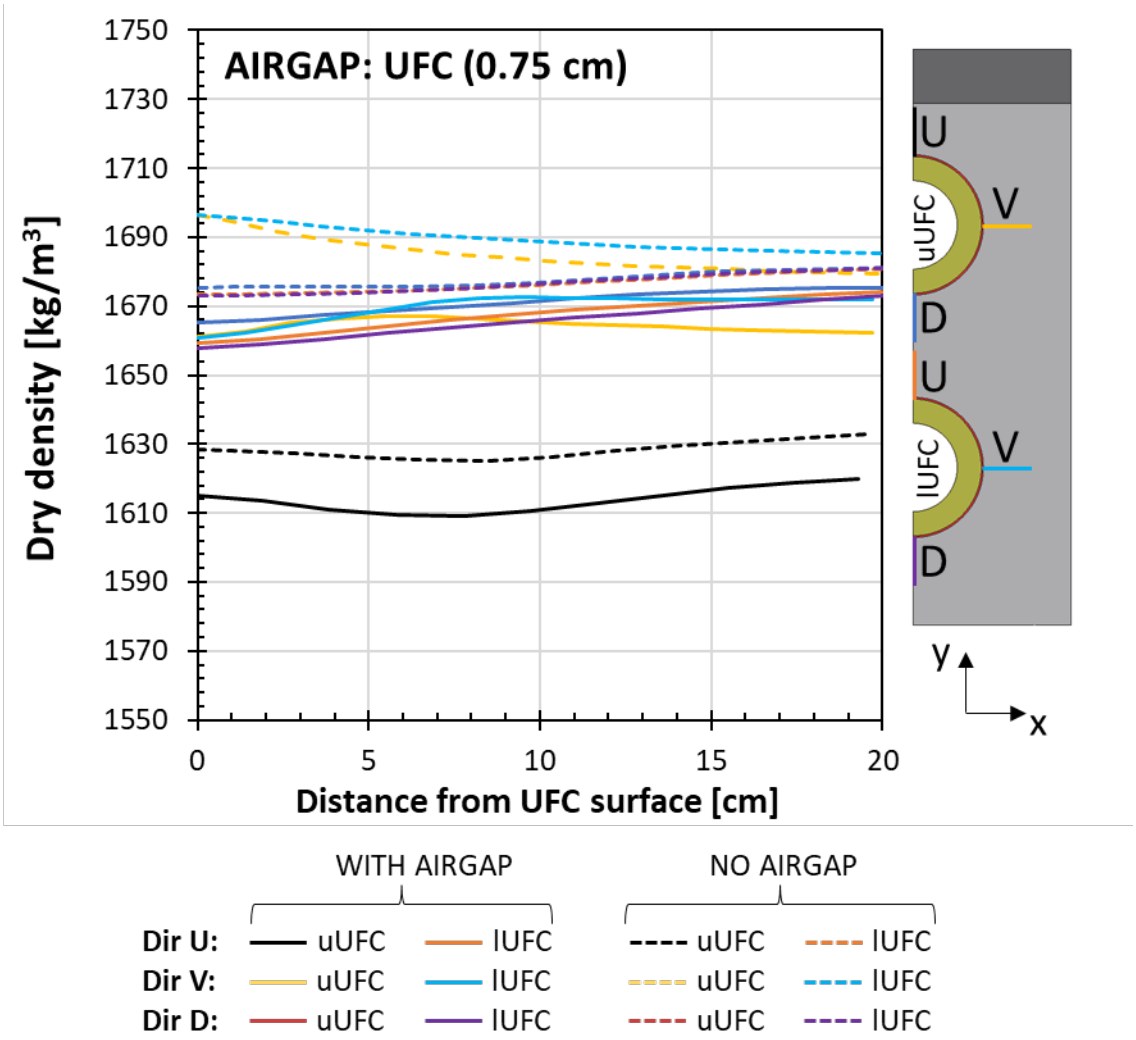

Figure 8-35: Dry density from model with airgap around the UFC (initial width 0.75 cm)

The results shown in Figure 8-35 and Figure 8-36 indicate that a larger initial airgap leads to a larger decrease in dry density of the bentonite buffer at full saturation. The density above the upper UFC is close to or below 1600 kg/m^3 in the models. This can be an issue because the weighted (volume averaged) buffer dry density should be no less than 1600 kg/m^3 as part of the current buffer design requirements.

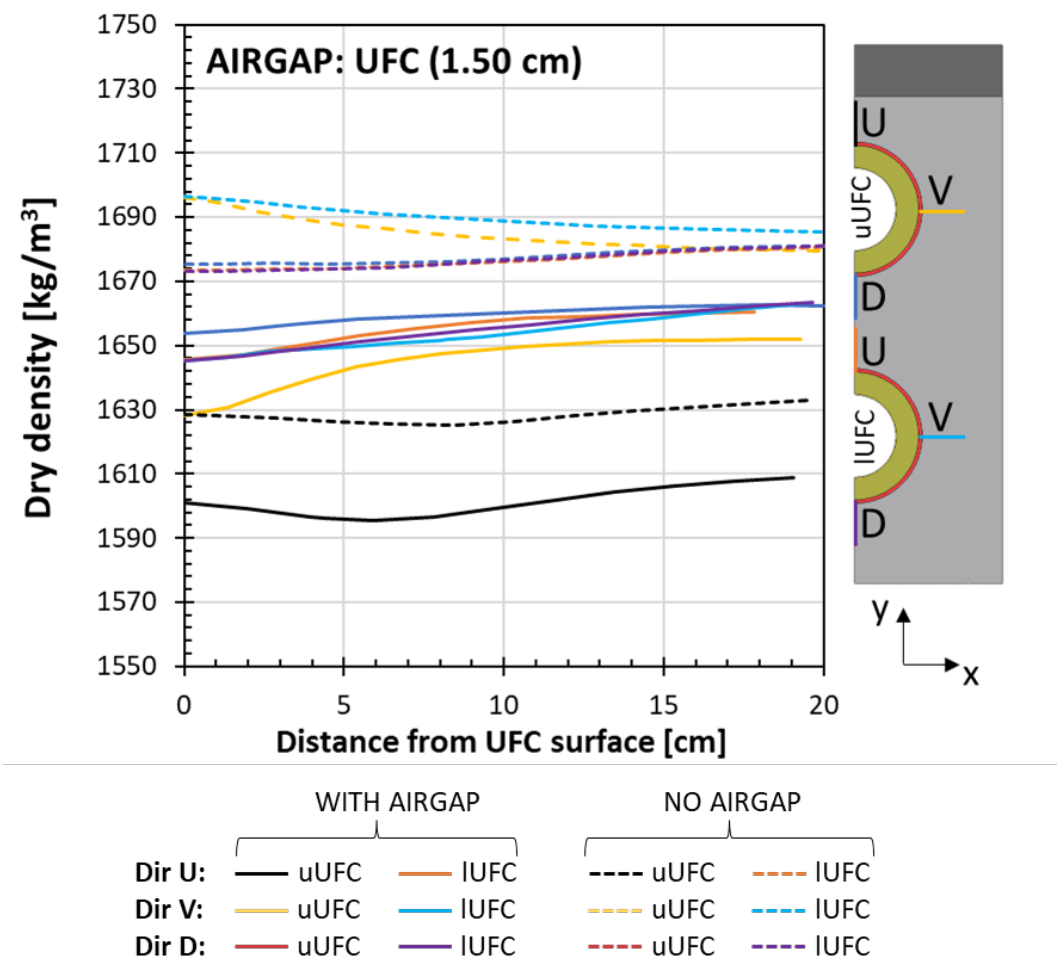

Figure 8-36: Dry density from model with airgap around the UFC (initial width 1.5 cm)

8.2.2.2 Swelling Pressure Near the UFC

In the 3D models (Section 8.1.3.2), the maximum swelling pressure (approximately 13 MPa) was seen on the side of the UFC at mid-length. The 2D geometry represents a plane cut through the center of the UFC, and hence the region where the maximum swelling pressure occurred in the 3D models is included in the 2D geometry.

To assess the effect of the airgap on the swelling pressure near the UFC at full saturation, the net mean stress in the models was analyzed in the same region used to evaluate the dry density. The net mean stress in the models with a thin airgap around the UFC (0.75 cm) is shown in Figure 8-37 and the swelling pressure in the model with a thick airgap (1.5 cm) is shown in Figure 8-38. In the figures the solid lines identify data from the models with airgaps and the dashed lines data from the model without airgaps. The results from the model without airgaps correspond well with the net mean stress seen in the 3D models (see Figure 8-17). For example, the net mean stress on the side of the UFC (yellow lines in in Figure 8-37) was approximately 13 MPa in the 3D models, and 12.8 MPa in the 2D model with no airgap (dashed yellow line in Figure 8-37).

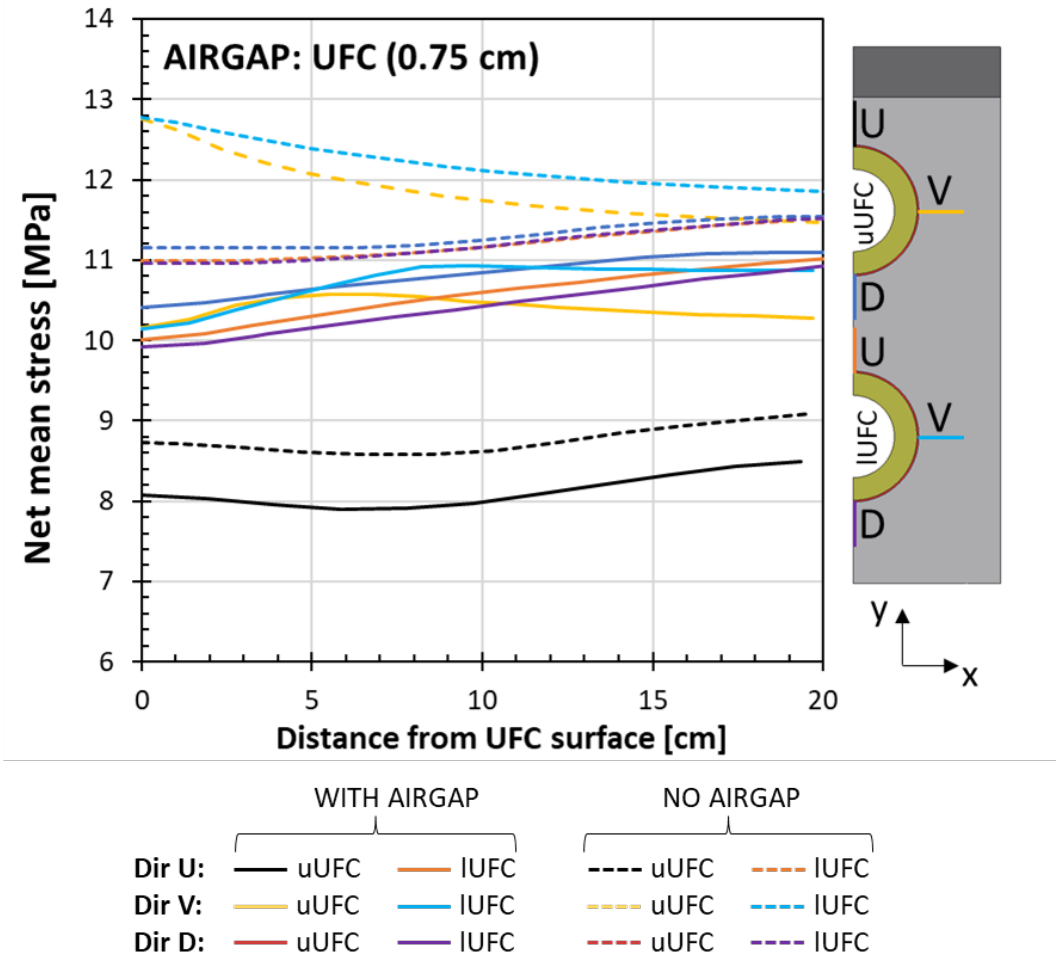

Figure 8-37: Net mean stress in the model with a thin airgap (0.75cm) around the UFC

The net mean stress in the models with an airgap around the UFC shows a clear reduction compared to the model without an airgap, particularly in the horizontal scan lines (yellow and blue lines in Figure 8-37 and Figure 8-38). The net mean stress on the side of the UFC shows a reduction from a value of 12.8 MPa in the model without airgaps to 10.2/9.2 MPa for the models with a thin/thick initial airgap between the buffer box and UFC, e.g., about 20% reduction for the thin airgap model and almost 30% for the thick airgap model. This is a discernable reduction in stress, which indicates that the models presented in Section 8.1 overestimate the maximum load on the UFCs by as much as 30%.

It is worth pointing out that in the 2D models presented here the reduction in net mean stress is much larger in the two horizontal scanlines than in the four vertical scanlines. In the model without an airgap (dashed lines in Figure 8-37 and Figure 8-38) the maximum value of net mean stress is found in the two horizontal scanlines (blue and yellow dashed lines in), but in the model with airgaps the maximum net mean stress can be found in the vertical scanline below the upper UFC (dark blue solid line in Figure 8-37 and Figure 8-38).

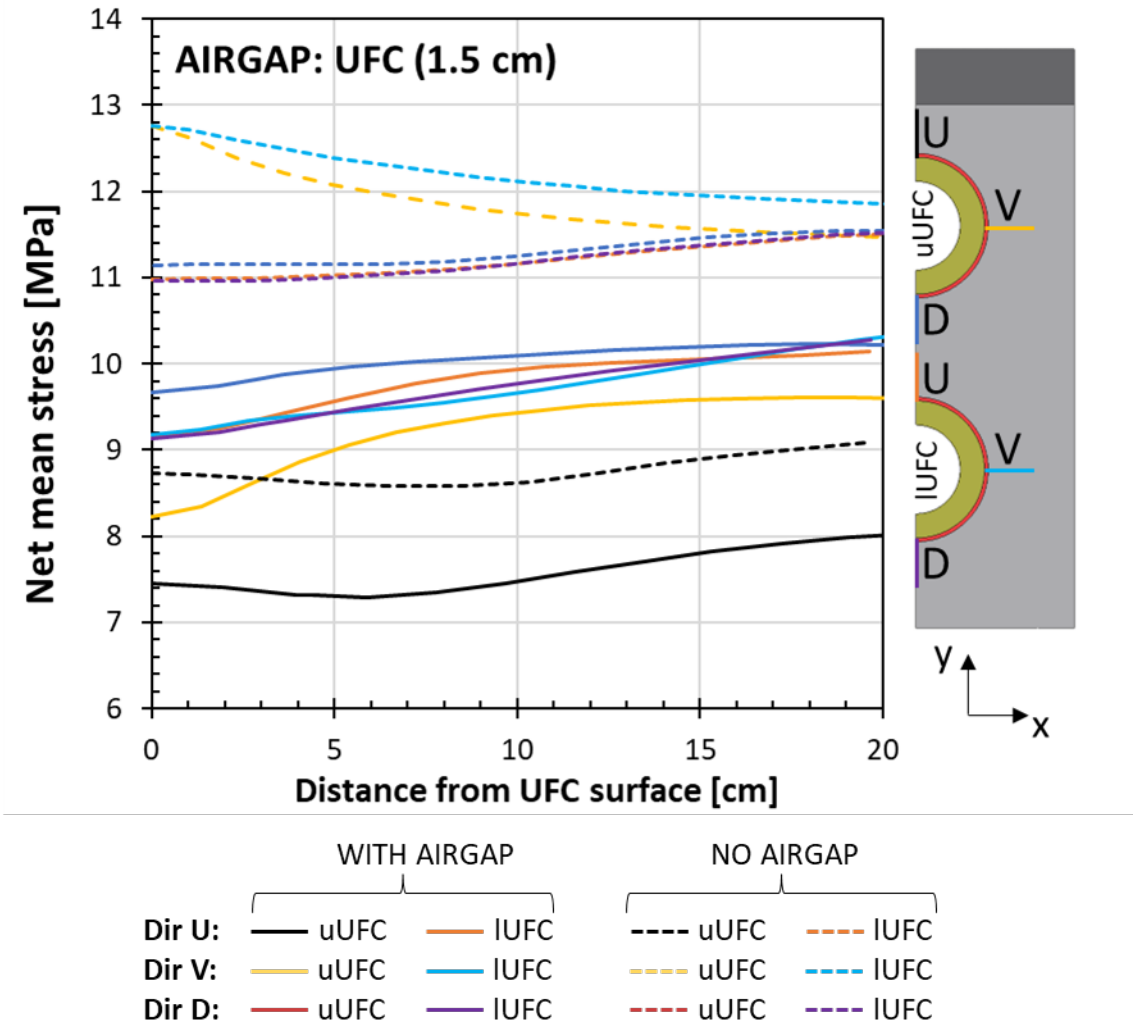

Figure 8-38: Net mean stress in the model with a thick airgap (1.5cm) around the UFC

8.3 Conclusions

The sensitivity analysis was conducted to assess the evolution from different initial buffer densities and various cross-sections of the emplacement room. The second part of the modelling in Task 3 aimed at evaluating the effect from including airgaps. Conclusions drawn from the assessment are provided in this section. The findings from the two sets of models are given in separate sections below.

8.3.1 Conclusions for Sensitivity Analysis

A sensitivity study was performed by varying the initial dry densities of the buffer components and GFM thickness (placement room dimensions). The altered initial conditions led to updating several material parameters for the different realizations. The simulations were analyzed in terms of dry density, net mean stress, UFC displacements, and normal stress acting on the UFCs. Analytical models were developed and utilized to evaluate the outcome of the FE-models. Buffer design requirements were also tested on the FE-solutions. Below follows a short recapitulation of the main findings.

One of the current buffer design requirements states that the weighted (volume averaged) buffer dry density should be no less than 1600 kg/m^3. The two models with high initial dry densities (models 3 and 8) clearly met the criteria, the two models with low initial dry densities (models 2 and 7) did not meet the criteria. The rest of the models met the criteria, but only with a small margin. Due to the uncertainties in how well the models represents reality, one should therefore be cautious when evaluating these.

Another of the buffer design requirements states that the swelling pressure upon saturation should be $\geq$ 0.1 MPa in all parts of the buffer. All eight models met this requirement by a significant margin. The displacement of the UFCs could in theory challenge the buffer design requirement of no less then 0.3 m of bentonite buffer between the UFC and the geosphere. The results, however, showed that the requirement was satisfied by a large margin.

The normal stress acting on the UFC could also be of interest for evaluating the potential for UFC failure. The evaluated normal stresses in the FE-models had a maximum value of about 17 MPa horizontally and a minimum value of about 4 MPa vertically.

Analytical approaches were found applicable both for estimating the dry density field at the hemi-head and for obtaining quick and reasonable estimates of normal stresses acting on the UFC.

8.3.2 Conclusions for Models with Airgaps

Models of several different airgaps after installation were presented. The models were simplified compared to the full 3D models presented in Section 2 in that only a 2D cross-section at mid-length of the UFC was analyzed. This was necessary to include airgaps in the models while keeping the numerical efficiency at a reasonable level. The model results show that the inclusion of airgaps leads to a general reduction in dry density as compared to a model without airgaps. This is easily understood as the airgaps were included as an extra empty volume in the geometries, giving the bentonite more room to swell. The increase in volume leads to lower final dry density.

Including airgaps near the UFC led to a significant reduction in the swelling pressure of the clay near the UFCs in the analyzed region (i.e., at the mid length of the UFC). The maximum swelling pressure was reduced from a value of 12.8 MPa in the model without airgaps to a value of 10.2 MPa in the model with an initial airgap around the UFC with thickness 0.75 cm.

9. TASK 4: SEDIMENTARY HOST ROCK & DRYING BEFORE INSTALLATION

The modelling carried out in Task 4 consisted of two separate modelling exercises. The first part was to analyze the evolution in the NWMO emplacement room situated in sedimentary rock in Southern Ontario, Canada, (Section 9.1) and the second considered drying before installation (Section 9.2).

9.1 Sedimentary Host Rock in Southern Ontario, Canada

The purpose of this task was to analyze the behavior of the bentonite buffer components included in the Canadian repository design for the case where the repository is located in a sedimentary rock geosphere in Southern Ontario.

The main focus of the task was on understanding the HM processes in the repository. For example, how water uptake of the buffer would generate swelling, homogenize the density of the buffer and produce stress. The hydraulic process was, however, dependent on the thermal process, due to thermally driven vapour diffusion and thus fully coupled THM models were simulated.

9.1.1 Sedimentary vs Crystalline Host Rock

A sedimentary host rock has different thermal and hydraulic properties from a crystalline host rock. The groundwater at the sedimentary host rock site in consideration has significantly higher levels of salinity than the groundwater at the crystalline host rock site. Saline groundwater affect hydraulic and mechanical properties of bentonite. This section contains an overview of differences between the sedimentary and crystalline case and how the simulations were set up to incorporate these.

9.1.1.1 Thermal and Hydraulic Properties of the Host Rock

The difference in thermal properties between the two host rocks will change the temperature evolution in the repository. The average value of the thermal conductivity in the Cobourg sedimentary rock is about 2.27 W/m°C (Guo, 2018), which is lower than in crystalline rock (3.0 W/m°C, Guo 2017) leading to a slower transport of heat from the repository. Thus, to meet the temperature criteria (the temperature at the UFC surface should be < 100 °C (Birch and Mielcarek 2017) the spacing between the UFC needs to be increased. This will be accomplished by using 0.7 m thick HCB spacer blocks in the updated model geometry.

As in the previous crystalline host rock modeling, the host rock was not included in the geometry. Hence, the thermal conductivity value of the host rock was not explicitly specified in the models. Instead, the host rock's influence on the buffer was included using boundary conditions (i.e., water inflow to the buffer, thermal energy outflow from the buffer and the mechanical confinement of the buffer).

For the thermal problem, this was done by prescribing a varying temperature boundary condition on the rock wall-bentonite interface. The varying temperature was, for these models taken from a thermal model described in Guo (2018). The initial temperature was 17 °C.

The hydraulic properties of the host rock determine how water enters the buffer. Differences in the hydraulic properties of the host rock may change the saturation evolution of the EBS, both in terms of the rate of water inflow and the mode of wetting (from fractures or matrix). In this modelling, however, the host rock was only represented indirectly by using two different hydraulic boundary conditions to simulate fast and slow water uptake.

9.1.1.2 Effect of Groundwater Salinity on Bentonite Properties

The chemical composition of the groundwater in the host rock has a very strong effect on the bentonite properties. Much of the characteristics of bentonite clay, such as swelling/shrinking and magnitude of swelling pressure, can be attributed to the interplay between the negatively charged montmorillonite particles, the counterions in the interlayer between the particles, and their binding to the dipolar water molecules (hydration) (Karnland 1997 and Birgersson et al. 2017). The thermodynamics describing this is outlined in Appendix G.

When bentonite is contacted with saline groundwater, the salt (ions) can enter and interact with it. This can significantly change the characteristic properties of the bentonite. For the present case, considering the dry densities and level of salinity, it is expected that the swelling pressure is lowered, and the hydraulic conductivity increases, compared to the non-saline case (see, for example, Dixon 2018). This was considered when developing the models for the sedimentary rock, new representations for the swelling pressure and hydraulic conductivity as function of dry density were used.

The retention properties of bentonite also change with varying salinity (see, for example, Dixon 2019). As the surrounding host rock was not simulated in the models, any change in the retention properties of the HCB and GFM would mostly affect how water is distributed between these two materials during the saturation phase. However, very little data on the retention capacity of the buffer components was available and it was considered that any changes would play a small role on the THM evolution. Therefore, any change in retention properties with salinity was not included in these models. Retention curves derived for the models in the crystalline geosphere (see Section 3.3.4) were used instead.

9.1.2 Model Description

9.1.2.1 Geometry and Components

The geometry, dimensions, and components of the model are shown in Figure 9-1.

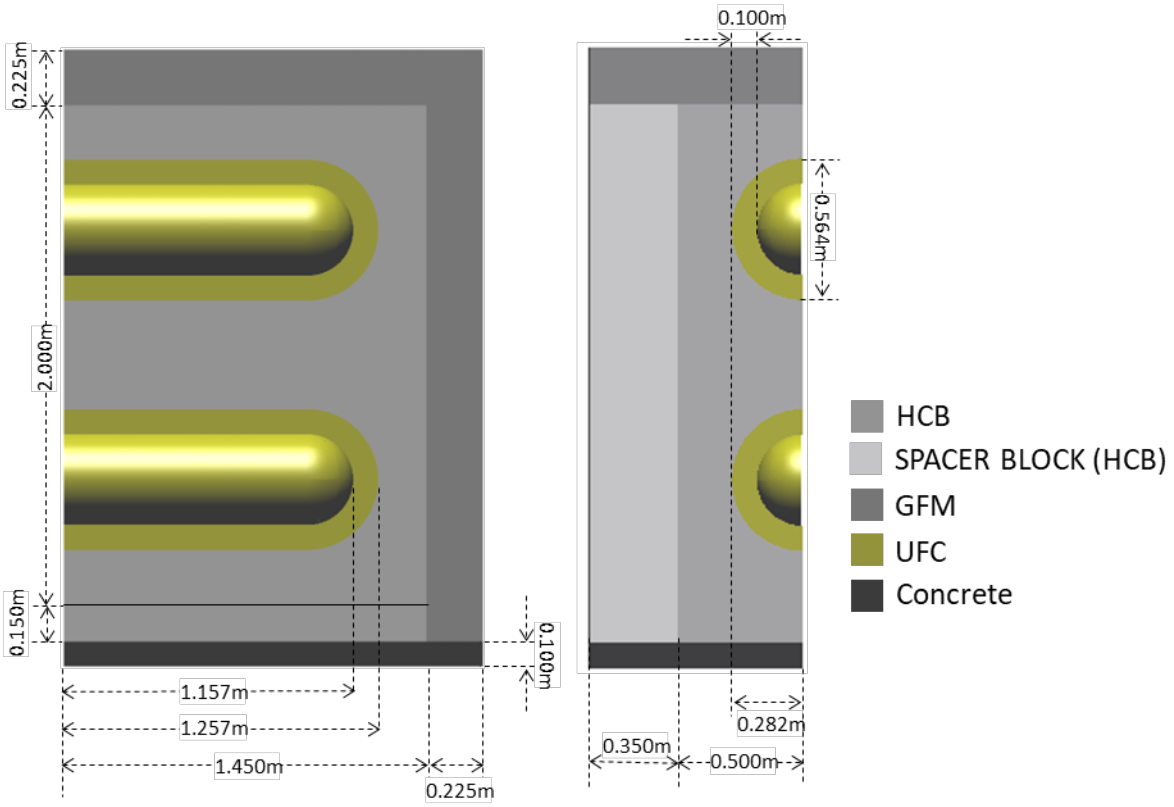

Figure 9-1: Overview of the geometry with components and dimensions indicated

Similar to the previous work for the crystalline rock, the UFC was represented as a single component/material and as being hollow to reduce the size of the numerical representation and simplify the meshing. The properties of the “shell” were assigned for the correct weight and rigidity of the UFC. Below, the concrete slab is identified by the letter C.
The geometry was discretized using 15,918 hexahedra elements resulting in 18,310 nodes. The elements were linear quadrilateral prism elements which had 8 points and used selective numerical integration.

9.1.2.2 Initial Conditions

Table 9-1 and Table 9-2 show the initial conditions of the components. The solid particle density for all clay components was 2750 kg/m^3.

Table 9-1: Initial conditions

Material	Temperature [°C]	Initial water content [%]	Liquid pressure [MPa]	Porosity [-]	Total stress (isotropic) [MPa]
HCB	16.9	20	-22.9	0.382	-0.11
GFM	16.9	3	-141.2	0.487	-0.11
UFC	16.9	-[c]	-22.9	0.01	-0.11
C	16.9	-[c]	-22.9/-141.2[a]	0.01[b]	-0.11

[a] Set equal to the pressure in the material (HCB or GFM) above the concrete (C).
[b] This value was chosen for numerical convenience and is a bit low for concrete, however it does not affect the modelling results.
[c] This value is of no importance to the simulations.

Table 9-2: Dry density, void ratio and porosity for clay components

Material	Dry density [kg/m^3]	Void ratio [-]	Porosity [-]
HCB, 1.7	1700	0.618	0.382
GFM, 1.41	1410	0.950	0.487

9.1.2.3 Boundary Conditions

Besides what is described below, the simulations were “pre-initialized” using a mechanical equilibration procedure where gravity was ramped up to its full strength. This pre-initialization procedure was used to make the task easier for the numerical solver.

There are two thermal boundary conditions present in the models:

- The heat load from the used fuel.
- The heat exchange with the surroundings.

The heat load from the used fuel was incorporated by prescribing a heat flux per unit area on the inner surface of the UFC. The heat flux was taken from Guo (2017). In the left part of Figure 9-2 the positions where the thermal boundary conditions are applied is shown. The heat flux per unit area prescribed on the inner hollow surface of the UFCs is shown in the graph to the upper right. Red lines indicate data used to formulate a boundary condition file containing the data indicated by the black symbols.

The heat exchange with the surroundings was incorporated by prescribing a temperature evolution on the outer boundary of the GFM. The temperature evolution was obtained from a thermal simulation of a repository in a sedimentary host rock (Guo 2018). The temperature data from Guo (2018) that was prescribed on the outer surfaces of the GFM and on the bottom surface of the concrete slab is shown in the lower right graph in Figure 9-2. This temperature was prescribed on all the red colored surfaces in the geometry as shown in the left image in Figure 9-2.

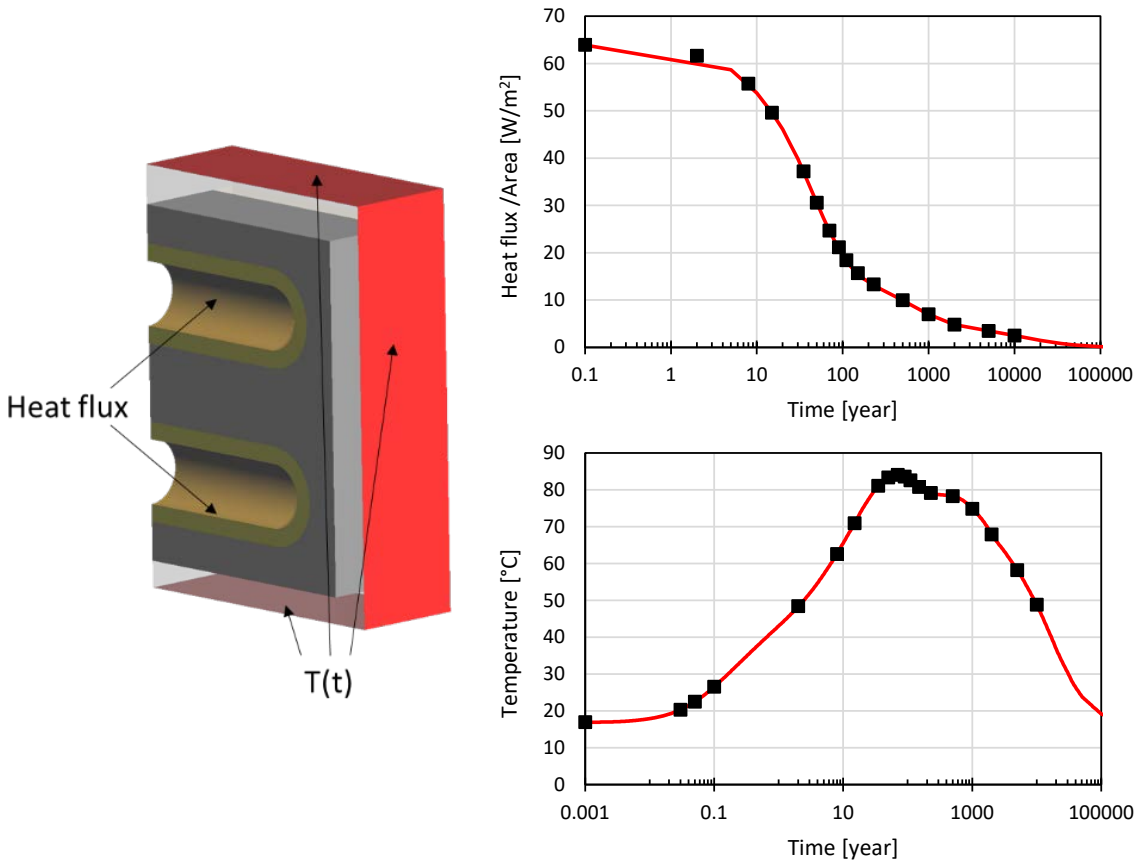

Figure 9-2: Thermal boundary condition

Two types of hydraulic boundary conditions were used in the simulations,

- No-flow conditions were used on all symmetry planes
- Inflow conditions were generally prescribed on the outer surfaces of the geometry

One exception was at a horizontal line belonging to the concrete slab lower boundary, just below the vertical HCB/GFM interface, where no-flow conditions were prescribed. This was done to facilitate the numerical solution.

Both types of hydraulic boundary conditions were formulated in terms of a specified liquid flux:

$$j_{\mathrm{l}} = \gamma\left(p_{\mathrm{l}}^{0} - p_{\mathrm{l}}\right), \tag{9-1}$$

where p_{l}^{0} denotes a prescribed liquid pore pressure, p_l the liquid pressure in the point, and γ a "flux transfer coefficient" which sets the "strength" of the boundary condition.

To prescribe a liquid pore pressure p_{l}^{0} at a boundary, a high value, $\gamma = 10^{5}$ [kg/(MPa·s·m²)], was used, which provided enough water as to assure that $p_{\mathrm{l}} = p_{\mathrm{l}}^{0}$. If simulating conditions with limited access to water, a lower value, $\gamma = 2 \cdot 10^{-10}$ [kg/(MPa·s·m²)], was used, and for no-flow conditions $\gamma = 0$ [kg/(MPa·s·m²)]. As the repository is located deep below the ground surface it can be expected that the value of p_{l}^{0} should be much greater than atmospheric pressure.

However, to reduce convergence issues in the simulations, a value of 0.1 MPa (e.g., the atmospheric pressure) was prescribed. If a higher value had been used, the final water uptake phase would be quicker. To facilitate the numerical solution the boundary pressures were ramped from the initial values to the desired value during 3.65 days.

Two types of mechanical boundary conditions were used in the simulations.

- Roller conditions were prescribed on all outer and symmetry boundaries, i.e., no displacement was allowed in the surface's normal direction and the tractions (stress components) was prescribed to zero in the tangential direction.
- Traction-free boundary conditions were prescribed on the inner surface of the hollow waste container, i.e., stress components in the normal and tangential orientation to the inner surface were zero. This boundary condition allows for displacement of the UFC when the clay swells or shrinks.

9.1.2.4 Material Representations

Parameter values used in the constitutive relations are given in this section. It should be mentioned that all materials except the UFC-material had a full two-way hydromechanical coupling. In the material used for the UFC, volumetric strain effects on hydraulics were not considered.

9.1.2.4.1 Hydraulic and Thermal Material Representations

The retention properties were given by van Genuchten relations described in Section 3.3.4. Parameter values are given in Table 9-3. The advective mass flux, was given by Darcy's law (see Section 3.3.3). The intrinsic and relative permeabilities are given in Table 9-4. The diffusive mass flux was described by Fick's law (see Section 3.3.2). The tortuosity was assumed to be constant, i.e., $\tau = \tau_0$, and the values in Table 9-5 were used. The conductive heat flux was given by Fourier's law (see Section 3.3.2). In Table 9-6 the constants and functions $\tilde{\lambda}(S_l)$, used for representing the HCB and GFM, are shown.

To improve the numerical performance, the thermal expansion of the liquid, α, present in Equation (3-31), was suppressed by using a low value of $\alpha = 10^{-24}$ °C^{-1}.

Table 9-3: Retention parameters of porous media

Constituent	P_0 [MPa]	λ [-]	P_d [MPa]	λ_d [-]
HCB	65.385	0.18	400	1.2
GFM	2.979	0.21	400	3.25
UFC	10	0.3	-	-
C	9	0.3	-	-

Table 9-4: Intrinsic and relative permeabilities

Constituent	k_{in} [m²]	k_{rl} [-]
HCB	$3.746 \cdot 10^{-19}\exp(35.574(\phi - 0.418))$	${S_l}^3$
GFM	$3.746 \cdot 10^{-19}\exp(35.574(\phi - 0.418))$	${S_l}^3$
UFC	10^{-30}	1
C	10^{-20}	1

Table 9-5: Tortuosity

Component	τ_0 [-]
HCB	1
GFM	1
UFC	0.01
C	0.01

Table 9-6: Thermal conductivity

Component	λ [W/(m·K)]
HCB	$\tilde{\lambda}(S_l) = 0.5\cos^2\left(\frac{\pi S_l}{2}\right) + 1.3\sin^2\left(\frac{\pi S_l}{2}\right)$
GFM	$\tilde{\lambda}(S_l) = 1.3^{S_l} \cdot 0.35^{(1-S_l)}$
UFC	300
C	1.2

9.1.2.4.2 Mechanical Material Representations

Table 9-7 shows an overview of the mechanical material models used for the solid phase in all materials. In Table 9-8 and Table 9-9, the different mechanical material models are described, and the parameter values are given, respectively.

Table 9-7: Overview of the solid phase mechanical material models

Constituent	Mechanical material model	Comment
HCB GFM	Modified BBM	The parameter set in Task 3, where a crystalline host rock was considered, was used with the following modifications: • A new swelling pressure curve was calibrated using experimental data (Dixon 2019). • Plastic parameters were determined using the new swelling pressure curve. The dry density dependent von Mises stress at failure was (as indicated by experiments) identical to that used in Task 3. • For the hydraulic strain increment, p_{ref}, was lowered to achieve enough swelling/pressure build-up.
UFC C	Linear elastic	Same parameter set as in Task 3.

Table 9-8: Linear elastic model and parameter values

		Parameter	UFC	C
Total strain increment	$d\boldsymbol{\varepsilon} = d\boldsymbol{\varepsilon}^e$			
Elastic strain increment:	$d\boldsymbol{\varepsilon}^e = -\frac{1}{3}d\varepsilon_v^e\mathbf{1} + d\boldsymbol{e}^e$	*E* [GPa]	200	200
	$d\varepsilon_v^e = \frac{dp\prime}{K}$, $K = \frac{E}{3(1-2\upsilon)}$	*v*	0.3	0.3
	$d\boldsymbol{e}^e = \frac{d\boldsymbol{s}}{2G}$, $2G = \frac{E}{1+\upsilon}$			

Table 9-9: Modified BBM model and parameter values

		Parameter	HCB	GFM
Total strain increment	$d\boldsymbol{\varepsilon} = d\boldsymbol{\varepsilon}^e + d\boldsymbol{\varepsilon}^p + d\boldsymbol{\varepsilon}^h$			
Void ratio	$e_0 = \phi_0/(1-\phi_0)$ [(a)]	e_0	0.618	0.95
	$d\boldsymbol{\varepsilon}^e = -\frac{1}{3}d\varepsilon_v^e\mathbf{1} + d\boldsymbol{e}^e$	κ_{i0}	0.12	0.12
Elastic strain increment:	$d\varepsilon_v^e = \frac{dp'}{K}$, $K = \max\left\{\frac{(1+e)p'}{\tilde{\kappa}_i(s)}, K_{min}\right\}$	α_i	-0.043	-0.0062
	$\tilde{\kappa}_i(s) = \kappa_i(1+\alpha_i s)$	v	0.2	0.2
	$d\boldsymbol{e}^e = \frac{d\boldsymbol{s}}{2G}$, $2G = \frac{3(1-2v)}{(1+v)}K$	K_{min} [MPa]	20	6
Plastic strain increment:	$d\boldsymbol{\varepsilon}^p = d\Lambda\frac{\partial g}{\partial \boldsymbol{\sigma}}$	α	0.5	0.5
	$f = q^2 - M^2(p'+p_s)(p_0-p')$	p_0^* [MPa]	4.138	0.9807
	$g = \alpha q^2 - M^2(p'+p_s)(p_0-p')$	λ_0	0.158	0.178
	$p_0 = p_0^*$	p_s [MPa]	0.7592	0.2174
	$dp_0^* = \frac{1+e}{\lambda_0-\kappa_{i0}}p_0^* d\varepsilon_v^p$	M	1.056	1.373
Hydraulic strain increment:	$d\boldsymbol{\varepsilon}^h = -\frac{1}{3}d\varepsilon_v^h\mathbf{1}$	κ_{s0}	0.3	0.3
	$d\varepsilon_v^h = \frac{\kappa_s}{(1+e)(s+p_{atm})}ds$	p_{ref} [MPa]	0.1	0.1
	$\kappa_s = \kappa_{s0}f^m(p',e)\exp(\alpha_{ss}(p_g - p_l))$	α_{ss}	-0.03	0
	[(b)] $f^m(p',e) =$	c_0	-2.44	-2.44
	$\begin{cases} 1 & \text{if } p' < p_{ref} \\ 10^{-20} & \text{if } p' > p_{swell}(e) \\ 1 - \frac{\ln p' - \ln p_{ref}}{\ln(\tilde{p}_{swell}(e)) - \ln p_{ref}} & \text{otherwise} \end{cases}$	c_1	$4.12\cdot10^{-3}$	$4.12\cdot10^{-3}$
		c_2	$-3.94\cdot10^{-7}$	$-3.94\cdot10^{-7}$
	$\log(\tilde{p}_{swell}(e)) = -3 + c_0 + c_1\frac{\rho_s}{1+e} + c_2\left(\frac{\rho_s}{1+e}\right)^2$			

[(a)]The initial void ratio is used as an input parameter to the modified BBM model. It should be set as to match the initial condition porosity.
[(b)]The function $f^m(p',e)$ is a feature developed at Clay Technology in which $\tilde{p}_{swell}(e)$ is obtained in MPa.

9.1.2.4.3 Material Parameter Differences

In Table 9-10 the material parameter values are given for the crystalline and sedimentary representations where they differ. Changes were made with regard to the intrinsic permeability, the hydraulic strain, and the plastic strain of the HBC and GFM parameters. The changes of the relations concerning the strains come from adopting the new swelling pressure curve.

The values of two elastic parameters, c_0 and p_{ref}, and all plastic parameters in BBM were changed for both HCB and GFM as compared to the previous modelling. c_0 is present in the swelling pressure function and was changed to match the swelling pressure data. p_{ref}, present in the hydraulic strain component, was decreased to allow for sufficient swelling when using the new swelling pressure curve. The calibration procedure of the plastic parameters is given in Appendix H.

Table 9-10: Values for material model parameters where there is a difference in the crystalline and sedimentary representation.

	Crystalline host rock	Sedimentary host rock
Permeability, HCB & GFM	$\kappa_{in} = 0.104 \cdot 10^{-19} e^{20.726(\phi - 0.418)}$	$\kappa_{in} = 3.746 \cdot 10^{-19} e^{35.574(\phi - 0.418)}$
Hydraulic strain, HCB	$c_0 = -1.74$ $p_{ref} = 1$ MPa	$c_0 = -2.44$ $p_{ref} = 0.1$ MPa
Hydraulic strain, GFM	$c_0 = -1.74$ $p_{ref} = 0.3$ MPa $p_0{}^* = 18.66$ MPa	$c_0 = -2.44$ $p_{ref} = 0.1$ MPa $p_0{}^* = 4.138$ MPa
Plastic strain, HCB	$\lambda_0 = 0.159$ $p_s = 1.80$ MPa $M = 0.252$ $p_0{}^* = 4.31$ MPa	$\lambda_0 = 0.158$ $p_s = 0.7592$ MPa $M = 1.056$ $p_0{}^* = 0.9807$ MPa
Plastic strain, GFM	$\lambda_0 = 0.178$ $p_s = 0.458$ MPa $M = 0.348$	$\lambda_0 = 0.178$ $p_s = 0.2174$ MPa $M = 1.373$

9.1.3 Results and Discussion

In this section different parts of the solutions are studied and discussed. The primary focus was on the hydro-mechanical evolution of the buffer during hydration. The following results were analyzed:

- Temperature evolution in selected points
- Degree of saturation evolution in selected points
- Mechanical evolution in selected points (p' – e)
- Dry density at full saturation
- Stress field at full saturation
- UFC displacement
- Normal stress acting on the UFC

Results from two models are presented here; one model in which the buffer had free access to water, and another where the water inflow was restricted (see Table 9-11). Solutions from these models are compared to results obtained for similar models carried out for the crystalline host rock as follows:

- Free access to water: **SED_FREE** compared with **CRY_FREE**
- Flux limited inflow: **SED_LIM** compared with **CRY_LIM**

Here CRY_FREE is the base case simulated as part of Task 1, identified by "NWMO_T1_M01_V01" in Section 6.2. CRY_LIM is the flux-limited model simulated in the Step 2 modelling, identified by "THM_NO_FL" in Section 5.

As described in Section 9.1.1, due to the different groundwater salinity of the host rocks, bentonite in a sedimentary host rock has a higher hydraulic permeability and lower swelling pressure. Furthermore, the sedimentary rock has different thermal properties and the temperature boundary condition on the rock wall thus had to be updated.

Ideally, the compared crystalline and sedimentary models should not have any additional differences except for those coming from changing the host rock. This is, however, not the case here, which limits the conclusions which can be drawn from comparing the two models.
One difference between the sedimentary rock models and the crystalline rock models was the initial water content of the GFM. In the crystalline rock models used for comparison the water content was 2% and in the sedimentary rock models a value of 3% was used. The cause for this difference is not due to the different host-rock sites but instead changes made in the NWMO reference design.

The differences between the compared models (except for those due to the saline groundwater) are:

SED_FREE compared with CRY_FREE

- The reference initial water content in the GFM has been changed from 2% in CRY_FREE, to 3% in the sedimentary model.

SED_LIM compared with CRY_LIM

- The reference initial water content in the GFM has been changed from 2% in CRY_LIM, to 3% in the sedimentary model.
- Water inflow through the floor was not permitted in CRY_LIM, while in SED_LIM, flux-limited access to water was prescribed on all outer surfaces.

Table 9-11: Models of the evolution in sedimentary rock

Model ID	Model File
SED_FREE	NWMO_sedim_V07B_CB2022.gid
SED_LIM	NWMO_sedim_V07D_limflux_CB2022.gid

The models presented in this section were simulated until the buffer reached the final state and then up to the nearest multiple of 10. For the free access to water this meant that the simulation time was 10 years and for the flux-limited case the simulation time was 10 000 years.

9.1.3.1 Validation and Verification

Before analyzing the results, a validation of the accuracy of the mechanical material model representing the buffer (the modified version of BBM) was conducted. In previous tasks the numerical accuracy of the model was also verified by running models with

1) a higher mesh density, and
2) shorter time-steps.

As the geometry only differs in the spacer block thickness from what was used in the modelling reported in Task 1 and the same mesh density and time-stepping was used in those models as in the models presented here, no additional verification of the numerical accuracy was carried out for the sedimentary rock models.

The material model was validated using the same procedure in previous modelling, two parameter combinations at the final state of the simulation were analyzed:

- (x, y) = (net mean stress, void ratio). All points in the buffer should lie in the region between 0.9 times the swelling pressure curve and 2 times the swelling pressure curve
- (x, y) = (net mean stress, deviatoric stress). All points should be close to or below the von Mises stress at failure curve as defined in Åkesson et al 2010a.

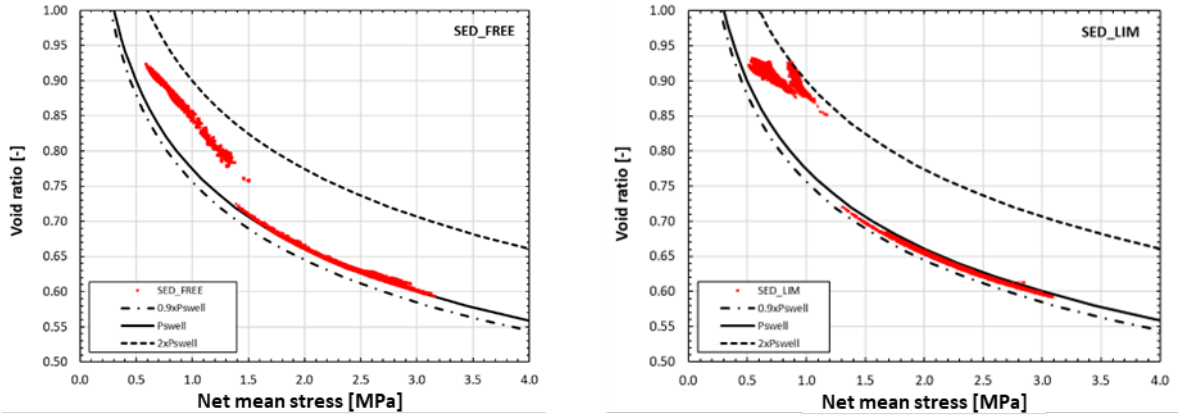

Figure 9-3: Final stress-void ratio state in the models

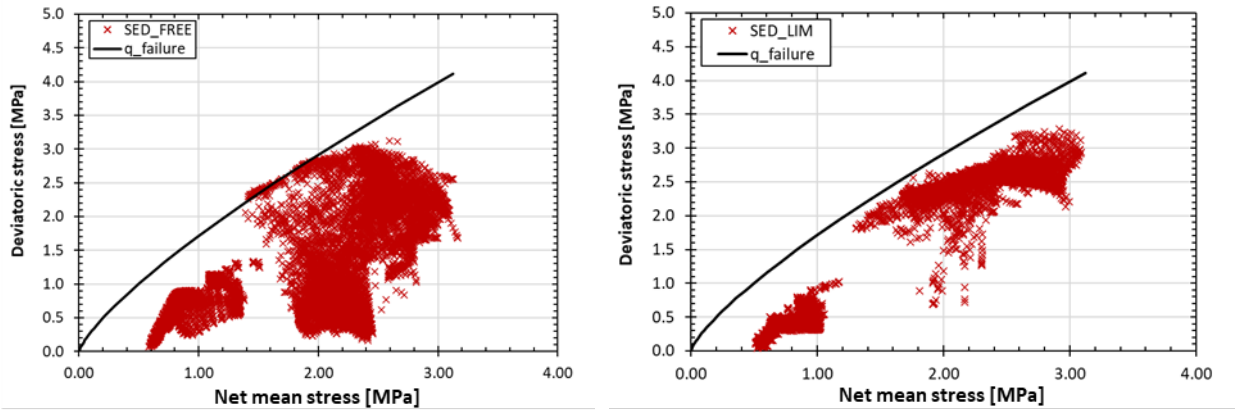

Figure 9-4: Final net mean stress vs deviatoric stress state in the models

In Figure 9-3 and Figure 9-4 the final state in the models is shown in terms of net mean stress vs void ratio (Figure 9-3) and deviatoric stress (Figure 9-4). As can be seen in the first figure all points lie in the region bounded by 0.9 times the swelling pressure curve and 2 times the swelling pressure curve and hence the model result is acceptable.

In Figure 9-4 some points in the buffer lie just above the von Mises stress at failure curve (solid black line) in the left graph (model SED_FREE). As discussed above this is due to the parameterization in the BBM model and the model result is therefore considered acceptable.

These two validation-exercises indicate that the material in the model behaves as intended.

9.1.3.2 Evolution of Temperature

The temperature in the flux-limited model, SED_LIM, is compared to the temperature evolution in CRY_LIM in Figure 9-5 and in Figure 9-6, with the only difference between the graphs being that Figure 9-5 shows time on a log scale to clearly see the initial evolution. The sedimentary model is slightly warmer due to higher temperature at the larger depth of the repository and the different thermal conductivity of the sedimentary rock. The maximum temperature in the buffer is just below 90°C and occurs 50 years after installation in the center point between the upper and lower UFCs. The peculiar shape of the temperature during the first few years of the simulation seen in Figure 9-5 is due to the linear ramping used between time intervals when prescribing the temperature on the boundary in combination with the plot showing the time logarithmically.

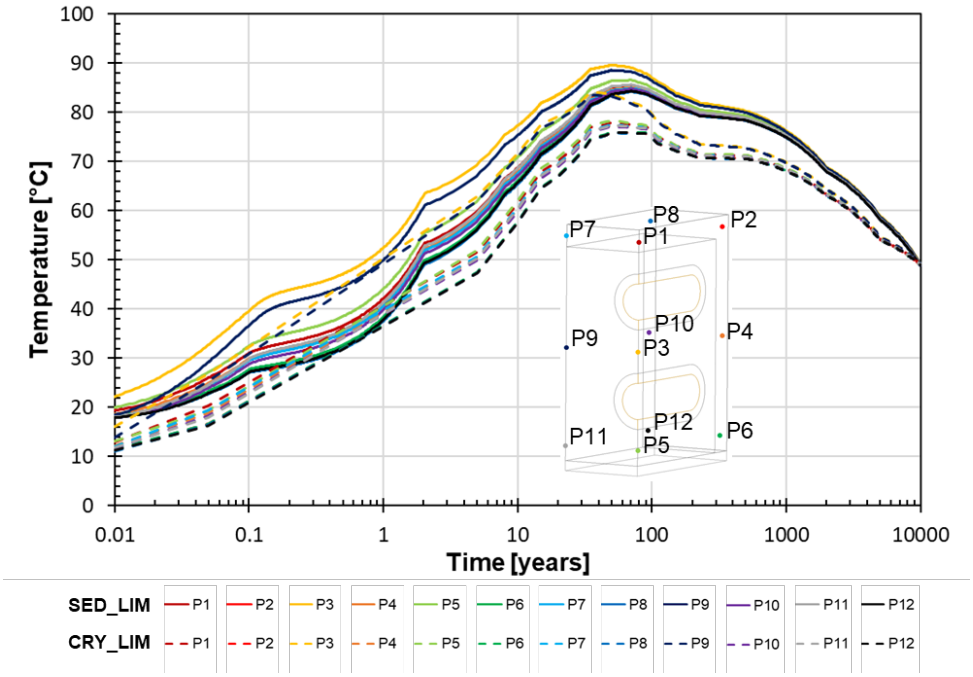

Figure 9-5: Temperature evolution in SED_LIM (solid lines) and CRY_LIM (dashed lines) with time in log scale on the horizontal axis

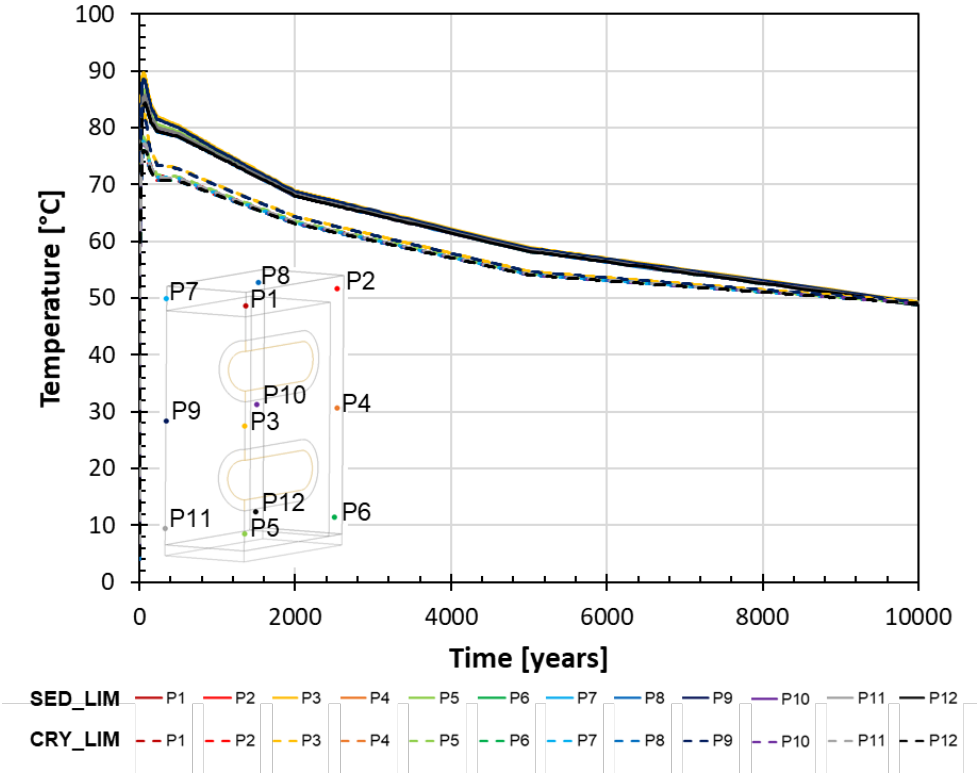

Figure 9-6: Temperature evolution in SED_LIM (solid lines) and CRY_LIM (dashed lines) with linear time on the horizontal axis

9.1.3.3 Evolution of Degree of Saturation

The saturation evolution in the models with free access to water is shown in Figure 9-7. As can be seen, the saturation evolution in the sedimentary model (solid lines) is very fast, with all studied points in the buffer being saturated within 2 years after installation. By contrast, the crystalline rock evolutions (dashed lines) become fully saturated after about 30 years.
The extremely short time for saturation obtained in the model with free access of water is not a realistic estimate. The fast saturation is due to the high (but relevant) hydraulic conductivity in the bentonite, caused by the high salinity in the groundwater, paired with the boundary condition providing an unrestricted access to water to the buffer. A real host rock could not provide the buffer with unrestricted access to water, at some point it would dry out in the vicinity of the buffer and the restricted inflow of groundwater to the host rock would act as a limit on the water flux.

Looking at the hydraulic evolution in the flux-limited case shown in Figure 9-8, the sedimentary model (solid lines) saturates faster than the crystalline rock model (dashed lines). As mentioned before, this is due to the higher hydraulic conductivity in the bentonite. The difference in saturation evolutions between the different host rock types, however, is significantly less here since the hydraulic boundary conditions prescribe a limit on the water inflow. It is likely that this model (SED_LIM) is a more realistic example of the saturation time in the sedimentary host rock. The free access to water model is kept and analyzed to compare how different water inflow rates change the mechanical evolution and final state.

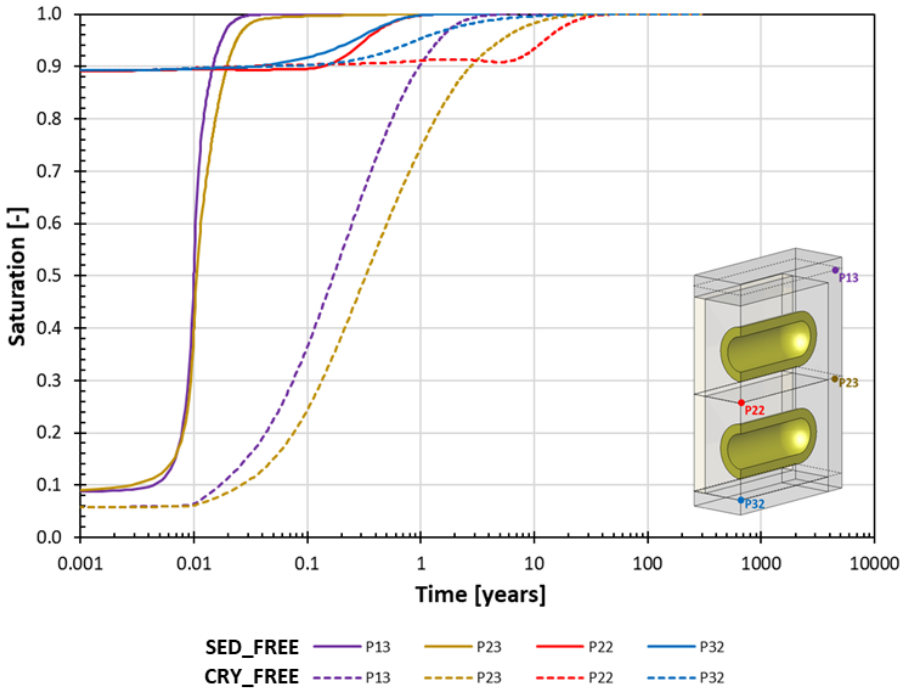

Figure 9-7: Degree of saturation as function of time from the models with free access to water

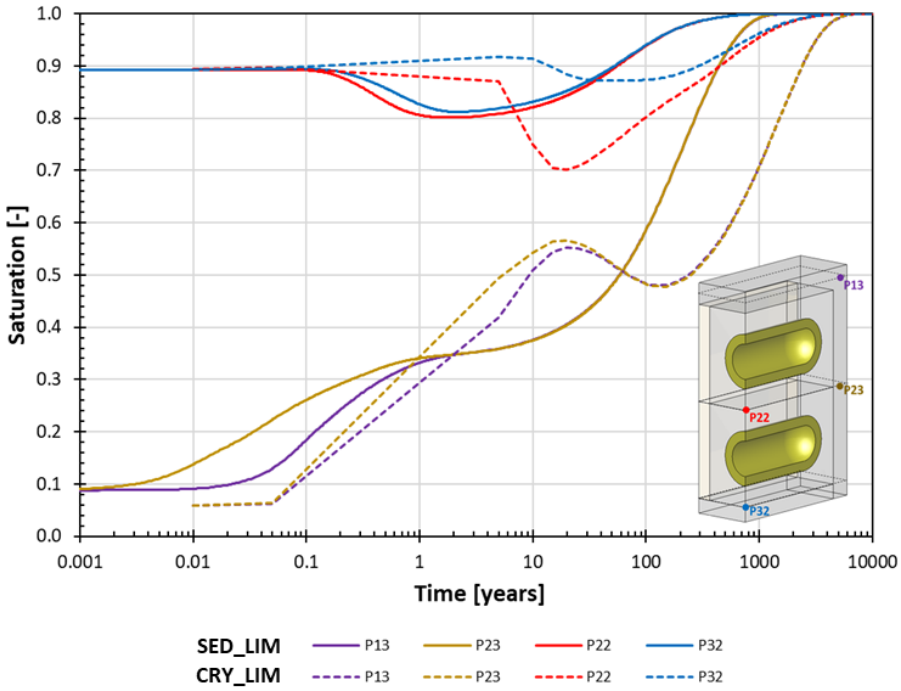

Figure 9-8: Degree of saturation as function of time from the flux limited models

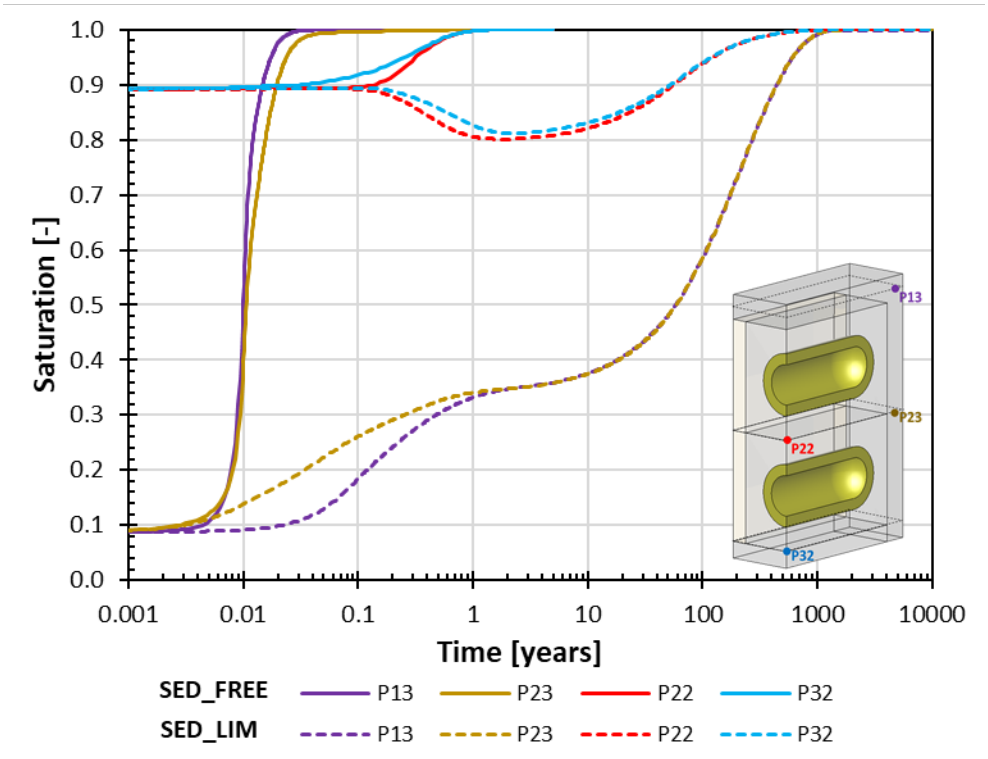

Figure 9-9: Degree of saturation as function of time from the free access to water model (solid lines) and the flux limited model (dashed lines)

In Figure 9-9 the saturation evolution in the two models simulated here is shown to simplify comparison between the two. As can be seen the free access to water model saturates much faster than the flux-limited model.

9.1.3.4 The Mechanical Evolution and End State

To study the mechanical process in the buffer, the evolution of the net mean stress (see Equation 3-15) was plotted against that of void ratio for points in the buffer. The final state was studied in terms of dry density and net mean stress. Finally, the normal stresses acting on the UFC and the displacements of the UFCs are discussed.

9.1.3.4.1 Evolution in Net Mean Stress - Void Ratio

For a saturated bentonite sample taking up water under confined conditions, there is a relation between the net mean stress and void ratio, the so-called swelling pressure relation/curve (see the discussion on swelling pressure in Appendix G). This type of hydromechanical process is valid for most points in the HCB-components in the model. The hydromechanical process in the GFM, however, is in general more complicated. Typically, the GFM first undergoes wetting-swelling, which is followed by compaction. The compaction is generated by HCB-components undergoing wetting-swelling.

Bentonite which undergoes compaction usually attains a higher mechanical pressure as compared to the mechanical pressure obtained by a sample undergoing continuous wetting under constant or increasing volume to the same dry density. Hence, material undergoing compaction will have a higher pressure than that given by the swelling pressure relation. This type of behavior indicates that the material shows a path dependency.

What was described above can be seen in Figure 9-10 and Figure 9-11, where void ratio is given as a function of net mean stress for some selected points in the buffer (solid lines) for the free water access and limited flux models, respectively. The simulation results are color coded according to the colored points inserted in the geometry given in the figures. The grey and black solid lines represent the evolution in the GFM, while the colored solid lines show the evolution in the HCB. The swelling pressure relation (dashed line) and a relation where swelling pressure has been doubled for a given void ratio (dotted line) are also shown in the graphs below. The higher (dotted) curve has proven to be fairly representative as an upper bound for the pressures obtained in bentonite undergoing compaction.

A remaining difference in the HCB and GFM void ratios at the final state, i.e., heterogeneity in the dry density, is what is expected due to the path dependence of the material. What is surprising in the results is that the faster water inflow generates less heterogeneity.

Slower wetting is likely to result in a more homogeneous wetting, and this has been thought of generating a more homogeneous dry density field. This is generally what is seen in experiments. However, this is not the case when studying the results in Figure 9-10 and Figure 9-11. The difference in final void ratios between the HCB and GFM is clearly larger for the flux limited model. This is also seen in Figure 9-3 where the final state for all nodes is plotted in terms of pairs of (net mean stress, void ratio) for the two wetting cases.

However, to differentiate the mechanical behavior between the two wetting scenarios a material model with a proper hydromechanical coupling would be needed, which is not available in the current version of CODE_BRIGHT.

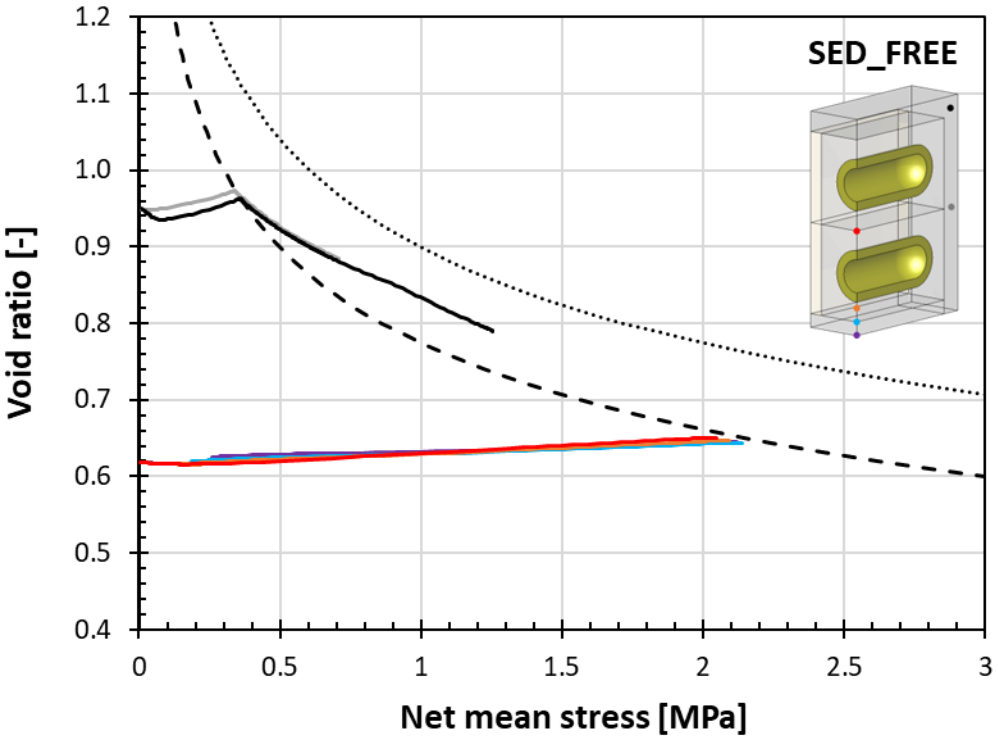

Figure 9-10: Net mean stress vs void ratio in the sedimentary rock model with free access to water

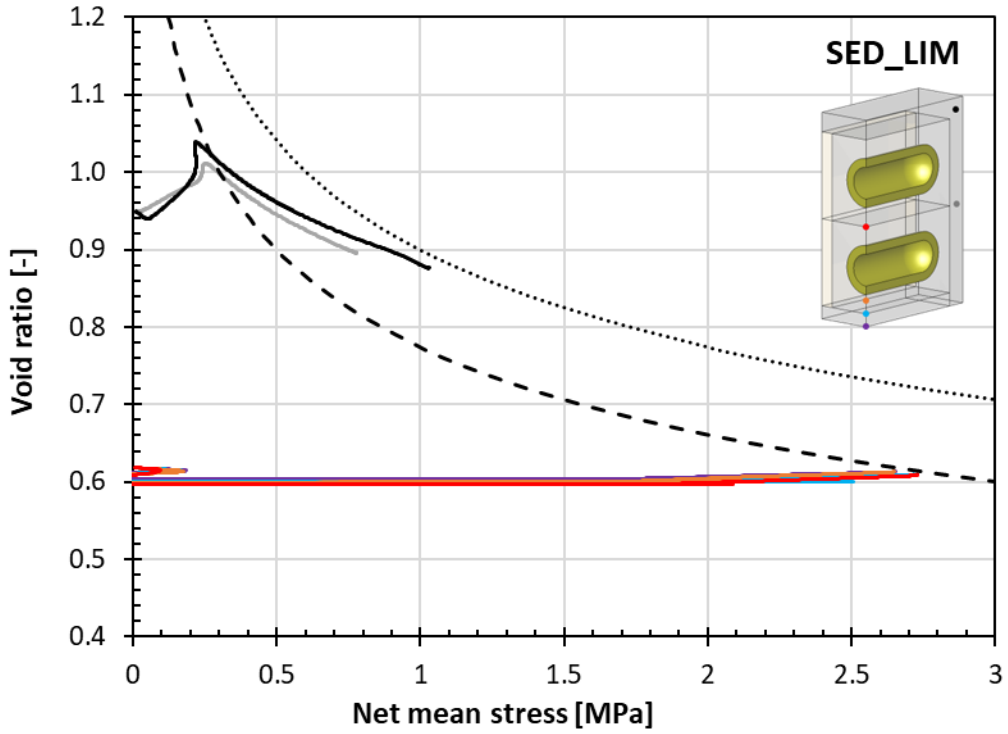

Figure 9-11: Net mean stress vs void ratio in the sedimentary rock model with flux limited access to water

9.1.3.4.2 Dry Density and Stress Field at Full Saturation

One important part of the simulations is the final mechanical state. When studying this, it should be mentioned that the final state of the simulations, i.e., the state at full saturation, is not necessarily a state that will prevail forever. When this state is reached, further mechanical evolution may take place due to, for example, creep in the bentonite and/or chemical changes due to long-term interaction with the groundwater.

The dry density and stress field at full water saturation is of particular importance as these closely relate to the safety function of the buffer. For example, to suppress microbial activity the swelling pressure must be sufficiently high, which, since the swelling pressure is closely related to the dry density in the buffer, effectively sets a lower limit on the dry density. In NWMO's emplacement room the weighted (volume averaged) buffer dry density should be ≥ 1600 kg/m^3 (Birch and Mielcarek 2017).

In Figure 9-12 the dry density fields in the model with free access to water (left) and flux-limited access to water (right) are shown in the upper row. As can be seen there are volumes close to the UFC with a dry density lower than 1600 kg/m^3 in both models. In general, these areas occur near the hemi-head of the UFC. Also, in the volume initially occupied by the GFM, the dry density is low in both models, with values in the range 1400 – 1500 kg/m^3. The dry density field in the model with free access to water is more homogenous than the flux-limited model in this study.

Another feature seen in the models is that the dry density field for the sedimentary rock model is much more heterogeneous than that of the crystalline rock models. The dry density field after full saturation from models CRY_FREE and CRY_LIM is shown in the lower row of Figure 9-12. The models for a crystalline rock repository show a more even density distribution, indicating that the HCB blocks swelled more (and thus had a lower dry density) while the GFM was compressed. In comparison, the sedimentary rock model with the free water access had a dry density minimum and maximum of 1430 kg/m^3 and 1710 kg/m^3, whereas the crystalline rock model had 1525 kg/m^3 and 1690 kg/m^3. This is discussed further in Section 9.1.3.5.

As discussed in 9.1.3.4.1, the flux-limited case shows less homogenization. This can also be seen in Figure 9-12 where the difference in dry density between the HCB block and GFM in the final state is larger in the flux-limited model than in the free access to water model. This goes against what has been observed in other previous numerical studies (see Åkesson et al 2010b). It is unlikely that the present representation of the system captured these finer effects correctly, and therefore, this result should be interpreted with caution.

In Figure 9-13 the field of net mean stress (see Equation 3-15) at full saturation is shown for both models of sedimentary rock (upper row) and the corresponding models for crystalline rock (lower row). Note that different color scales have been used.

The values of the net mean stress are much lower in the sedimentary rock models compared to those obtained in the crystalline host rock models. For example, in the crystalline case with free access to water, the min and max values of net mean stress were 5.7 MPa and 12.2 MPa, respectively. In the sedimentary rock model with free access to water the minimum and maximum values were 0.5 MPa and 3.1 MPa. This is a consequence of lowering the swelling pressure curve (see also Appendix G). The potential impact on the safety function of the buffer is not further discussed in this report.

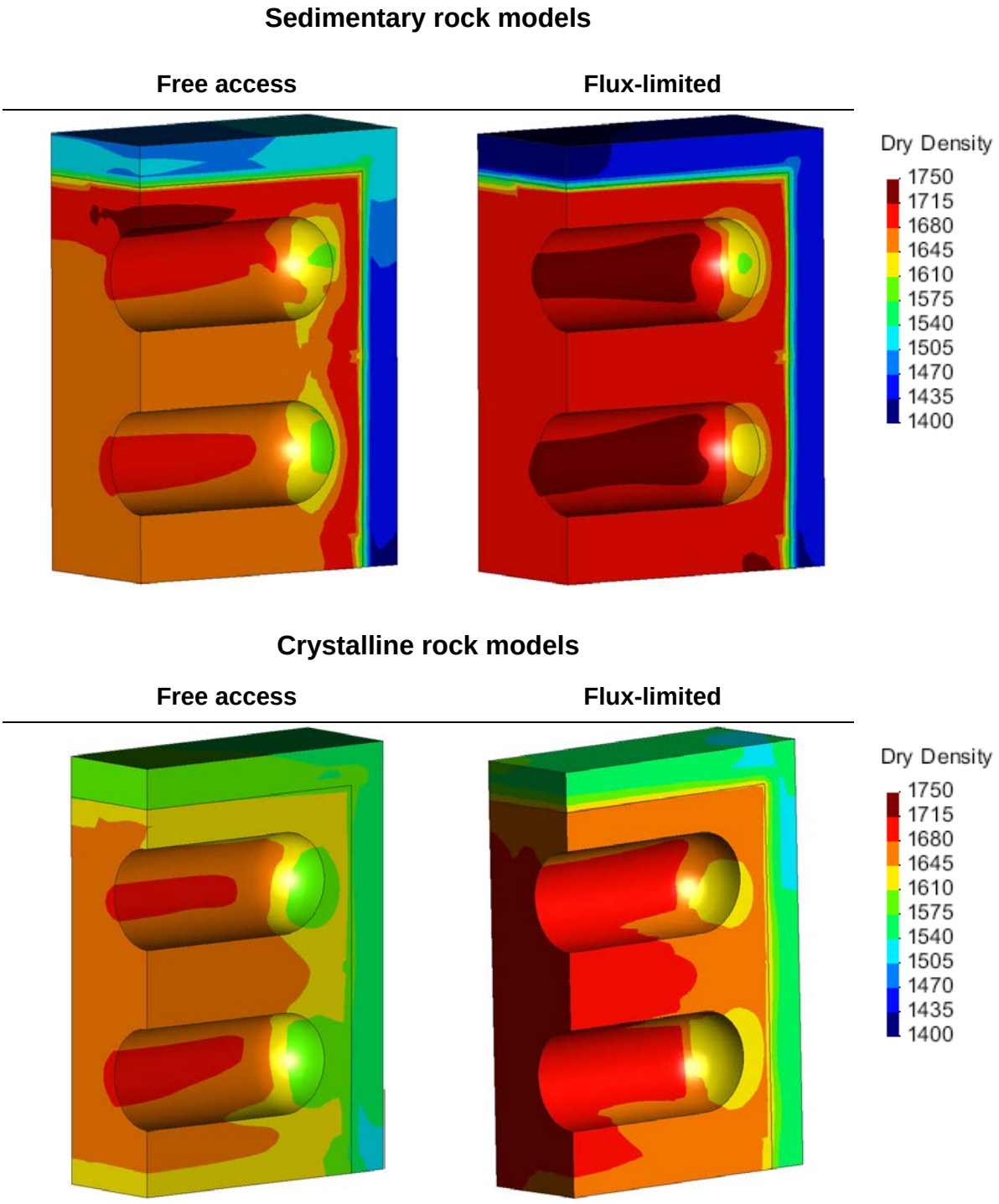

Figure 9-12: Dry density in the final state from the model with free access to water (left) and flux-limited access to water (right)

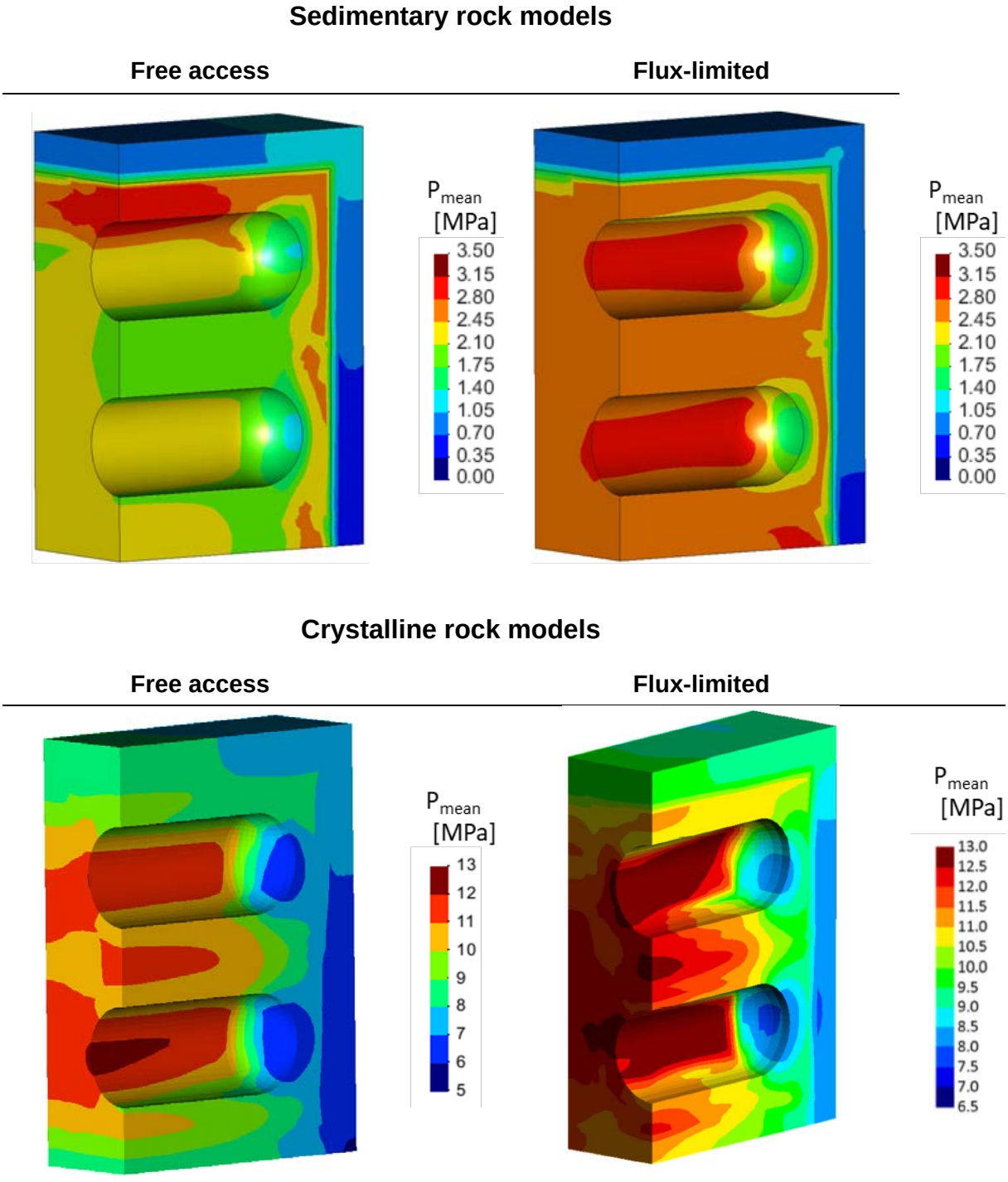

Figure 9-13: Net mean stress in the final state from the model with free access to water (left) and flux-limited access to water (right)

9.1.3.4.3 Normal Stress Acting on the UFC

The stresses generated by the swelling buffer and which acts on the UFC may be interesting from the perspective of the design and function of the UFC. The compressive normal stresses acting on the UFCs along three different horizontal scan-lines are studied. Figure 9-14 shows the results for the case of free access of water and Figure 9-15 shows the results for the flux-limited water access model.

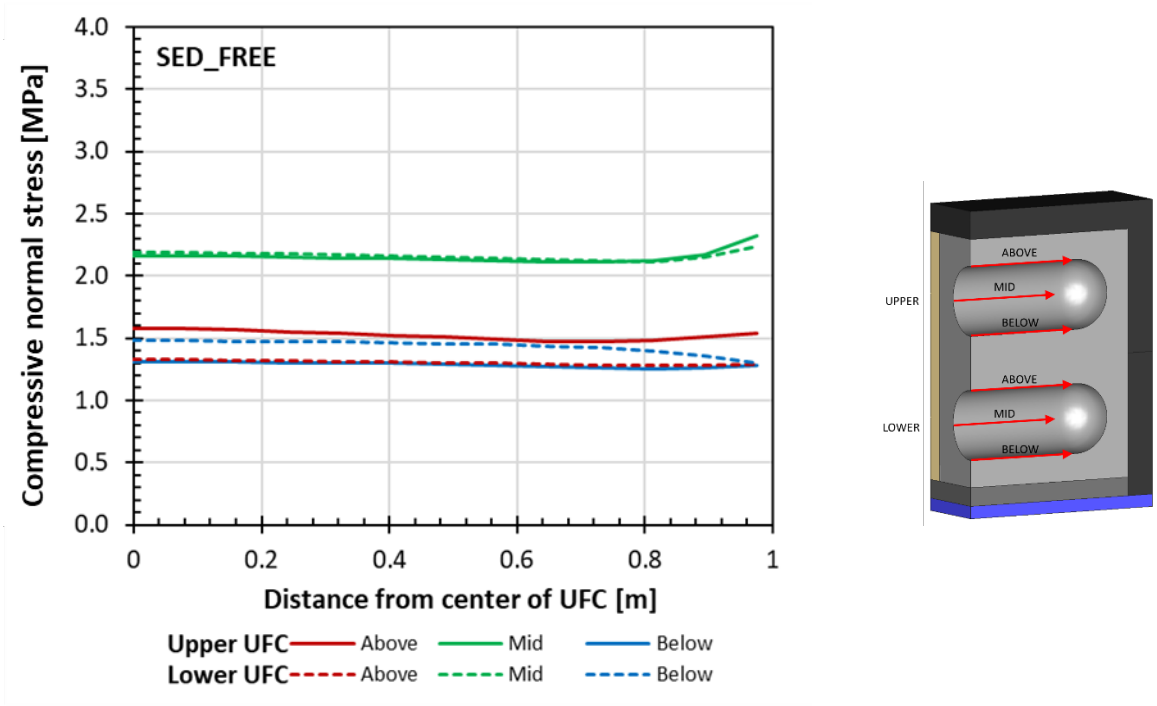

Figure 9-14: Compressive normal stress on the upper and lower UFCs in the model with free access to water

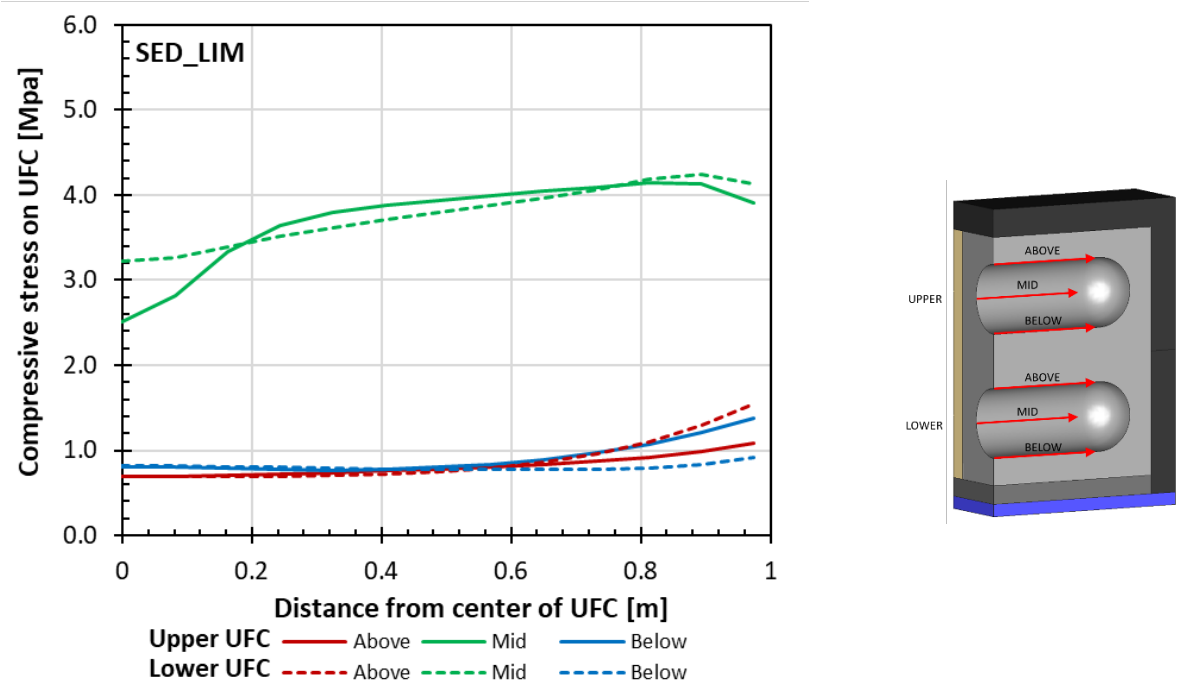

Figure 9-15: Normal stress on the upper and lower UFCs in the model with flux-limited access to water

In the model with free access to water the compressive normal stresses of the upper and lower UFCs are similar and evenly distributed along the axis of the UFC. The value on the “mid” scanline is considerably higher than that of the other two scanlines. This agrees with the results from the models for the crystalline rock. It comes from that, in the direction of the emplacement room tunnel there is only high-density buffer material.

The compressive load in the flux-limited case shows a similar trend for the scanlines above and below the UFC. At the mid scanline for the upper UFC, however, there is a minor decrease in compressive stress near the center of the UFC. This trend was not seen when evaluating the net mean stress, and hence was due to the anisotropic stress state in the model at this point.

9.1.3.4.4 Displacement of the UFCs

Aside from the compressive stress on the UFCs it is also valuable to evaluate the displacements of the UFCs during the swelling of the buffer. In Figure 9-16 the vertical displacement of the center of both the upper and lower UFCs is shown as a function of time in both models with sedimentary rock, as well as from the models with crystalline rock for comparison.

The displacements in the sedimentary rock models are in general small; in the free access to water case (red lines) some upward movements of both UFCs are seen, with a maximum displacement of about 17 mm. The magnitude of the displacements is similar to those seen in

crystalline rock model with free access to water (orange lines) where about 19 mm of upwards displacement was seen for the upper UFC and 12 mm for the lower UFC.

In the flux-limited model (blue lines) there are initially some downward movements, but as the buffer reaches full saturation and swells the UFCs move back to their original positions. This is slightly different from the model in crystalline rock (green lines). The crystalline model showed that the upper UFC reached an upwards displacement of 17 mm and the lower container an upwards displacement of about 6 mm.

Due to the symmetries used in the setup of the model, and given that the UFC is very stiff, no horizontal movement of the UFCs could occur in these models, and hence these are not shown in the plot.

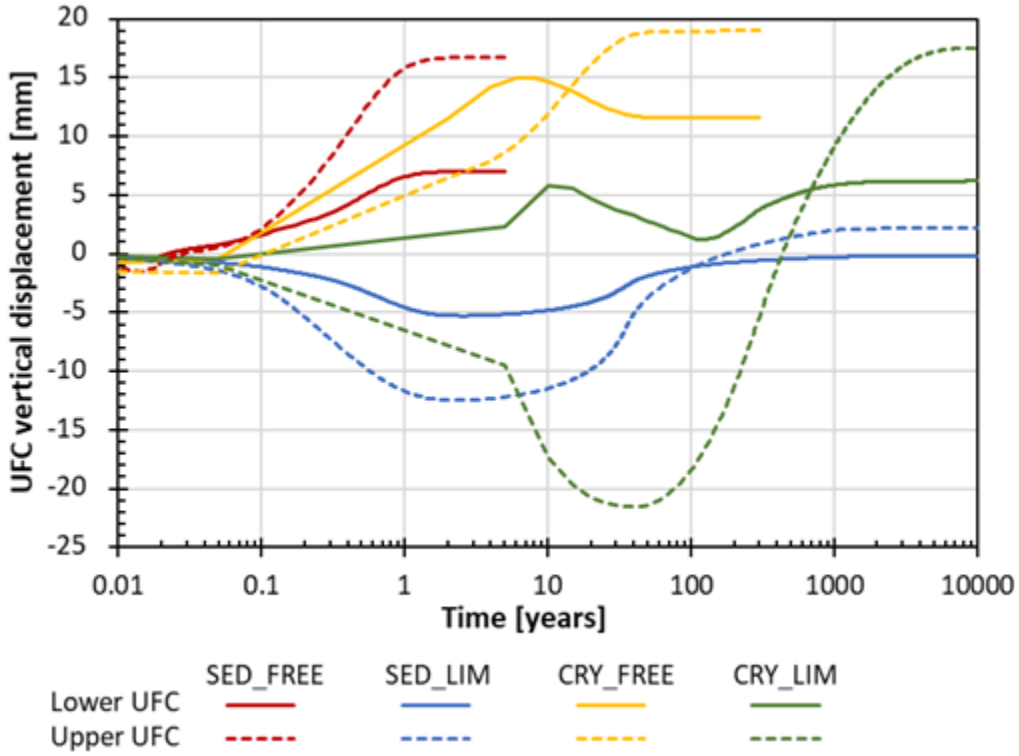

Figure 9-16: Vertical displacement of the center points of the upper and lower UFCs

9.1.3.5 Additional Discussion

In Section 9.1.3, the results from models for a sedimentary host rock were presented and compared with the results from models for the crystalline host rock. The host rock was not incorporated explicitly. Two hydration processes were considered: 1) free access to water which gives a lower bound on the saturation time, and 2) flux-limited access to water which gives an upper bound on the saturation time. The comparison of results obtained from the two different host rock types gave that the buffer in the sedimentary rock case would:

- Experience higher temperatures
- Saturate faster (when only considering the flow properties of the bentonite)
- Undergo less homogenization
- Exert much lower swelling pressure on the UFC and rock wall

These points are discussed in more detail below.

Higher Temperatures
The higher temperatures seen in the sedimentary rock models are simply a result of the difference in thermal initial and boundary conditions, derived from large scale thermal models presented in Guo et al (2017 & 2018).

Saturation Evolution
The sedimentary simulations indicated faster saturation. An increase in hydraulic conductivity means that the water flow within the bentonite will increase and this promotes faster water uptake and saturation. It should, however, be mentioned that there are some issues with the hydraulic representation which result in an underestimation of the time to saturation.

The first issue is present for both free and limited access to water. It is related to the retention curve, which in the present models is identical to that used in the crystalline simulations. The increased salinity is expected to lower the retention curve. Using the higher retention curve could contribute to increasing the inflow rate and shorten the time to full saturation. A change of the retention curve was, however, not within the scope of this first attempt to simulate the sedimentary case.

The second issue is the “representation” of the rock’s hydraulic boundary condition. This mostly affects the free access to water model, imposing nonrestricted water flow from the rock which is unphysical. A real host rock would limit the flow.

Considering the effect of the two issues, the second would likely be more significant. The lower bound for the saturation time, obtained from the case of free access to water, is therefore considered unrealistic, and should only be considered to understand the change in mechanical evolution due to different rates of water uptake.

Homogenization
The density field in the fully saturated state shows much less homogenization than that of the crystalline models. This is as expected, due to the much lower swelling pressures in the models with high-salinity groundwater.

The cause of the lower levels of homogenization in the density field could be due to the low swelling pressure curve in combination with the relation governing the swelling/hydraulic strain increment. The swelling strain increment is governed by the difference between the net mean stress (the pressure invariant of the net stress, see Equation 3-15) and the prescribed swelling pressure curve. Somewhat simplified, the higher the difference the higher the increment in swelling strain. When the difference is zero, i.e., when the net mean stress equals the value given by the swelling pressure curve at the current dry density, the swelling strain increment becomes zero. Since the relation is expressed in terms of the pressure invariant, it is only the isotropic part of the stress tensor which affects the swelling strain increment.

Anisotropic stress states may therefore suppress homogenization if the stress components not contributing to homogenization (i.e., those not acting in the direction of the density gradient), grow faster and become large, compared to the components that contribute to the homogenization process. When investigating how the setup of the HCB and GFM worked together, 1D-models (not reported here) representing a thin column with HCB and GFM parts were constructed. These showed that anisotropic stress states working against homogenization were indeed present. The 1D-models do represent a more constrained system, compared to the buffer in the 3D-model, but the main findings are still valid. The low swelling pressure curve would likely amplify the effect from the anisotropy as well.

Swelling Pressure on UFC (and Rock Wall)
The increase in salinity of the groundwater when considering a sedimentary host rock has a significant effect on the HM properties of the bentonite. These effects were, in the modelling presented, manifested through use of a significantly lower swelling pressure curve and an increase in hydraulic conductivity. The model was calibrated based on the data provided by Dixon (2019). The observations of much lower pressures acting on the UFC and the rock wall are a direct consequence of using a significantly lower swelling pressure curve in the sedimentary rock case.

9.1.3.5.1 Future Improvements

Below follows a listing of areas in which the models could be improved.

- The swelling pressure curve for highly saline water, derived from data in Dixon (2019) may underestimate the swelling pressure, particularly for dry densities > 1400 kg/m^3. This issue is discussed in Appendix G and stems from the scatter in experimental data for high TDS systems when the dry density is larger than about 1400 kg/m^3. In Figure 9-17 the swelling pressure curve (black) can be compared with that used in the crystalline case (red) and a “best estimate” curve (orange), developed from our theoretical and practical understanding of how saline pore water changes the swelling pressure, as described in Appendix G. More experimental data, and/or performing a sensitivity analysis of the models by varying the swelling pressure curve, could improve the reliability of the modelling results.
- The retention curve, identical to that used for crystalline conditions (water with low salinity), is probably not representative for highly saline conditions. I.e., the buffer’s potential for attracting water is too high in the sedimentary models. As discussed in Appendix G, there should also be a correspondence between the swelling pressure curve and the retention curve.
- If more accurate estimates of the upper and lower bounds on saturation times are sought, the representation of the water supply from the rock needs to be improved. This could, for example, be done by incorporating the rock mass in the model or trying to calibrate a flux limited boundary condition. As mentioned earlier, the estimated lower bound on the saturation time, obtained from the model with free access to water, can only be used to understand how fast the bentonite buffer theoretically could take up water. In reality the host rock would limit the possible inflow rate. In that respect the flux limited model provides a more realistic water uptake, but the question is how limited the water inflow should be. Including the host-rock in fully coupled THM models, however, would be computationally challenging. If an analysis of the expected saturation times at the different host rock sites is wanted, a large set of TH combined with detailed hydraulic descriptions of the host rock could be used (Sellin et al. 2017).

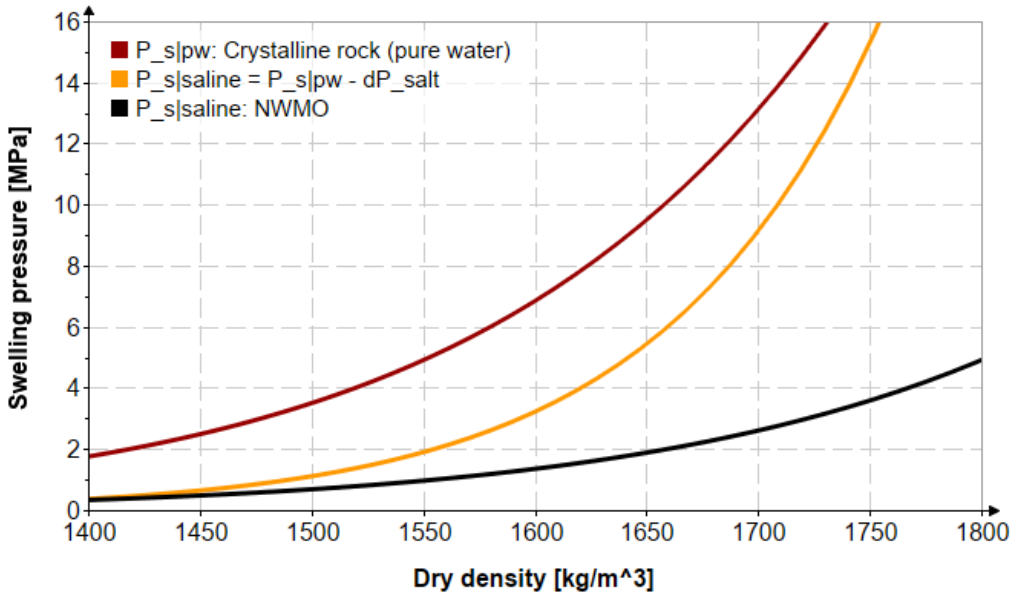

Figure 9-17: Swelling pressure curves used for crystalline and sedimentary host rock

9.1.3.5.2 Recommendations on Laboratory Work

To further develop the material models, and to validate the modelling for bentonite in high salinity groundwater, further laboratory work is recommended. These include, but are not necessarily limited to:

- **Swelling pressure measurements at high water salinity:** As discussed in Dixon (2019) and in Appendix G, measurements of the swelling pressure of MX-80 bentonite at very high salinity (300 g/L) and high dry density are limited and the data shows a significant scatter. This leads to an uncertainty in the parametrization of the swelling pressure as function of dry density, a very important part of the models in this investigation. Further laboratory measurements of the swelling pressure, particularly at higher (above 1500 kg/m^3) dry densities, could improve the accuracy of the models significantly.
- **Experimental studies of homogenization with high salinity water:** This could include swelling into voids, as well as analyzing the degree of homogenization after full saturation in tests combining HCB and GFM. The influence of the hydration rate on the homogenization process could also be studied.
- **Retention capacity of MX-80 bentonite at high salinity:** It would be beneficial to evaluate this further, particularly at low RH. Doing so would allow for an accurate retention curve in models of the bentonite in sedimentary rock, which would increase the accuracy of the modelling.

9.1.4 Conclusions

The models presented in Section 9.1 simulated the THM evolution in the bentonite buffer at the sedimentary rock host site. In this type of rock, the high salinity in the groundwater causes

several changes in the behaviour of the bentonite with respect to the properties in a low-salinity groundwater environment. Swelling pressures are lower, hydraulic conductivity higher and the different thermal properties of the rock require significantly thicker spacer blocks to satisfy the repository requirements. Several important conclusions could be drawn from the models.

Due to the significantly decreased swelling pressure in bentonite contacted with high-salinity groundwater, the mechanical response of the clay was different. For example, the normal stress on the UFC was reduced from around 9 MPa in the crystalline rock models, presented in Section 6.2, to 1 - 3 MPa in the sedimentary models. The results also indicate that once fully saturated, the buffer will be more heterogeneous in terms of dry density as compared to models of the buffer in crystalline rock.

The increase in the bentonite's hydraulic conductivity, due to the high-salinity groundwater, means that the saturation time of the bentonite buffer will essentially be completely dependent on the water inflow rate. If the rock could provide unlimited access to water, a rather unphysical assumption, the simulations showed that full saturation was reached about one year after installation. A more realistic boundary condition was used in a flux-limited model which gave a saturation time of about 1000 years.

9.2 Drying Before Installation

The focus of this subtask was to analyse the moisture redistribution during the period between assembling the buffer box and installing it in the emplacement room and the impact this had on the potential for fracture formation. The buffer box will be assembled in a surface-based plant whereafter it will be placed inside a steel container and transported to the emplacement room. During this transport, with a duration of less than 300 h, water will be redistributed in the HCB.

The temperature gradient induced by the hot UFC will drive vapour outwards, which will cause drying of the buffer closest to the UFC and thereby wetting of the outer parts. The water redistribution will be dependent on the climate surrounding the buffer box inside the steel container. Decreased water content (drying) will lead to shrinkage of the bentonite and increased water content (wetting) to swelling. As described in Section 7, localized drying and wetting may generate stress states which cause formation of cracks/fractures in the HCB.

Typical experimental findings (Börgesson 2001) for bentonite exposed to free drying conditions are shown in Figure 9-18. The obtained graphs are commonly called "shrinkage curves". Note that the additional left vertical scale shows the dry density, ρ_d, corresponding to the void ratio, e, in the original graph. The dry density is calculated as:

$$\rho_d = \frac{\rho_s}{1+e}, \tag{9-2}$$

where the grain density was set to $\rho_s = 2750$ kg/m^3 (Dixon 2019). The legend in Figure 9-18 shows the initial conditions for each shrinkage curve.

The thick solid line in Figure 9-18 represents the water content at full saturation with varying void ratio. One common feature for all shrinkage curves shown in Figure 9-18 is that above a water content of about 0.2, the slope of all curves aligns with that for $S_r = 100\%$, but below this value the slope of the shrinkage curves deviate and become shallower. This limiting value (w = 0.2) is henceforth denoted the shrinkage limit.

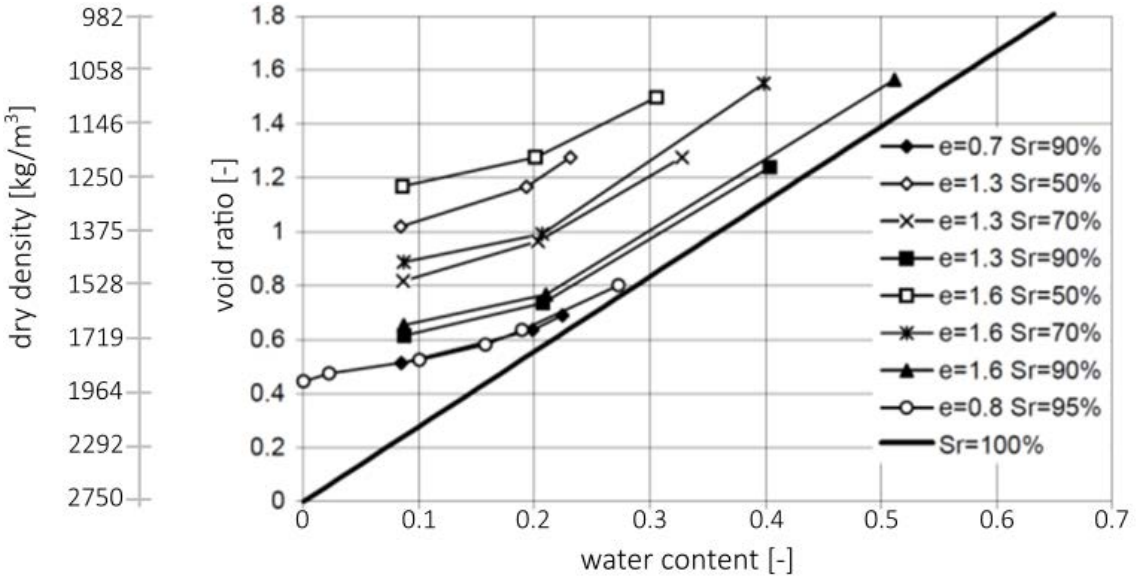

Figure 9-18: Shrinkage curves of MX-80 with different initial void ratio (or dry density) and water content (denoted water ratio in the diagram).

9.2.1 Methodology

To estimate the risk of fracture formation in the buffer box during transport, TH-models of the buffer box enclosed in a steel container were simulated using CODE_BRIGHT. The results from these simulations were used in combination with shrinkage curves to analytically evaluate the mechanical behaviour in the parts of the HCB that dries. Using the water content, w, from the model in the shrinkage curve gave an updated void ratio. This was used to evaluate the risk of fracturing through the method described in Section 7.

The potential for fracture formation was analyzed using two variables, the volume element ratio (negative volumetric strain), v, and its gradient, ∇v. The volume element ratio is defined using a volume element at the initial state, dV_0, and at the deformed state, dV (or can be expressed using the corresponding void ratios e and e_0),

$$v = \frac{dV_0 - dV}{dV_0} = \frac{e_0 - e}{1 + e_0}, \tag{9-3}$$

and the volume element ratio gradient is defined as,

$$\nabla v = \frac{\partial v}{\partial \boldsymbol{X}}, \tag{9-4}$$

where $\boldsymbol{X}$ denotes the position vector.

Water content is not directly accessible from CODE_BRIGHT and was calculated using:

$$w = \frac{\rho_l}{\rho_s} S_l e_0 \,, \tag{9-5}$$

where ρ_l denotes the water density, ρ_s the solid density and S_l the degree of saturation.

9.2.2 Numerical Approach and Model Setup

To estimate the open volumes caused by drying-shrinkage-fracturing, the method described above was implemented using Python. The data needed to estimate the risk of shrinkage fractures from the CODE_BRIGHT simulations are given in Table 9-12. In the table it is also specified if the output data was given on nodal or elemental level.

Table 9-12: Description of data storage format of CODE_BIGHT output data

Property	CODE_BRIGHT file	onNodes	onGaussPoints (Element)
Temperature, T	xxx_Temperature.post.res	X	
Liquid Density, ρ_l	xxx_Liq_Dens.post.res	X	
Liquid Pressure, p_l	xxx_Liquid_Pressure.post.res	X	
Permeability, $\boldsymbol{k}$	xxx_Permeability.post.res		X
Fluid flow, $\boldsymbol{q}$	xxx_q_liquid_advective.post.res		X

*xxx is the model name

The variables given on Gauss points from CODE_BRIGHT were recalculated to the corresponding nodal values, by computing the Jacobian for each element.

The degree of saturation in the buffer box was calculated directly from the liquid pressure instead of using the degree of saturation calculated automatically by CODE_BRIGHT. The latter was an element wise variable and therefore point values on the surface or along material interfaces were average values calculated over adjacent elements which were incorrect at material interfaces.

The extended van Genuchten curve was used to calculate the degree of saturation as:

$$S_l = \left(1 + \left(\frac{p_g - p_l}{P_0}\right)^{\frac{1}{1-\lambda_0}}\right)^{-\lambda_0} \left(1 - \left(\frac{p_g - p_l}{P_d}\right)^{\lambda_d}\right) \tag{9-6}$$

Here, p_g is the gas pressure, p_l the liquid pressure, and λ_0, λ_d and P_d are model parameters. Lastly, $P_0 = P\frac{\sigma}{\sigma_0}$ where P_0 and σ_0 are the pressure and surface tension at reference temperature. From the degree of saturation, the water content was calculated as:

$$w = \frac{\rho_l(p_l)}{\rho_s} S_l(p_l) e_0 \tag{9-7}$$

Furthermore, the shrinkage curve was determined numerically using the CubicSpline function in the SciPy library. The created spline function and the dataset used in the calculations are both shown in Figure 9-19.

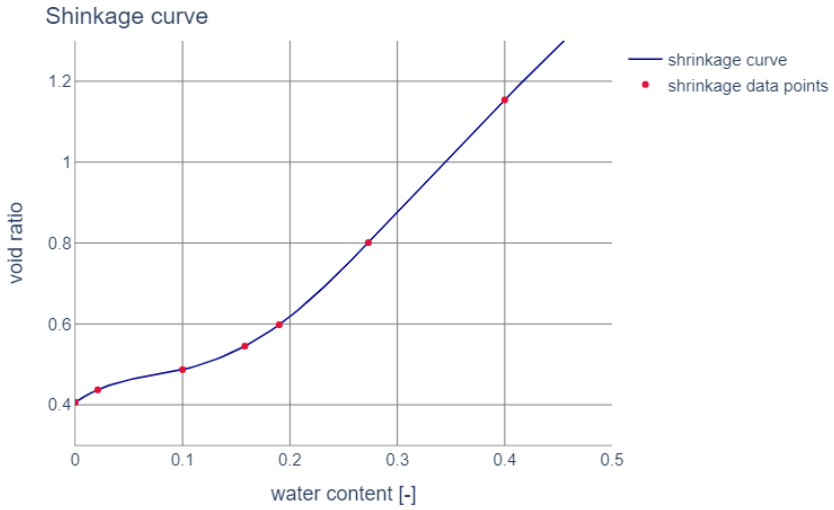

Figure 9-19: The used shrinkage curve used in the analysis (blue solid line) and experimental data points (red dots) from Börgesson (2001)

9.2.2.1 Computing the Gradient of the Volume Ratio

As mentioned in the previous section, the volume element ratio gradient, ∇v, was used to identify where stress concentrations, which might lead to an increased risk of fracture formation, were likely to occur. The gradient $\nabla v = \frac{\partial v}{\partial \boldsymbol{X}}$ was calculated as:

$$\nabla v = \frac{\partial v}{\partial \boldsymbol{X}} = \frac{\partial v}{\partial e_{dry}} \frac{\partial e_{dry}}{\partial w} \left(\frac{\partial w}{\partial \rho_l} \frac{\partial \rho_l}{\partial p_l} + \frac{\partial w}{\partial S_l} \frac{\partial S_l}{\partial p_l} \right) \frac{\partial p_l}{\partial \boldsymbol{X}} \tag{9-8}$$

The derivative of the volume ratio, v, with respect to the void ratio during shrinkage, e_{dry}, was given by:

$$\frac{\partial v}{\partial e_{dry}} = \frac{e_0 - 1}{e_0 + 1} \tag{9-9}$$

The same Python routine used to create the shrinkage curve was also used to compute $\partial e_{dry}/\partial w$. Furthermore, the derivative of the water content with respect to liquid density was given by:

$$\frac{\partial w}{\partial \rho_l} = \frac{S_l e_0}{\rho_s} \tag{9-10}$$

The liquid density, ρ_l was defined according to Equation (3-31). The derivative of the liquid density can then be written as:

$$\frac{\partial \rho_l}{\partial p_l} = \rho_{l0}\, \beta \exp[\beta(p_l - p_{l0}) + \alpha T] \tag{9-11}$$

The derivative of the water content with respect to the degree of saturation was calculated as:

$$\frac{\partial w}{\partial S_l} = \frac{\rho_l e_0}{\rho_s} \tag{9-12}$$

The derivative of the retention curve defined by Equation (9-6) was:

$$\frac{\partial S_l}{\partial s} = -\frac{\lambda_0 \left(\frac{s}{P_0}\right)^{\frac{1}{1-\lambda_0}-1}\left(1+\left(\frac{s}{P_0}\right)^{\frac{1}{1-\lambda_0}}\right)^{-\lambda_0}\left(1-\frac{s}{P_d}\right)^{\lambda_d}}{P_0(1-\lambda_0)} - \frac{\lambda_d \left(1-\frac{s}{P_d}\right)^{\lambda_d-1}\left(1+\left(\frac{s}{P_0}\right)^{\frac{1}{1-\lambda_0}}\right)^{-\lambda_0}}{P_d}, \quad (9\text{-}13)$$

with $s = p_g - p_l$. Finally, the gradient of the liquid pressure was calculated from the fluid flow.

$$\frac{\partial p_l}{\partial \boldsymbol{X}} = -\boldsymbol{q}\frac{\mu}{k_{tot}} + \rho_l \boldsymbol{g} \quad (9\text{-}14)$$

Here $\boldsymbol{q}$ is the fluid flow, $k_{tot} = kk_{rl}$ the permeability defined according to Equation (3-21), μ the viscosity of water and $\boldsymbol{g}$ the gravity.

9.2.2.2 Model Setup

The thermo-hydraulic simulations were conducted using CODE_BRIGHT. The dimensions of the steel container used for the buffer box, as provided by the NWMO, are shown in Figure 9-20, the dimensions of the buffer box and UFC in Figure 9-21 and the resulting geometry and mesh is shown in Figure 9-22. The airgap in this model was set up as a single connected volume. The RH in the airgap was essentially uniform at all times and trapped gas with different RH values in different parts of the airgap volume was not studied. This simplification was in part due to limitations of CODE_BRIGHT, which could not include, for example, convective transport of gas. A more realistic study would require the use of other FEM solvers.

The setup of the FEM models was taken from previous modelling presented in this report. However, since the evolution in a single buffer box with no surrounding GFM was simulated, the geometry was updated. To save computational time the model was reduced using the dual symmetry of the problem.

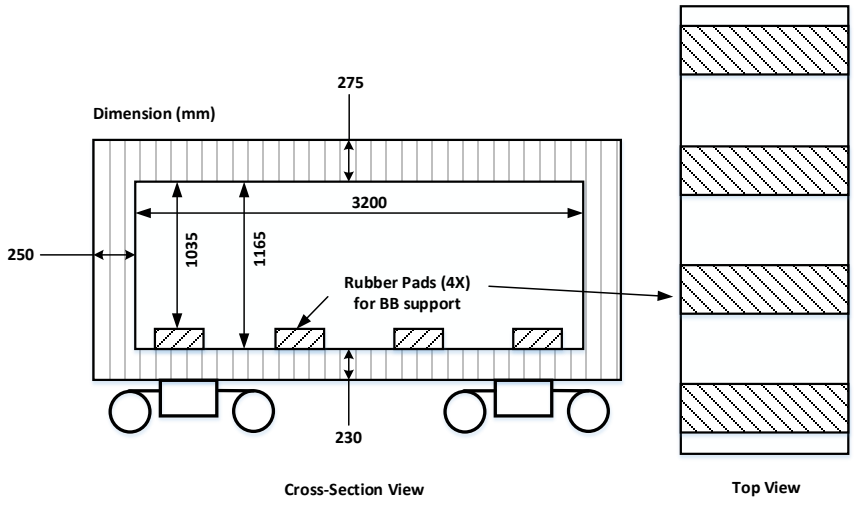

Figure 9-20: Dimensions of the buffer box steel container

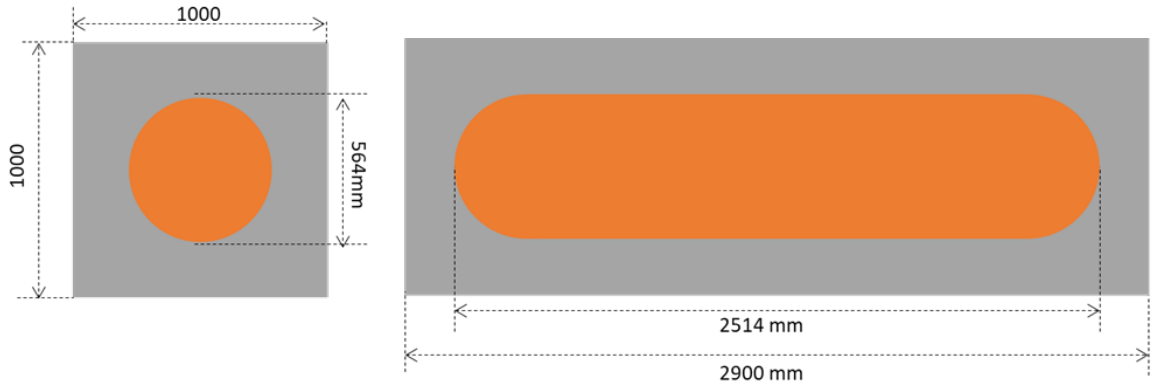

Figure 9-21: Dimensions of the buffer box and UFC

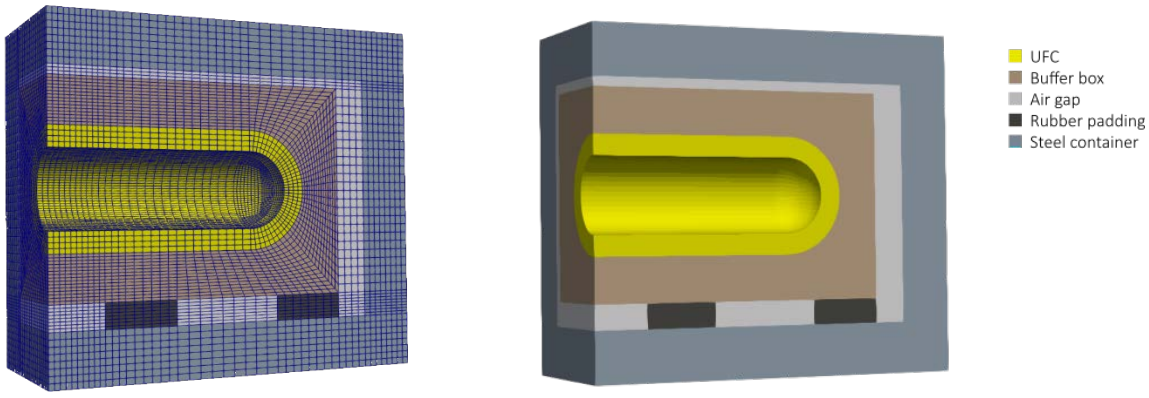

Figure 9-22: Geometry and mesh used for TH-simulation in CODE_BRIGHT

9.2.2.3 Initial Conditions

Two cases were studied using CODE_BRIGHT. In the first case the initial RH in the airgap was assumed to be 50 %, corresponding to a liquid pressure (suction) of -93.7 MPa at T = 20 °C. For the second case the relative humidity in the airgap was assumed to be in equilibrium with the HCB, which meant that a relative humidity of 84 % was prescribed, corresponding to a liquid pressure of -22.9 MPa at T = 20 °C. The initial conditions of all materials are given in Table 9-13. It should be noted that the air in the airgap can move freely inside the steel container. In CODE_BRIGHT all modelled constituents are porous materials and hence must be assigned an initial porosity. For the airgap (that is not a porous material) the value was set to 0.99, to be as good of a representation of empty air as possible. This value was also used in (Johannesson et al. 2014) when simulating airgaps in contact with buffer blocks.

Table 9-13: Initial values

Parameter		UFC	Buffer box	Airgap	Rubber padding	Steel container	Unit
Porosity	n_0	10^{-3}	0.378	0.99	10^{-3}	10^{-3}	-
Water content	w	-	0.19	-	-	-	-
Suction	s_0	-22.9	-22.9	-93.7/-22.9[1)]	-93.7/-22.9[1)]	-93.7/-22.9[1)]	MPa
Temperature	T_0	23	20	20	20	20	°C

[1)]Case-1/Case-2

9.2.2.4 Material Parameters

In this section all the material parameters used in the CODE_BRIGHT simulations are given in Table 9-14 and Table 9-15. The constitutive laws are described in Section 3. For parameters not included in the tables the default values given in CODE_BRIGHT (Olivella et al., 2023) were used.

Table 9-14: TH-parameter values

			HCB	UFC	Airgap	Rubber	Steel
Retention curve	P_0	MPa	65.385	10	0.1	10	10
	λ_0	-	0.18	0.3	0.6	0.3	0.3
	P_d	MPa	400	-	-	-	-
	λ_d	-	1.2	-	-	-	-
Intr. perm.	k_0	m^2	$1.04x10^{-20}$	10^{-30}	10^{-30}	10^{-30}	10^{-30}
	n_{ref}	-	0.418	-	-	-	-
Rel. perm.	k_{rl}	-	S_l^3	1	S_l^3	1	1
Diffusive Flux of vapour	τ	-	1	0.01	1	0.01	0.01
Conductive Flux of heat	λ_{dry}	W m^{-1} K^{-1}	0.5	300	0.27	0.2	45
	λ_{sat}	W m^{-1} K^{-1}	1.3	300	0.27	0.2	45

Table 9-15: Phase properties for buffer box material

			HCB	UFC	Airgap	Rubber	Steel
Specific heat for solid	C_s	J kg^{-1} K^{-1}	800	715	1000	1050	490
Solid density	ρ_s	kg m^{-3}	2750	7951	1	1150	7850

9.2.2.5 Boundary Conditions

Two types of boundary conditions (thermal and hydraulic) were prescribed in the model. The thermal boundary conditions consist of the heat flux generated by the UFC and the cooling of the steel container due to contact with the surrounding air.

A heat flux of 42.25 W was prescribed on the inner hollow surface of the UFC (see Figure 9-22). The value was calculated from the total heat flux generated in the UFC (169 W) divided by four, since only a ¼ of the UFC is included in the simulation.

The cooling effect of the surrounding air was simulated by prescribing a boundary condition on the form:

$$j_{\mathrm{h}} = \gamma(T_0 - T). \tag{9-15}$$

The value of T_0 was set to room temperature (20 °C) and the value of the heat transfer coefficient was set to $\gamma = 10$ J/s/K, to simulate heat convection into the surrounding air (see also Johannesson et al. 2014).

As for the hydraulic problem, zero flow condition was assumed on all outer and inner boundaries.

9.2.3 Results and Discussion

Figure 9-23 shows the maximum and minimum values of the water content in the bentonite buffer box for both Case-1 and Case-2. A rapid decrease in the minimum water content can be seen in Case-1 during the first 20 hours, while the behaviour in Case-2 is initially much slower. The initial quick drying of the bentonite in Case-1 is most likely driven by the initial relative humidity of the air in the steel container. After about 50 hours the minimum water content in both modelled cases show similar trends and values, with a clear decrease of the minimum water content over time.

In both modelled cases the maximum water content increases over time. In Case-2 the results show that a slight increase in water content, (from 19.4 % to 19.5 %), occurs during the first 20 hours and about 50 hours after the start of the simulations the maximum water content in the models starts to increase in both cases. This can be attributed to the transport of water vapour from the inner to the outer parts of the buffer box. The increase in maximum water content seen in Figure 9-23 indicates that some part of the buffer may undergo swelling. However, as mechanical processes were not simulated using CODE_BRIGHT that could not be analyzed as part of this study.

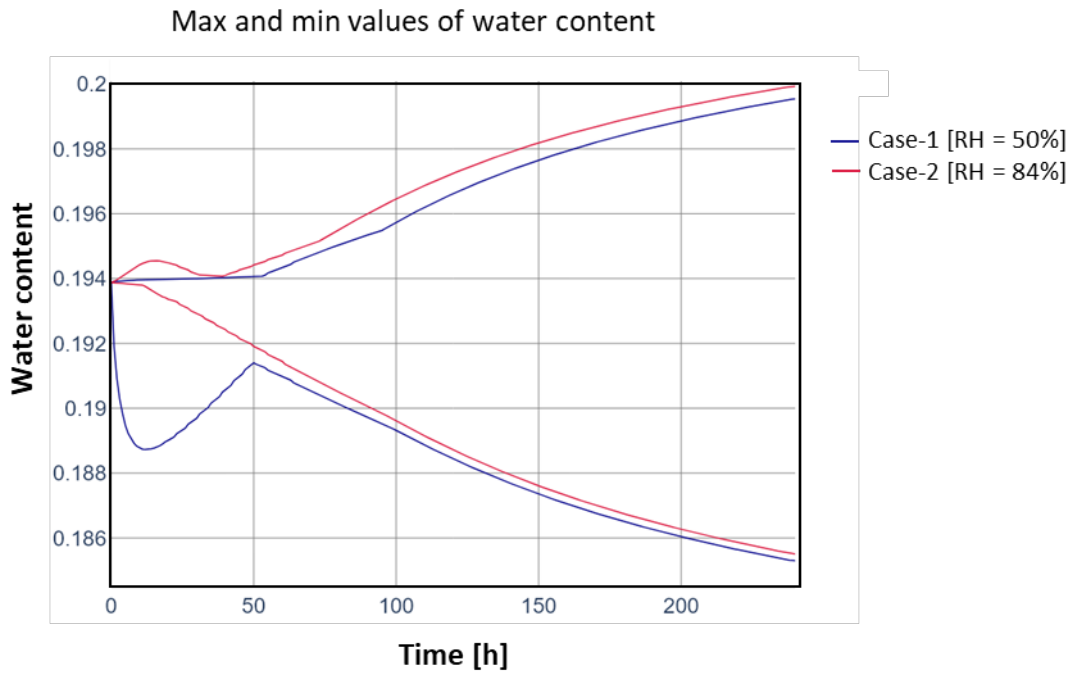

Figure 9-23: The graphs represent the maximum and minimum values of the water content in the buffer box during 240 hours

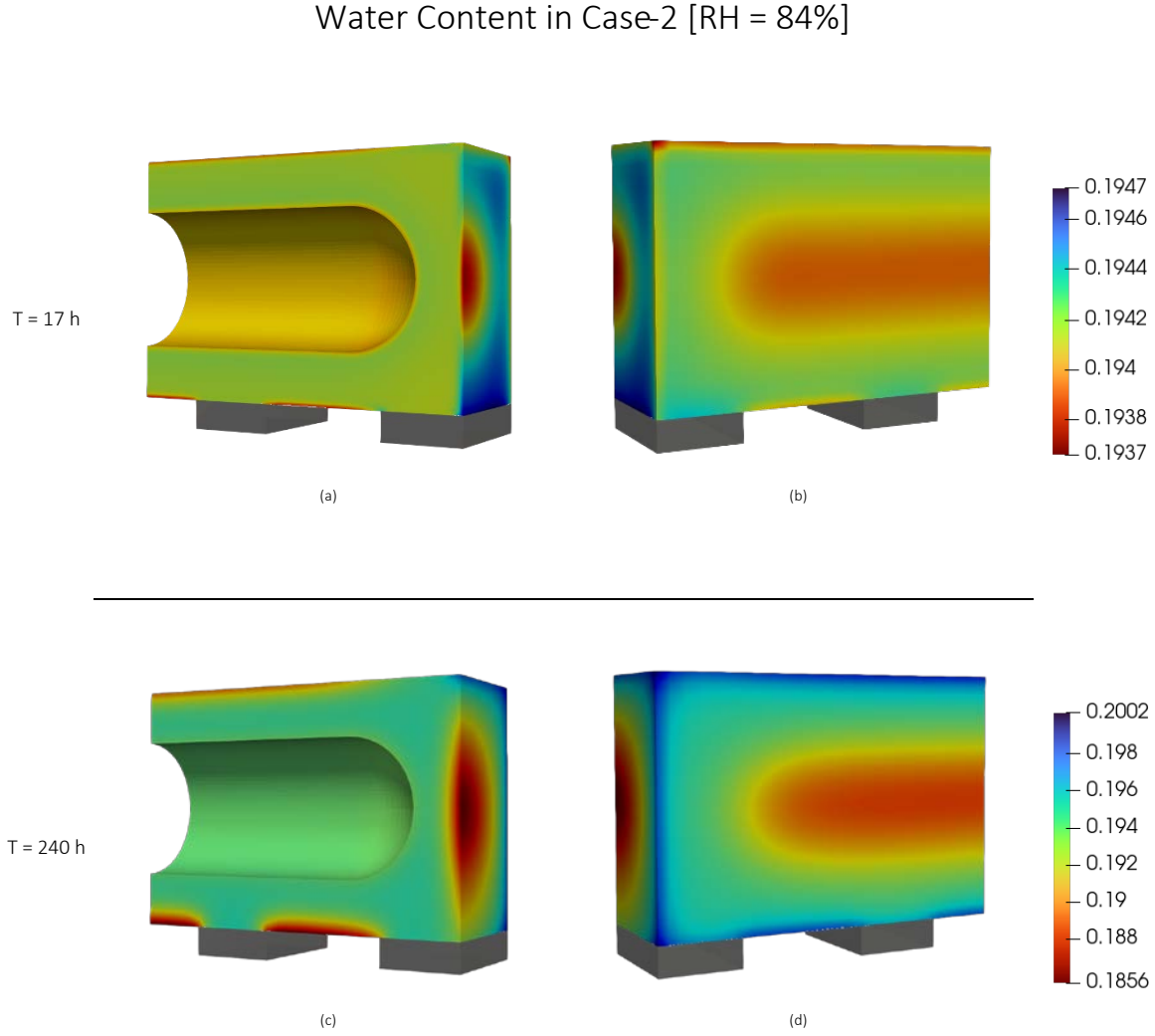

Figure 9-24: The water content distribution in the bentonite buffer box after 17 hours and after 240 hours

To get a better picture of which parts of the buffer that might undergo swelling, Figure 9-24 shows the water content distribution in Case-2 after 17 hours (approximately corresponding to the time when the water content reach its local maximum value as seen in Figure 9-23) and 240 hours. The results show that after 17 hours the water content increased along the outer horizontal surface of the buffer box, while the edges of the buffer box exhibited a slight decrease in water content.

From Figure 9-24 it can also be seen that, if the buffer box is left for a prolonged time (240 hours) in the steel container, the water content will increase along the outer edges of the buffer box. While only the results from Case-2 are shown in Figure 9-24 this behaviour could also be seen in Case-1.

In Figure 9-25 the maximum volume ratio due to shrinkage in the buffer box is shown. The graphs clearly show the influence of the dry air in Case-1, leading to a spike in the maximum

value of the volume ratio during the first fifty hours. After the first fifty hours the moisture redistribution due to the heat from the UFC starts to dominate the drying process in both cases.

In Sandén et. al. (2013) the effect of drying on buffer blocks were evaluated by exposing compacted MX-80 blocks to different RH at room temperature. The conclusion of these experiments was that for the tested blocks, a change in the total volume of a block of around 0.5% could lead to fracture formation. This corresponds to a volume ratio of 0.005, which is shown as the dashed black line in in Figure 9-25. The maximum value of the volume ratio in Figure 9-25 reached this value for the model with initially dry air (Case-1) already after about 15 hours, which indicates a risk that fracturing will occur if the buffer box is stored under such conditions. The buffer box stored in conditions with a higher initial RH (Case-2) shows a much slower increase in the maximum volume ratio, indicating that the risk of any fractures developing during the first 2-3 days after enclosure of the steel container is very small.

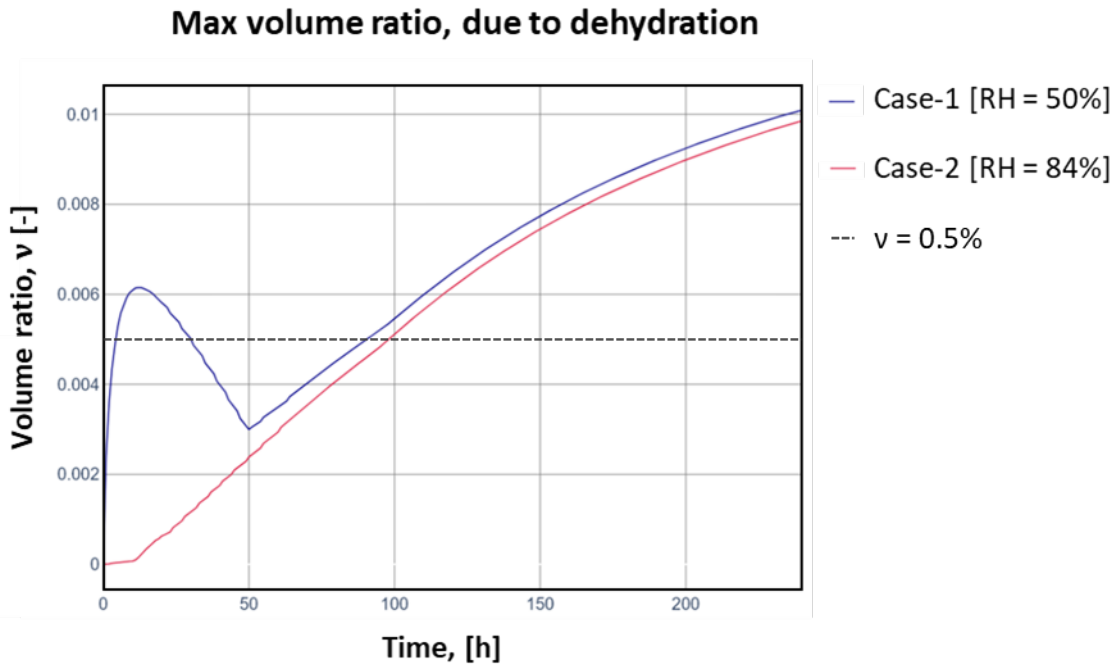

Figure 9-25: The maximum value of the volume ratio in Case-1 (blue solid line) and Case-2 (red solid line)

Figure 9-26 shows the volume ratio distribution in the bentonite after 10, 50 and 240 hours. The scale was defined to be in the interval 0 % to 0.5 %, as values above 0.5 % indicate an increased risk for crack formation (Sanden et al 2013). By comparing the state of the volume ratio after 10 hours in Case-1 and Case-2 respectively it can be seen that Case-1 shows an increase in the volume ratio on the vertical outer surface of the buffer box, while in Case-2 the volume ratio remains very close to zero. This indicates that early on the initial relative humidity of the air inside the steel container is the major driving force of any volume change.

After approximately 50 hours, the results are relatively similar for both cases, and the volume changes are still relatively small, at most around 0.2 % in the outer edges of the buffer box.

After 50 hours the effect of the impermeable rubber pads also starts to show, as the volume ratio increases in the area between the rubber pads. After 240 hours, the volume ratio reaches around 0.5 %, which could indicate an increased risk of fracture formation (Sanden et al 2013). Furthermore, the results in Figure 9-26**,** give a good overview of where large gradients of the volume ratio might be seen.

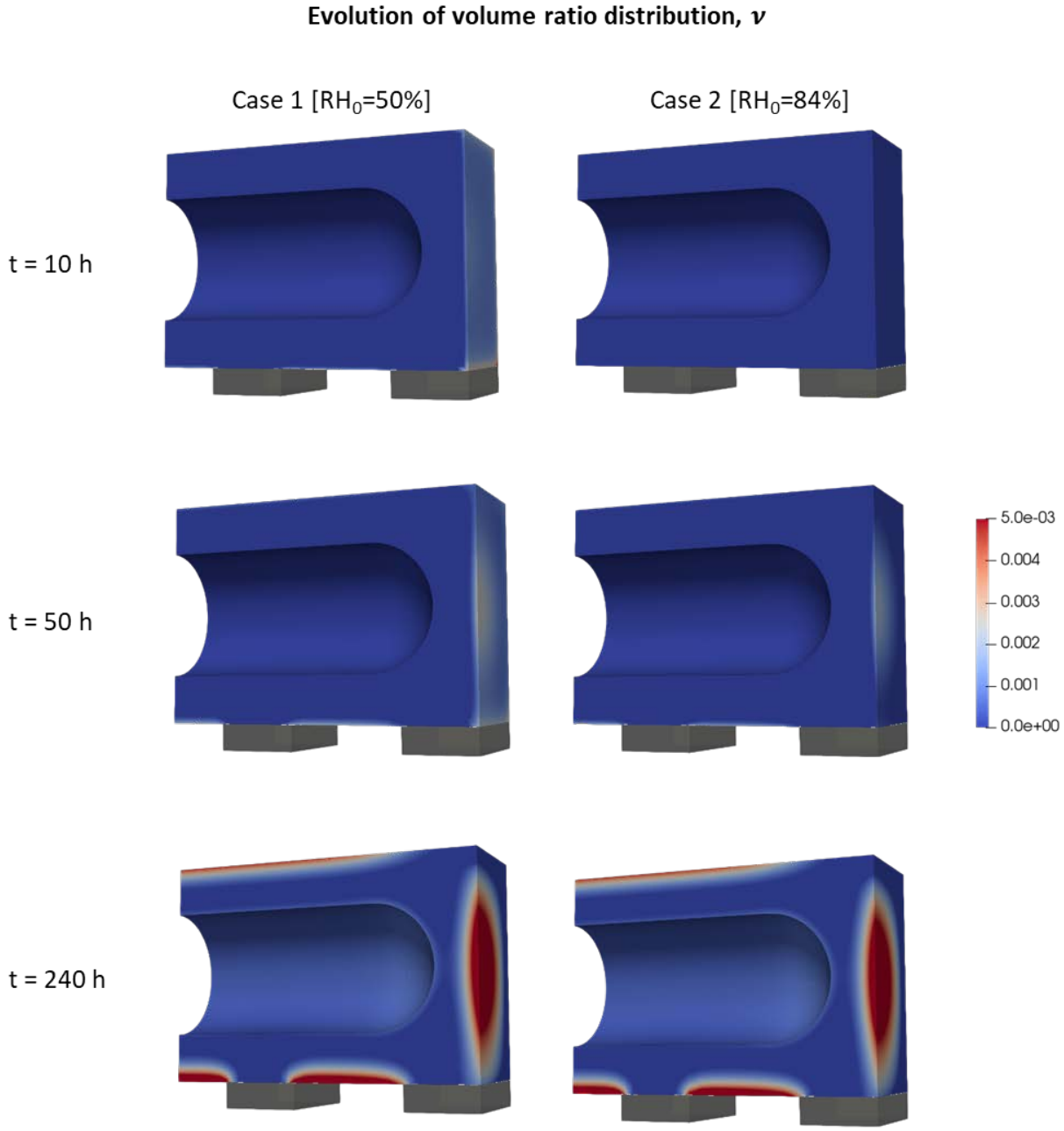

Figure 9-26: The volume ratio distribution on the surface of the bentonite buffer box at Time = 10, 50 and 240 hours

The risk of fracture formation is highest in regions where neighbouring points have a large difference in volume change. To get a graphical representation of this, the gradient of the volume ratio field, ∇v, was used. Taking the gradient of a scalar field in more than one-dimension results in a vector field. To simplify the visualization of this field, the length of the vectors, $\|\nabla v\|$, was calculated. A large value of $\|\nabla v\|$ means that neighbouring points have a large difference in volume change and there is a potential risk for fracture formation.

Figure 9-27 show $\|\nabla v\|$ over the boundary close to the UFC hemi head, the blue shaded face in the geometry at the upper right corner. In Figure 9-28 $\|\nabla v\|$ is shown over the bottom of the buffer box, also indicated in blue in the geometry at the upper right corner. Results are shown for the two cases with different initial RH at 10, 50 and 240 hours.

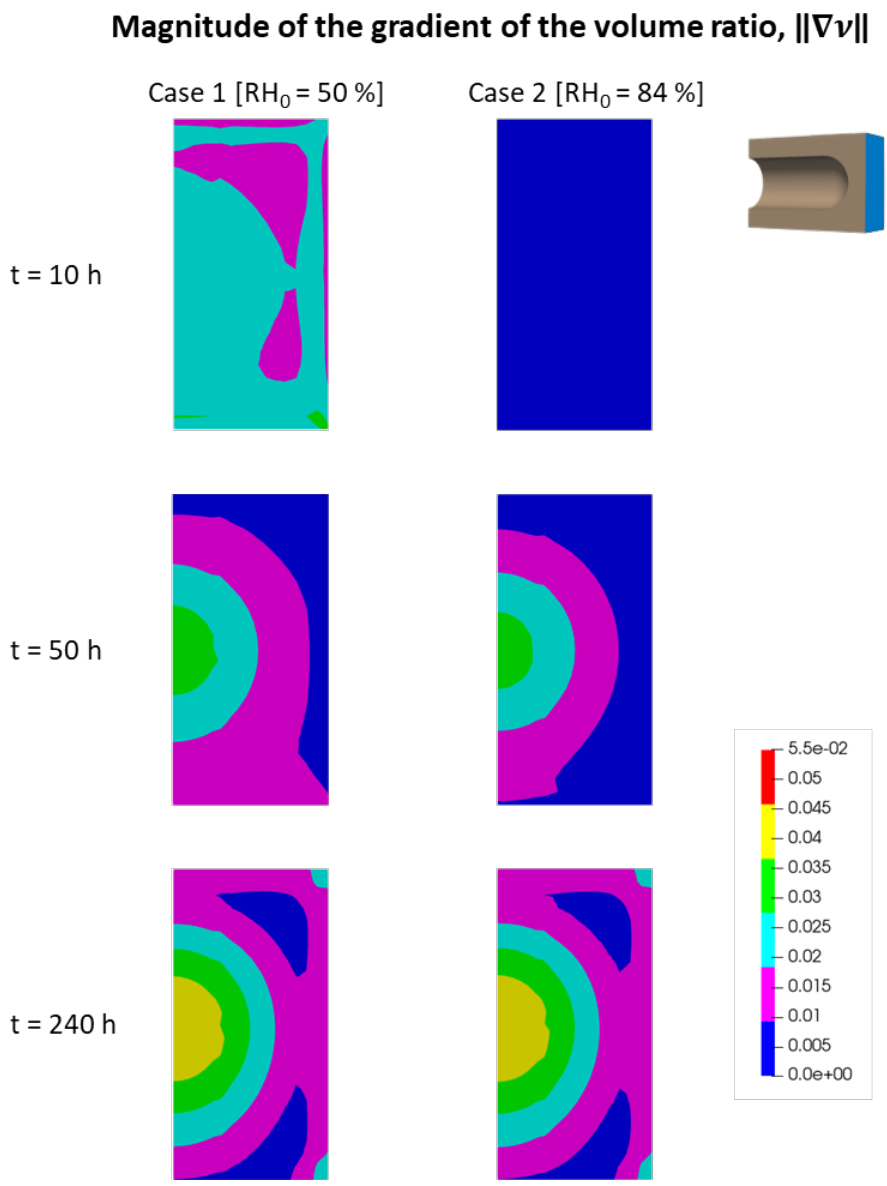

Figure 9-27: The magnitude of the gradient of the volume ratio on the outer right boundary of the buffer box as indicated by the blue colour in the top right corner

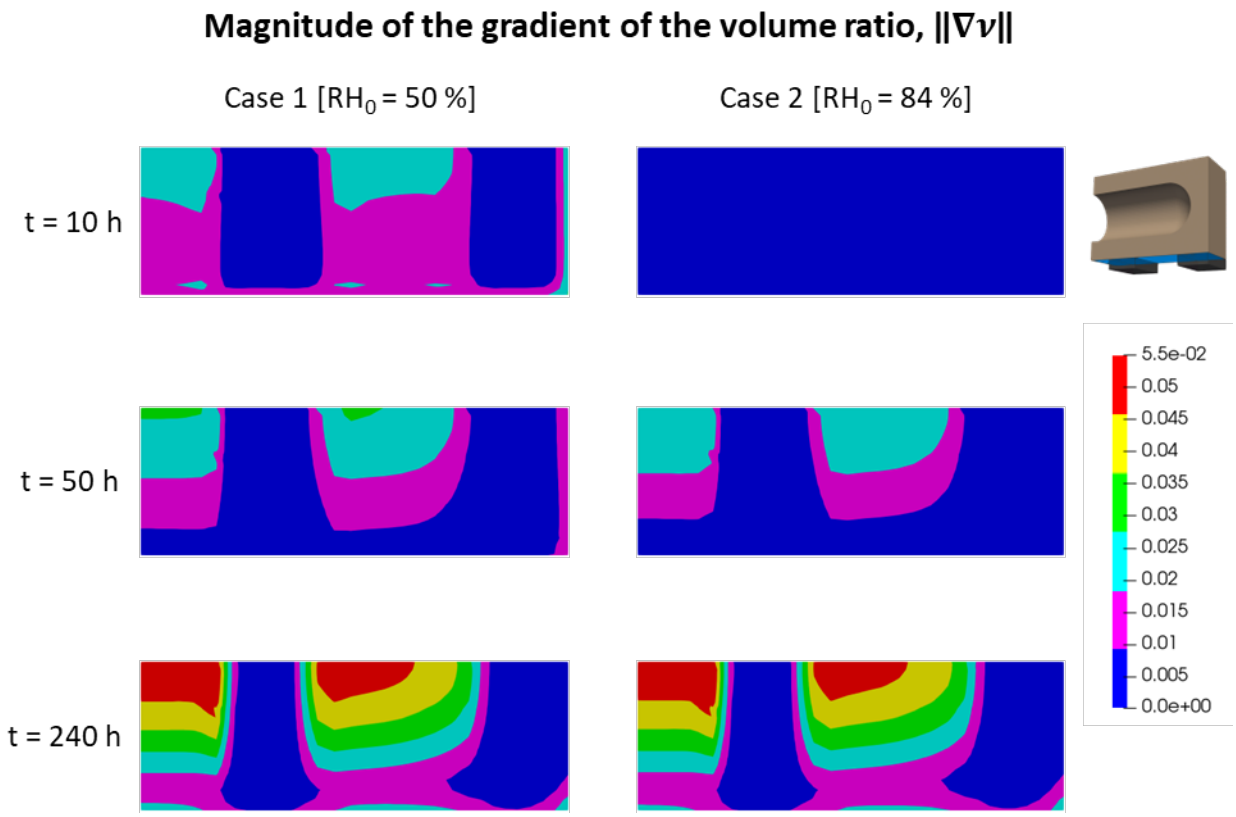

Figure 9-28: The distribution of the gradient of the volume ratio along the bottom of the bentonite buffer box as indicated by the blue colour in the top right corner

Figure 9-27 shows a local maximum of $\|\nabla\nu\|$ at the center of the buffer box and Figure 9-28 shows two local maxima between the rubber feet and about the vertical center section. The values at the local maxima between the rubber feet are higher as compared to those shown in Figure 9-27. This indicates that these are the positions where fracture formation is most likely to occur when the buffer box is in the steel container prior to installation.

9.2.4 Conclusions

The modelling and analysis presented in this section was carried out with the purpose of studying how the HCB in the buffer box will behave during transport from the surface facility to the emplacement room. The study aimed at quantifying the risk that fractures could develop in the HCB block due to moisture re-distribution. It utilized a combination of numerical models of the TH evolution in the HCB block in combination with analytical models of the shrinkage of the bentonite based on experimental data. Several conclusions could be drawn from the models and these are discussed below.

Initial RH in the Airgap
The initial RH in the airgap between the HCB and the steel container plays an important role:

- If the RH in the airgap is in, or close to, equilibrium with the RH in the HCB the amount of moisture redistribution during the first 2-3 days will be small (Case-2).
- If the initial RH in the airgap is significantly lower than in the HCB (Case-1) significant drying will take place in the outer parts of the HCB within one day which may lead to significant shrinkage (see Figure 9-25) and thus fractures may occur.

It is thus recommended that the airgap between the buffer box and steel container is climate-controlled so that the relative humidity in the airgap is always kept in equilibrium with the HCB to minimize the risk of fractures. Although a climate-controlled airgap was not directly simulated in this work, experimental studies (such as Sandén et al. 2013) support the notion that this will minimize the risk of fracturing. If this is indeed the choice made, it is also recommended that further modelling of this setup is undertaken.

Duration of Transport Phase

If the bentonite was initially in, or very close to, moisture equilibrium with the airgap (Case-2), the models showed that essentially nothing happened during the first 2-3 hours. Thereafter, the heat generated in the UFC started to build up a temperature gradient, leading to a moisture redistribution in the HCB, potentially causing fractures in the bentonite. If the bentonite was not in equilibrium with the surrounding air, the models indicated that drying or swelling on the surface of the bentonite took place very quickly. However, it should be noted that experimental data (Sandén et al. 2013) showed that it took about 16 hours for surface fractures to develop on blocks placed in dry conditions, and up to four days before the stability of the blocks were significantly affected (i.e., could no longer handled without breaking apart). These laboratory tests did, however, not include any heating of the blocks as is the case here, and thus the process may be quicker. It is thus recommended to keep the transport phase as short as possible. According to the models, the probability that fractures develop is greatest on the outside of the HCB block, in particular near the rubber feet on which the buffer box rests during transport.

Limitations and Further Analysis

There were several limitations to this study which could motivate further analysis. This is described below:

- Simplified treatment of the moisture transport in the airgap: For example, convective transport of gas in the airgap was not simulated (not available in CODE_BRIGHT). Also, the airgap was given parameters such that the RH in the airgap was essentially uniform. This could have implications on the local moisture balance between air and bentonite blocks. A more detailed study with other FEM codes, such as COMSOL Multiphysics, could be used to study the behavior in the airgaps in more detail.
- The steel container of the transport box was assumed to always be exposed to an environment with room temperature. Cooler and/or hotter environments could impact the evolution. Varying the thermal boundary as part of a sensitivity study could be carried out in the future.
- Only two initial values of the RH in the airgap were simulated. Very dry and very wet initial conditions were not analyzed, and if there is a possibility that such RH values may occur, further simulations should be carried out to quantify how this affects the probability of fracturing.
- No mechanical processes were simulated. Hence, the models did not take swelling of the HCB into account. To do that, a THM model would have to be used.

10. LESSONS LEARNED

In this section the lessons learned from all the reported work is discussed. The section is arranged into subsections, each covering a certain topic which was addressed in one or more of the different steps/tasks described in this report. At the end, some remaining questions is given with recommendations for further work.

10.1 Modelling Strategy

When initiating the modelling of the NWMO's emplacement room concept, simplified representations in terms of geometry and physical processes were utilized. The first models only included a single buffer box and isothermal conditions were assumed. These simple models, however, provided insight into possible difficulties with the modelling. During the advanced modelling the representations were gradually made more realistic and complex. That resulted in some challenges for the numerical solver (CODE_BRIGHT).

One "simple" example of the increased complexity and realism of the models was the incorporation of thermal physics. When only considering isothermal conditions in the simple Step 1 and 2 models, drying of the bentonite near the UFC was neglected. More advanced models in those steps included thermal processes and thereby simulated the drying near the UFC. In this case the increase in complexity (incorporation of the thermal physics) gave rise to an effect on the hydraulic process as temperature gradients drive vapour diffusion, which also affected the mechanical process by shrinkage. From those results it was clear that to capture the HM evolution in a representative way, thermal processes must be included in the models.

Another important conclusion from the early modelling concerned which geometrical simplifications that could be made. In the design of the emplacement room, the buffer boxes in the top and bottom rows were placed with an offset corresponding to one spacer block. This meant that it was not possible to construct a model geometry of only a single stack of buffer boxes by using symmetry planes. From earlier work it was known that there were computational limitations which made it important to minimize the geometrical domain of the model as far as possible. The asymmetric offset of the buffer boxes, however, made it difficult to create local/restricted realizations of the real geometry of the repository.

This was handled by creating two local geometries where the top and bottom row were either aligned ("minimum offset") or offset symmetrically ("maximum offset") – these geometries were discussed in more detail in Section 5.1.1. This made it possible to investigate the influence from the offset between the upper and lower rows of buffer boxes. By simulating the THM evolution in both geometries it was shown that the HM evolution differed very little between the two. Thus, the actual design was suitably bounded within the symmetrical representations. Perhaps a more important conclusion was that the local geometry could be simplified as to only include one stack of buffer boxes. The modelling in Step 2 also showed that the geometry with aligned buffer boxes was numerically favourable, so this geometry was used in the rest of the modelling. One consequence of this is that the maximum temperature recorded in the models presented in Sections 6 - 9 might be slightly higher than in a "true" geometry where the spacing between the UFCs is larger.

Starting out with simplified models also meant that boundary conditions which led to numerical problems could easily be identified. For example, it was discovered that prescribing a high-water

inflow from the floor of the emplacement room directly at the HCB blocks led to severe convergence problems. This was circumvented by including the concrete slab that is planned to be cast to even out the floor after the blast excavation.

10.2 Rate and Mode of Water Inflow

An important goal of the modelling was to understand how the character of the water inflow from the host rock affects the buffer. Bentonite, a material which displays a very strong coupling between hydraulic and mechanical behavior, can respond differently if supplied water at a high or low inflow rate, and if the “mode” (homogeneously, heterogeneously from side/sides/top/bottom) of water access is changed. The modelling in Task 1 and 2 primarily focussed on analysing the buffer behavior under different water access scenarios. Different rates of water inflow (fast, slow and no inflow) and different variations of the mode of water access was analyzed.

One conclusion from the models is that for the crystalline host rock fast or slow inflow primarily affected the transient evolution (stress paths, evolution of UFC displacement etc.) but the influence on the final state was limited. The final dry density fields in the buffer were rather similar between the models simulated in Task 1, although some variations were seen in front of the UFC's hemi head.

Of greater significance is if the inflow is limited to a few high-flowing features in one emplacement room. In such a scenario, analyzed in subtask 1.1 (Section 6.1), swelling of the buffer box(es) near the fracture in an otherwise dry emplacement room may lead to low final dry densities near the inflow region. Several engineering solutions could be used if such a scenario occurred, for example HCB blocks with no UFC could be placed where high-flowing fractures intersect the emplacement room. It should be noted that engineering solutions require careful mapping of the emplacement room tunnels.

Scenarios of heterogeneous inflow from fracture planes or points have not been studied here. One important aspect of such inflows, which also makes them difficult to model, is the possibility of formation of highly permeable “pipes” in less dense materials if the inflow is sufficiently high. The emergent “free pathways” for water and high inflow could in turn lead to erosion and thereby lowered dry densities. The erosion of buffer material has been studied in the laboratory for pellets fillings (see, for example, Laurila et al 2013 and Börgesson et al 2015). In granular materials, however, piping formation and erosion is to our knowledge not as well studied. It would therefore be valuable with studies of the piping phenomenon and what the effects of piping may be.

10.3 Dry Densities at Installation and Emplacement Room Geometry

In Task 3, a sensitivity analysis was carried out to analyze how variations in installation dry densities and dimensions of the emplacement room cross-section could influence the buffer evolution during water uptake and the final state. Understanding how such variations affect the state of the buffer after full saturation is reached is important as it provides information about the long-term safety function of the buffer. Thus, it can be used to identify constraints on the dry density at installation.

A set of models were constructed with different initial dry densities in the GFM and HCB, and different thickness of the GFM. The range of dry densities at installation was 1410 kg/m^3 - 1550 kg/m^3 and 1600 kg/m^3 - 1750 kg/m^3, in the GFM and HCB, respectively. Some models also had different dry densities in the GFM situated between the buffer box and emplacement room walls as compared to the dry density in the GFM between the buffer box and the ceiling of the emplacement room.

The cases were chosen to include the most extreme scenarios expected in terms of combinations of low and high dry densities in the different components. Using this strategy one can understand if any of these extremes pose a problem to the safety function of the buffer.

The thickness of the GFM volume (i.e., the emplacement room cross-section) was also varied from the original 0.225 m to 0.300 m. A larger thickness of the GFM decreases the average dry density and should therefore result in lower dry densities after swelling.

As an example, the case with a low installed dry density in both GFM and HCB and an increased thickness of the GFM resulted in the lowest dry density of all models. At full saturation, this model showed a volume averaged dry density of 1540 kg/m^3 and a minimum dry density of 1440 kg/m^3 which both are below the target dry density of 1600 kg/m^3.

While the case of low dry-density is important, as important safety functions of the buffer (such as decreased microbial activity and low permeability) is dependent on the dry density being high enough, the case of very high dry densities may also be problematic, as it can lead to high mechanical pressures acting on the UFC. In the models with high initial dry densities in both the GFM and HCB, the normal stress on the UFC reached values of around 18 MPa once the buffer reached full saturation, as compared to around 12 MPa in the base case scenario.

10.4 Airgaps

In most of the modelling, the presence of airgaps between different components were neglected. Some airgaps will undoubtedly be left after installation of the components in the emplacement room; between HCB components, between the UFC and buffer box, between the GFM and the ceiling of the emplacement room. In the 3D simulations, airgaps were neglected for several reasons: swelling into airgaps is complicated to simulate and require a very high mesh density, the geometry of the airgap between the UFC and HCB is very complicated to mesh when including gravity (as the UFC rests on the HCB block) and to handle the mechanics properly, friction between the components should ideally be included, which in turn is numerically demanding.

As part of Task 3, a set of simplified models including airgaps were developed. These utilized a plane 2D geometry and excluded gravity. An identical model excluding the airgaps was used for comparison. In this way, the influence from including airgaps could be studied qualitatively.

As for all studies in this work, the focus was to understand the effect on the HM evolution. The airgap between the HCB and UFC will change the temperature gradient at the interface, but CODE_BRIGHT is not well suited at simulating heat transfer through airgaps and conclusions on the effect on the maximum temperature is better analyzed with other tools.

The main effect of the airgaps on the HM evolution was a change in mechanical pressure (i.e., swelling pressure) acting on the UFC. It decreased by as much as 30% in some locations and

the distribution of normal stress on the UFC was significantly altered. Hence, the models constructed in full 3D without airgaps should be considered as overly conservative in terms of how high the reported net mean stress acting on the UFCs is.

10.5 Host Rock

The type of host rock at the repository site, either crystalline or sedimentary, will influence the behavior of the buffer. The thermal and hydraulic properties are different between the two rock types and the groundwater also has different salinity.

Modelling carried out in Step 1 & 2 as well as Task 1 – 3 assumed a crystalline rock site. The choice of host-rock type is reflected in the thermal and hydraulic boundary and the HM properties of the MX-80 bentonite.

As the site of the repository remains undecided at the time of writing, Task 4 was devoted to understanding how a change to a sedimentary host rock may change the results and conclusions drawn from the previous modelling.

From the viewpoint of the buffer, the most important change when switching to a sedimentary host rock was the high salinity in the groundwater. The TDS in the sedimentary rock is expected to be around 300 g/L, which will significantly reduce the swelling pressure and increase the hydraulic conductivity of the bentonite. While further laboratory work to quantify this effect would be useful, the data presented in Dixon (2019) shows a reduction in swelling pressure from around 10 MPa or slightly below to about 3 MPa at HCB buffer densities.

The simulations presented in Section 9 showed that this reduction in swelling pressure, as expected, led to a significant decrease in the normal stress acting on the UFCs, but also to significantly less homogenization of the buffer. Furthermore, the increase in hydraulic conductivity meant that the buffer, if provided with enough water, could saturate faster than in crystalline rock. The sedimentary host rock site currently evaluated in Canada, however, has very low permeability, and the water supply to the repository is expected to be very limited, which promotes scenarios where saturation times will be very long.

A general conclusion from the modelling of Task 4 is that, to estimate values of stress and homogenization in the buffer, the host rock and groundwater properties must be considered. If a sedimentary site is selected, the models in Task 1 - 3 would need to be updated.

10.6 Remaining Questions/Recommendations

Several questions remain after the work presented here. These comes both from modelling uncertainty as well as from uncertainties on a more fundamental level, i.e., uncertainties in the theoretical understanding of the hydro-mechanical behavior of bentonite.

A first important point to make is that results of this modelling can only be used to draw conclusions on the behaviour of the buffer up until full saturation. After the buffer is saturated, long-term effects, such as creep and ion exchange, may impact HM properties of the bentonite significantly. This could take the system out of the equilibrium established immediately after full saturation and further evolution may occur. Studies of such processes relate to the

understanding of the bentonite material on a more fundamental level and are highly recommended.

Another important point is that of piping and erosion. With discrete water inflows into the bentonite there comes the risk of piping, which in turn can lead to mechanical erosion of the material. The fundamental understanding of the piping process (i.e., under which conditions it occurs and under which circumstances pipes will be resealed by the swelling of the surrounding bentonite) is limited, particularly for granular bentonite materials.

In terms of modelling uncertainty, two major questions remain:

1) the swelling around the hemi-head of the UFC, and
2) the homogenization of bentonite in high-salinity groundwater.

The first item “the swelling around the hemi head of the UFC” is important since it is in the region where the lowest dry density after full saturation is observed. Thus, it is in the region that the safety function of the buffer is close to the design limits. Focused but simplified numerical studies have been attempted (Appendix E), but studies of bentonite swelling around spherical objects are novel and experimental data for calibration is scarce. Other waste management organizations use cylindrical containers with flat edges. Laboratory scale-tests of the swelling around the hemi-head of the UFC, in combination with modelling, would increase the confidence in the results.

The second item “the homogenization of bentonite in high-salinity groundwater” is important if a sedimentary host rock site is chosen. The models presented in Task 4 showed significantly less homogenisation and swelling pressure as compared to the crystalline site models. This can lead to volumes of the bentonite with low dry density, or alternatively high dry densities near the UFC after full saturation is reached. To verify if these results are correct, laboratory studies of the homogenization process of bentonite (swelling into gaps, swelling of HCB/GFM in confined volumes) supplied with external water of different salinity and water-uptake rates would be valuable.

11. REFERENCES

Åkesson, M., L. Börgesson and O. Kristensson. 2010a. 'SR-Site Data Report. THM Modelling of Buffer, Backfill and Other System Components.' SKB TR-10-44. Svensk Kärnbränslehantering AB.

Åkesson, M., O. Kristensson, L. Börgesson, A. Dueck and J. Hernelind. 2010b. 'THM Modelling of Buffer, Backfill and Other System Components - Critical Processes and Scenarios'. SKB TR-10-11. Svensk Kärnbränslehantering AB.

Birch, K. and M. Mielcarek M, 2017. 'Development of NWMO Buffer Program – from Concept to Full Scale Demonstrations.' Proceedings of the American Nuclear Society International High-Level Radioactive Waste Management Conference. Charlotte, USA.

Birgersson, M., M. Hedström, O. Karnland and A. Sjöland, 2017. 'Bentonite buffer: macroscopic performance from nanoscale properties. Geological Repository Systems for Safe Disposal of Spent Nuclear Fuels and Radioactive Waste.' Elsevier.

Börgesson L, L-E Johannesson, T Sandén, J Hernelind, 1995. 'Modelling of the physical behavior of water saturated clay barriers'. SKB TR-95-20. Svensk Kärnbränslehantering AB.

Börgesson, L. 2001. 'Äspö Hard Rock Laboratory – Compilation of Laboratory Data for Buffer and Backfill Materials in the Prototype Repository.' SKB IPR-01-34. Svensk Kärnbränslehantering AB.

Börgesson L., T. Sandén, A. Dueck, L. Andersson, V. Jensen, U. Nilsson, S. Olsson, M. Åkesson, O. Kristensson, U. Svensson, 2015. Consequences of water inflow and early water uptake in deposition holes. EVA Project. SKB TR-14-22. Svensk Kärnbränslehantering AB.

Olivella, S., J. Vaunat and A. Rodriguez-Dono. 2023. CODE_BRIGHT 2023 User's Guide, UPC, Barcelona, Spain.

Coll, A, R Ribó, M Pasenau, E Escolano, JS Perez, A Melendo, A Monros, and J Gárate. 2018. 'GiD User Manual'. CIMNE. https://www.gidsimulation.com/.

Dixon, D., A. Man, R. Santosh, J. Stone and G. Siemens, 2018. Bentonite Seal Properties in Saline Water. NWMO TR-2018-20. Nuclear Waste Management Organisation.

Dixon, D. 2019. 'Review of the T-H-M-C Properties of MX-80 Bentonite.' NWMO-TR-2019-07. Nuclear Waste Management Organisation.

Dueck, A. 2004. 'Hydro-Mechanical Properties of a Water Unsaturated Sodium Bentonite. Laboratory Study and Theoretical Interpretation'. Doctoral Thesis (monograph), Soil Mechanics and Foundation Engineering, Lund University.

Dueck, A. and U. Nilsson. 2010. 'Thermo-Hydro-Mechanical Properties of MX-80 - Results from Advanced Laboratory Tests'. SKB TR-10-55. Svensk Kärnbränslehantering AB.

Dueck A, L-E Johannesson, O Kristensson, S Olsson, 2011. ‘Report on hydro-mechanical and chemical-mineralogical analyses of the bentonite buffer in Canister Retrieval Test’. SKB TR-11-07. Svensk Kärnbränslehantering AB.

Dueck, A., L. Börgesson, O. Kristensson, D. Malmberg, M. Åkesson and J. Hernelind. 2019. ‘Bentonite Homogenisation - Laboratory Study, Model Development and Modelling of Homogenisation Processes’. TR-19-11. Svensk Kärnbränslehantering AB.

Guo, R. 2017. Thermal response of a Canadian conceptual deep geological repository in crystalline rock and a method to correct the influence of the near-field adiabatic boundary condition. Engineering Geology 218 (2017) 50–62. http://dx.doi.org/10.1016/j.enggeo.2016.12.014"

Guo, R. 2018. ‘Thermal Response of a Conceptual Deep Geological Repository in Sedimentary Rock’. NWMO-TR-2018-09. Nuclear Waste Management Organisation.

Johannesson, L-E., O. Kristensson, M. Åkesson, P. Eriksson, and M. Hedin. 2014. ‘Tests and Simulations of THM Processes Relevant for the Buffer Installation.’ SKB P-14-22. Svensk Kärnbränslehantering AB.

Karnland O., 1997. Bentonite swelling pressure in strong NaCl solutions – Correlation between model calculations and experimentally determined data. SKB TR 97-31, Svensk Kärnbränslehantering AB.

Karnland O, T Sandén, L-E Johannesson, 2000. ’Long term test of buffer material’. SKB TR-00-22. Svensk Kärnbränslehantering AB.

Karnland O, S. Olsson, U. Nilsson, 2006. ’Mineralogy and sealing properties of various bentonites and smectite-rich clay materials.’ SKB TR-06-30. Svensk Kärnbränslehantering AB

Laurila T., M. Olin, K. Koskinen, P. Sane (ed), 2013. Current Status of Mechanical Erosion Studies of Bentonite Buffer. Posiva 2012-45, Posiva OY.

Olivella, S., A. Gens, J. Carrera, and E.E. Alonso. 1996. ‘Numerical Formulation for a Simulator (CODE_BRIGHT) for the Coupled Analysis of Saline Media’. *Engineering Computations* 13 (7): 87–112. https://doi.org/10.1108/02644409610151575.

Sandén, T., U. Nilsson, and L. Andersson. 2016. ‘Investigation of Parameters Influencing Bentonite Block Quality - Laboratory Investigation.’ SKB P-16-06. Svensk Kärnbränslehantering AB.

Sandén, T., S. Olsson, L. Andersson, A. Dueck, V. Jensen, E. Hansen and A. Johnsson. 2013. ‘Investigation of Backfill Candidate Materials’. SKB R-13-08. Svensk Kärnbränslehantering AB.

Sellin, P., M. Åkesson, O. Kristensson, D. Malmberg, L. Börgesson, M. Birgersson, A. Dueck, O. Karnland, and J. Hernelind. 2017. ‘Long Re-Saturation Phase of a Final Repository - Additional Supplementary Information’. SKB TR-17-15. Svensk Kärnbränslehantering AB.

SKB, and POSIVA. 2017. ‘SKB and Posiva (2017). Safety Functions, Performance Targets and Technical Design Requirements for a KBS-3V Repository - Conclusions and Recommendations from a Joint SKB and Posiva Working Group.’ Svensk Kärnbränslehantering AB and Posiva Oy, Posiva SKB Report 01.

van Genuchten, M.Th. (1980). ‘A closed-form equation for predicting the hydraulic conductivity of unsaturated soils’. Soil Science Society of America Journal. 44 (5): 892–898.

APPENDIX A: NUMERICAL VERIFICATION AND MATERIAL MODEL ACCURACY OF MODELS SIMULATED IN STEP 1

In this appendix the numerical verification carried out for the models simulated in Step 1 (reported in Section 4) as well as the validation of the material model is described.

A.1 Verification of Numerical Solution – HM Models

The numerical solution was verified by constructing two additional models, one in which a finer mesh (8470 as compared to 5742 elements, i.e., almost 50 % more elements) was used and one in which the timestep was always kept at least a factor of two below the timestep in the base case model.

The results were evaluated in terms of both the mechanical and hydraulic evolution:

1) The minimum and maximum net mean stress at steady state was compared between the three different models. Only the stress in the buffer component was analysed. The verification criteria used was to check that the solution changed by 1% or less. The values were as follows:

Model	p'_{min}	$\Delta p'_{min}$**[%]**	p'_{max} **[MPa]**	$\Delta p'_{max}$**[%]**
Base case	5.17	-	10.94	-
Fine mesh	5.13	-0.8	10.92	-0.2
Short time-step	5.17	0	10.94	0

2) The time until saturation in the buffer was evaluated by analysing the total degree of saturation in the buffer sample (by integrating the degree of saturation over the volume of the buffer components). The verification criteria used was to check that the time until 98% saturation changed by 1% or less.

Model	$t_s^{98\%}$	$\Delta t_s^{98\%}$ **[%]**
Base case	15.79	-
Fine mesh	15.79	0
Short time-step	15.63	-1

As the base case model fulfilled the defined criteria the verification of the numerical solution was completed successfully.

A.2 Verification of Numerical Solution – THM Models

The numerical solution in the THM models was verified by constructing two additional models: one with a finer mesh (8470 as compared to 5742 elements) and one with a factor of two shorter time-steps, and comparing the results from these with those of the base case THM model. The results for minimum and maximum net mean stress change were:

Model	p'_{min}	$\Delta p'_{min}$[%]	p'_{max} [MPa]	$\Delta p'_{max}$[%]
Base case	5.33	-	10.90	-
Fine mesh	5.30	-0.6	10.92	0.2
Short time-step	5.32	-0.4	10.87	-0.3

The time until saturation in the last point changed as followed:

Model	$t_s^{98\%}$	$\Delta t_s^{98\%}$ [%]
Base case	19.5	-
Fine mesh	19.5	0
Short time-step	19.4	-0.5

As the base case model fulfilled the defined criteria the verification of the numerical solution was completed successfully.

A.3 Material Model Validation

The material model used to describe the bentonite in the models was validated by analysing the net-mean stress – void ratio evolution, as well as the net-mean stress – deviatoric-stress evolution. These are discussed separately below.

A.4 Net-mean Stress – Void Ratio Evolution

To validate the material model used for the bentonite it was required that after full saturation, all points in the net mean stress (p') – void ratio (e) space should lie between the swelling pressure curve and the swelling pressure curve multiplied by a factor of two. In Figure A-1 the p'-e evolution in seven different points in the buffer box/GFM from the HM base case model are shown.

The behaviour in the HCB and GFM is quite different, which is as expected. The points in the GFM (red and orange dashed lines) first underwent swelling (during the water-uptake phase) whereafter they were compressed as the HCB took up water and swelled. All analysed points were, after full saturation, found inside the region bounded by the swelling pressure (grey line) and the swelling pressure multiplied by two (dashed grey line). The points in the GFM showed an increase in both net mean stress and void ratio and in the final water-saturated state. The points in the blocks (green, pink, cyan, black and purple solid lines) all end up on the swelling pressure curve.

In Figure A-2 the evolution in p'-e space is plotted from the base case THM model. The evolution was very similar to that seen in the HM model (Figure A-1) discussed above.
The final state in both models fulfilled the defined criteria and hence the material model was validated.

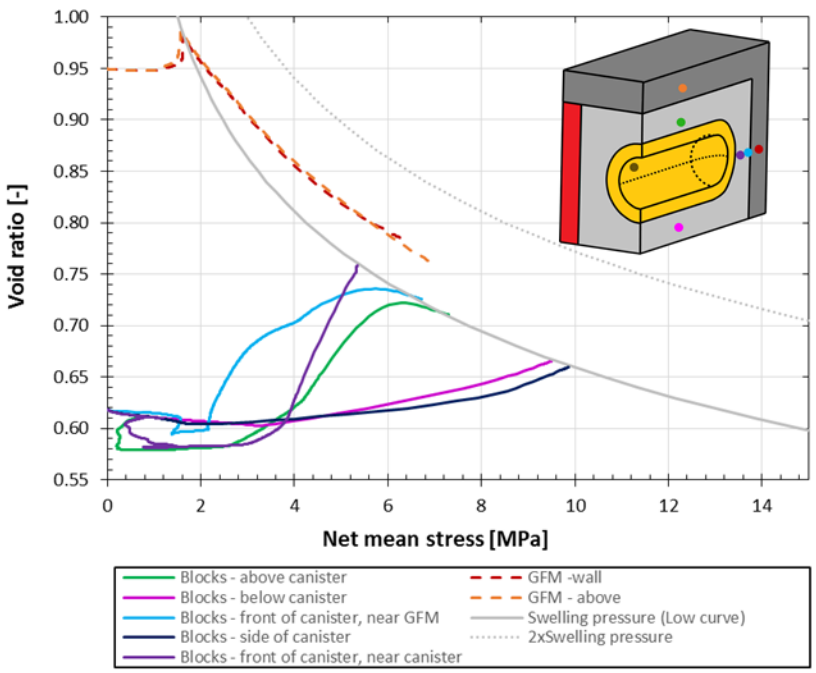

Figure A-1: Net-mean stress – void ratio evolution in seven points in the buffer from the base case HM model

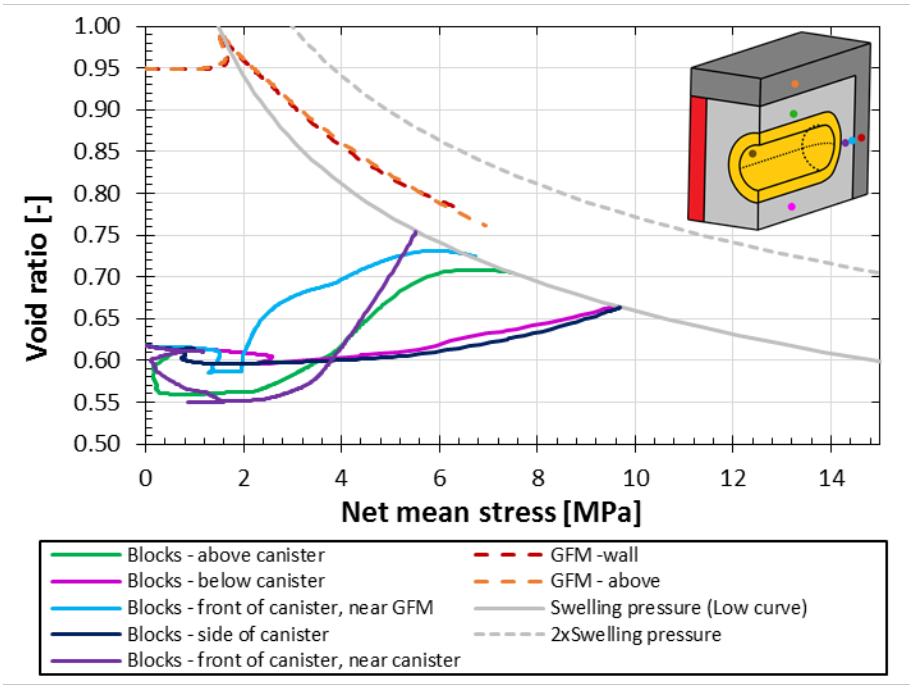

Figure A-2: Net-mean stress – void ratio evolution in seven points in the buffer from the base case THM model

A.5 Net Mean Stress – Deviatoric Stress

Using compression tests a relation between the net mean stress and deviatoric stress at which the sample is driven to failure can be derived see (Åkesson et al., 2010). No points in the buffer should lie significantly above this relation, as this would indicate that the material did not behave as experimentally shown. In Figure A-3 the final state in the HM and THM base case models are shown. The black solid line represents the failure relation, the blue crosses represent the final state in all nodes situated in the buffer components of the HM Base case model and the filled red dots represent the final state in all nodes in the buffer from the THM Base case model. As is seen no points in the models are found above the failure curve.

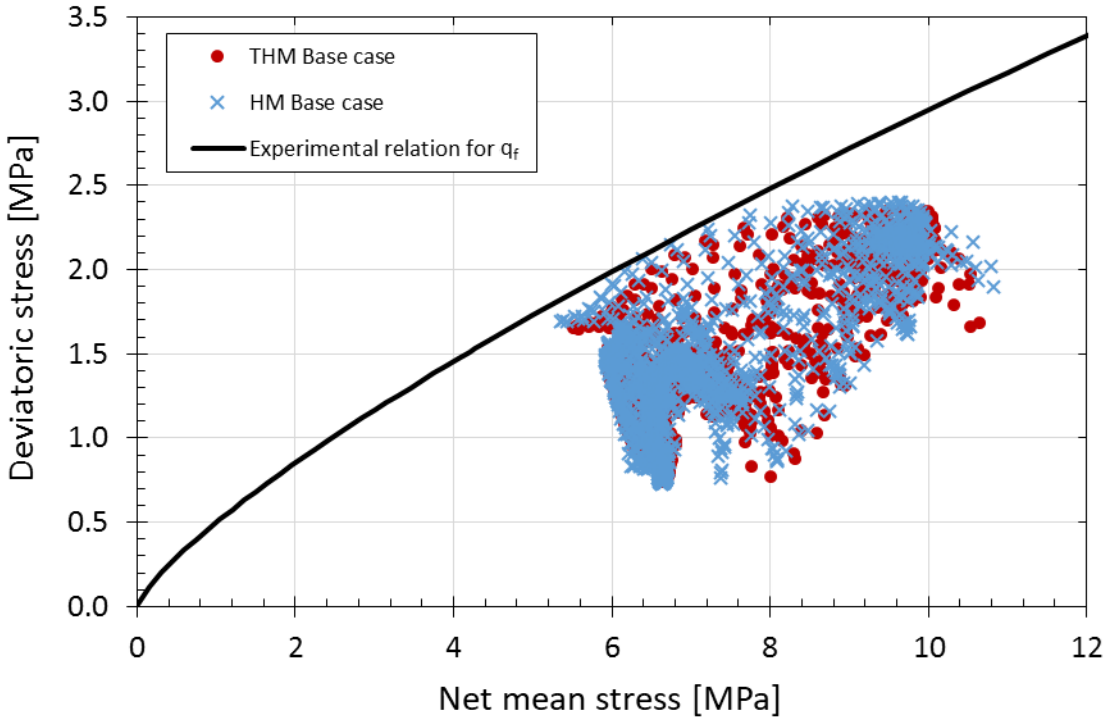

Figure A-3: Net mean stress versus deviatoric stress

A.6 REFERENCES

Åkesson, M, L. Börgesson and O. Kristensson. 2010. SR-Site Data Report. THM Modelling of Buffer, Backfill and Other System Components.' SKB TR-10-44. Svensk Kärnbränslehantering AB.

APPENDIX B: NUMERICAL VERIFICATION AND MATERIAL MODEL ACCURACY OF MODELS SIMULATED IN STEP 2

In this appendix a description of the numerical verification carried out for the models in Step 2 (reported in Section 5) is given, as well as the validation exercise carried out of the material model.

B.1 Verification of Numerical Solution

The numerical solution was verified by constructing a model with a finer mesh (14 722 nodes as compared to 11 138 nodes in the base case), and using significantly shorter time steps. The comparison presented below applies to the model THM_NO_NFW.
The results were:

1) The maximum net mean stress at steady state was compared between the three different models. Only the stress in the buffer component was analysed. The verification criterium was that the solution changed by 1% or less. The results were:

Model	p'_{min}	$\Delta p'_{min}$**[%]**	p'_{max} **[MPa]**	$\Delta p'_{max}$**[%]**
Base case	6.5634		12.903	
Fine mesh/Short time step	6.5508	-0.19	12.932	0.22

2) The time until saturation in the buffer was evaluated – this was accomplished by analysing the total degree of saturation in the buffer sample (checked by integrating the degree of saturation over the volume of the buffer components). The verification criterium was that the time until 98% saturation changed by 1% or less.

Model	$t_s^{98\%}$	$\Delta t_s^{98\%}$ **[%]**
Base case	26.171	
Fine mesh/Short time-step	26.114	-0.22

As the model (THM_NO_NFW) met both the defined verification criteria it was considered acceptable.

B.2 Material Model Validation

The material model was validated by analysing the net-mean stress – void ratio evolution, as well as the net-mean stress – deviatoric-stress evolution. These are discussed separately below.

B.3 Net-Mean Stress – Void Ratio Evolution

By analysing the evolution in net-mean stress (p') – void ratio it can be checked that the buffer generated pressure and/or swelled in accordance with experimental results.

For these models it was required that all points in the buffer should lie between 0.9 times swelling pressure curve and twice the swelling pressure curve in the final state.

In Figure B-1 the final state in the p'-e plane is shown for all nodes in the buffer from the HM and THM base case models. As can be seen no points lie outside the two bounding lines (0.9xPswell, dash-dotted black line and 2xPswell, dashed black line). The blue crosses represent the final state in all nodes situated in the buffer components in the HM model (HM_NO_BC) and the red crosses represents the final state in all nodes situated in the buffer components in the THM model (THM_NO_BC).

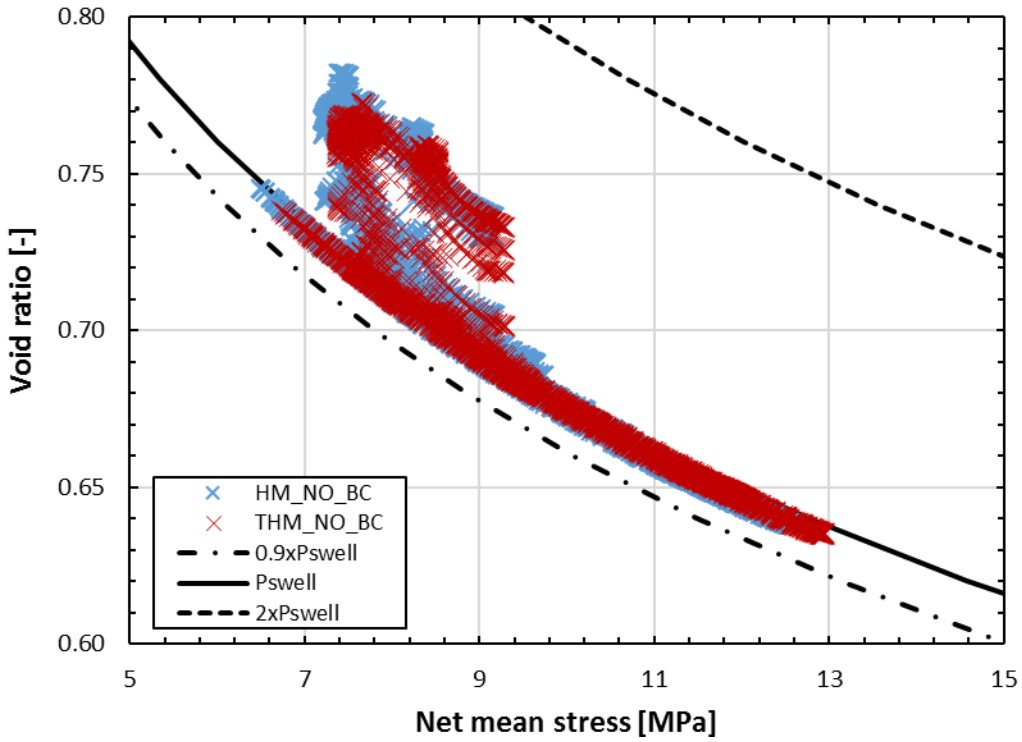

Figure B-1: Net-mean stress – void ratio at full water saturation

B.4 Net Mean Stress – Deviatoric Stress

Using compression tests a relation between the net mean stress and deviatoric stress at which the sample is driven to failure can be derived see (Åkesson et al., 2010). No points in the buffer should lie significantly above this relation, as this would indicate that the material did not behave as experimentally shown. In Figure B-2 the final state in the HM and THM base case models is shown. The black solid line represents the failure relation, the blue crosses represent the final state in all nodes situated in the buffer components in the HM model (HM_NO_BC) and the red crosses represents the final state in all nodes situated in the buffer components in the THM model (THM_NO_BC). As is seen no points in the models are found above the failure curve and hence the material model has been validated.

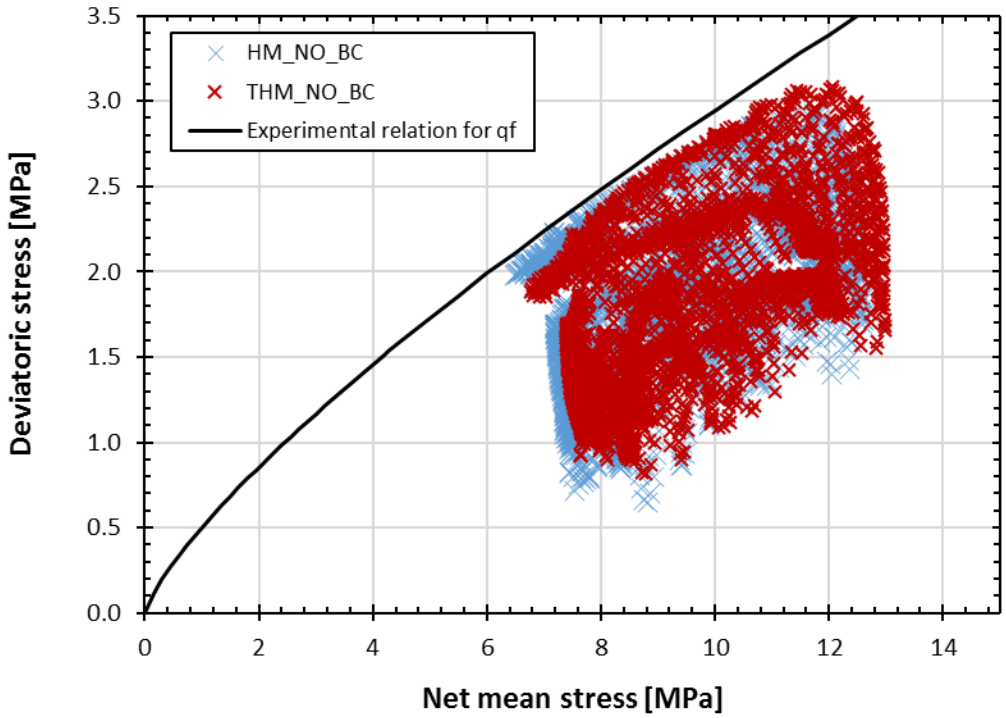

Figure B-2: Final state in net mean stress versus deviatoric stress

B.5 References

Åkesson, M, L. Börgesson and O. Kristensson. 2010. SR-Site Data Report. THM Modelling of Buffer, Backfill and Other System Components.' SKB TR-10-44. Svensk Kärnbränslehantering AB.

APPENDIX C: NUMERICAL VERIFICATION AND MATERIAL MODEL ACCURACY OF MODELS SIMULATED IN TASK 1

In this appendix a description of the numerical verification carried out for the models in Task 1 (reported in Section 6) is given, as well as a description of the validation of the material model. In Section C.1 the verification and validation of the models in subtask 1.1 is reported, whereafter the verification for subtask 1.2 is reported in Section C.2.

C.1 Subtask 1.1

C.1.1 Numerical Accuracy

The numerical accuracy was evaluated by constructing two identical models to the base case model with one exception in each model:

1) In the mesh verification model, the number of nodes were increased by a factor of two
2) In the time-step verification model the number of time-steps were increased by a factor of two

Only the numerical solution of the mechanical part was evaluated, as the hydraulic problem was fully prescribed. The exercise to verify the numerical accuracy and the acceptance criteria are given in Table C-1.

Table C-1: Numerical accuracy and acceptance criteria in subtask 1.1

Process	Analyzed result	Acceptance criteria
Mechanical	Force exerted on the gap material by the swelling buffer box at full water saturation, as evaluated on the surface defining the interface between the two materials	The deviation from the base case is less than 1%

The results of the numerical accuracy evaluation are given in Table C-2. As can be seen, the acceptance criteria defined in Table C-1 are fulfilled. Hence, the both the mesh and time-step setup of the base case model gives reliable results.

Table C-2: Evaluation of numerical accuracy of base case model in subtask 1.1

Model	S3_S11_M001	S3_S11_M001FM0	S3_S11_M001T
Number of nodes	4358	13856	4358
Number of time-steps	1252	9581	2477
Force	-9.6659	-9.7386	-9.6678
Relative difference vs M001 [%]		0.75%	-0.02%

C.1.2 Material Model Verification

To validate that the parameter set used in the models gives a good representation of the behavior of MX-80 bentonite, the verification procedure in Table C-3 was carried out.

Table C-3: Material model verification exercises and acceptance criteria

Verification procedure	Acceptance criteria
Comparison of the net-mean stress as function of void ratio at full water saturation to the measured relation for p_{swell}	The stress state in the selected reference points in the buffer lies between $0.9x p_{swell}(e)$ to $2x p_{swell}(e)$, where $p_{swell}(e)$ is defined from equation 10.10 in Åkesson et al. 2010

The net mean stress against void ratio in the final water saturated (final) state in the base case model is shown in Figure C-1. The plot shows that all points lie close to the swelling pressure curve (solid black line) or somewhat above. The points that align with the swelling pressure curve are those that have only undergone swelling (e.g. situated in the buffer blocks) while the points found above the swelling pressure curve have undergone both swelling and compression, these points are found in the GFM.

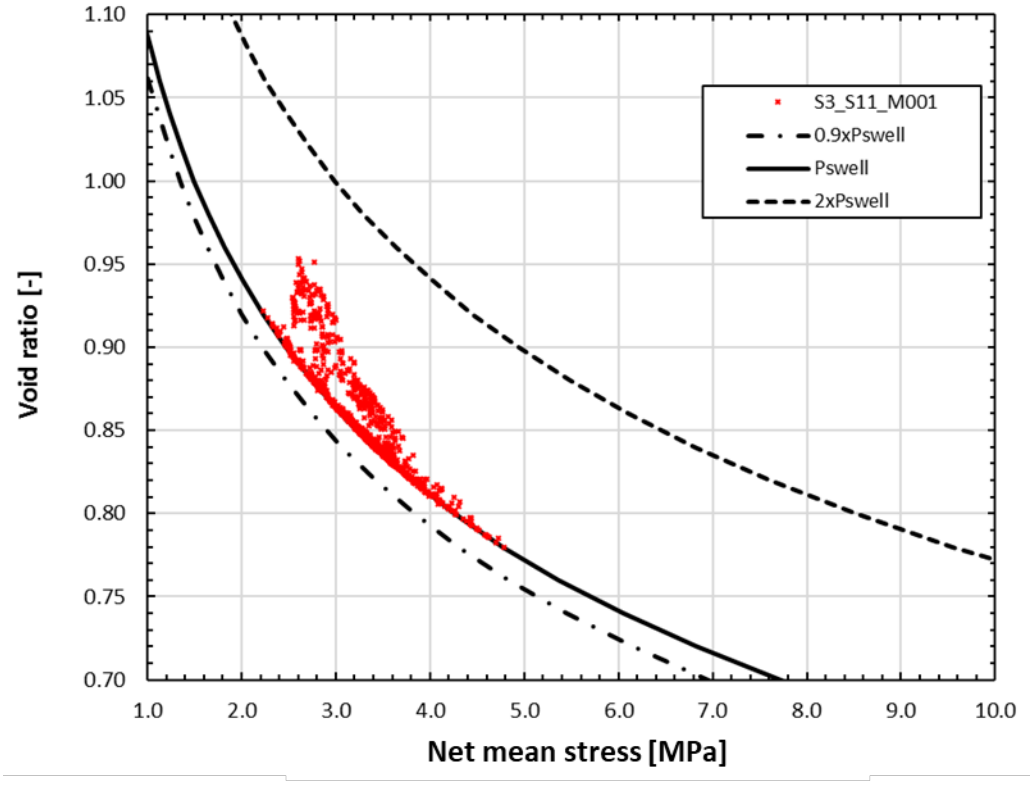

Figure C-1: Net mean stress versus void ratio once all points in the buffer were fully water saturated (data from the base case model in subtask 1.1, S3_S11_M001)

The variation in void ratio for a given value of the net mean stress in the final state would be expected from laboratory experiments due to the hysteretic behavior of bentonite. Bentonite follows different paths in the void ratio – net mean stress space when undergoing swelling and consolidation respectively. While CODE_BRIGHT could not explicitly reproduce this behaviour the material parameters were calibrated to have a similar behaviour in the models. A requirement on the material model/parameter set was that after full water saturation all points in the buffer must lie between the two bounding lines in Figure C-1 (dashed and dash-dotted lines) which, as can be seen, was the case.

C.2 Subtask 1.2

C.2.1 Numerical Accuracy

The numerical accuracy was evaluated by constructing two identical models to the base case model with one exception in each model:

1. In the mesh verification model, the number of nodes were increased by a factor of two
2. In the time-step verification model the number of time-steps were increased by a factor of two

Both thermal, hydraulic, and mechanical processes were evaluated. The numerical evaluations performed, and the related acceptance criteria are listed in Table C-4.

The results of the numerical accuracy evaluation are given in Table C-5. As can be seen, the acceptance criteria defined in Table C-4 are fulfilled.

Table C-4: Exercises to verify numerical accuracy in subtask 1.2

Process	Analysed result	Acceptance criteria
Temperature	Maximum temperature in the buffer box	The deviation from the base case is less than 1%
Hydraulic	Time until integrated liquid saturation in the buffer box reach 99%	The deviation from the base case is less than 1%
Mechanical 1	Maximum net mean stress in the buffer box	The deviation from the base case is less than 1%
Mechanical 2	Final vertical displacement of the lower UFC, as measured on the top/middle of the UFC	The deviation from the base case is less than 1%

Table C-5: Results from evaluation of numerical accuracy in subtask 1.2

	M101	M101_FM	M101_FT
Number of nodes			
Number of time-steps			
Maximum temperature [°C]	83.09	83.10	83.10
Relative difference vs M101 [%]	-	0.011	0.006
Time until $\int_{V_{BBox}} S_l = 0.99$	15.66	15.62	15.66
Relative difference vs M101 [%]	-	0.000	-0.255
Maximum net mean stress [MPa]	12.194	12.207	12.191
Relative difference vs M101 [%]	-	0.107	-0.025
Final vertical displacement of the lower UFC [mm]	11.53	11.56	11.52
Relative difference vs M101 [%]	-	0.260	-0.087

C.2.2 Material Model Verification

To validate that the parameter set utilized in the models gives a good representation of the behavior of MX-80 bentonite, two validation procedures were carried out, these are listed in Table C-6 together with the acceptance criteria.

Table C-6: Material model verification exercises and acceptance criteria

Verification procedure	Acceptance criteria
Comparison of the net-mean stress/principal stress as function of void ratio at full water saturation to the measured relation for p_{swell}	The stress state in the selected reference points in the buffer lies between 0.9xp_{swell} to 2xp_{swell}, where p_{swell} is defined from equation 10.10 in Åkesson et al.2010
Comparison of the deviatoric stress in the bentonite with the measured stress at failure at a given net-mean stress (see, for example, Åkesson 2010).	The deviatoric stress in the reference points in the buffer is not larger than the measured stress at failure

C.2.2.1 Final Stress – Void Ratio Relation at Full Water Saturation

The net mean stress against void ratio in the final water saturated state from the base case model is shown in Figure C-2. The plot shows that all points lie just below the swelling pressure curve or somewhat above. The points that align with the swelling pressure curve (solid black line) are those that have only undergone swelling (e.g. situated in the buffer blocks) while the points found above the swelling pressure curve have undergone both swelling and compression, these points are found in the GFM.

The variation in void ratio for a given value of net mean stress agrees with the hysteretic behavior of bentonite. Essentially, bentonite follows different paths in the void ratio – net mean stress space when undergoing swelling and consolidation respectively. A requirement on the material model/parameter set employed is that after full water saturation all points in the buffer lie between the two bounding lines in Figure C-2 (dashed and dash-dotted lines). As can be seen this is indeed the case in the base case model.

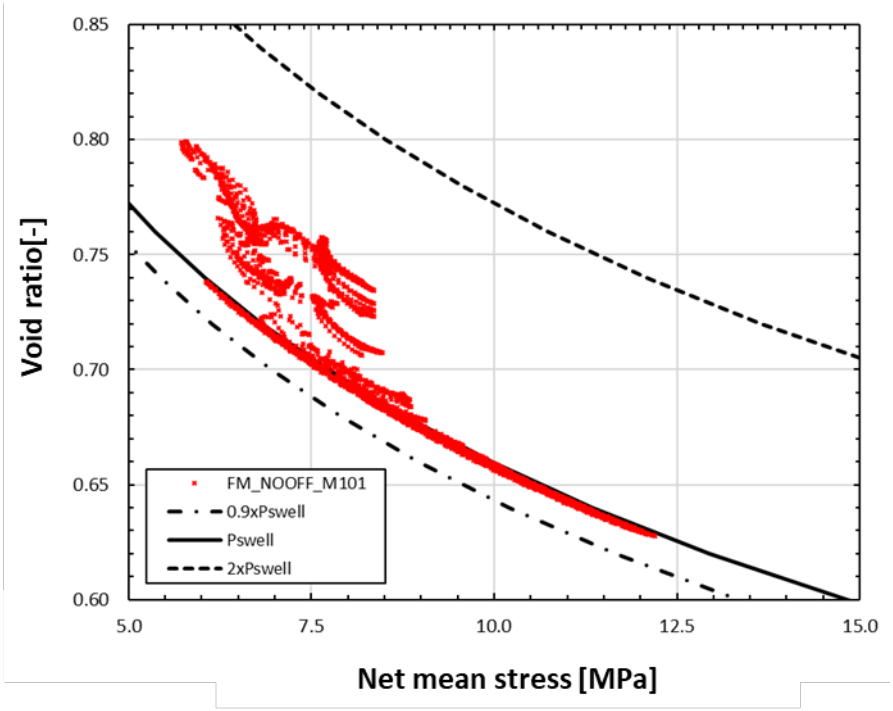

Figure C-2: Net mean stress versus void ratio once all points in the buffer were fully water saturated (data from the base case model FM_NOOFF_M101)

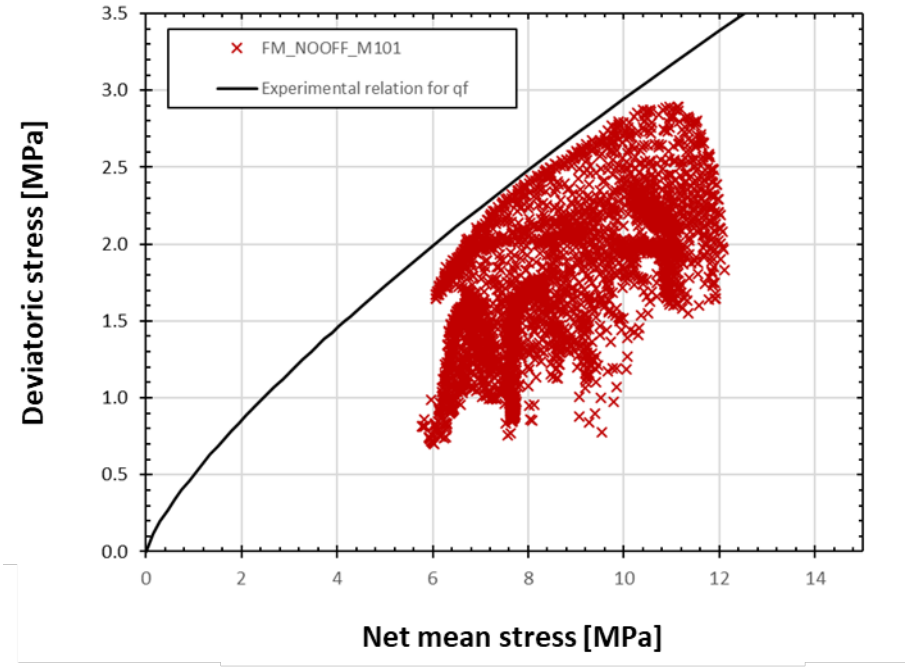

Figure C-3: Data from the final state in the model

C.2.2.1 Deviatoric Stress in the Bentonite

A further check on the material model was carried out by analysing the relation between deviatoric and net mean stress in the buffer blocks. This can be compared to the measured stress at failure at a given net-mean stress for saturated bentonite (see, for example, Åkesson et al. 2010). No points should lie significantly above this relation, which is shown as the black solid line in Figure C-3. The results from the base case model (FM_NOOFF_M001) are shown as the red crosses in figure (only the points in the bentonite were analysed). All points lie below the yield stress – net mean stress relation and hence also this constraint on the material model is fulfilled.

C.3 REFERENCES

Åkesson, M, L. Börgesson and O. Kristensson. 2010. SR-Site Data Report. THM Modelling of Buffer, Backfill and Other System Components.' SKB TR-10-44. Svensk Kärnbränslehantering AB.

APPENDIX D: NUMERICAL VERIFICATION AND MATERIAL MODEL ACCURACY OF MODELS WITH AIRGAPS SIMULATED IN TASK 3

The numerical verification and the material model validation of the models with airgaps in Task 3 is reported in this appendix.

The numerical accuracy of the models was verified only for the model with airgap UFC, as the models in general are very similar. The numerical accuracy was evaluated by comparing the max and min values of the net mean stress at full water saturation (in practice at the end of the simulation, which was run for 200 years) as well as the time to 99% total saturation in the HCB component between three different models:

- M01C – Reference model
- M01CM – Fine mesh model
- M01CT – Fine time-step model

The number of nodes and time-steps taken in these three models are given in Table D-1.

Table D-1: Number of nodes and elements in the verification models

Model	M01C	M01CM	M01CT
Number of nodes	2 672	4141	2672
Number of time steps	1 223	1659	4454

The max and min values of net mean stress and the time to 99% saturation in the buffer block component, as well as the relative difference to the reference model, is given in Table D-2.

Table D-2: Numerical varication of models - Results

	M01C	M01CM	M01CT
MIN <Peff> [MPa]	7.7279	7.7487	7.7256
Difference vs M01C	-	0.27%	-0.03%
MAX <Peff> [MPa]	11.340	11.337	11.341
Difference vs M01C	-	-0.03%	0.01%
Time to 99% saturation [years]	29.2	29.1	29.0
Difference vs M01C	-	-0.34%	-0.68%

All deviations are below 1% which was defined as the acceptance criteria, and hence the numerical accuracy of the models has been verified.

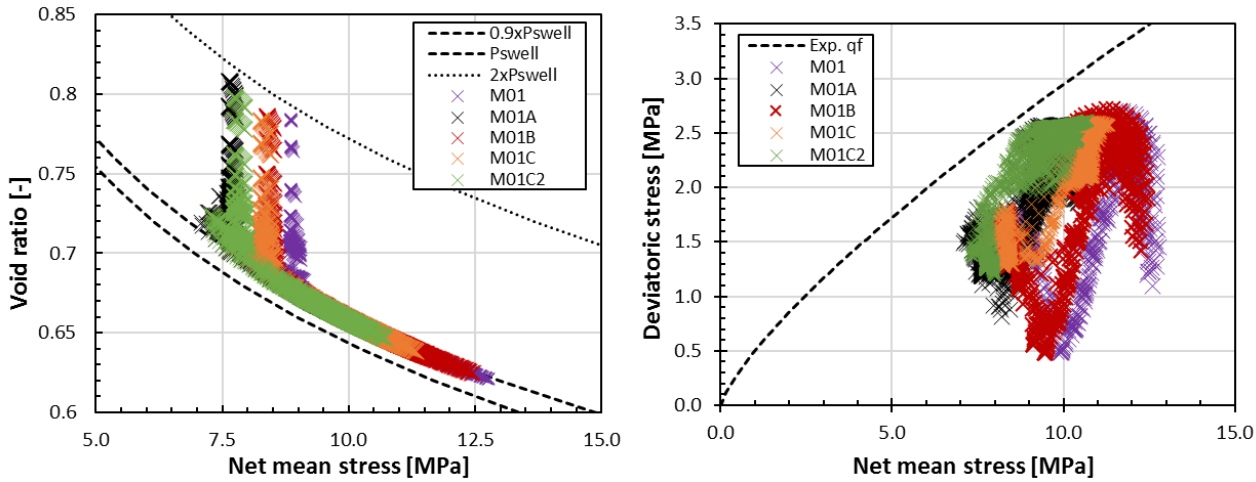

Figure D-1: Evaluation of the final state of the models in terms of net mean stress versus void ratio (left) and deviatoric stress (right)

The material model accuracy was evaluated by analyzing the final water-saturated state in the buffer components. In Figure D-1 (left), a void ratio – net mean stress diagram is shown while Figure D-1 (right) shows a deviatoric stress – net mean stress diagram. Results from all the models are included in the diagrams. It was checked that the results meet the acceptance criteria, which are defined for the final saturated state (evaluated at the end of the simulations):

- all points in the buffer must lie in the interval defined by the curves $0.9xP_{swell}$ and $2xP_{swell}$, in the net mean stress – void ratio phase space. The upper bounding value was chosen to allow for realistic final states in the gap-fill material that undergoes swelling and compression. The lower bounding value was chosen to allow values just below the swelling pressure in the block material, which, from experience, is known to be difficult to avoid in the models.
- all points in the buffer must lie below or just above the failure cure in the net mean stress – deviatoric stress phase space.

As is seen in Figure D-1 this is the case for all models, and hence they are considered acceptable.

APPENDIX E: STUDY OF THE DRY DENSITY AT THE UFC HEMI HEAD

During the modelling carried out in Step 1 (see Section 4) it was found that the dry density field around the UFC hemi head showed a decrease in magnitude close to the surface of the UFC. This can be seen in Figure E-1 where the dry-density distributions in front of the UFC are shown for two different models. The profiles are obtained along the same direction as the UFC axis along the purple line in the illustration of the modelled geometry in the lower-left corner of the graph.

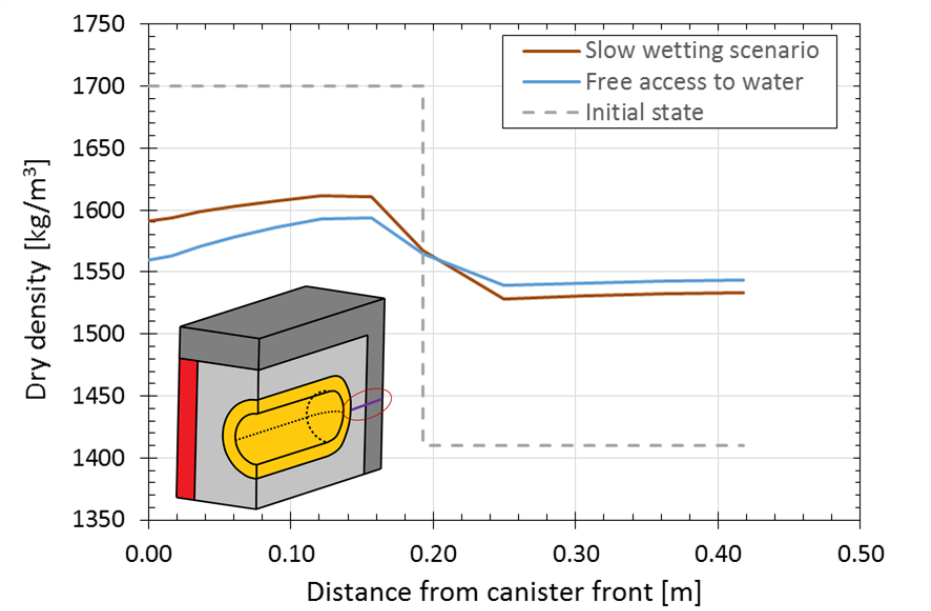

Figure E-1: The dry-density distribution in front of the UFC evaluated at the purple line in the illustration in the lower-left corner of the graph

As is evident in Figure E-1, the dry density in the buffer blocks increases when looking from the UFC surface towards the GFM. In general, higher density is expected near the UFC as compared to near the GFM (i.e., an outwards decreasing density gradient), even if the gradient may be small. The cause of the obtained outwards increasing gradient, and whether it was an effect to be expected in reality or artefacts in the model was further analyzed using simplified geometries as part of the modelling in Step 2.

New models with similar setup to that used in Step 1, except for the geometry, were developed to facilitate an investigation of the dry density field at the UFC hemi head. The geometry was simplified by assuming UFCs which had rectangular parallelepiped shape, and the discretization was coarser as well, see Figure E-3. The same appearance of the dry density field was again found for the new models, see Figure E-2. Thus, the governing mechanism seems to be independent on the shape of the UFC. This enabled use of the much-simplified geometry in the study.

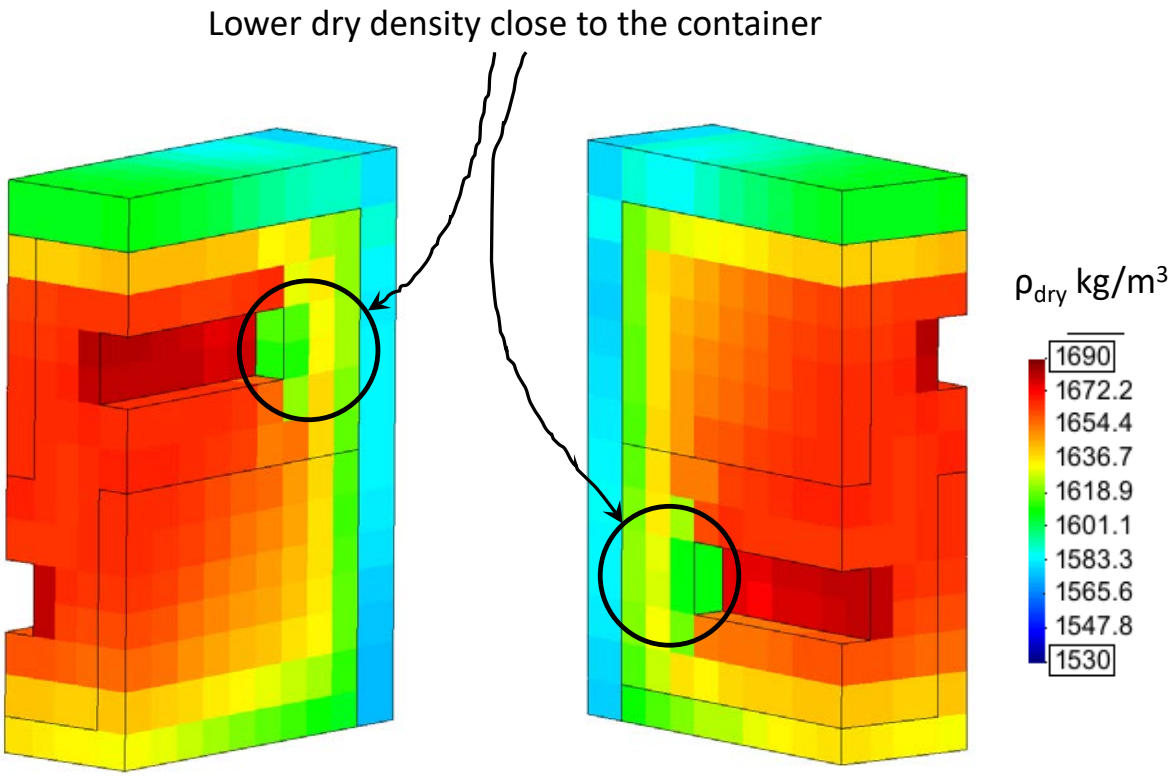

Figure E-2: The dry-density distribution at the UFC gable has low values close to the rectangular parallelepiped shaped UFC

To study this phenomenon in a convenient way, hydro-mechanical plane 2D models with different features were developed. The setup of these is described in the following section and after that the investigation itself is described.

E.1 Model Description

The study was limited to hydromechanical processes since these are considered to have the most significant effect for the deformation field in the buffer. As mentioned above, the geometry of the models was plane (the out-of-plane deformation was zero). This is of course not a proper way to represent the actual repository, but convenient for the study. The plane section that defined the 2D geometry was obtained from performing a vertical cut through the 3D model with the simplified UFC geometry at the centre of the upper UFC, see Figure E-3. The dimensions, initial conditions, and boundary conditions were equal for 3D (full water access case) and 2D models. The material representations were also equal between the 2D and 3D models, see Section 4.

An additional material model was used in one plane model when trying to incorporate slip at the interface between the UFC and buffer, see Table E-1. When using this material model, the option using the “updated Lagrangean method” (updating the coordinates at each time step) had to be deactivated since the “slip model” did not support this feature.

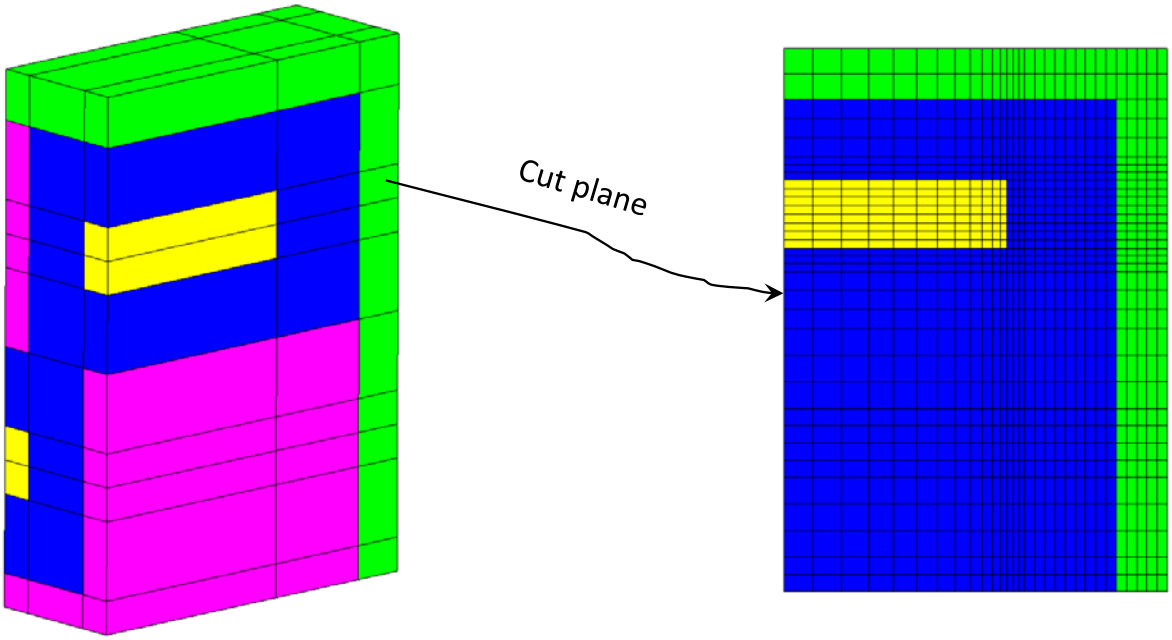

Figure E-3: 2D model geometry generated from cutting the simplified 3D model vertically through the centre of the upper UFC with the finite element shown

Table E-1: Elastic-viscoplastic interface model and parameter values

Increment	Equation	Variable	Value
Total displacement	$d\boldsymbol{u} = d\boldsymbol{u}^{e} + d\boldsymbol{u}^{vp}$		
Increment			
Elastic displacement increment:	$d\boldsymbol{t}' = \boldsymbol{K}' d\boldsymbol{u}^{e}$ $d\sigma'\boldsymbol{e}_n + d\tau\boldsymbol{e}_t = K'_{nn} du^{e}{}_n \boldsymbol{e}_n + K'_{tt} du^{e}{}_t \boldsymbol{e}_t$ $K'_{nn} = \begin{cases} \frac{m}{a - a_{min}} \text{ if } a > a_{min} \\ m + 10 \text{ otherwise} \end{cases}$ $K_{tt} = K_s$	$\boldsymbol{m}$ **[MPa]** $\boldsymbol{a_{min}}$ **[m]** $\boldsymbol{K_s}$ **[MPa/m]**	100 10^{-4} 100
Viscoplastic strain increment:	$d\boldsymbol{u}^{vp} = \dot{\boldsymbol{u}}^{vp} dt$ $\dot{\boldsymbol{u}}^{vp} = \begin{cases} \Gamma \left(\frac{f}{f_0}\right)^{N} \frac{\partial g}{\partial \boldsymbol{t}'} \text{ if} \frac{f}{f_0} \geq 0 \\ \boldsymbol{0} \text{ if} \frac{f}{f_0} < 0 \end{cases}$ $f_0 = 1 \text{ Mpa}^2$ $f = \tau^2 - (c - \sigma' \tan\phi_0)^2$ $\frac{\partial g}{\partial \boldsymbol{t}'} = 2\tau\boldsymbol{e}_t$ $^{(a)} \quad c = c_0 \left(1 - \frac{u_t^{vp}}{u_c^*}\right)$	$\boldsymbol{\Gamma}$ **[m/(MPa·s)]** $\boldsymbol{N}$ **[-]** $\boldsymbol{\phi_0}$ **[°]** $\boldsymbol{c_0}$ **[MPa]** $\boldsymbol{u_c^*}$ **[m]**	10^{-3} 1 10 10^{-6} 10^{3}

(a) $c \approx c_0$ If $u_c^* \gg u_t^{vp}$ which will be the case with the chosen parameter value.

E.2 Investigation, Discussion, Conclusions

First, the effect from including the stiff steel UFC in the swelling clay was studied by comparing a model with and without the steel UFC. This can also be seen as having one model with a "steel UFC" and another with a "clay UFC". To get an understanding of the mode of deformation taking place in the models, the undeformed and deformed finite element meshes are shown in Figure E-4. It should be noted that the deformation in the figures is obtained by using 6 times the actual displacements. The undeformed outline of the components is indicated by the red line in the drawings showing the deformed geometries. The lower drawing shows a close-up of the deformed mesh of the steel UFC model where the shearing deformation mode is clearly seen along the interface towards the UFC. The shown deformation is obtained after simulating 200 years of full water access. There are a lot in common between the deformed meshes, in the vicinity of the UFC however, the mode of deformation is quite different.

Especially so about the UFC gable where the steel UFC introduces a constraint for the deformation. This is evident when studying the lower drawing in Figure E-4 showing a close-up of the deformed mesh of the steel UFC model. The perfect bond between the buffer and UFC makes the UFC act as a retaining constraint on the surrounding swelling buffer, which introduce a significant shearing mode of deformation.

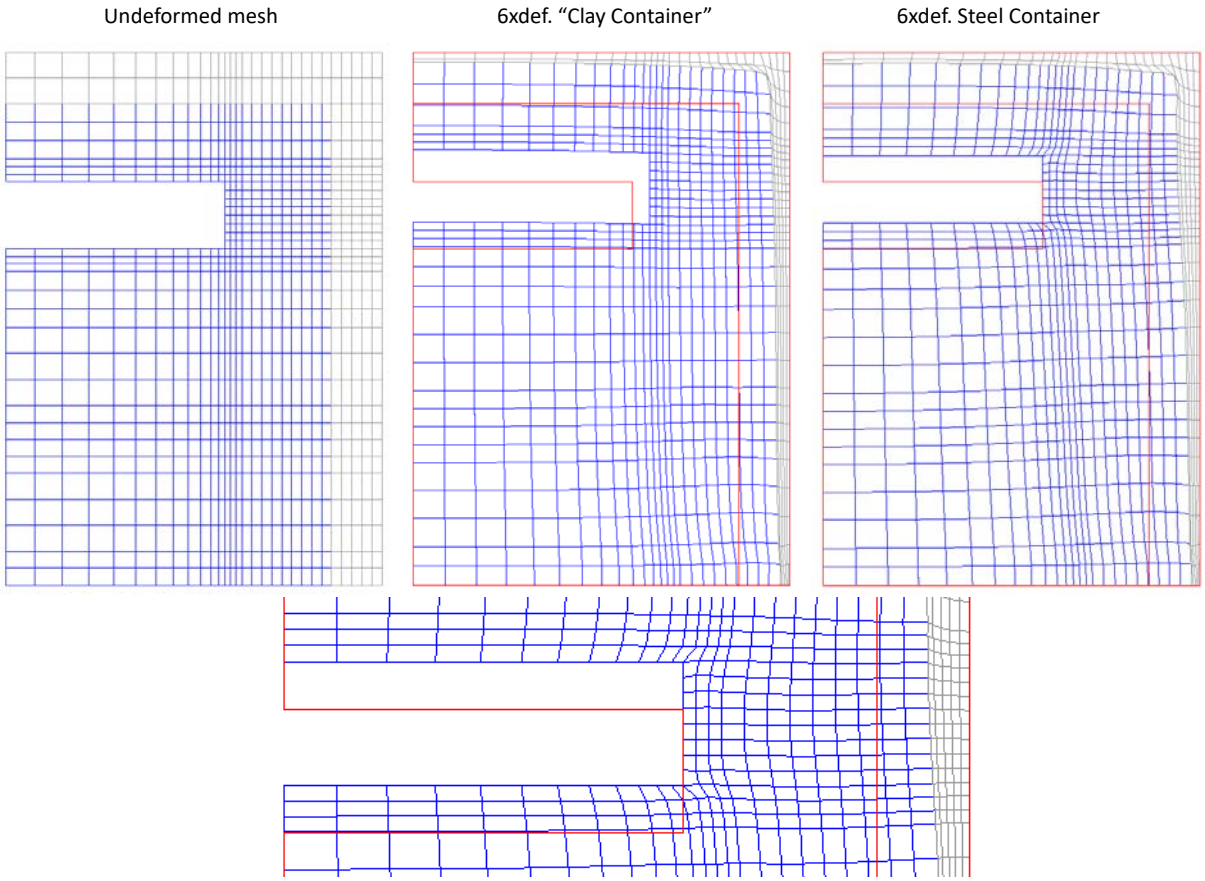

Figure E-4: The undeformed and deformed finite element mesh, for the “clay” and steel UFC models

The corresponding final dry density fields are given in Figure E-5. The difference between the dry density fields around the UFC is obvious, with significantly lower values at the UFC gable for the steel UFC model. Since the steel UFC does not swell, a horizontal homogenization of the buffer components will give a lower fully homogenized dry density for a section through the UFC as compared to another section:

- Horizontally fully homogenized non-UFC section: $\rho_d = 1661$ kg/m^3
- Horizontally fully homogenized UFC section: $\rho_d = 1607$ kg/m^3

Thus, an overall lower dry density is expected for buffer sections outside of the UFC gable as compared to sections at some distance below the UFC.

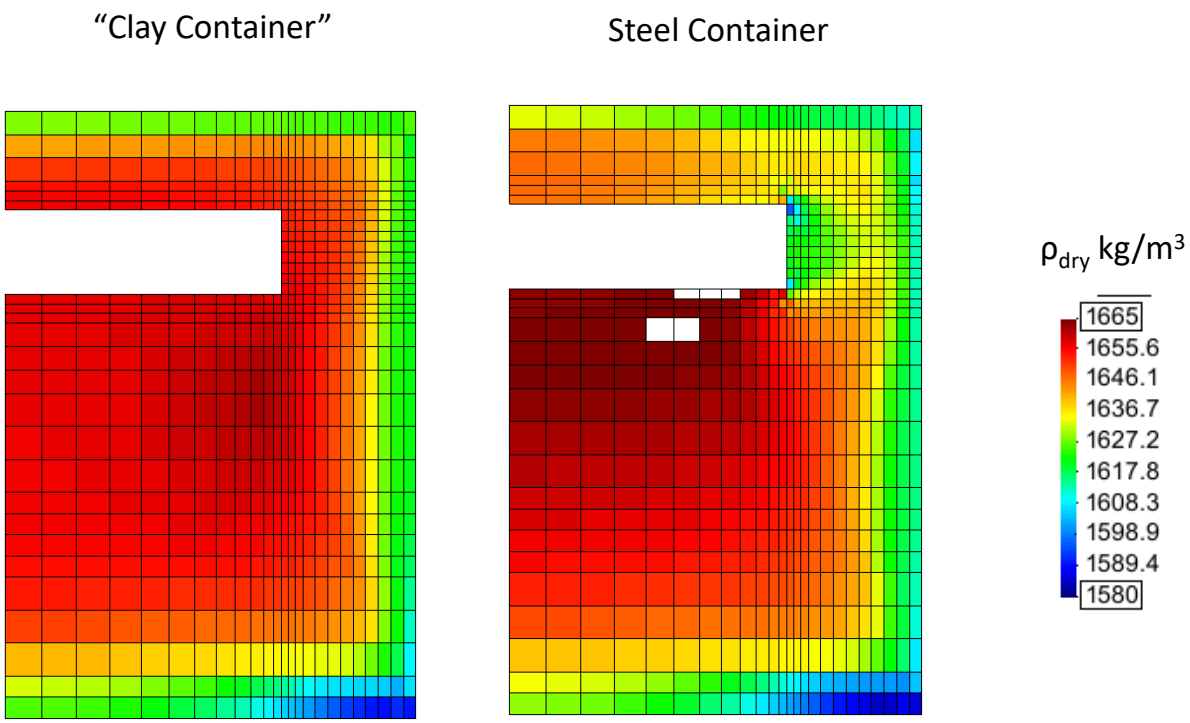

Figure E-5: The dry density fields obtained from models including a “clay UFC” (no steel UFC) and a steel UFC

To make the quantitative difference in dry density between the two models clearer, profiles of dry density along several horizontal lines from the UFC gable and outwards are shown in Figure E-6.The profiles were obtained from models without an UFC (i.e., with a clay UFC), (grey solid) and with a steel UFC (black dotted). The fully horizontally homogenized dry densities for the two models, with (blue hatched) and without the steel UFC (red hatched), are also indicated.

The effect that is studied becomes visible when looking at the profiles obtained from the model including the steel UFC, i.e., the dip of the dry density profiles when getting closer to the UFC.

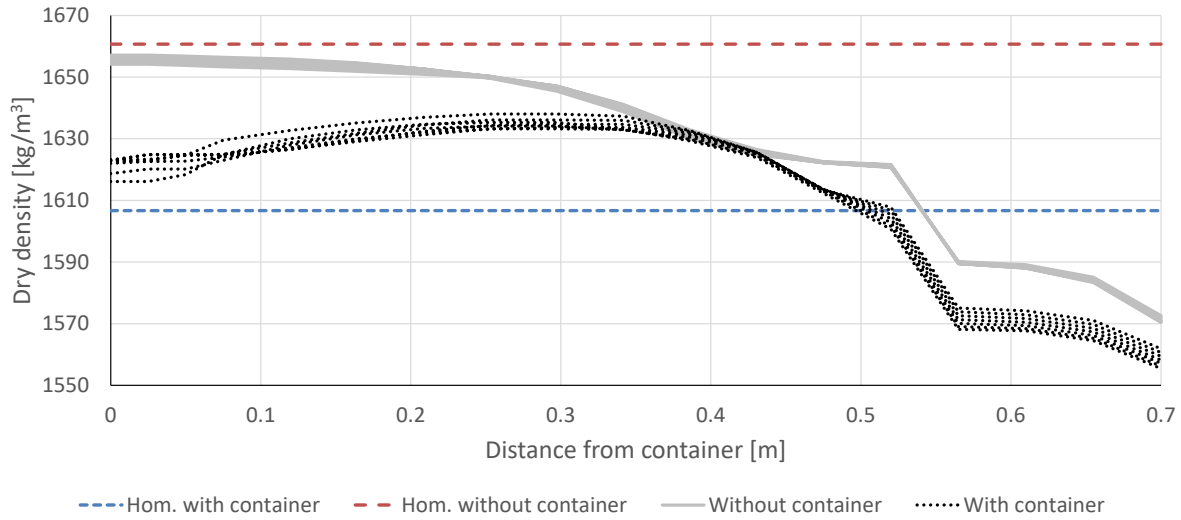

Figure E-6: The dry density profile along several horizontal lines from the centre of the UFC gable and outwards

When studying and comparing the models the following can be concluded:

- The effect of lower dry density close to the UFC is still occurring for a differently shaped UFC as compared to the one in the actual design.
- The steel UFC can be seen as a constraint acting on the deformation.
- The UFC can also be seen as a “shield”, protecting the buffer close to the gable from mechanical influence from other parts of the buffer.
- In the steel UFC model, the normal stresses at the UFC/buffer interface are always compressive. This indicates that no gaps would open even if there was a possibility for this in the model.

There is however a mechanism which potentially could have a significant effect on the deformation around the UFC, namely slip between the UFC and clay buffer. To evaluate whether slip along the UFC surface could be active in the model, the stress state (σ_{xy} and σ_{yy}) at the UFC/buffer interface is inserted into a slip condition:

$$\begin{aligned} &\text{if } \sigma_{xy} < \sigma_{yy}\tan\phi \text{ then no slip ocurs} \\ &\text{if } \sigma_{xy} = \sigma_{yy}\tan\phi \text{ then slip ocurs} \end{aligned} \quad ’$$

and the corresponding friction angle, ϕ, can be computed and compared to an experimentally motivated value (5°). To the left in Figure E-7 the stress components inserted into the slip condition are indicated and to the right, positions where the slip is evaluated to be possible are indicated by the red marking.

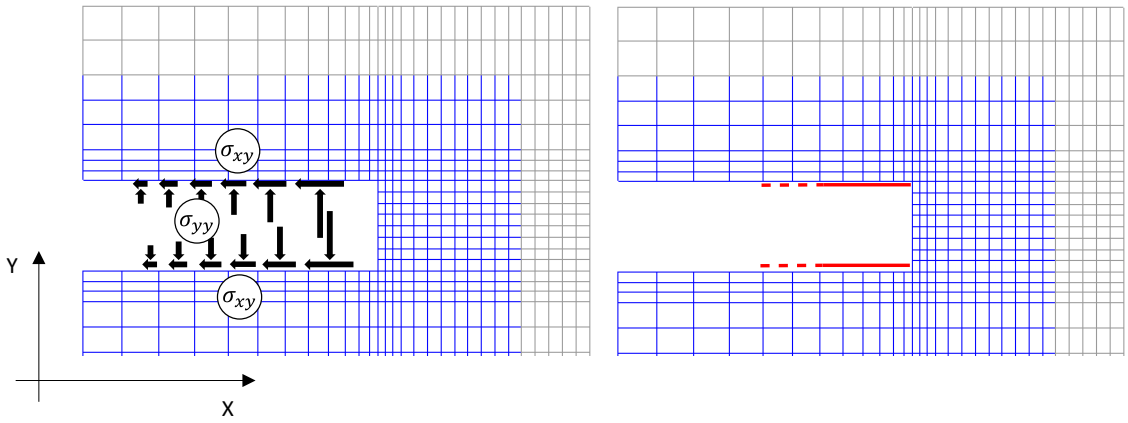

Figure E-7: Stress components at the UFC/buffer interface used when evaluating if slip may occur in the present model and positions where slip might occur according to the evaluation (right)

Since activated slip was found possible in the evaluation described above, a new model including this feature was developed. In this model the possibility for slip was introduced along the horizontal lines indicated by red in Figure E-8. The lines include the horizontal UFC/buffer interface, but also “internal” buffer interfaces continued from the UFC/buffer interfaces. The internal interfaces were created to avoid an overly constrained representation at the edge of the UFC. The internal slip could give rise to a somewhat exaggerated effect from the introduction of slip. On the other hand, a friction angle as low as 5°, which is indicated by experiments considering an interface between steel/clay, was not used in the model due to numerical issues. A friction angle of 10°, which is more in line with the property of a clay/clay interface, was used instead. As mentioned in the model description, when using the slip representation model the option using an “updated Lagrangean method” (updating the coordinates at each time step) had to be deactivated. To make proper comparisons with/without the slip mechanism yet a model, without the slip representation and without updating the coordinates, was developed.

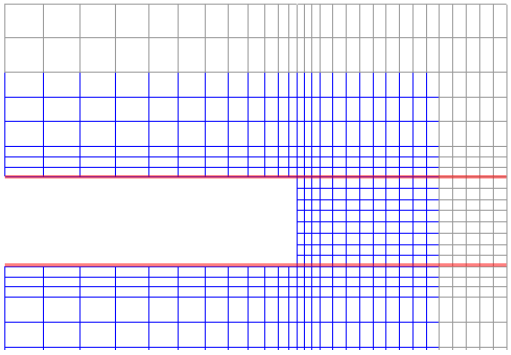

Figure E-8: Prescribed lines where slip may occur

Figure E-9 contains similar information about the effect of including slip as compared to what was given above in Figure E-4 regarding the presence of the UFC. The deformed meshes at the top in Figure E-9 were obtained by using 6 times the actual displacements. The undeformed outline of the components is indicated by the red line. In the bottom graph a close-up of the undeformed mesh (grey) and deformed mesh (blue and turquoise), on top of each other, is shown for the model where slip may occur. In the close-up, the deformed mesh was obtained by using 1 time the displacements. If comparing the deformation of the no-slip and slip meshes around the UFC gable, the effect from an active slip mechanism is visible. Also, when studying the close-up of the undeformed and deformed mesh (Figure E-9, bottom), where 1 time the displacements has been used, slip above and below the UFC is visible.

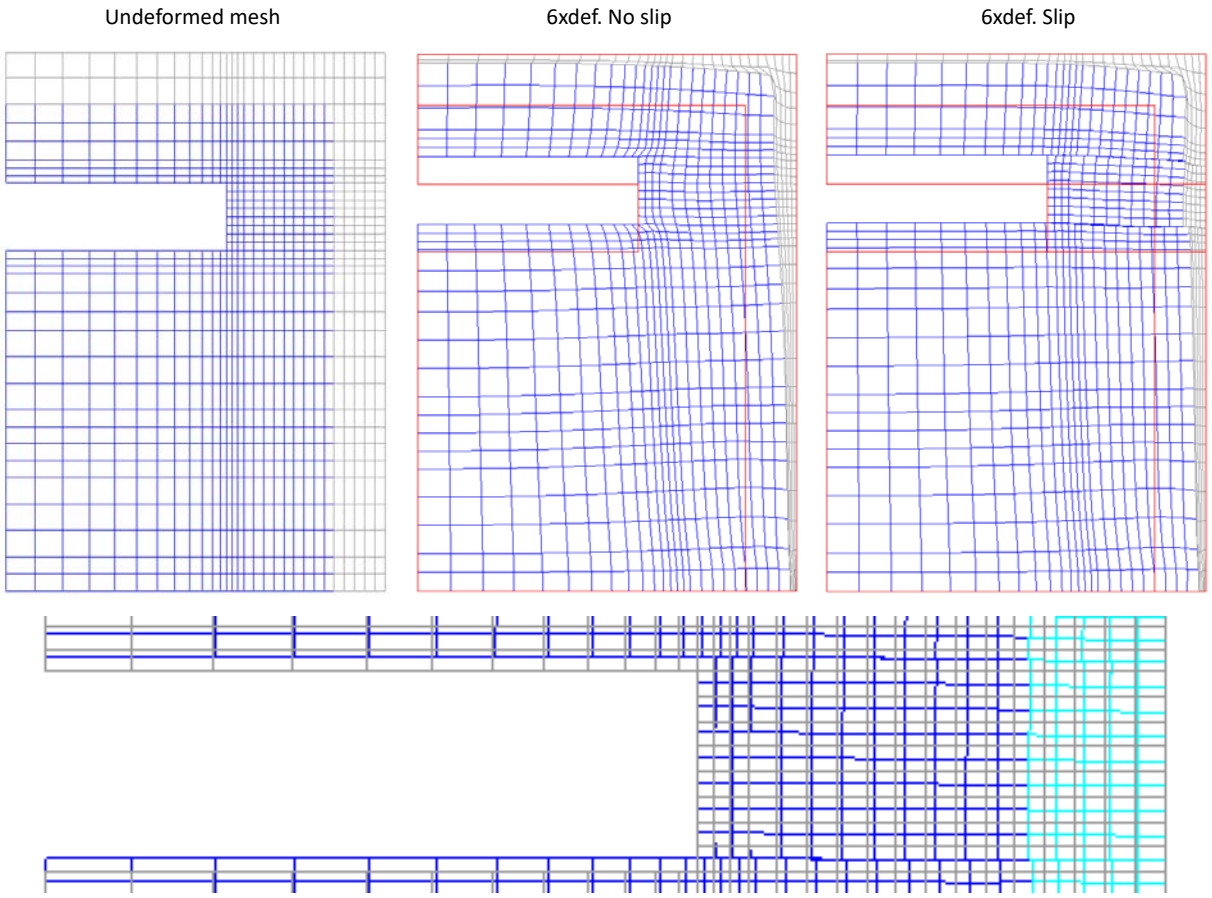

Figure E-9: (top) The undeformed and deformed finite element mesh, for the models where slip is not allowed (upper middle) and is allowed (upper right), with a close-up of the undeformed and deformed mesh with slip (below)

Figure E-10 shows the dry density fields obtained from excluding and including slip in the model. The appearance from the UFC center and downwards differs somewhat between models. The model with slip has a more distinct change in magnitude of the dry density between the buffer section on the outside of the UFC and the section below the UFC. The local variation in dry density at the UFC edge is also less pronounced (the field is smoother) in the model

where slip is permitted. Thus, there is a qualitative effect from including slip, but in terms of quantity it seems to be quite limited.

To investigate the quantitative aspect of the effect, Figure E-11 shows profiles of dry density from the model without and with the representation of the slip mechanism, black hatched and grey solid lines, respectively. The fully horizontally homogenized dry densities for sections with (blue hatched) and without the steel UFC (red hatched), are also shown. The profiles were taken along horizontal scan lines from the UFC gable and outwards. There are some differences in the dry density field of the models, but the studied feature, a decrease in dry density close to the UFC, is present for both models. The overall trend is that the dip in dry density is slightly less pronounced for the model where slip is made possible, but the feature is nevertheless present.

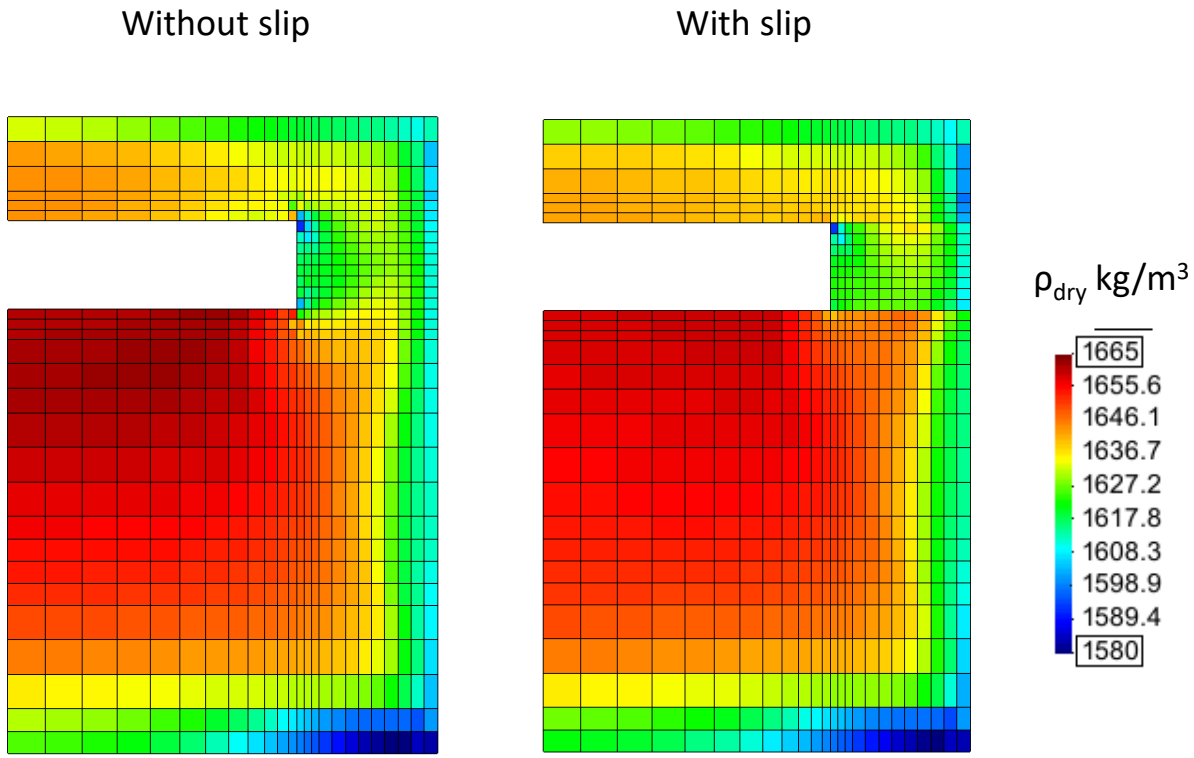

Figure E-10: The dry density fields in the buffer block material obtained from models without and with slip representation

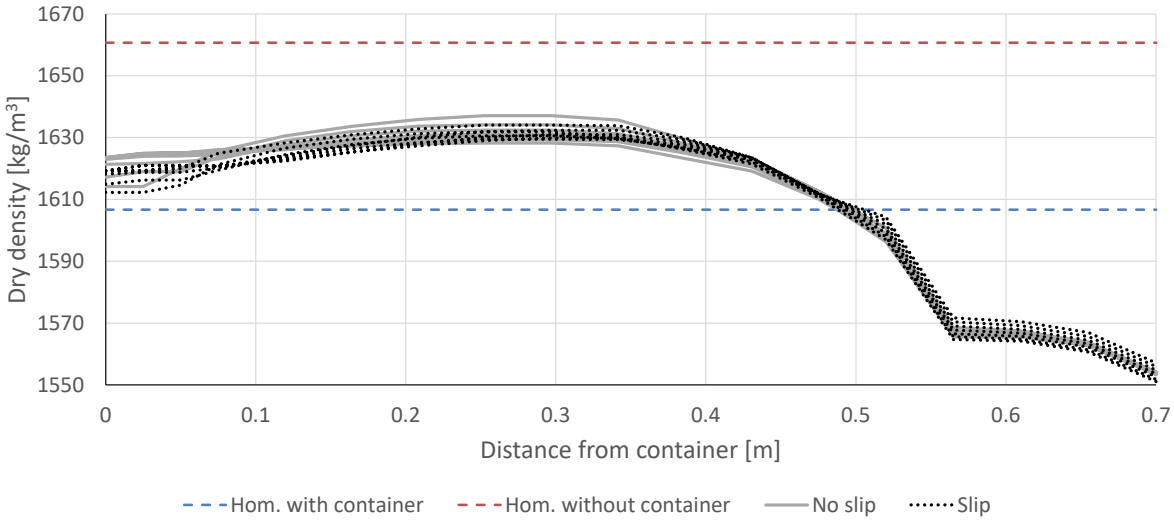

Figure E-11: The dry density profile along several horizontal lines from the UFC gable and outwards obtained from the models without and with slip representation

APPENDIX F: ANALYTICAL MODEL OF DRY BUFFER BOX DISPLACEMENT

The model describing the displacement of buffer boxes due to water inflow and swelling in one end of the emplacement room was developed assuming no offset between the buffer boxes in the upper and lower rows.

Each buffer-box stack was assumed to be separated to the next stack by a distance w_{gap}, which was assumed to be equal between all stacks (the layout is illustrated in Figure F-1). No other gaps between individual buffer blocks were considered. The underlying assumption was that water uptake and swelling of the buffer-box stack at one end of the emplacement room caused the buffer in that stack to expand and close the open gap between it and the neighboring buffer-box stack. Once the gap had closed, the swelling buffer-box stack would exert a force on its neighbor corresponding to the swelling pressure multiplied by the contact area. If this force was greater than the friction force generated when sliding a dry buffer-box stack, the dry stack would be pushed towards its neighbor.

The friction force generated by sliding N_{stack} buffer boxes scales linearly with N_{stack} while the force generated by the swelling buffer box stack decrease as the buffer expands. Hence, an equilibrium state exists where the friction force from displacing N_{stack} dry buffer-box stacks corresponds to the swelling force generated after the wet buffer-box stack has expanded a distance N_{stack} x w_{gap}. In the analytical model derived below the friction force as function of N_{stack} was derived and some simple estimates of the effects of swelling was then quantified by estimating the swelling force as function of N_{stack}.

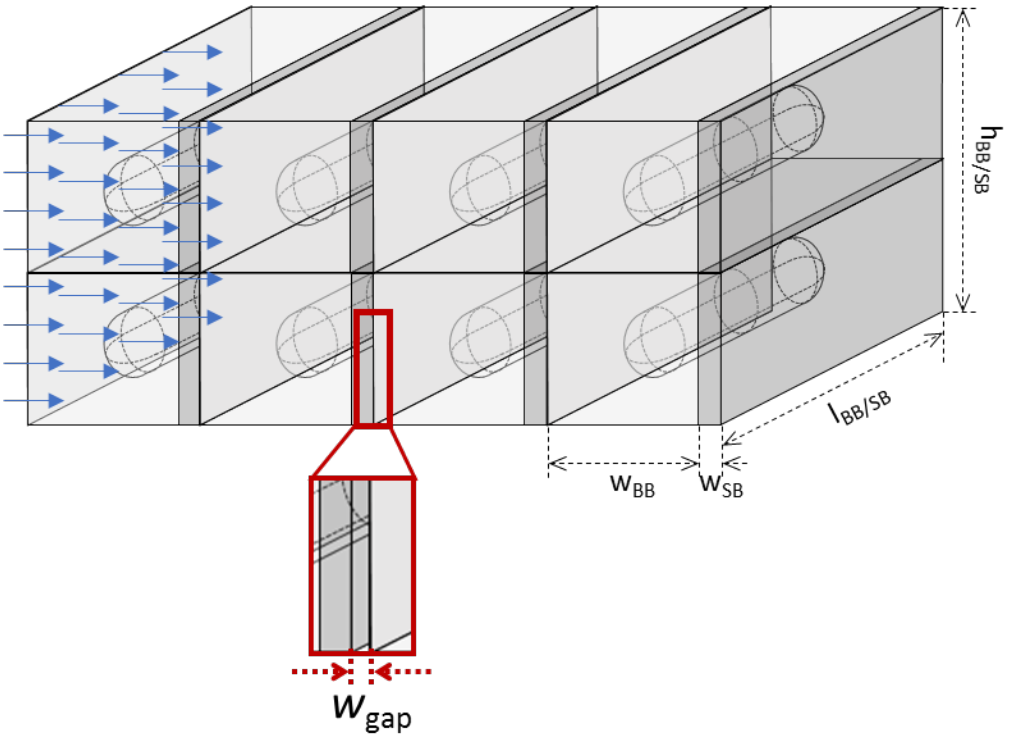

Figure F-1: Basic geometry assumed when developing the analytical model

F.1 Friction force

The friction force generated from one stack of buffer boxes can be divided into wall friction and floor friction (Figure F-2). The floor friction generated by a single stack of buffer boxes is the normal force on the floor multiplied with the tangent of friction angle, θ_{floor}:

$$F_{\text{f, floor}} = [2 \times (M_{\text{BBox}} + M_{\text{UFC}} + M_{\text{SB}}) + M_{GFM}] g \tan \theta_{\text{floor}}. \quad \text{(F-1)}$$

Here, M_{BBox} is the mass of the buffer blocks in a single buffer box, M_{UFC} is the mass of a single UFC, M_{SB} is the mass of a single spacer block and M_{GFM} is the mass of GFM situated on top of the upper buffer-box stack. For compactness, the mass of a buffer box stack is defined as:

$$M_{\text{Stack}} = [2 \times (M_{\text{BBox}} + M_{\text{UFC}} + M_{\text{SB}}) + M_{\text{GFM}}] \quad \text{(F-2)}$$

By combining Equation (F-1) and Equation (F-29 the friction force can be written as:

$$F_{\text{f, floor}} = M_{\text{Stack}} g \tan \theta_{\text{floor}}. \quad \text{(F-3)}$$

The friction against the wall is assumed to be generated in the interface between the buffer blocks and GFM. The normal stress on the buffer blocks at depth *z* depends on the weight of the GFM above. To accurately calculate the normal pressure on the buffer blocks the friction between the GFM and the wall, which acts to reduce that pressure, must be accounted for. Given the geometry the normal pressure can be derived in a similar way as when calculating the so-called silo pressure.

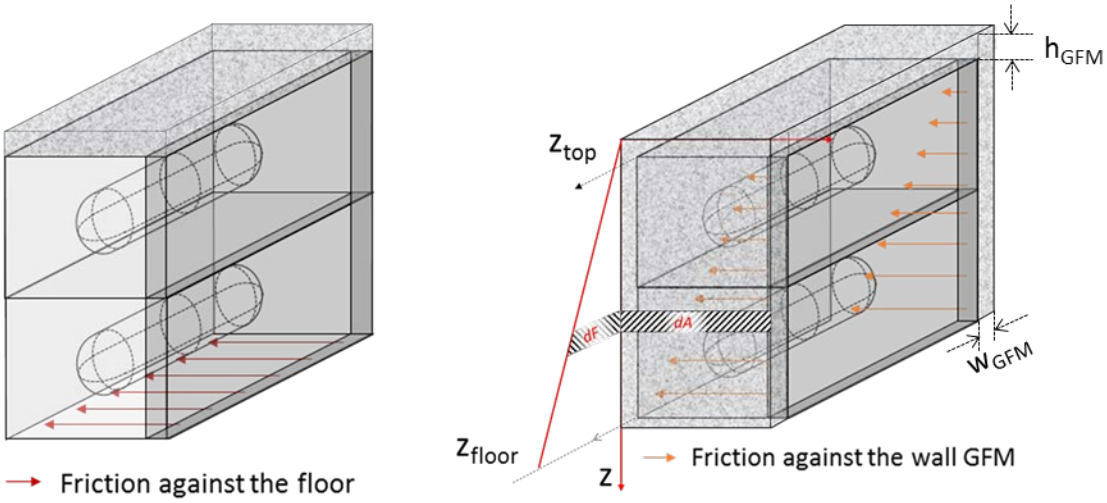

Figure F-2: Friction force generated (left panel: floor friction, right panel: wall friction)

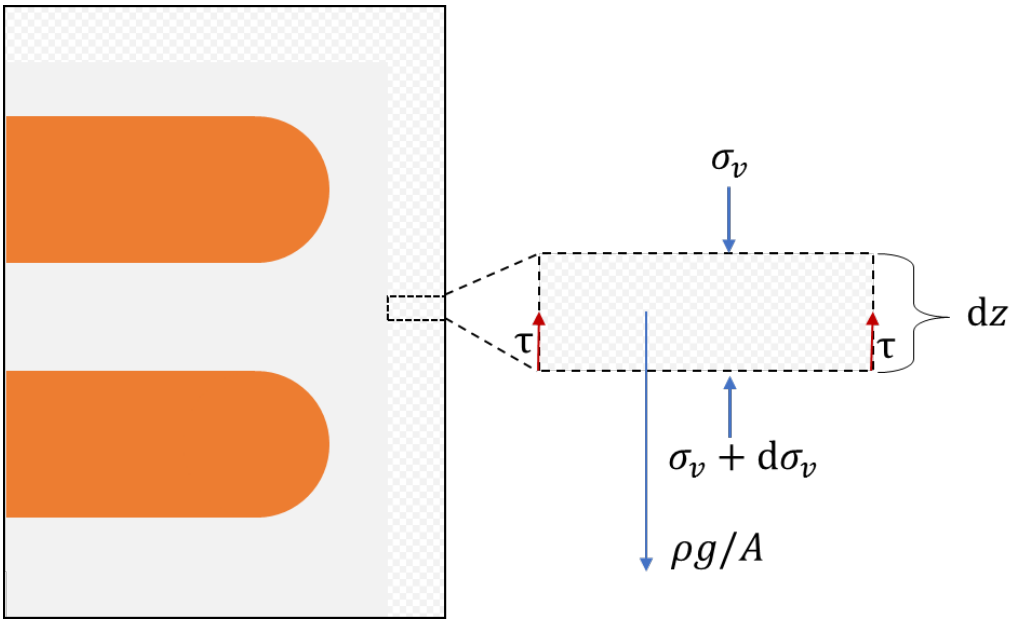

Figure F-3: Stress balance in a thin slice of the GFM

In a thin slice of the GFM the stress balance is as depicted in Figure F-3. Assuming steady state (e.g. balance of forces):

$$(\sigma_{\mathrm{v}} + d\sigma_{\mathrm{v}})A_{\mathrm{h}} + 2\tau A_{\mathrm{W}} = \sigma_{\mathrm{v}}A_{\mathrm{h}} + \rho g A_{\mathrm{h}} dz \quad \text{(F-4)}$$

Here A_h is the horizontal cross-section area in the GFM, A_w the area facing the wall and τ the friction stress in the rock/GFM interface. The horizontal cross-section area is:

$$A_h = w_{\mathrm{GFM}}[w_{BB} + w_{SB}] \quad \text{(F-5)}$$

and the area facing the wall is:

$$A_w = [w_{BB} + w_{SB}]\mathrm{dz} \quad \text{(F-6)}$$

Here w_{GFM} is the width of the GFM column between the bentonite blocks and the emplacement room's walls (Figure F-1), w_{BB}/w_{SB} is the width of a single buffer box/spacer block (Figure F-2).

These equations give:

$$d\sigma_{\mathrm{v}} + \frac{2\tau dz}{w_{\mathrm{GFM}}} = \rho g dz \quad \text{(F-7)}$$

The wall friction stress, τ, can be written as a function of the normal stress and friction angle:

$$\tau = \sigma_{\mathrm{h}}\tan(\theta_{\mathrm{GFM}}) = K\sigma_{\mathrm{v}}\tan(\theta_{\mathrm{GFM}}) \quad \text{(F-8)}$$

Here σ_h is the horizontal stress and it is assumed that $\sigma_h = K\sigma_v$, hence *K* is the ratio between the vertical and horizontal stress. The change in vertical stress with depth can be written:

$$\frac{d\sigma_{\mathrm{v}}}{dz} + \frac{2K\tan(\theta_{\mathrm{GFM}})}{w_{\mathrm{GFM}}}\sigma_{\mathrm{v}} = \rho g \quad \text{(F-9)}$$

The variation of σ_{v} with depth z is:

$$\sigma_{\mathrm{v}}(z) = \frac{\rho g w_{\mathrm{GFM}}}{2K\tan(\theta_{\mathrm{GFM}})}\left(1 - e^{-2K\tan(\theta_{\mathrm{GFM}})/w_{\mathrm{GFM}}}\right) \quad \text{(F-10)}$$

Here it has been assumed that the vertical stress is zero at the ceiling, hence the GFM does not push on the emplacement room's ceiling. The derivation also assumes that the friction angle is the same in all three different interfaces considered (GFM-GFM, GFM-blocks and GFM-Rock wall). While this may be an oversimplification it will not significantly affect the analysis; as can be seen in the results the dependence on the friction angle is relatively weak.

The friction generated between the gliding buffer blocks and the wall can be calculated as:

$$F_{\mathrm{f,wall}} = \int_{z_{\mathrm{top}}}^{z_{\mathrm{floor}}} K\sigma_{\mathrm{v}}(z)\tan(\theta_{\mathrm{GFM}})\,(w_{\mathrm{BB}} + w_{\mathrm{SB}})dz \quad \text{(F-11)}$$

The total friction force is thus:

$$F_{\mathrm{f,single}} = \int_{z_{\mathrm{top}}}^{z_{\mathrm{floor}}} \frac{\rho g w_{\mathrm{GFM}}}{2\tan(\theta_{\mathrm{GFM}})}\left(1 - e^{-2K\tan(\theta_{\mathrm{GFM}})z/w_{\mathrm{GFM}}}\right)\tan(\theta_{\mathrm{GFM}})\,(w_{\mathrm{BB}} + w_{\mathrm{SB}})dz + M_{\mathrm{stack}} g\tan\theta_{\mathrm{floor}} \quad \text{(F-12)}$$

Assuming $\theta_{\mathrm{GFM}} = \theta_{\mathrm{floor}} = \theta$ and re-arranging:

$$F_{\mathrm{f,single}} = \frac{\rho g w_{\mathrm{GFM}}(w_{\mathrm{BB}} + w_{\mathrm{SB}})}{2}\int_{z_{\mathrm{top}}}^{z_{\mathrm{floor}}}\left(1 - e^{-2K\tan(\theta)z/w_{\mathrm{GFM}}}\right)dz + M_{\mathrm{stack}} g\tan\theta \quad \text{(F-13)}$$

The friction force scales linearly with the number of sliding buffer box stacks, N_{stacks}. This is a function of how much the swelling buffer box has expanded, *u,* and the size of the initial gap between the buffer box stacks, w_{gap}:

$$N_{\mathrm{stacks}} = \frac{u}{w_{\mathrm{gap}}} \quad \text{(F-14)}$$

The total friction force is thus:

$$F_{\mathrm{f,total}} = N_{\mathrm{stacks}} \times F_{\mathrm{f,single}} = \frac{u}{w_{\mathrm{gap}}}F_{\mathrm{f,single}} = \frac{u}{w_{\mathrm{gap}}} \times \left[\frac{\rho g w_{\mathrm{GFM}}(w_{\mathrm{BB}}+w_{\mathrm{SB}})}{2}\int_{z_{\mathrm{top}}}^{z_{\mathrm{floor}}}\left(1 - e^{-2K\tan(\theta)z/w_{\mathrm{GFM}}}\right)dz + M_{\mathrm{stack}} g\tan\theta\right] \quad \text{(F-15)}$$

F.2 Swelling Pressure

The total friction force generated by displacing N_{stacks} buffer box stacks will reach an equilibrium with the force caused by the swelling of the hydrated buffer box stack at the end of the tunnel. The swelling pressure of the buffer box stack directly corresponds to the dry density of the buffer blocks in the final (water saturated) state. The swelling pressure as function of dry density can be parameterised according to Åkesson et al (2010):

$$log_{10}(P_{\mathrm{swell}}) = c_0 + c_1\rho_{\mathrm{d}} + c_2\rho_{\mathrm{d}}^2 \quad \text{(F-16)}$$

with the parameter values: c_0= -1.74 c_1= $4.12\cdot10^{-3}$; c_2 = $-3.94\cdot10^{-7}$ (p_{swell} in kPa; ρ_d in kg/m^3). To estimate the number of buffer box stacks that can be displaced due to water inflow at the end of the emplacement room it was assumed that:

- the force pushing on the dry buffer block stacks was generated by the buffer blocks in the buffer box/spacer blocks in the region taking up water, and

- the swelling only led to a volume increase in the direction parallel to the axis of the emplacement room tunnel.

The force pushing on the dry buffer box stacks is then:

$$F_{\mathrm{swell}} = P_{\mathrm{swell}}(\rho_{\mathrm{d}}) \times h_{\mathrm{BB/SB}} \times l_{\mathrm{BB/SB}} \quad \text{(F-17)}$$

An example of how the swelling force (red solid line) and friction force (blue solid line) depends on the displacement (e.g. expansion) of the swelling buffer box stack is shown in Figure F-4. Here a friction angle of 30° and an initial gap of 10 mm of was prescribed. Where the two curves intersect is the point at which equilibrium would be reached, hence for this configuration the buffer box stack taking up water would swell by about 0.4 m. In this calculation the ratio between the horizontal and vertical stress in the gap-fill material (e.g. the variable K in Equation (F-8)) was set to 1.

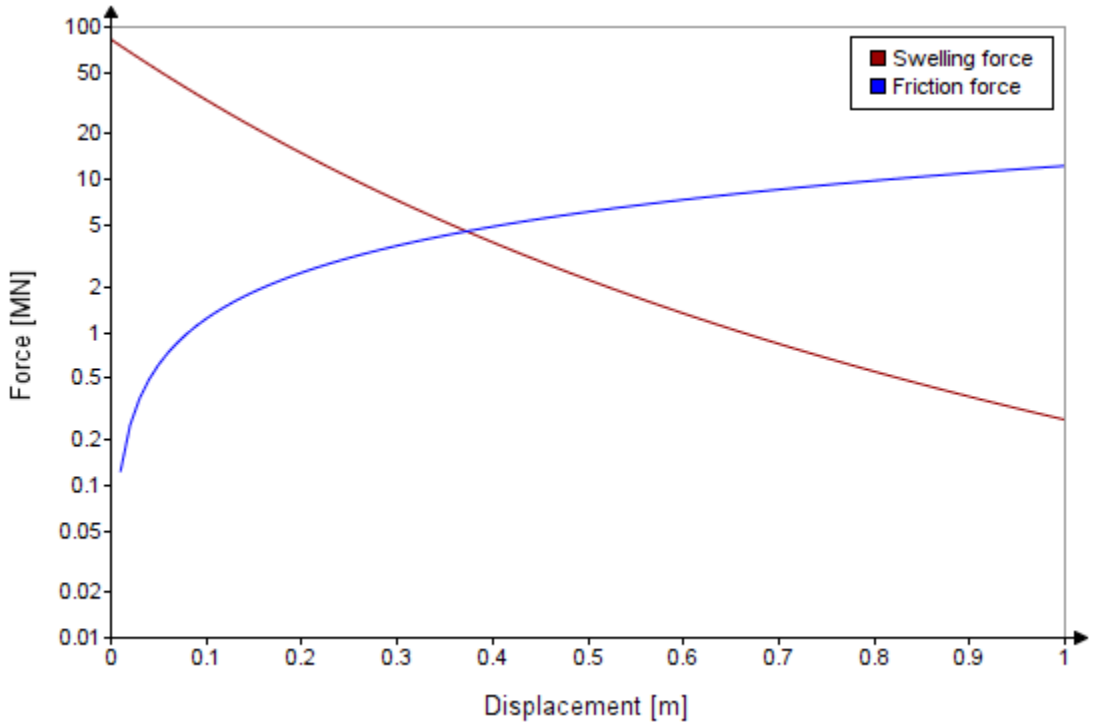

Figure F-4: Swelling force (red solid line) and Friction force (blue solid line)

The dry density in the swelling buffer box stack is:

$$\rho_{\mathrm{d}}(u) = \rho_{d0} \frac{V_{0,buffer}}{V_{0,buffer} + dV(u)} \quad \text{(F-18)}$$

Here $V_{0,\mathrm{buffer}}$ is the initial volume of the buffer blocks in the buffer box and spacer block. The displacement can be written $u = N_{\mathrm{stacks}} w_{\mathrm{gap}}$, where w_{gap} is the initial gap and N_{stacks} is the number of displaced buffer box stacks:

$$\rho_{\mathrm{d}}(N_{\mathrm{stacks}}) = \rho_{d0}\frac{h_{\mathrm{BB/SB}} \times l_{\mathrm{BB/SB}} \times (w_{\mathrm{BB}} + w_{\mathrm{SB}}) - 2 \times V_{UFC}}{h_{\mathrm{BB/SB}} \times l_{\mathrm{BB/SB}} \times (w_{\mathrm{BB}} + w_{\mathrm{SB}}) - 2 \times V_{UFC} + h_{\mathrm{BB/SB}} \times l_{\mathrm{BB/SB}} \times N_{\mathrm{stacks}} w_{\mathrm{gap}}} \quad \text{(F-19)}$$

By combining Equation (F-15), Equation (F-17) and Equation (F-19) the value of the number of displaced buffer box stacks and the average dry density in the “swelling” buffer box can be calculated while varying the friction angle and initial gap.

F.3 REFERENCES

Åkesson, M, L. Börgesson and O. Kristensson. 2010. SR-Site Data Report. THM Modelling of Buffer, Backfill and Other System Components.’ SKB TR-10-44. Svensk Kärnbränslehantering AB.

APPENDIX G: BENTONITE IN CONTACT WITH GROUNDWATER WITH HIGH SALINITY

To better understand the basis why the swelling pressure and water retention of bentonite decrease when contacted with groundwater of high salinity as compared to groundwater of low salinity, the thermodynamics used for representing our material for the two groundwaters is briefly outlined below. The description is in line with what has been reported in Karnland (1997).

The binary system with wet clay on one side and host rock permeated by groundwater on the other may be viewed as being separated by a semipermeable membrane between the clay and rock. In such a system the chemical potential, μ, is a central entity which describes the change in free energy when a unit of mass (or number of particles) is changed. This system can be analyzed using the chemical potential for the water inside the clay, μ_c, and for the groundwater in contact with the clay, μ_{gw}.

Assuming the groundwater being *unpressurized pure water*, its chemical potential may be expressed as,

$$\mu_{gw} = \mu_0 \,, \tag{G-1}$$

i.e., water at this state defines a reference level. The chemical potential of the clay-water when the clay sample is pressurized, can be expressed as,

$$\mu_c = \mu_0 + RT\ln\frac{p_c}{p_0} + P\nu \,, \tag{G-2}$$

where R denotes the gas constant, T temperature, and ν the molar volume of water. Isothermal conditions are only considered in this discussion, i.e., the temperature is constant. P is the system pressure, i.e., the mechanical pressure acting on the clay sample, p_c denotes the vapour pressure measured above the clay saturated with pure water, and p_0 denotes the vapour pressure measured above pure water. Subtracting the clay-water chemical potential from that of the groundwater and divide by ν results in,

$$-\frac{\mu_c - \mu_{gw}}{\nu} = -\frac{RT}{\nu}\ln\frac{p_c}{p_0} - P \,. \tag{G-3}$$

The left-hand side relation involving the difference between clay-water and groundwater chemical potentials is defining what usually is called suction,

$$s \equiv -\frac{\mu_c - \mu_{gw}}{\nu} \,. \tag{G-4}$$

Using this,

$$s + P = -\frac{RT}{\nu}\ln\frac{p_c}{p_0} \,. \tag{G-5}$$

The relation above directly relates suction to the system pressure through the expression containing temperature and partial pressures of clay-water and pure water.

If the groundwater is *unpressurized saline water,* its chemical potential can be expressed as,

$$\mu_{gw} = \mu_0 + RT\ln\frac{p_e}{p_0}. \tag{G-6}$$

Thus, there will be an osmotic pressure contribution for the groundwater since a vapour pressure p_e ($< p_0$) is measured above the saline groundwater (the index e indicates electrolyte). Due to the interaction between the groundwater and clay, salt (ions) from the groundwater may enter the clay and thereby introduce yet an osmotic contribution to the chemical potential of the clay-water. This can be expressed by a vapour pressure p_{ie} ($< p_0$) for the internal electrolyte. The resulting clay-water chemical potential can be expressed,

$$\mu_c = \mu_0 + RT\ln\frac{p_c}{p_0} + RT\ln\frac{p_{ie}}{p_0} + P\nu\ . \tag{G-7}$$

Following the same procedure as for pure water, the relation below can be formulated,

$$-\frac{\mu_c - \mu_{gw}}{\nu} = -\frac{RT}{\nu}\ln\frac{p_c}{p_0} - \frac{RT}{\nu}\ln\frac{p_{ie}}{p_0} - P + \frac{RT}{\nu}\ln\frac{p_e}{p_0}, \tag{G-8}$$

and if introducing the suction,

$$s + P = -\frac{RT}{\nu}\ln\frac{p_c}{p_0} - \frac{RT}{\nu}\ln\frac{p_{ie}}{p_0} + \frac{RT}{\nu}\ln\frac{p_e}{p_0}\ . \tag{G-9}$$

If the “saline relation” (G-9) is compared to the “pure water relation” (G-5), the effect from having a saline external water becomes evident. For the saline case the difference between the external and internal osmotic pressures should be subtracted from the pure water osmotic pressure.

G.1 Swelling Pressure

Introducing the condition $\mu_c = \mu_{gw}$, i.e., suction is zero, for the *case of pure water* (G-5), results in,

$$P = -\frac{RT}{\nu}\ln\frac{p_c}{p_0}. \tag{G-10}$$

Thus, the system pressure measured when $\mu_c = \mu_{gw}$ equals the right-hand side, containing the clay-water vapour pressure which can be measured when the system is unpressurized. (G-10) is often taken as the definition of swelling pressure, P_s. This can be stated formally as,

$$P_s|_{pw} \equiv -\frac{RT}{\nu}\ln\frac{p_c}{p_0}, \tag{G-11}$$

where the index pw indicate pure water.

Considering the *case of saline water* (G-9) when $\mu_c = \mu_{gw}$, the system pressure is obtained by,

$$P = -\frac{RT}{\nu}\ln\frac{p_c}{p_0} - \left(\left(-\frac{RT}{\nu}\ln\frac{p_e}{p_0}\right) - \left(-\frac{RT}{\nu}\ln\frac{p_{ie}}{p_0}\right)\right), \tag{G-12}$$

which, using the definition of $P_s|_{pw}$, given above, and new definitions,

$$P_{gw}{}^{osm} \equiv -\frac{RT}{v}\ln\frac{p_e}{p_0} \quad \text{and} \quad P_c{}^{osm} \equiv -\frac{RT}{v}\ln\frac{p_{ie}}{p_0}, \tag{G-13}$$

can be used to express the swelling pressure at saline conditions,

$$P_s|_{saline} \equiv P_s|_{pw} - \left(P_{gw}{}^{osm} - P_c{}^{osm}\right). \tag{G-14}$$

Thus, the obtained system pressure (swelling pressure) for a bentonite contacted by a saline groundwater is given by the swelling pressure obtained for pure water subtracted with the difference in osmotic pressures in the external and internal electrolyte.

In the simulations the representation of swelling pressure [MPa], was obtained by use of,

$$\tilde{p}_{swell}(e) = 10\text{^}\left[-3 + c_0 + c_1\frac{\rho_s}{1+e} + c_2\left(\frac{\rho_s}{1+e}\right)^2\right], \tag{G-15}$$

also given in Table 9-9, and calibrating its parameters to match data provided by NWMO.

The provided data was obtained by weighting the experimentally motivated expressions given in Table 5-5 in Dixon (2019), more specifically the expressions for TDS 200-225 g/L and TDS>335 g/L. When comparing the resulting curve with that used in the crystalline case the former was found to be significantly lower, see Figure G-1. As discussed above, this general decrease in swelling pressure in saline conditions is what to be expected from theoretical considerations.

By studying, for example, Figure 5-20 in Dixon (2019) one can see that the number of data points for the swelling pressure for dry densities above 1500 kg/m^3 at high salinities (e.g. SR-L and SR-Sh), is quite limited, and also that the spread in measured swelling pressure is not insignificant. This can be seen more clearly in Figures E5 and E6 in the same report (Dixon 2019). The measured swelling pressure at high salinity for a given dry density appears to be relatively uncertain.

Thus, in an attempt to evaluate if the adopted curve was representative, equation (G-14) was used. The difference $P_{gw}{}^{osm} - P_c{}^{osm}$ was calculated by considering the ion concentrations in reference water SR-270 and subtracted from the swelling pressure curve used for crystalline host rock, i.e., the expression in (G-15) equipped with the parameter set appropriate for pure water.

Two representations of swelling pressures at saline conditions could now be compared,

1. one obtained from evaluating the data in Dixon (2019) and
2. another obtained from using a swelling pressure curve for pure water and adjusted for salinity according to (G-14).

Comparison shows that the two representations differ quite significantly, see Figure G-1. The swelling pressure curve used for crystalline host rock with pure groundwater is shown as the red solid line. The swelling pressure curve #1, obtained from data in Dixon (2019), is shown as the black solid line. The swelling pressure curve #2, calculated from the pure water curve and an estimate of the difference in osmotic pressures in the external and internal electrolyte, is shown as the orange solid line. Comparing #1 and #2, the first representation generally predicts lower swelling pressures for dry densities relevant for the present analysis.

Possible reasons for the discrepancy between #1 and #2:

- Equation (G-14) does not accurately describe how the swelling pressure change with changing salinity:
    - Karnland (1997) evaluated this expression at different salinities and compared it with experimental data. They found that equation (G-14) agreed well with laboratory data.
- Poor representation of the swelling pressure curve in freshwater conditions:
    - The swelling pressure curve for saturated MX-80 bentonite in pure water conditions has been tested and revised extensively over the years, which make this unlikely to be the cause.
- Swelling pressure data in Dixon (2019) underestimates the actual swelling pressure:
    - As discussed in Dixon (2019), Section 5.5.2 the scatter in the measured swelling pressures is high, particularly for high TDS systems.

In conclusion it can be said that more experimental data for high TDS systems, especially at HCB densities, would be beneficial to increase the confidence in the models. Furthermore, sensitivity analyses of the impact using different swelling pressure curves to represent the bentonite in high TDS systems could be valuable. That was, however, not feasible withing the scope of this modelling project.

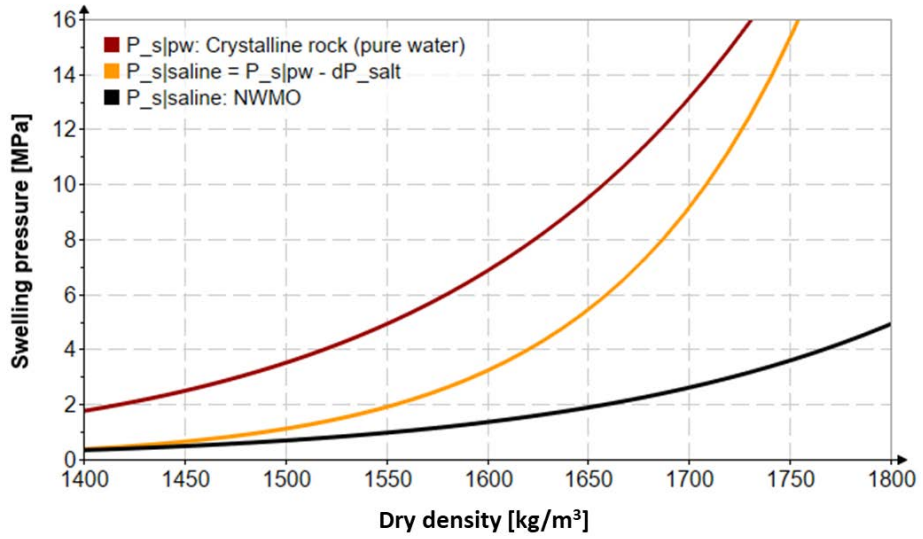

Figure G-1: Swelling pressure curves

G.2 Retention Under Free Swelling Conditions

Using equation (G-5) and assuming $P = 0$, i.e., free swelling conditions, free retention can be defined as,

$$s_{free}\big|_{pw} \equiv -\frac{RT}{v}\ln\frac{p_c}{p_0}. \tag{G-16}$$

Free retention is thus defined as the suction measured when the system pressure is zero. The partial pressure ratio is equal to the relative humidity as measured above the clay sample, thus $RH = p_c/p_0$. This can be used when determining the retention properties of a material sample by measuring RH (and temperature) above the sample for gravimetric different water contents $w = dm_w/dm_s$ so that a set $\{RH, w\}$ is obtained. Relative humidity can then be converted into suction using (G-16).

Assuming free swelling conditions for saline groundwater results in,

$$s_{free}\big|_{saline} \equiv s_{free}\big|_{pw} - \left({P_{gw}}^{osm} - {P_c}^{osm}\right), \tag{G-17}$$

which indicates that the saline free retention is given by the pure water free retention subtracted with the difference in osmotic pressures in the external and internal electrolyte.
From the relations defining the swelling pressures, (G-11) and (G-14), it follows that,

$$s_{free}\big|_{pw} = P_s|_{pw} \text{ and } s_{free}\big|_{saline} = P_s|_{saline}, \tag{G-18}$$

indicating that measurements of free retention (under unconfined conditions) should be matched by measurements of swelling pressure (under confined conditions) when the external water is identical.

G.3 Retention Under Confined Conditions

As in the case of the formulation used in CODE_BRIGHT, the retention property of a material is often defined by a relation between suction and degree of saturation measured under confined conditions. This is typically represented by models such as van Genuchten. For the case of pure water, this can be expressed using Equations (G-5) and (G-16),

$$s = s_{free}\big|_{pw} - P, \tag{G-19}$$

$s_{free}\big|_{pw}$ is usually given by a relation in terms of water content, but for confined conditions this can be translated to degree of saturation if the dry density is known. The system pressure will, during water uptake, increase from zero at the initial state to the full swelling pressure at full saturation. A simple assumption is that the system pressure increases linearly with increasing degree of saturation. A connection between the thermodynamic formulation, measurements, and models such as van Genuchten, assuming confined conditions, is thereby established for pure water systems.

For saline water systems, retention under confined conditions can be expressed as,

$$s = s_{free}\big|_{saline} - P = s_{free}\big|_{pw} - P - \left({P_{gw}}^{osm} - {P_c}^{osm}\right), \tag{G-20}$$

where the osmotic pressure difference is subtracted from the pure water relation. Either the osmotic pressure difference could be calculated from knowing the external water composition or free retention could in theory be measured using the correct external water composition. From a practical standpoint, there could be challenges carrying out the latter measurements.

It is here again mentioned that in the present work only the effect of salinity on the swelling pressure curve is considered. The effect on the retention is left for future investigations.

G.4 References

Dixon, D. 2019. ‘Review of the T-H-M-C Properties of MX-80 Bentonite.’ NWMO-TR-2019-07. Nuclear Waste Management Organisation.

Karnland O., 1997. Bentonite swelling pressure in strong NaCl solutions – Correlation between model calculations and experimentally determined data. SKB TR 97-31, Svensk Kärnbränslehantering AB.

APPENDIX H: SETTING THE PLASTIC PARAMETERS IN BBM

The plastic parameters $p_0{}^*$, M and p_s were obtained by using a similar strategy as described in Åkesson et al. (2010). This is based on identifying three stress states at yielding ($f = 0$):

$$\left(p'_A, q_A\right) = (p_s + 2p_{swell}, 0), \tag{H-1}$$

$$\left(p'_B, q_B\right) = \left(p_{swell}, q_f\right), \tag{H-2}$$

$$\left(p'_C, q_C\right) = \left(-q_f/6\,, q_f/2\right), \tag{H-3}$$

and insert these into the yield function,

$$f = 0 = q^2 - M^2(p' + p_s)(p_0 - p')\,, \tag{H-4}$$

to obtain three equations from which the plastic parameters can be obtained. The three points are defined by swelling pressure, p_{swell}, von Mises stress at failure, q_f, and the parameter p_s.

For the case with a **crystalline host rock**, where the groundwater has low salinity and is close to pure water,

$$p_{swell} = \tilde{p}_{swell}|_{pw}(e), \tag{H-5}$$

$$q_f = \tilde{q}_f(p') = \tilde{q}_f\left(\tilde{p}_{swell}|_{pw}(e)\right). \tag{H-6}$$

For models with the emplacement room in a **sedimentary host rock**, where the groundwater has a high salinity, a new swelling pressure curve was used, i.e.

$$p_{swell} = \tilde{p}_{swell}|_{saline}(e). \tag{H-7}$$

The von Mises stress at failure was given by,

$$q_f = \tilde{q}_f(p') = \tilde{q}_f\left(\tilde{p}_{swell}|_{pw}(e)\right), \tag{H-8}$$

Hence., the swelling pressure curve for pure water was used in the pressure dependent expression of the von Mises stress at failure for both crystalline and sedimentary host rock.

The motivation of the chosen functions used for swelling pressure and von Mises at failure is described in Åkesson et al. (2010). The swelling pressure was defined according to Equation H-9, with $\tilde{p}_{swell}(e)$ in MPa and the coefficients used are given in the Section 3.3.8.2 (crystalline host rock) and Section 9.1.2.4.2 (sedimentary host rock) respectively.

$$\tilde{p}_{swell}(e) = 10\text{^}\left[-3 + c_0 + c_1\frac{\rho_s}{1+e} + c_2\left(\frac{\rho_s}{1+e}\right)^2\right], \tag{H-9}$$

The von Mises at failure is given by,

$$\tilde{q}_f(p') = 0.5{p'}^{0.77}, \tag{H-10}$$

where the unit is MPa. The void ratio used for calculating p_{swell} was taken as the homogenized void ratio, e_H.

The value of the plastic stiffness λ_0 is obtained from,

$$\lambda_0 = -\frac{\tilde{p}_{swell}(e_H)}{\frac{d}{de}\tilde{p}_{swell}(e_H)}, \tag{H-11}$$

for the HCB-material, and,

$$\lambda_0 = -\frac{e_0 - e_H}{\ln\left(\tilde{p}_{swell}(e_0)\right) - \ln\left(\tilde{p}_{swell}(e_H)\right)}, \tag{H-12}$$

for the GFM-material, respectively.

H.1 References

Åkesson, M., L. Börgesson and O. Kristensson. 2010. 'SR-Site Data Report. THM Modelling of Buffer, Backfill and Other System Components.' SKB TR-10-44. Svensk Kärnbränslehantering AB.